PNNL-29079

Pacific Northwest
NATIONAL LABORATORY

Potential Impacts of Accelerated Climate Change

4th Annual Report of Work for NRC Agreement NRC-HQ-60-14-D-0025

January 2020

LR Leung
R Prasad

U.S. DEPARTMENT OF ENERGY

Prepared for the U.S. Nuclear Regulatory Commission
under an Interagency Agreement with the U.S. Department of Energy
Contract DE-AC05-76RL01830

PACIFIC NORTHWEST NATIONAL LABORATORY
operated by
BATTELLE
for the
UNITED STATES DEPARTMENT OF ENERGY
under Contract DE-AC05-76RL01830

Printed in the United States of America

Available to DOE and DOE contractors from the
Office of Scientific and Technical Information,
P.O. Box 62, Oak Ridge, TN 37831-0062;
ph: (865) 576-8401
fax: (865) 576-5728
email: reports@adonis.osti.gov

Available to the public from the National Technical Information Service
5301 Shawnee Rd., Alexandria, VA 22312
ph: (800) 553-NTIS (6847)
email: orders@ntis.gov <http://www.ntis.gov/about/form.aspx>
Online ordering: http://www.ntis.gov


This document was printed on recycled paper.
(8/2010)

PNNL-29079

Potential Impacts of Accelerated Climate Change

4th Annual Report of Work for NRC Agreement NRC-HQ-60-14-D-0025

January 2020

LR Leung
R Prasad

Prepared for the U.S. Nuclear Regulatory Commission
under an Interagency Agreement with the U.S. Department of Energy
Contract DE-AC05-76RL01830

Pacific Northwest National Laboratory
Richland, Washington 99352

Abstract

This study is part of the U.S. Nuclear Regulatory Commission's (NRC) Probabilistic Flood Hazard Assessment (PFHA) research plan that aims to develop regulatory tools and guidance to support and enhance the NRC's capacity to perform thorough and efficient reviews of license applications and license amendment requests. Pacific Northwest National Laboratory (PNNL) was contracted by the NRC to prepare a summary of current state of climate research and results regarding hydrometeorological phenomena that are of interest in safety assessments and environmental impact assessments for commercial nuclear power plants. In Year 1, Pacific Northwest National Laboratory (PNNL) staff prepared an annual report that summarized recent scientific findings about global and regional climate change, with a particular focus on climatic elements that are relevant to NRC concerns on a regional level (i.e., increasing air and water temperatures, decreasing water availability, increasing frequency and intensity of storms and flooding, and sea-level rise). In Year 2 and Year 3, PNNL staff summarized recent research findings about climate change for the southeast and midwest regions, respectively, including discussions of historical and projected changes in air temperature, precipitation, hurricanes, sea-level rise, storm surge, tornadoes, severe convective storms, flooding, low flows, and Great Lakes water levels. In Year 4, the focus of this report, region-specific scientific findings about climate change for the northeast region were reviewed. According to the U.S. Global Change Research Program (USGCRP) Third National Climate Assessment (NCA3) and the Climate Science Special Report (NCA4, Volume I), the northeast region consists of 12 states—Connecticut, Delaware, Maine, Maryland, Massachusetts, New Hampshire, New Jersey, New York, Pennsylvania, Rhode Island, Vermont, and West Virginia—and the District of Columbia. Within the northeast region, Connecticut, Delaware, Maryland, Massachusetts, New Hampshire, New Jersey, New York, and Pennsylvania have operating nuclear power plants. A new nuclear power reactor permit was approved by the NRC for the PSEG site in Delaware, which also hosts currently operating reactors. Therefore, having an improved understanding of potential climate changes and their hydrologic impacts in the northeast region is important to informing the PFHA research plan.

Climatic features relevant to the NRC for the northeast region include high-temperature extremes, precipitation extremes, tropical and extratropical cyclones, summer convective storms, sea-level rise and storm surge, hydrology and water level of Lake Ontario, and floods and seasonality. Drawing primarily from the NCA reports and peer-reviewed literature, this Year 4 annual report summarizes the observed climate, its past changes, and its projected changes, as well as 21st century hydrologic impacts in the northeast region. The northeast region exhibits long-term warming trends in all seasons in the 20th century. Warming is projected to continue in the future, with greater warming in winter and summer than spring and fall. Annual mean precipitation and extreme precipitation show a long-term increasing trend in the 20th century. Precipitation is projected to increase particularly in winter and spring while changes in summer are not significant. Extreme precipitation (0.02 annual exceedance probability) is projected to increase between 10% to 22% by the mid- and late-century. North Atlantic hurricanes are projected to increase in intensity, rainfall, and storm size. Projections of extratropical cyclone activity changes remain uncertain but theory suggests that convection associated with extratropical cyclones will become more vigorous even if extratropical cyclone activity may decrease. With warmer temperatures and more moisture, an increase in mesoscale convective system track density and intensity is projected for the mid-Atlantic/northeast region. The northeast region is a hotspot of accelerated sea-level rise in recent decades. Sea-level rise in the region is projected to be highest among cities worldwide due to weakening of the Atlantic Meridional Overturning Circulation. Combining increases in tropical cyclone intensity and sea-level rise, storm surge is projected to increase in the future but a shift of cyclone tracks towards offshore may cancel the effect of increase storm intensity, resulting in little change in storm surge in the future. As warming increases, the ratio of snow to total precipitation is declining and the center-volume date for winter-spring streamflow is shifting earlier in the year. These changes together are affecting seasonality of streamflow in the tributaries of Lake Ontario and show a marked dependence on latitude of the

tributary drainage area. Recent efforts point to promising approaches towards using more spatially-explicit models over the entire Lake Ontario drainage basin for streamflow simulations. PNNL staff presented updates summarizing these findings at the Fourth Annual PFHA Research Workshop in February 2020, at Rockville, Maryland.

Executive Summary

The study reported here is part of the U.S. Nuclear Regulatory Commission's (NRC's) Probabilistic Flood Hazard Assessment (PFHA) research plan that aims to develop regulatory tools and guidance to support and enhance the NRC's capacity to perform thorough and efficient reviews of license applications and license amendment requests. Pacific Northwest National Laboratory (PNNL) was contracted by the NRC to prepare a summary of current state of climate research and results regarding hydrometeorological phenomena that are of interest in safety assessments and environmental impact assessments for commercial nuclear power plants. In Year 1, PNNL staff prepared an annual report that summarized recent scientific findings about global and regional climate change, focusing in particular on climatic elements that are relevant to NRC concerns broadly across the conterminous United States (i.e., increasing air and water temperatures, decreasing water availability, increasing frequency and intensity of storms and flooding, and sea-level rise). In Year 2, PNNL staff summarized recent research findings about climate change for the southeast region (i.e., historical and projected changes in air temperature, precipitation, hurricanes, sea-level rise, storm surge, tornadoes, flooding, and low flows). In Year 3, the activities focused on reviewing region-specific scientific findings about climate change for the midwest region (i.e., historical and projected changes in air temperature, precipitation, severe storms, Great Lakes water levels, flooding, and low flows). In Year 4, the focus of this report, region-specific scientific findings about climate change for the northeast region were reviewed. According to the U.S. Global Change Research Program (USGCRP) Third National Climate Assessment (NCA3) and the Climate Science Special Report (NCA4, Volume I), the northeast region consists of 12 states—Connecticut, Delaware, Maine, Maryland, Massachusetts, New Hampshire, New Jersey, New York, Pennsylvania, Rhode Island, Vermont, and West Virginia—and the District of Columbia. Within the northeast region, Connecticut, Delaware, Maryland, Massachusetts, New Hampshire, New Jersey, New York, and Pennsylvania have operating nuclear power plants. A new nuclear power reactor permit was approved by the NRC for the PSEG site in Delaware, which also hosts currently operating reactors. Therefore, having an improved understanding of potential climate changes and their hydrologic impacts in the northeast region is important to informing the PFHA research plan.

Climatic features relevant to the NRC for the northeast region include high-temperature extremes, precipitation extremes, tropical and extratropical cyclones, summer convective storms, sea-level rise and storm surge, hydrology and water level of Lake Ontario, and floods and seasonality. Drawing primarily from the NCA reports and peer-reviewed literature, this Year 4 annual report summarizes the observed climate, its past changes, and its projected changes, as well as 21st century hydrologic impacts in the northeast region. The northeast region exhibits long-term warming trends in all seasons in the 20th century. In recent decades, the frequency of heat waves was moderately high while the frequency of cold waves was below average since a peak in 1970s/1980s. Temperature is projected to increase quite uniformly across the region, with greater warming in winter and summer than spring and fall. The annual number of days with daily maximum temperatures >95°F is projected to increase by up to 15 days comparing 2041–2070 with 1980–2000. Annual mean precipitation and extreme precipitation show a long-term increasing trend in the 20th century. The 0.05 annual exceedance probability (AEP) seasonal daily precipitation totals have increased, particularly in spring and fall seasons. Precipitation is projected to increase particularly in winter and spring while changes in summer are not significant. Extreme precipitation (0.02 AEP) is projected to increase between 10% to 22% by the mid- and late-century.

Mechanisms contributing to extreme precipitation in the northeast region include tropical cyclones, extratropical cyclones, and mesoscale convective systems embedded in frontal systems so understanding how these storms are projected to change in the future is important for understanding hydrologic impacts in the region. North Atlantic hurricanes are projected to increase in intensity, number of category 4-5 storms, rainfall, and storm size, similar to the projections of the global average, but differences among

different ocean basins are significant. Modeling experiments suggest that climate change since the pre-industrial period had not significantly changed tropical cyclone intensity, but continued warming in the future will significantly enhance tropical cyclone intensity as well as rain rate in the 21st century. Climate models projected a significant decrease in North American storm-track activity, with the largest decrease in summer and the smallest decrease in spring. Despite large differences among model projections, less than 20% of the models show an opposite sign of change. While projections of extratropical cyclone activity changes remain uncertain, theory suggests that convection associated with extratropical cyclones will become more vigorous even if extratropical cyclone activity may decrease in summer in northern hemisphere. There are broad declines in snowstorm frequency projected for the northeast region by the later 21st century but reduction in extreme snowfall is much less than the reduction in mean snowfall. With warmer temperatures and more moisture, an increase in mesoscale convective system track density and intensity is projected for the mid-Atlantic/northeast region.

Between 1950-1979 and 1980-2009, sea-level rise in the northeastern U.S. was 3-4 times higher than the global average, making it a hotspot of accelerated sea level rise. The higher local sea-level rise in the northeastern U.S. has been attributed to land subsidence induced by glacial isostatic adjustment and weakening of the Gulf Stream. Sea-level rise in the region is projected to be highest among cities worldwide due to weakening of the Atlantic Meridional Overturning Circulation. In the RCP8.5 scenario, the likely range of local sea-level rise for New York City is 0.7-1.3 m between the 17th and 83rd percentile levels by 2100. Uncertainty in oceanographic processes contributes importantly to uncertainty in the projection. At the Battery tide gauge in New York City, the present-day 100-yr storm surge is estimated to be about 1.74 m. Considering the changes in hurricane climatology may increase the 100-yr and 500-yr storm tide levels by about 0.7 – 1.2 m by the end of this century, which is comparable to the sea-level rise of 0.5 – 1.5 m projected for the region. Combining increases in tropical cyclone intensity and sea-level rise, storm surge is projected to increase in the future but a shift of cyclone tracks towards offshore may cancel the effect of increase storm intensity, resulting in little change in storm surge in the future.

Comparison between two lumped models and two sources of precipitation data to drive the models show that runoff into Lake Ontario can be reasonably well predicted by lumped model. Good prediction skills were also shown by an aggregated model where the whole Lake Ontario watershed was treated as a single drainage basin. While lumped and aggregated models work well for basinwide prediction, spatially explicit model predictions are desirable for more local planning. Studies comparing spatially distributed snow-hydrology models also showed good skills. Efficient calibration of these models can be speeded up using novel approaches. As warming increases, the ratio of snow to total precipitation is declining in the northeast region. Changes in seasonality of streamflow show dependence of latitude of drainage basins. Springtime streamflow peaks show a clear shift to earlier in the season by as much as 10 days in 2014 compared to mid-20th century. As the 21st century progresses, winter-spring mean temperatures, particularly in the northern parts of the northeast region are expected to cross the freezing threshold resulting in reduced snow to total precipitation ratio and large shifts in winter-spring center-volume date to earlier in the spring.

PNNL staff presented updates summarizing these findings at the Fourth Annual PFHA Research Workshop in February 2020, at Rockville, Maryland.

Glossary

Apparent temperature	Apparent temperature is the temperature equivalent perceived by humans, caused by the combined effects of air temperature, relative humidity and wind speed. This generic measure is most commonly applied to the perceived outdoor temperature but it also applies to indoor temperature.
Atmospheric static stability	Atmospheric static stability is defined as the stability of the atmosphere in hydrostatic equilibrium with respect to vertical displacements. Hydrostatic equilibrium of the atmosphere occurs when the gravitational force is balanced by the pressure-gradient force. In an atmosphere with higher static stability, buoyancy is less likely to induce turbulent motion and storm development.
Clausius-Clapeyron relationship	The Clausius-Clapeyron relationship relates the change in precipitation with the change in temperature during transition between two phases of matter. In meteorology and climatology, this relationship is used to calculate the change in saturation water vapor pressure per unit change in air temperature. Based on this relationship and under typical atmospheric conditions, saturation water vapor pressure changes approximately exponentially with temperature and the water-holding capacity of the atmosphere increases by about 7 percent for every 1°C rise in temperature.
climate change	Changes in average weather conditions that persist over multiple decades or longer. Climate change encompasses both increases and decreases in temperature, as well as shifts in precipitation, changing risk of certain types of severe weather events, and changes in other features of the climate system.
climate variability	Natural changes in climate that fall within the observed range of extremes for a particular region, as measured by temperature, precipitation, and frequency of events. Drivers of climate variability include the El Niño Southern Oscillation and other phenomena.
convective available potential energy (CAPE)	CAPE is the amount of energy a parcel of air would have if lifted a certain distance vertically through the atmosphere. CAPE effectively represents the positive buoyancy of an air parcel and is an indicator of atmospheric instability that can lead to thunderstorms.
convection-permitting simulations	Convection-permitting simulations are atmospheric simulations performed at grid spacings of 4 km or less. At such horizontal resolutions, deep convection is explicitly resolved so the deep convection or cumulus parameterization is turned off.
cyclone phase space	Cyclone phase space is used to describe cyclones using the parameters of storm-motion-relative thickness asymmetry (in terms of symmetric/non-frontal versus asymmetric/frontal) and vertical derivative of horizontal height gradient (in terms of cold- versus warm-core). A cyclone's life cycle can be analyzed within the phase

	space to provide substantial insight into the cyclone structure evolution.
cyclostationary statistical relationship	Relationship between two variables where underlying statistical properties vary cyclically with time on an annual scale but remain stationary on interannual scales.
Eady growth rate	Eady growth rate is a function of the vertical gradient of horizontal wind and the Brunt-Vaisala frequency, which is an indicator of the static stability of the atmosphere. The maximum Eady growth rate is a measure of baroclinic instability based on the Eady Model for baroclinic instability of the atmosphere, with assumptions for the mid-latitude.
eddy kinetic energy	Eddy kinetic energy is the component of the kinetic energy of atmospheric flow that represents a departure from the mean, time average, flow. It can be used as a measure of extratropical cyclone activities.
extratropical cyclone (ETC)	Extratropical cyclones, sometimes called mid-latitude cyclones or wave cyclones, are large-scale (synoptic) low-pressure areas that drive mid-latitude weather. They are classified as baroclinic because they form along zones of temperature and dewpoint gradient known as frontal zones.
extratropical transition (ET)	Extratropical transition refers to the transformation of tropical cyclones into extratropical cyclones at the end of their tropical existence, usually between 30^{o} and 40^{o} latitude. During this process, a cyclone in extratropical transition forms or connects with nearby fronts and/or troughs so it's size usually appears to increase while the core weakens.
extreme event	An extreme event is defined by its frequency of occurrence or return period. The definition of "extreme" is a statistical concept that varies depending on the location, season, and length of the historical record. For example, 99.9 percent precipitation, which refers to the precipitation that has an annual occurrence probability of 1/1000, or a return period of 1000 years, is one definition of extreme precipitation used in this report.
forcing	Factors that affect the Earth's climate. For example, natural factors such as volcanoes and human factors such as the emission of heat-trapping gases and particles through fossil fuel composition.
greenhouse gases	Gases that absorb heat in the atmosphere near the Earth's surface, preventing it from escaping into space. If the atmospheric concentrations of these gases rise, the average temperature of the lower atmosphere will gradually increase—a phenomenon known as the greenhouse effect. Greenhouse gases included, for example, carbon dioxide, water vapor, and methane.

global climate models (GCM)	Mathematical models that are used to numerically simulate the physics, chemistry, and biology that influence the climate system.
heat wave	A period of abnormally hot weather lasting days to weeks.
La Niña	La Niña is a coupled ocean-atmosphere phenomenon that is the counterpart of El Niño as part of the broader El Niño Southern Oscillation climate pattern. During a period of La Niña, the sea surface temperatures across the equatorial Eastern Central Pacific Ocean will be lower than normal by 3 to 5°C. In the United States, La Niña persists for at least five months. It has extensive effects on the weather in North America, even affecting the Atlantic and Pacific hurricane seasons.
land cover	The physical characteristics of the land surface, such as crops, trees, or concrete.
land use	Activities taking place on land, such as growing food, cutting trees, or building cities.
mean available potential energy (MAPE)	The energy of the atmosphere includes three components, internal, latent, and gravitational potential energy but only a part of this energy associated with the mean state of the atmosphere is available for conversion to kinetic energy. This part is called “mean available potential energy” or MAPE. MAPE depends only on the three-dimensional distributions of temperature and humidity of the atmosphere. It increases with increasing horizontal temperature gradients, decreasing static stability, and latent heat release when the phase of water changes.
MCS	MCSs are cumulonimbus clouds that aggregate and develop into a single entity. They produce precipitation that covers a horizontal scale of hundreds of kilometers and lasts up to 24 hours.
Representative Concentration Pathways (RCPs)	These are four greenhouse gas concentration (not emission) trajectories adopted by the Intergovernmental Panel on Climate Change (IPCC) for its fifth Assessment Report (AR5) in 2014. The report supersedes the Special Report on Emissions Scenarios (SRES) published in 2000. The four scenarios—RCP2.6, RCP4.5, RCP6, and RCP8.5—all of which are possible, are named after a possible range of radiative forcing values in the year 2100 relative to pre-industrial values (+2.6, +4.5, +6.0, and +8.5 Wm^{-2}, respectively).
return period	A return period, also called an average recurrence interval, is a measure of the likelihood of an event of a specified magnitude to occur. As the inverse of the annual probability of exceedance, it gives the average time interval between events of a similar size or intensity.
wet-bulb globe temperature	The wet-bulb globe temperature is determined by a linear combination of the temperatures of an unshielded black globe, an ordinary shielded

	thermometer, and a wet-bulb thermometer. Hence wet bulb globe temperature depends on temperature, humidity, wind, and incident radiation combined in a way to mimic a human working outdoors.
wet-bulb temperature	The wet-bulb temperature is the temperature that a parcel of air would have if it were cooled to saturation by the evaporation of water into it. It is largely determined by both the air temperature and the amount of moisture in the air.

Acronyms and Abbreviations

7Q10	90 percent exceedance probability lowest 7-day average streamflow
ACC	Antarctic Circumpolar Current
ADCIRC	Advanced Circulation (Model)
AEP	annual exceedance probability
AIS	Antarctic ice-sheet
AR5	(IPCC) Fifth Assessment Report
ARM	area-ratio method
AMC	air mass (isolated) convection
AMO	Atlantic Multi-Decadal Oscillation
AMOC	Atlantic Meridional Overturning Circulation
AO	Polar Vortex Oscillation
AWSSI	accumulated winter season severity index
BASINS	Better Assessment Science Integrating Point and Non-point Sources
BCSD	bias-correction spatial disaggregation
CaPA	Canadian Precipitation Analysis (dataset)
CAPE	convective available potential energy
CC	Clausius-Clapeyron relation adjustment
CCAWWG	(Federal) Climate Change and Water Working Group
CESM	Community Earth System Model
CMIP	Coupled Model Intercomparison Project
CMIP3	Coupled Model Intercomparison Project Phase 3
CMIP5	Coupled Model Intercomparison Project Phase 5
CNRM	Centre National de Recherches Météorologiques (France)
COOP	(NWS) Cooperative Observer
CPC	Climate Prediction Center
CPS	cyclone phase space
CSIRO-Mk2	Commonwealth Scientific and Industrial Research Organisation Atmospheric Research Mark 2 climate model
CSSR	Climate Science Special Report
DJF	December-January-February
DRB	Delaware River Basin
E3SM	Energy Exascale Earth System Model
ECHAM	Max Planck Institute for Meteorology atmospheric general circulation model
ECB	Engineering and Construction Bulletin
ENSO	El Niño – Southern Oscillation
EPA	(U.S.) Environmental Protection Agency

ETC	extratropical cyclone
FRT	extratropical cyclone near a front
GAGES	Geospatial Attributes of Gages for Evaluating Streamflow (dataset)
GAM	generalized additive model
GCM	global climate model
GEM	Global Environmental Multi-Scale (model)
GEOS	Goddard Earth Observing System
GEV	Generalized Extreme Value
GFDL	Geophysical Fluid Dynamics Laboratory
GHCND	Global Historical Climatology Network – Daily (dataset)
GIA	glacial isostatic adjustment
GIC	glaciers and ice caps
GISS	(NASA) Goddard Institute for Space Studies
GLAHF	Great Lakes Aquatic Habitat Framework
GLERL	(NOAA) Great Lakes Environmental Research Laboratory
GMSL	global mean sea level
GR4J	modèle du Génie Rural à 4 paramètres Journalier
GRIP-O	Great Lakes Runoff Inter-Comparison Project for Lake Ontario
GRU	grouped response unit
GSL	global sea level
HadCM3	Hadley Centre Coupled Model version 3
HadRM3P	Hadley Center Regional Climate Model based on HadCM3
HiFLOR	(GFDL) High-Resolution Forecast Version Low Ocean Resolution (model)
HiRAM	(GFDL) High-Resolution Atmospheric Model
HRB	Hudson River Basin
HSAMI	(Hydro-Québec) Service Hydrométéorologique Apports Modules Intermédiaires (model)
HUC	Hydrologic Unit Code
HURDAT	Hurricane Database
IGIM	Interagency Group on Integrative Modeling
IJC	(U.S.-Canada) International Joint Commission
IPCC	Intergovernmental Panel on Climate Change
IUGLSB	International Upper Great Lakes Study Board
IVT	integrated water vapor transport
JJA	June-July-August
LBRM	Large Basin Runoff Model
LCL	lifting condensation level
LOCA	Localized Constructed Analogs

LOESS	locally estimated scatterplot smooth (function)
LOWESS	locally weighted scatterplot smooth (function)
LSL	local sea level
MAM	March-April-May
MCS	mesoscale convective system
MESH	Environment Canada's Modélisation Environnementale – Surface et Hydrologie
MHHW	mean higher high water
MIROC	(Japan Agency for Marine-Earth Science) Model for Interdisciplinary Research on Climate
MJO	Madden-Julian Oscillation
NAM	North American monsoon
NAO	North Atlantic Oscillation
NARCCAP	North American Regional Climate Change Assessment Program
NASA	National Aeronautics and Space Administration
NBS	net basin supply
NCA	National Climate Assessment
NCA3	Third National Climate Assessment
NCA4	Fourth National Climate Assessment
NCAR	National Center for Atmospheric Research
NCDC	National Climatic Data Center
NCEI	National Centers for Environmental Information
NCEP	National Centers for Environmental Prediction
NESDIS	National Environmental Satellite, Data, and Information Service
NJCAA	New Jersey Climate Adaptation Alliance
NOAA	National Oceanic and Atmospheric Administration
NLDAS	North American Land Data Assimilation System
NRC	U.S. Nuclear Regulatory Commission
NRCC	Northeast Regional Climate Center
NSE	Nash-Sutcliffe efficiency
NYC	New York City
PDF	probability density function
PDO	Pacific Decadal Oscillation
PFHA	Probabilistic Flood Hazard Assessment
PNA	Pacific North American (Teleconnection)
PNNL	Pacific Northwest National Laboratory
PRISM	Precipitation Elevation Regression on Independent Slopes Model
QBO	Quasi-Biennial Oscillation
RCP	representative concentration pathways

RPI	Regional Precipitation Index
RSI	Regional Snowfall Index
RSL	regional sea level
SCE	snow cover extent
SLOSH	Sea, Lake, and Overland Surges from Hurricanes (Model)
SLP	sea-level pressure
SLR	sea-level rise
SLRD	sea-level rise difference
SNR	signal-to-noise ratio
SOI	Southern Oscillation Index
SON	September-October-November
SRB	Susquehanna River Basin
SRES	Special Report on Emissions Scenarios
SST	sea surface temperature
SVS	Soil, Vegetation, and Snow (land-surface scheme)
SWE	snow-water equivalent
TA	air temperature
TC	tropical cyclone
TG	tide gauge
UH	unit hydrograph
USACE	U.S. Army Corps of Engineers or Corps
USF	upslope flow precipitation
USGCRP	U.S. Global Change Research Program
USGS	U.S. Geological Survey
UW	University of Washington
WBGT	wet-bulb globe temperature
WBT	wet-bulb temperature
WRF	Weather Research and Forecasting (model)
WSCVD	winter-spring center volume date

Contents

Figures

Tables

1.0 Introduction

The study documented here is part of the U.S. Nuclear Regulatory Commission's (NRC) Probabilistic Flood Hazard Assessment (PFHA) research plan that aims to develop regulatory tools and guidance to support and enhance the NRC's capacity to perform thorough and efficient reviews of license applications and license amendment requests. The NRC contracted Pacific Northwest National Laboratory (PNNL) to prepare a summary of current state of climate research and results regarding hydrometeorological phenomena that are of interest in safety assessments and environmental impact assessments for commercial nuclear power plants. In Year 1, PNNL staff prepared an annual report that summarized recent scientific findings about global and regional climate change, focusing in particular on climatic elements relevant to NRC concerns broadly across the conterminous United States (U.S.) (i.e., increasing air and water temperatures, decreasing water availability, increasing frequency and intensity of storms and flooding, and rising sea levels). In Year 2, PNNL staff summarized recent research findings about climate change for the southeast region, including projected changes in air temperature, precipitation, hurricanes, sea-level rise, storm surge, tornadoes, and impacts on flooding, and low flows. In Year 3, PNNL staff summarized research findings about climate change for the midwest region, including projected changes in air temperature, precipitation, severe storms, Great Lakes water levels, and hydrologic impacts including impacts on flooding and low flows. This report summarizes Year 4 activities, which focused on reviewing region-specific scientific findings for the northeast region.

The U.S. Global Change Research Program (USGCRP) Third National Climate Assessment (NCA3) discussed the regional climate, historical trends, and future changes in 10 climate regions (Melillo et al. 2014). In the Fourth National Climate Assessment (NCA4), similar regions are used in the Climate Science Special Report except that the Great Plains are divided into northern and southern Great Plains and the Caribbean Islands are separated from the southeast region (USGCRP 2017). The region of interest for the purpose of this report consists of 12 northeastern states—Connecticut, Delaware, Maine, Maryland, Massachusetts, New Hampshire, New Jersey, New York, Pennsylvania, Rhode Island, Vermont, and West Virginia—and the District of Columbia (hereafter, the northeast region) (USGCRP 2017; Figure 1.1~~Figure 1.1~~). Within the northeast region, Connecticut, Delaware, Maryland, Massachusetts, New Hampshire, New Jersey, New York, and Pennsylvania have operating nuclear power plants (Figure 1.2). In addition, a new nuclear power reactor permit was approved by the NRC for the PSEG site in Delaware, which also hosts currently operating reactors. Figure 1.3 shows the locations of proposed nuclear power reactors in the United States. At one location within the northeast region (PSEG Site), the NRC approved an Early Site Permit for a new nuclear power reactor.

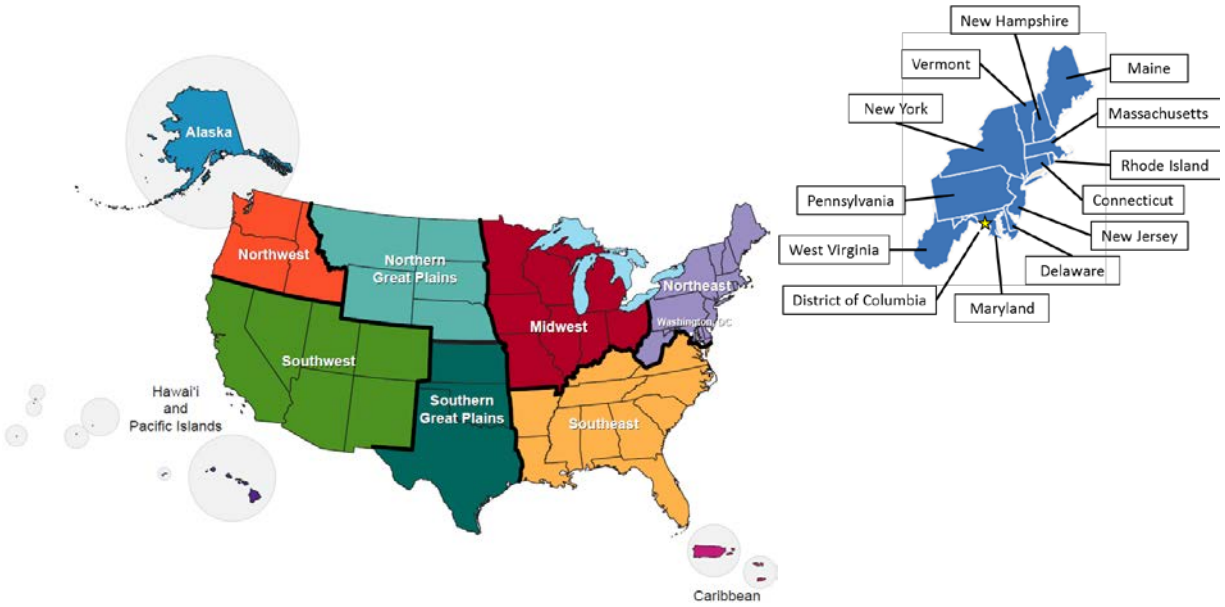

Figure 1.1. USGCRP NCA4 climate regions and the states (and District of Columbia) included in the northeast region. (Source: USGCRP 2017)

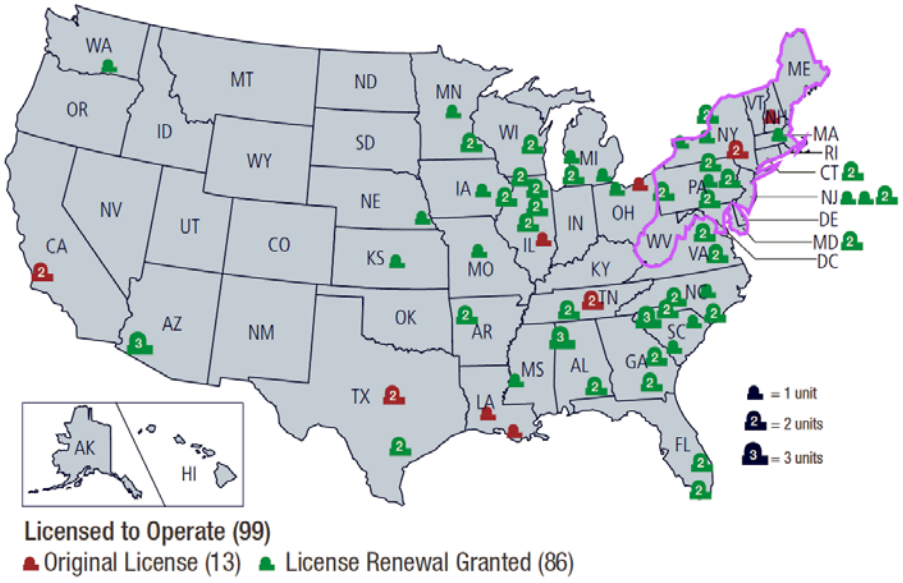

Figure 1.2. Operating nuclear power reactors in the United States as of May 2018 (source: NRC 2018).

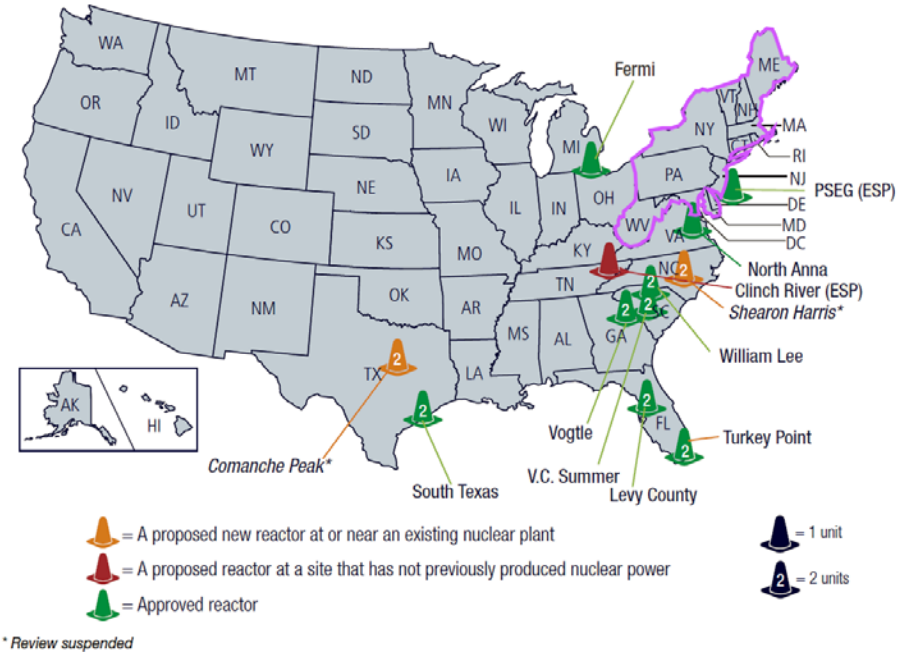

Figure 1.3. Proposed nuclear power reactors in the United States as of July 2018. (Source: NRC 2018)

To support the NRC's (1) PFHA research plan in developing a risk-informed licensing framework for flood hazards and design standards, (2) environmental reviews at existing and proposed facilities, and (3) significance determination tools for evaluating potential flood hazards and their protection at plant facilities, this report summarizes key findings available in the broad climate research literature about observed regional climate trends and projected climate change, as well as observed and potential hydrologic impacts in the northeast region. The contents are drawn from published reports including the National Oceanic and Atmospheric Administration (NOAA) Technical Report NESDIS 142-1, *Regional Climate Trends and Scenarios for the U.S. National Climate Assessment Part 1: Climate of the Northeast U.S.* (Kunkel et al. 2013) and Climate Change Impacts in the United States, Chapter 16: Northeast (Horton et al. 2014) for NCA3; the USGCRP Climate Science Special Report (USGCRP 2017) for NCA4; papers published in peer-reviewed journals; NOAA websites; USGS reports; and other sources including information available from the Northeast Regional Climate Center website.

As summarized in Chapter 1 of the Year 2 report, information summarized in NCA3 is mainly derived from (1) multimodel global climate simulations of the Coupled Model Intercomparison Project Phase 3 (CMIP3); (2) regional climate projections from the North American Regional Climate Change Assessment Project (NARCCAP), in which regional climate models were used to dynamically downscale a subset of CMIP3 models; and (3) statistically downscaled products at 1/8-degree resolution for the U.S. developed using the bias-correction spatial disaggregation (BCSD) method applied to the CMIP3 simulations. Future projections highlighted in NCA3 are associated with lower emissions (B1) and higher emissions (A2) corresponding to a mitigation scenario and a business-as-usual scenario, respectively. However, some regional climate models used in NARCCAP did not include a lake model so temperatures in the Great Lakes are not well represented. To the extent that the Great Lakes temperatures affect the regional climate of the northeast region, this caveat may introduce uncertainty in the NARCCAP regional projections. In contrast to NCA3, NCA4 draws information mainly from (1) multimodel global climate simulations of the Coupled Model Intercomparison Project Phase 5 (CMIP5; Taylor et al. 2012), (2) a limited number of high-resolution global climate simulations at ~25 km resolution, and (3) statistically downscaled products at 1/16-degree resolution for the U.S. developed using the Localized Constructed Analogs method applied to the CMIP5 simulations. Two scenarios, RCP4.5 and RCP8.5 comparable to

the lower and higher emissions scenarios of B1 and A2, are used. These scenarios correspond to a global radiative forcing of 4.5 and 8.5 Wm^{-2} by the end of the 21st century. Figure 1.4 summarizes the information used in NCA3 and NCA4.

Climate Information Used in NCA3 and NCA4

NCA3:

- CMIP3 global climate simulations and projections for the B1 and A1 scenarios
- NARCCAP dynamical downscaling of a small subset of CMIP3 simulations/projections for the A1 scenario at 50 km resolution
- BCSD statistical downscaling of CMIP3 simulations/projections for both scenarios at 1/8° resolution

NCA4:

- CMIP5 global climate simulations and projections for the RCP4.5 and RCP8.5 scenarios
- A limited number of high-resolution global climate simulations at ~25 km resolution
- LOCA statistical downscaling of CMIP5 simulations/projections for both scenarios at 1/16° resolution

Note that B1 and RCP4.5 are mitigation scenarios with comparable pathways of greenhouse gas concentrations and A2 and RCP8.5 are business-as-usual scenarios with comparable pathways of greenhouse gas concentrations

Figure 1.4. A comparison of climate information used in NCA3 and NCA4.

1.1 Report Contents and Organization

This annual report discusses the climate change projections for the northeast region summarized in both NCA3 and NCA4, so emissions scenarios B1 and A2 used in CMIP3 and RCP4.5 and RCP8.5 used in CMIP5 are discussed throughout the report. Chapter 2 provides an overview of the regional temperature characteristics of the northeast region, including observed historical changes and projected future changes. Chapter 3 summarizes observed historical and projected future changes in annual mean, seasonal mean, and extreme precipitation. Chapter 4 discusses past and future changes in tropical and extratropical cyclones and convective storms. Chapter 5 describes sea-level rise and storm surge in the northeast region. Chapter 6 discusses Great Lakes with emphasis on hydrologic characterization of Lake Ontario and its drainage area. Storms that produce the extreme precipitation most relevant to NRC PFHA are generally not captured in global climate simulations because of their relatively coarse spatial resolution, so Chapter 7 also summarizes the characteristics of a few large flooding events that occurred in the northeast region to provide context for extreme floods useful for NRC's consideration. Chapter 8 summarizes recent U.S. agency activities related to climate change and its impacts. Finally, Chapter 9 lists references cited in this report.

1.2 Climate Terminology Relative to NRC Permitting and Licensing

We note that the terminology used in the broad climate research community is not aligned with that used in the NRC permitting and licensing context. For example, Kunkel et al. (2013, Figure 8) describe trends in "extreme" precipitation events in the northeast region using the 24-hour, 0.2 annual exceedance probability precipitation events. In contrast, the NRC's interest in extreme events spans a much lower range of annual frequencies of exceedance—10^{-3} and lower (NRC 2016). The flood events of interest to the NRC may be generated by precipitation at a range of timescales—from 5 minutes to several days. Therefore, research results developed by the climate community should be carefully evaluated and

interpreted for use in the NRC permitting and licensing context. As far as possible, this report endeavors to explicitly state the event time scales and the annual exceedance probabilities or frequencies reported in the reviewed literature.

2.0 Temperature in the Northeast Region

This chapter summarizes different aspects of temperatures such as annual and seasonal mean temperatures and hot and cold extremes in the northeast region. The chapter includes information related to characteristics of observed temperatures and their historical trends (Section 2.1), and summarizes the projected temperatures (Section 2.2) from published papers and reports.

2.1 Observed Temperature Changes

- The northeast region exhibits long-term warming trends. Temperatures show statistically significant increases during all seasons.
- Occurrences of heat waves in recent decades shows similarity with early 20th century when the frequency of heat waves was moderately high. Frequency of cold waves are below average since a peak in 1970s/1980s.

The NOAA National Centers for Environmental Information (NCEI) summarize daily temperatures in the form of maps to visualize the information. The NCEI currently uses an averaging period of 1981–2010[1] to create climatology maps (NCEI 2016). The annual average minimum temperatures vary from the 40s (in degrees Fahrenheit) in the southern parts of the northeast region to the 20s-°F and 30s-°F in the northern parts of the region (Figure 2.1, top-left panel). The annual average maximum temperatures vary from the 60s-°F in the southern parts of the region to the 40s-°F in the northern parts (Figure 2.1, top-right panel). On average, January is the coolest month (average January temperatures vary from the 20s-°F in the southern parts to the 10s-°F and less in the northern parts; Figure 2.1, bottom-left panel) and July is the warmest month (average July temperatures vary from the 80s-°F in southern and coastal areas of the region to the 70s-°F at the northern edges of the region; Figure 2.1, bottom-right panel).

Record high temperatures in the northeast region can range from 47°F in December to 108°F in July (NCEI 2018). Across the northeast region, maximum daily average temperatures can exceed 90°F up to 13 days in July and up to 10 days in August (NCEI 2018). Record low temperatures in the northeast region can range from 56°F in July to -46°F in January (NCEI 2018). In the northeast region, minimum daily average temperatures can fall below freezing during all months and can fall below freezing for all days during the months of December through March (NCEI 2018).

As summarized in the Climate Science Special Report (CSSR) of NCA4, annual average temperatures over the contiguous United States have increased by 1.2°F for the 1986–2016 period relative to the 1901–1960 period, and surface observation and satellite data have consistently shown a rapid increase in temperature since 1979 (Vose et al. 2017). Figure 2.2 shows the distribution of observed changes in annual temperature. The change in annual average temperature for the same periods for the northeast region was reported as 1.43°F, while the change in annual average maximum temperature was 1.16°F and the change in annual average minimum temperature was 1.70°F.

[1] The Third National Climate Assessment used the 1971–2000 normals.

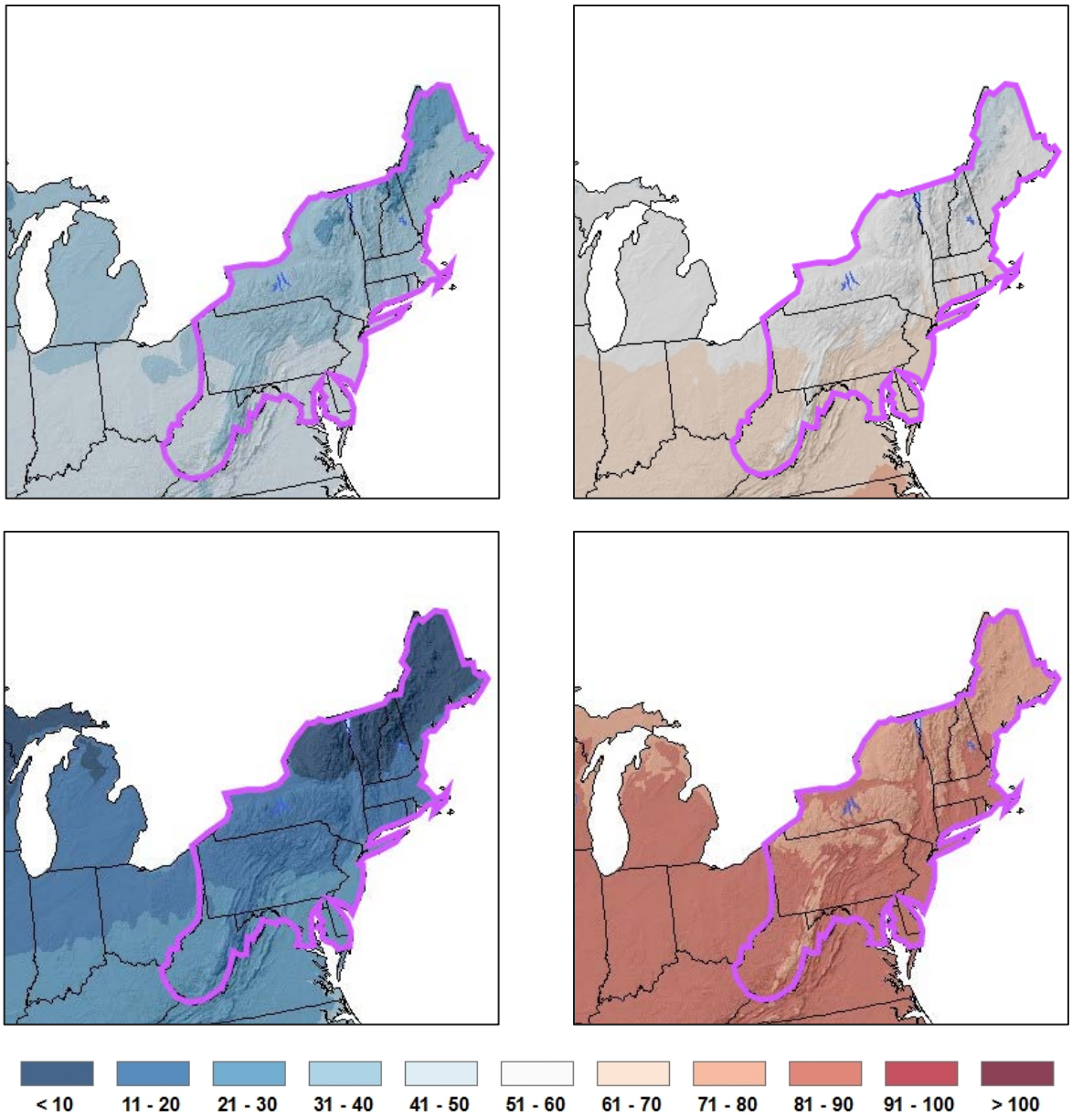

Figure 2.1. Average minimum (top-left panel) and maximum (top-right panel) annual temperatures (°F) and average minimum January (bottom-left panel) and maximum July (bottom-right panel) temperatures (°F) based on 1981–2010 normals. (Source: NCEI 2016.)

From Vose et al. (2017), the coldest daily temperature of the year has increased at most locations within the contiguous U.S. in the last 30 years compared to the first six decades of the 20th century (Figure 2.3, left panel). The regional average increase in the temperature of the coldest day of the year for the northeast region was 2.83°F. In contrast, the warmest daily temperature of the year showed a decrease for all eastern U.S. regions (Figure 2.3, right panel); for the northeast region, the regional average warmest daily temperature of the year decreased by 0.92°F. The report also states that across the United States, the frequency of cold waves has decreased since the early 1900s and the frequency of heat waves has increased since the 1960s. The report mentions that the number of high-temperature records set in the past two decades far exceeds the number of low-temperature records (Vose et al. 2017).

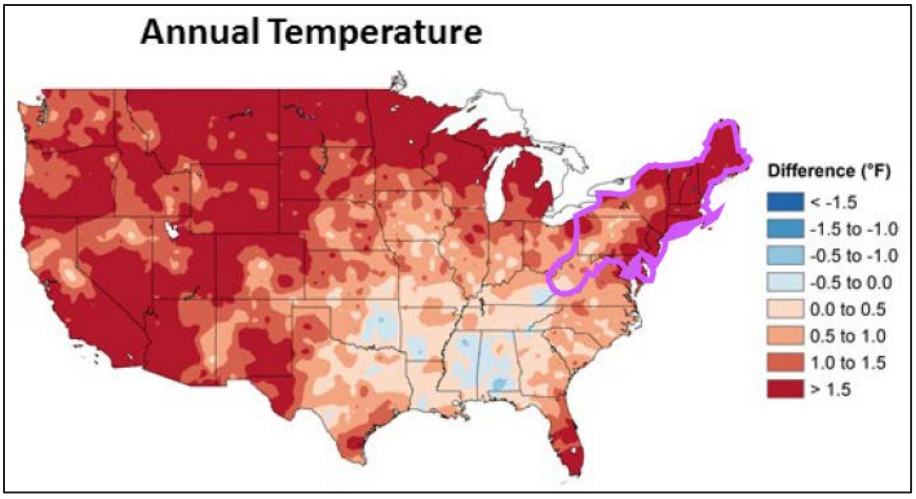

Figure 2.2. Observed changes in annual temperature (°F). Changes are the difference between the average for present day (1986–2015) and the average for the first half of the last century (1901–1960). (Source: Vose et al. 2017.)

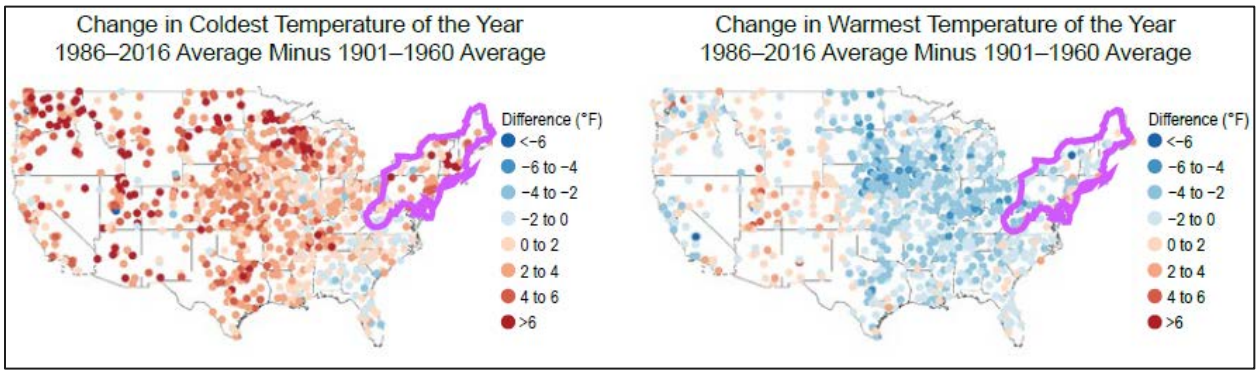

Figure 2.3. Changes in the average coldest and warmest daily temperatures between the 1986–2016 and 1901–1960 periods. (Source: Vose et al. 2017.)

Based on analysis of gridded NOAA Cooperative Observer Network weather data, Kunkel et al. (2013), reported that the northeast region showed a rising trend in temperatures throughout the 20th century and the rising trend has continued into the 21st century (Figure 2.4). Most of the temperature increase occurred during the winter and spring (see middle panels of Figure 2.4).

Temperatures exceeding 90°F for three or more consecutive days are common and occur almost every year; however, three consecutive days of temperatures 100°F are rare—occurring twice in over 130 years at Central Park, New York and twice in Philadelphia, Pennsylvania, and Washington, D.C (Kunkel et al 2013b). During the July 1995 heat-wave, temperatures exceeded 90°F on 24 of 25 consecutive days in Washington, D.C, resulting in 19 heat-related deaths. During the same event, New York City suffered 11 heat-related deaths.

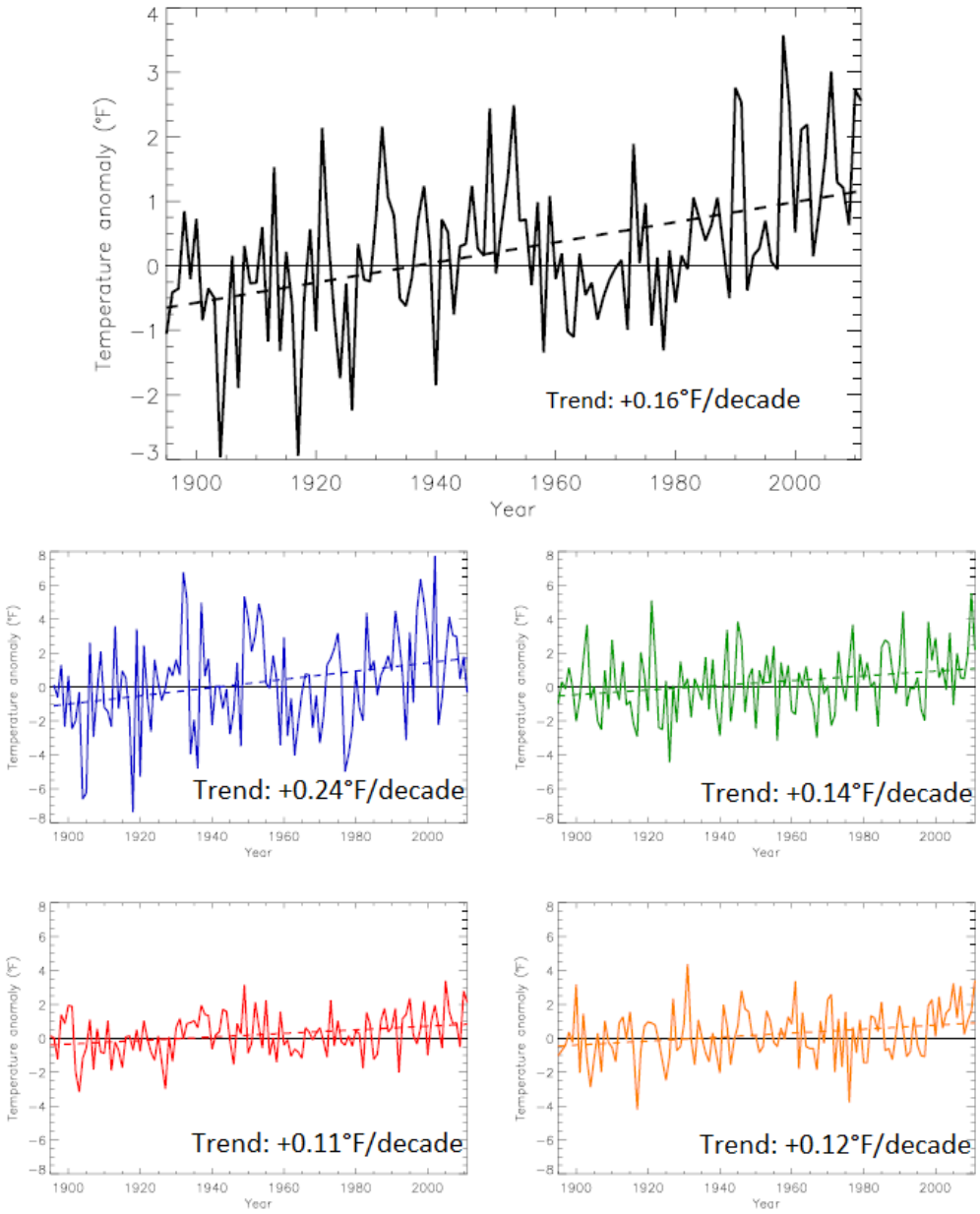

Figure 2.4 Trends in observed temperature anomalies (deviations from the 1901–1960 average) in the northeast region based on gridded NOAA Cooperative Observer Network data. The top panel shows the annual temperature anomalies, middle-left panel shows the winter temperature anomalies, middle-right panel shows the spring temperature anomalies, bottom-left panel shows the summer temperature anomalies, and the bottom-right panel shows the fall temperature anomalies. (Source: Kunkel et al. 2013.)

Kunkel et al. (2013) used time series of indices to represent heat and cold-wave events estimated from the Global Historical Climate Network station data. The indices are defined as 4-day periods that are hotter or colder than the threshold for 1 in 5-year recurrence. Heat or cold-wave events were identified by ranking all 4-day mean temperatures and selecting the highest and lowest fifth of the values at each station. The number of events for all stations in a 1°x1° box was averaged for each year. The regional average of all grids was taken as the index for that year. The heat-wave and cold-wave indices are shown in Figure 2.5.

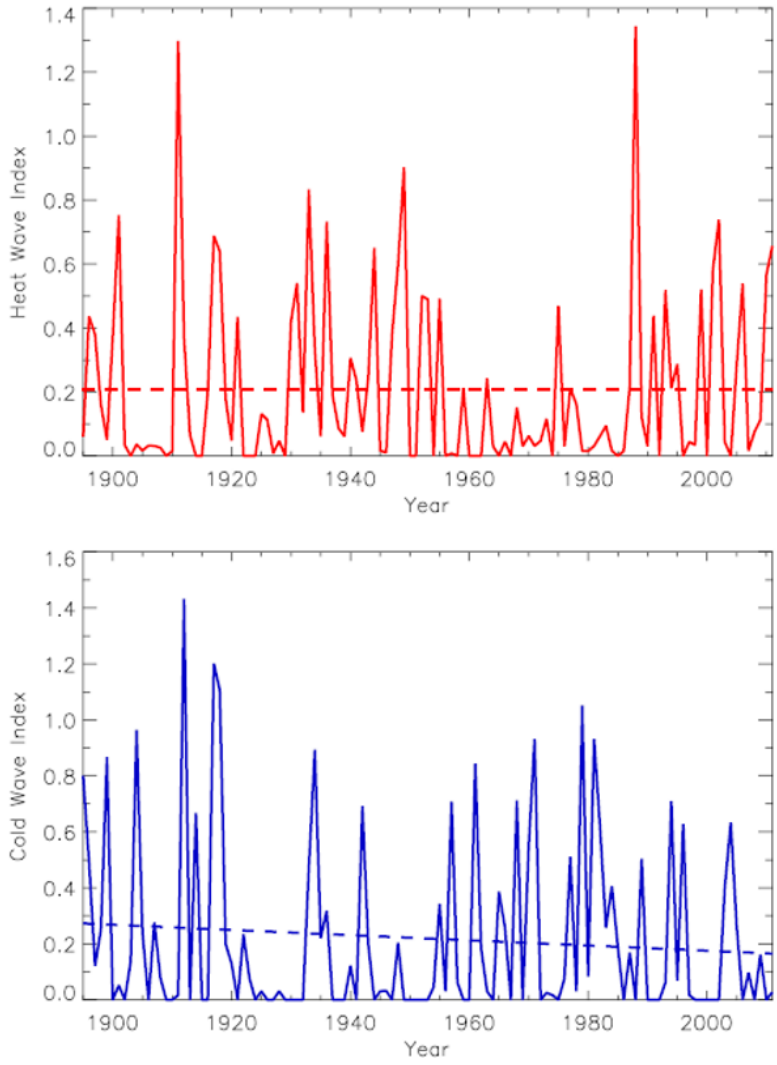

Figure 2.5. Time series of heat- and cold-wave indices. The dashed lines represent the linear fits. The trends were not statistically significant. (Source: Kunkel et al. 2013.)

The most intense heat waves occurred in the 1910s and 1980s. There was no detectable trend in heat waves. The most intense cold waves occurred in 1910s and 1970s/80s. Kunkel et al. (2013) noted that since 2000, there have been relatively few cold waves. However, the trends were not statistically significant.

Kunkel et al. (2013) noted that occurrence of heat waves was moderately high from late 19th century into the 1950s, followed by a period of few intense heat waves until the early 1980s. Since the 1980s, the frequency of heat waves has been similar to that of the first half of the 20th century. Kunkel et al. (2013) also stated that the frequency of cold waves was high early in the record, followed by a quieter period, and has been less than average since a peak in the 1970s and early 1980s.

2.2 Projected Temperature Changes

- The mean annual temperature is projected to increase by 4.5°F–6.5°F and 6.5°F–8.5°F under the B1 and A2 scenarios, respectively, by 2085.
- Projected warming is rather uniform spatially across the northeast region; greater warming occurs in winter and summer than in spring and fall.
- The annual number of days with daily maximum temperatures >95°F is projected to increase by up to 15 days comparing 2041–2070 with 1980–2000.

Consistent with the projections of global surface warming, temperatures in the northeast region are projected to increase in the future with greater warming in the higher emissions A2 scenario than in the lower emissions B1 scenario. Figure 2.6 shows the projected mean annual temperature changes from the CMIP3 multimodel ensemble for three future periods and the NARCCAP-projected mean annual and mean seasonal temperature changes for the mid-century. For 2035, the annual mean warming from the CMIP3 multimodel ensemble in the region is projected to be between 2.5 and 3.5°F, with small differences between the two scenarios in the southeastern part of the region. After the mid-century, differences between the two emissions scenarios increase over time; in 2085, warming in the A2 scenario is between 6.5 and 8.5°F compared to between 4.5 and 6.5°F for the B1 scenario. In general, spatial variations of the warming signals are small, except for greater warming in the northwestern part of the region by the late 21st century. Using dynamical downscaling, the NARCCAP-projected mean annual warming for the 2041–2070 period to be comparable to that of the CMIP3 global simulations for the same period. Larger spatial variations are noted in the seasonal mean temperature changes; greater warming is projected for winter and summer than for spring and fall.

Figure 2.7, top panel, shows the spatial distribution of the NARCCAP multimodel mean change in the average annual number of days with a maximum temperature exceeding 95°F between 2055 and the reference period of 1980–2000. The southern part of the region sees the largest increase of more than 15 days and there is a large north-south gradient in the change pattern. The changes are statistically significant across almost the entire northeast region. Corresponding to the warming, the average annual number of days with a minimum temperature of less than 10°F decreases throughout the region, and the largest decrease of up to 24 days occurs in the northeast portion of the region (Figure 2.7, bottom panel). As shown in Figure 2.6 of the Year 2 report, Diffenbaugh and Ashfaq (2010) found a substantial increase in heat waves by 2 to 3 events per year during the 2030–2039 period compared to the 1951–1999 period in the northeast region, particularly in the southern portion of the region.

In Chapter 18 of the NCA4 report on the Northeast, Dupigny-Giroux et al. (USCGRP 2018) noted that increases in temperatures would result in changes in seasonality (Figure 2.8). Increasing temperatures also increase the risk of heat-related deaths particularly because northeastern cities with an abundance of concrete and asphalt and relatively little vegetation tend to have higher temperatures than surrounding regions (the urban heat island effect). The Environmental Protection Agency (2017) estimated that the northeast region is expected to experience 660 additional premature deaths per year from extreme heat by 2050 (under both the RCP4.5 and 8.5 scenarios) and from 970 (under RCP4.5 scenario) to 2300 (under RCP8.5 scenario) additional premature deaths by 2090.

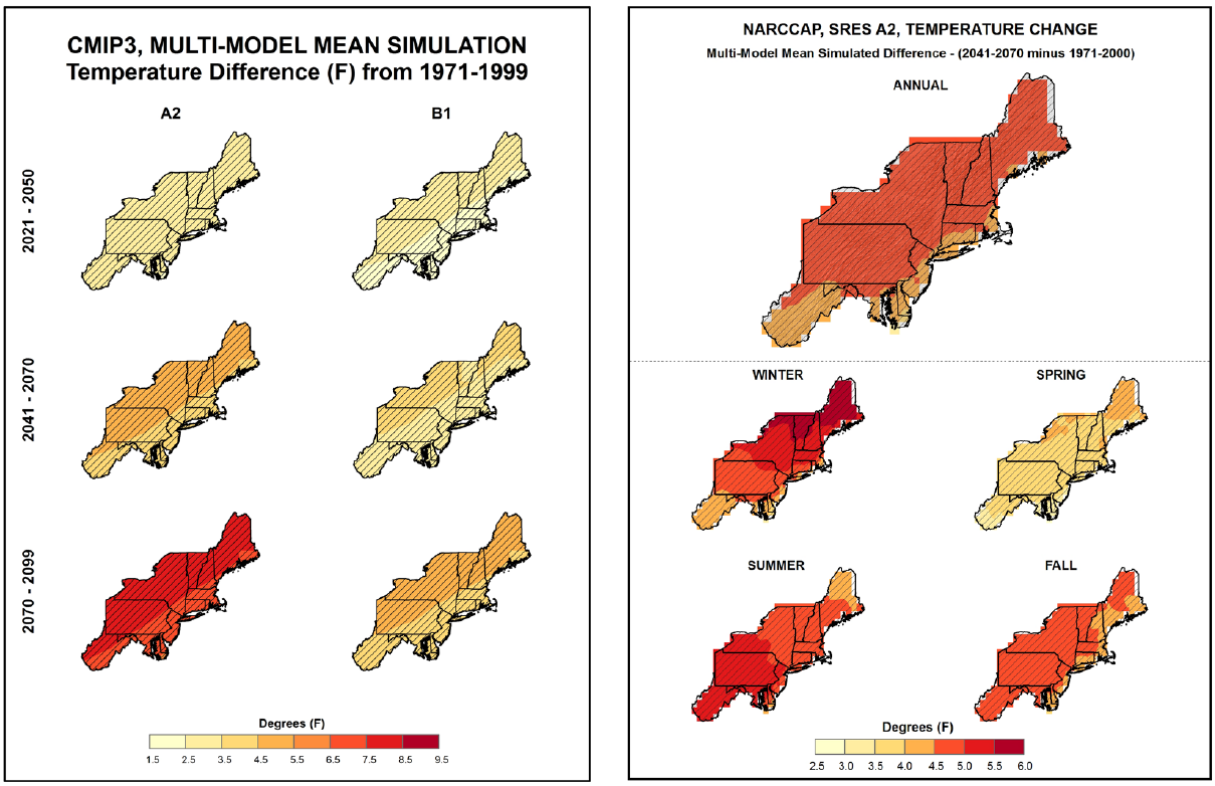

Figure 2.6. (Left) Simulated difference in annual mean temperature (°F) for the northeast region, for each future time period (2021–2050, 2041–2070, and 2070–2099) with respect to the reference period of 1971–1999, based on the multimodel means for the A2 and B1 emissions scenarios from the CMIP3 global climate simulations. Color with hatching indicates that more than 50 percent of the models show a statistically significant change in temperature, and more than 67 percent agree on the sign of the change. (Right) Similar to the left panel A2 scenario, except that the simulations are from NARCCAP instead of CMIP3, for 2041–2070 relative to 1980–2000 for the annual mean and four seasons. (Source: Kunkel et al. 2013.)

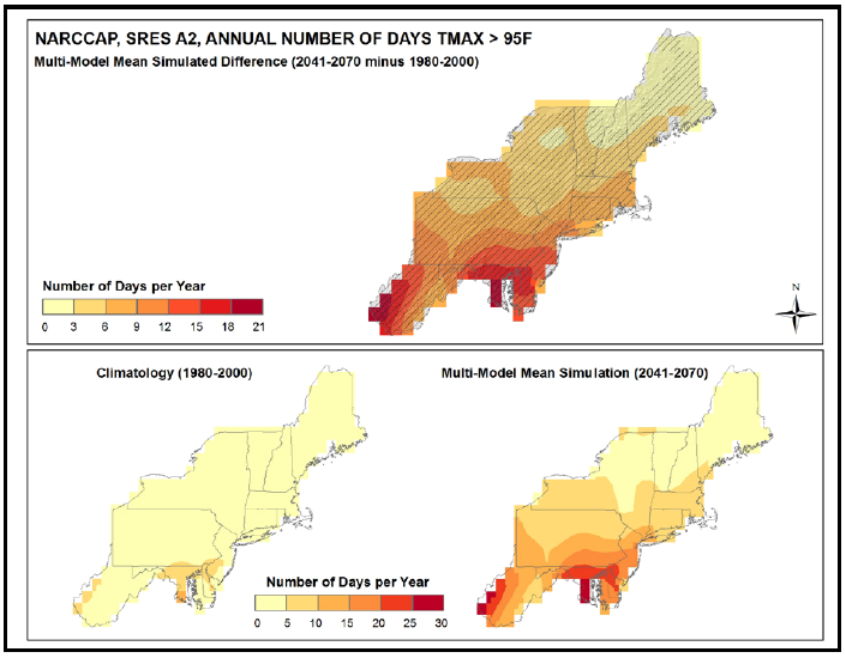

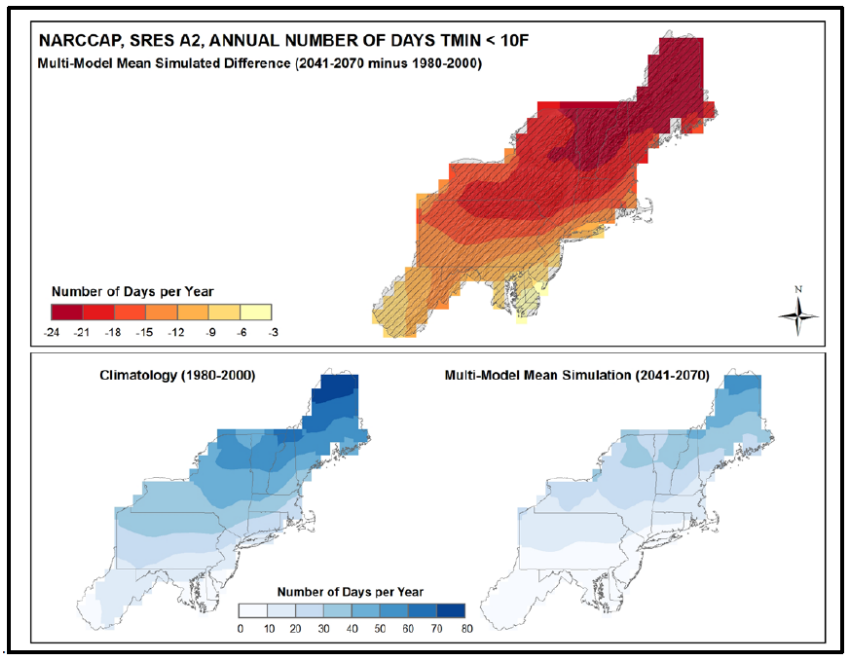

Figure 2.7. (Top) Simulated difference in the annual mean number of days with maximum temperatures greater than 95°F for the northeast region, for the 2041–2070 period with respect to the reference period of 1980–2000, based on the multimodel means from eight NARCCAP regional climate simulations for the high (A2) emissions scenario. Color with hatching indicates that more than 50 percent of the models show a statistically significant change in temperature, and more than 67 percent agree on the sign of the change. (Bottom) The simulated mean annual number of days with a maximum temperature greater than 95°F for the 1980–2000 (left) and the 2041–2017 future periods (right). Similar to top panel but for annual mean number of days with minimum temperatures less than 10°F. (Source: Kunkel et al. 2013.)

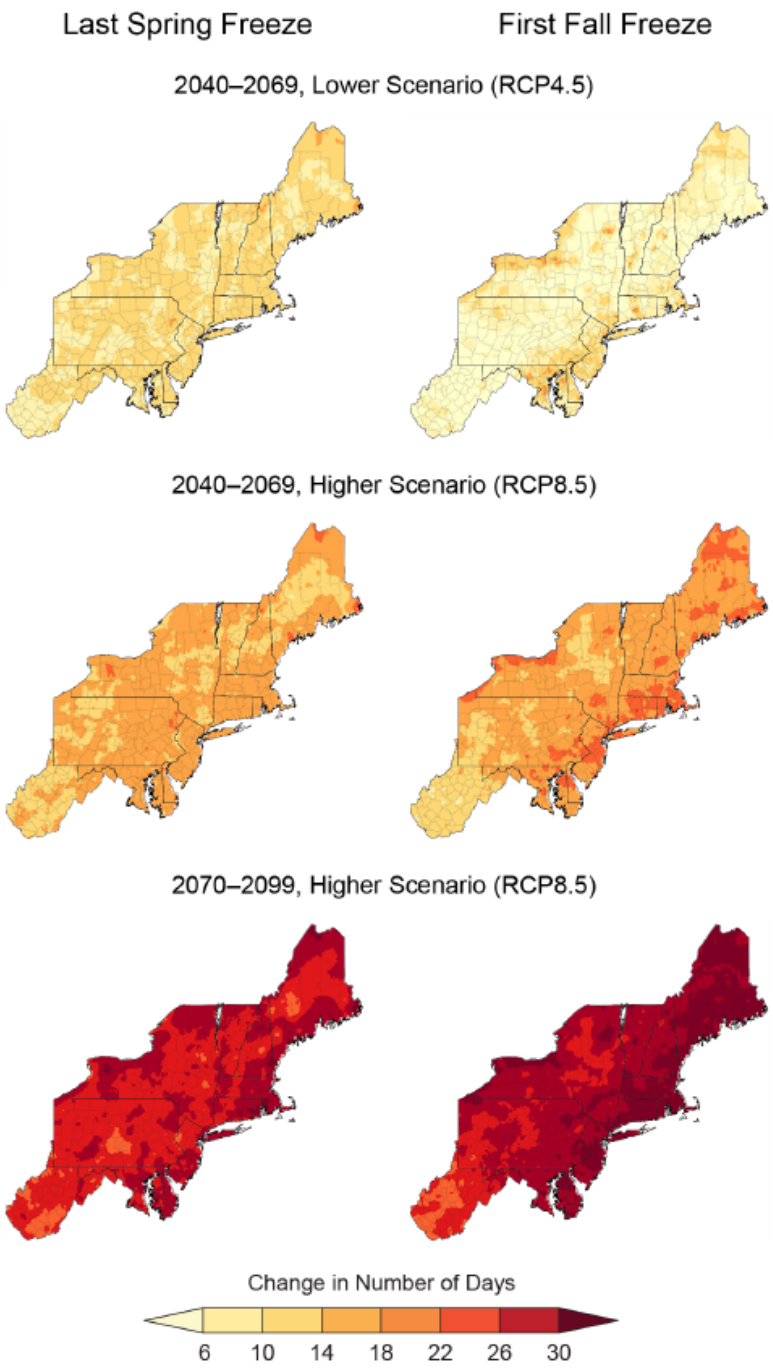

Figure 2.8. Projected shifts in the date of the last spring freeze (left column) and the date of the first fall freeze (right column) compared to 1979–2008 for the mid-21st century under RCP4.5 (top row), mid-21st century under RCP8.5 (middle row), and late-21st century under RCP8.5 (bottom row). By the mid-21st century, the freeze-free period across much of the northeast region is expected to lengthen by up to 2 weeks under RCP4.5 and by 2 to 3 weeks under RCP8.5. By the late-21st century under RCP8.5, the freeze-free period is expected to lengthen by at least 3 weeks over much of the region. (Source: USGCRP 2018.)

Lopez et al. (2018) used a hierarchical clustering algorithm to study heat extremes based on 2m air temperature in the U.S. for the present climate and future climate under the RCP8.5 scenario. They focused on four heat-wave clusters identified from the reanalysis data for the 20th century (1900-2010) that affect the largest U.S. population, including the western U.S., Northern Great Plains, Southern Great Plains, and the Great Lakes regions. The Great Lakes cluster covers a large area centered at the Great Lakes but includes the northeastern U.S. region (Figure 2.9a). Analysis of the CMIP5 multimodel ensemble and the CESM large-ensemble simulations for the 21st century (2010-2100) shows increasing trends in the ratio of warm-to-cold extremes for the Great Lakes cluster. Furthermore, the probability distribution of the 21st century heat-wave events shows a statistically significant signal-to-noise ratio (SNR) of 1.8 (**Error! Reference source not found.**b). The increase in heat extremes can be attributed to reduced atmospheric transient eddies or storminess in the northeastern U.S. that brings moist and cool air from the oceans to the continents. The analysis of Lopez et al. (2018) also indicated that a time of emergence (i.e., SNR > 1) could occur as early as the 2030s in the Great Lakes region.

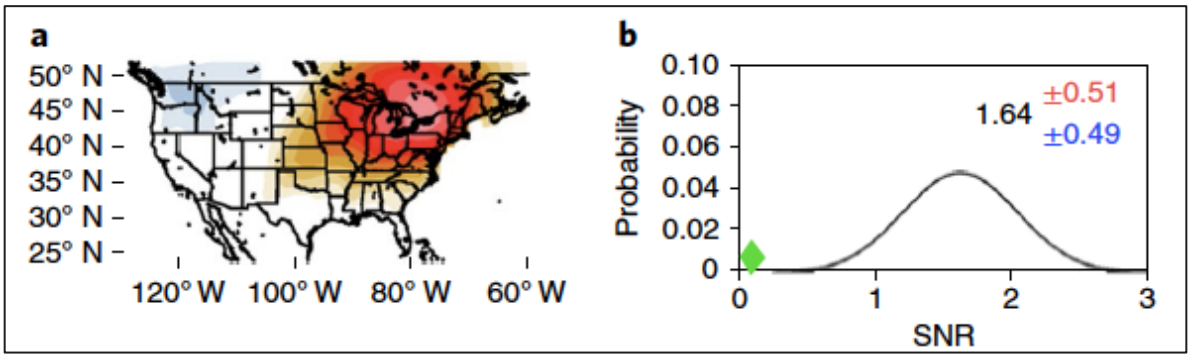

Figure 2.9. Geographic distribution of the 20th century 2 m temperature anomaly (a) and 21st century probability density function (PDF) of the SNR of heat-wave events for the Great Lakes cluster from the ensemble mean of CMIP5 models. The SNR PDF is obtained by randomly selecting eight models (ensembles) 1000 times from the CMIP5 simulations. The mean SNR is shown in black and 95 percent confidence interval in red (blue) from the CMIP5. The 20th century SNR is shown by the green diamond. (Source: Lopez et al. 2018.)

As atmospheric moisture increases with temperature, changes in heat stress are major concerns for public health and human mortality. Sherwood (2018) discussed three metrics commonly used to study heat stress, including the wet-bulb globe temperature (WBGT), wet-bulb temperature (WBT), and apparent temperature (AT). All three metrics depend on both temperature and humidity. The WBGT is a linear combination of the temperatures of an unshielded black globe, an ordinary shielded thermometer, and a wet-bulb thermometer. Although there are established safety thresholds for WBGT, instruments that properly measure WBGT are rare so Sherwood (2018) advocated for the use of WBT to study heat stress because it is directly related to the moist entropy of air and so it controls the heat flux into or out of a wet object according to the second law of thermodynamics. Among the three metrics, WBT is most sensitive to humidity, followed by WBGT and AT. When the WBT exceeds 35°C, evaporative cooling is significantly reduced so this WBT threshold has been considered the limit of human tolerance to heat stress.

Coffel et al. (2018) analyzed changes in heat stress using WBT as the metric. For each GCM grid cell, they calculated the monthly mean changes of daily maximum temperature and WBT for each year between 2020 and 2080 relative to 1985-2005 simulated by each of 18 GCMs in the CMIP5 archive. To reduce the impacts of model biases, they generated daily time series of maximum temperature and WBT for the future period by adding the monthly mean changes projected by the GCMs to the daily time series from the NCEP reanalysis II from 1985 to 2005. Figure 2.10 shows the changes in annual maximum air

temperature and WBT between 2060-2080 relative to 1985-2005 for the RCP4.5 and RCP8.5 scenarios. There are increases in air temperature and WBT everywhere, but the changes are generally larger in the tropics and for RCP8.5 compared to RCP4.5. Air temperatures increase at a faster rate and have more spatial variability than wet-bulb temperatures, partly because of the dependence of WBT on humidity. In the U.S., both air temperatures and WBT increase more along the eastern U.S. and California. Coffel et al. (2018) noted a divergence between the changes in mean and extreme air temperatures (i.e., larger increases in the annual maximum air temperatures than the mean daily maximum temperatures) in regions including the eastern U.S. that are likely driven by land-atmosphere interactions (e.g., Miralles et al. 2014) and dynamical changes (Coumou et al. 2014), but such divergence is not obvious in WBT.

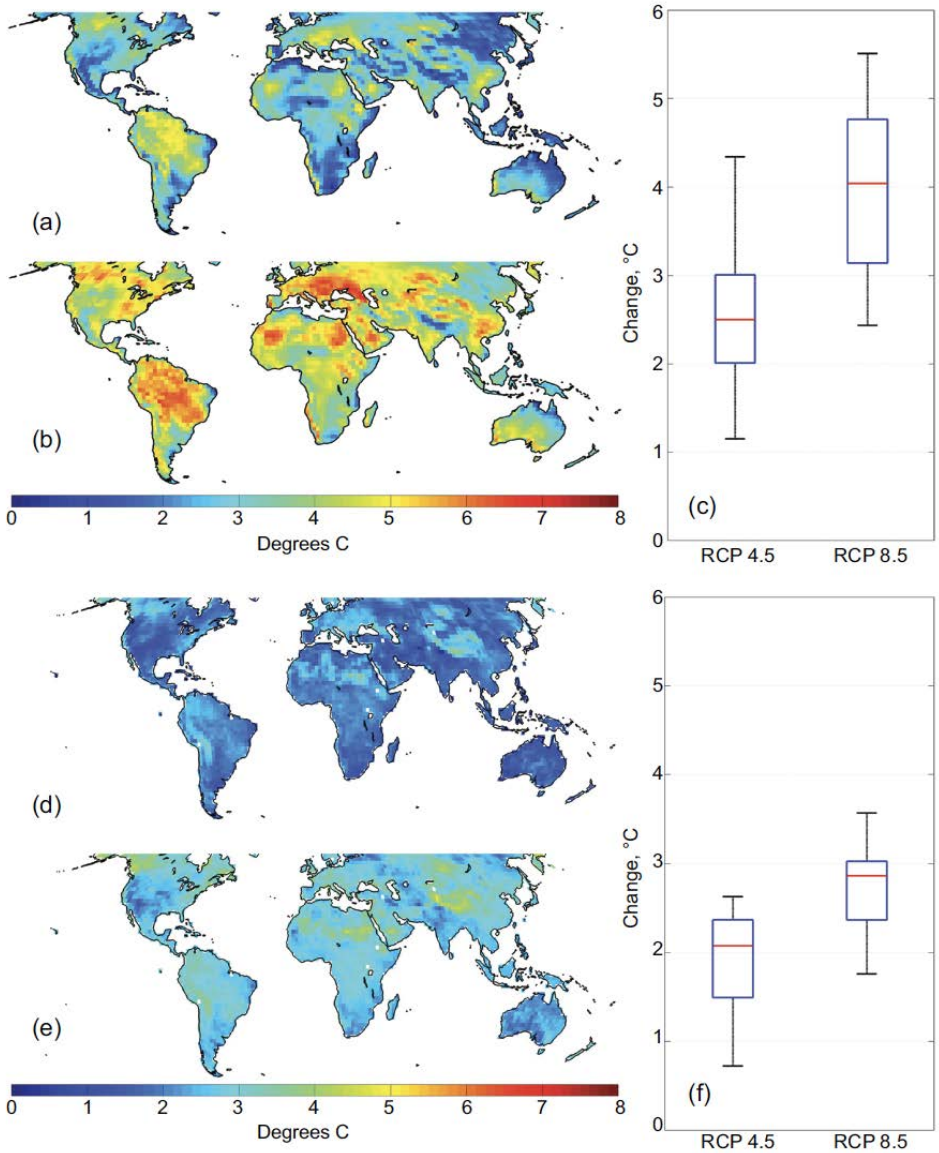

Figure 2.10. Changes in annual maximum air temperatures (a)-(c) and WBT (d)-(f) in 2060-2080 relative to 1985-2005 under RCP4.5 (a)&(d) and RCP8.5 (b)&(e). (c) and (f) show the range of projected annual maximum temperature increase spatially averaged over land for both emission scenarios over all 18 CMIP5 GCMs. (Source: Coffel et al. 2018.)

3.0 Precipitation in the Northeast Region

This chapter includes information related to observed precipitation (Section 3.1), including characteristics of observed precipitation and its historical trends (Section 3.1.1). This chapter also summarizes the projected changes in mean and extreme precipitation in the northeast region (Section 3.2). Data were obtained from the NOAA NCEI, the CSSR report, United States Geological Survey (USGS), and from published papers and reports in the broad climate research community.

3.1 Observed Precipitation

3.1.1 Current Climatology

The NOAA NCEI summarizes the average precipitation in the form of maps to visualize the information. The NCEI currently uses an averaging period of 1981 to 2010 to create climatology maps (NCEI 2016).

For the northeast region, precipitation variation is influenced by orographic effects (see Figure 3.1**Error! Reference source not found.**). Mean annual precipitation varies from 35 in. in parts of New York to 50 in. along the New England coast (Figure 3.1**Error! Reference source not found.**). Orographic effects result in local amounts exceeding 60 in. at inland locations in West Virginia and New York. Generally, the amount of precipitation decreases inland. During winters, blizzards and ice storms occur frequently. Storms that are driven by the strong temperature contrast between interior North America and the western Atlantic, also known as nor'easters, can be particularly severe (Kunkel et al. 2013). The combination of cold air to the northwest and warm and moist air to the southeast results in rapid development of extratropical cyclones. These storms can result in large amounts of snowfall, flood-inducing rainfall, hurricane-force winds, and very cold conditions. Lake-effect snowfall, caused by warm air moving from relatively warm, unfrozen lakes onto much colder onshore areas, can also cause frequent winter impacts. Lake-effects snowfall events are smaller spatially than nor'easters. The northeast region is also prone to freezing rain largely because of the prevalence of winter storm tracks and suitable topography. Remnants of tropical cyclones also produce large amounts of rain and widespread flooding.

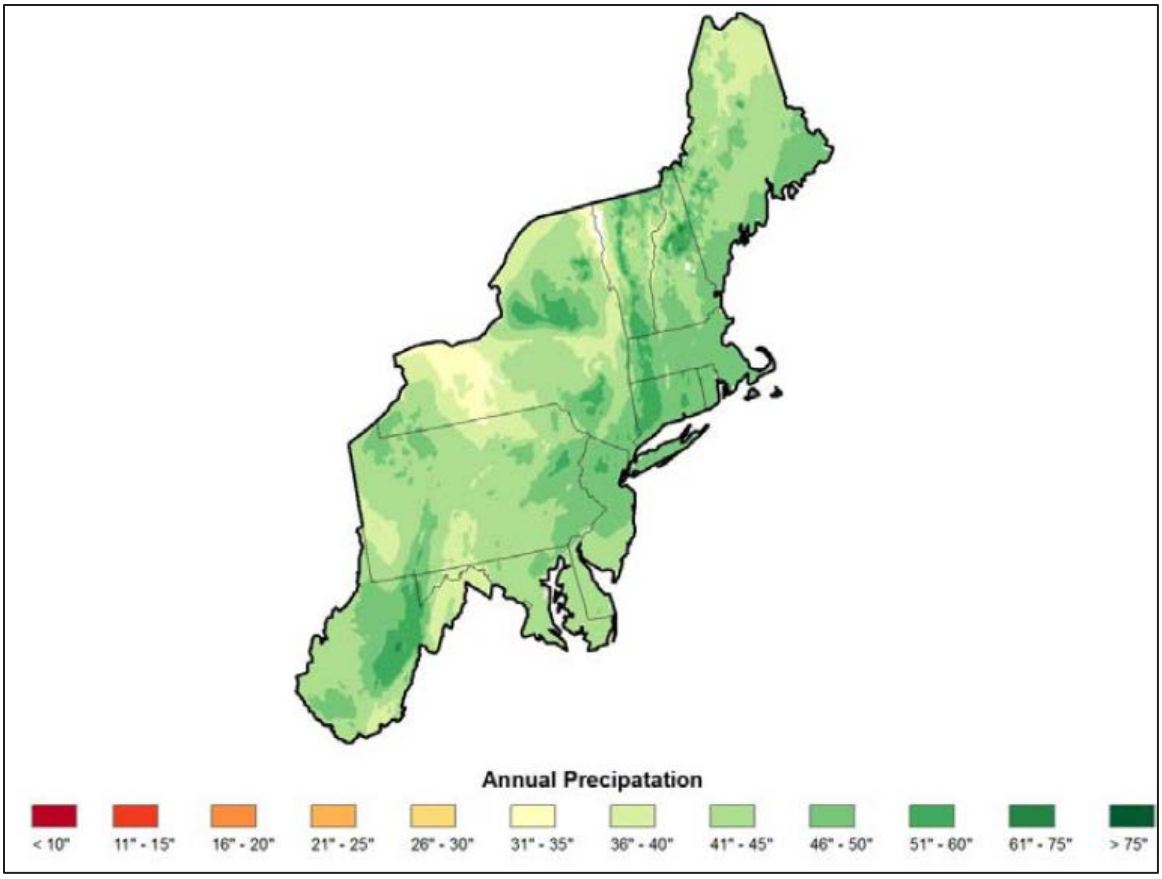

Figure 3.1. Average annual precipitation (1981–2010 normals). (Source: Kunkel et al. 2013.)

Figure 3.2 shows normal annual snow totals (as freshly-fallen snow depths) over the northeast region (NRCC 2019). Generally, snowfall increases to the north and inland and is locally influenced by orography and lake effects. Average annual snowfall varies from less than 20 in. in the south to over 140 in. in northern, inland areas. Figure 3.3 shows the average number of days with accumulated snow depths equal to or greater than 1 in. during any month of the year for the 1961-2018 period. The number of days with accumulated snow depths equal to or exceeding 1 in. varies from 7.5 in the south of the region (Salisbury area, New Jersey) to 137.4 in the north (Caribou area, Maine).

The Midwestern Regional Climate Center provides nationwide climatology of the accumulated winter season severity index (AWSSI, Boustead et al. 2015).[1] The AWSSI is updated on an ongoing basis.

[1] The AWSSI is an accumulated index of winter severity that takes into account temperature, snowfall, snow depth, and duration of winter-weather conditions (Boustead et al. 2015). AWSSI has a temperature component and a snow component that are calculated separately using daily data and is accumulated through a winter season. Onset of winter is defined as the earliest occurrence of one of (1) daily maximum temperature less than or equal to 32°F, (2) daily snowfall greater than or equal to 0.1 in., and (3) December 1. Winter ends at the last occurrence of one of (1) daily maximum temperature less than or equal to 32°F, (2) daily snowfall greater than or equal to 0.1 in., (3) snow depth greater than or equal to 1 in., and (4) last day of February. Daily AWSSI is a score assigned to the day based on thresholds of daily maximum and minimum temperatures, snowfall, and snow depth; scores in all categories are summed to obtain AWSSI for the day. Because snow data can contain significant uncertainties and

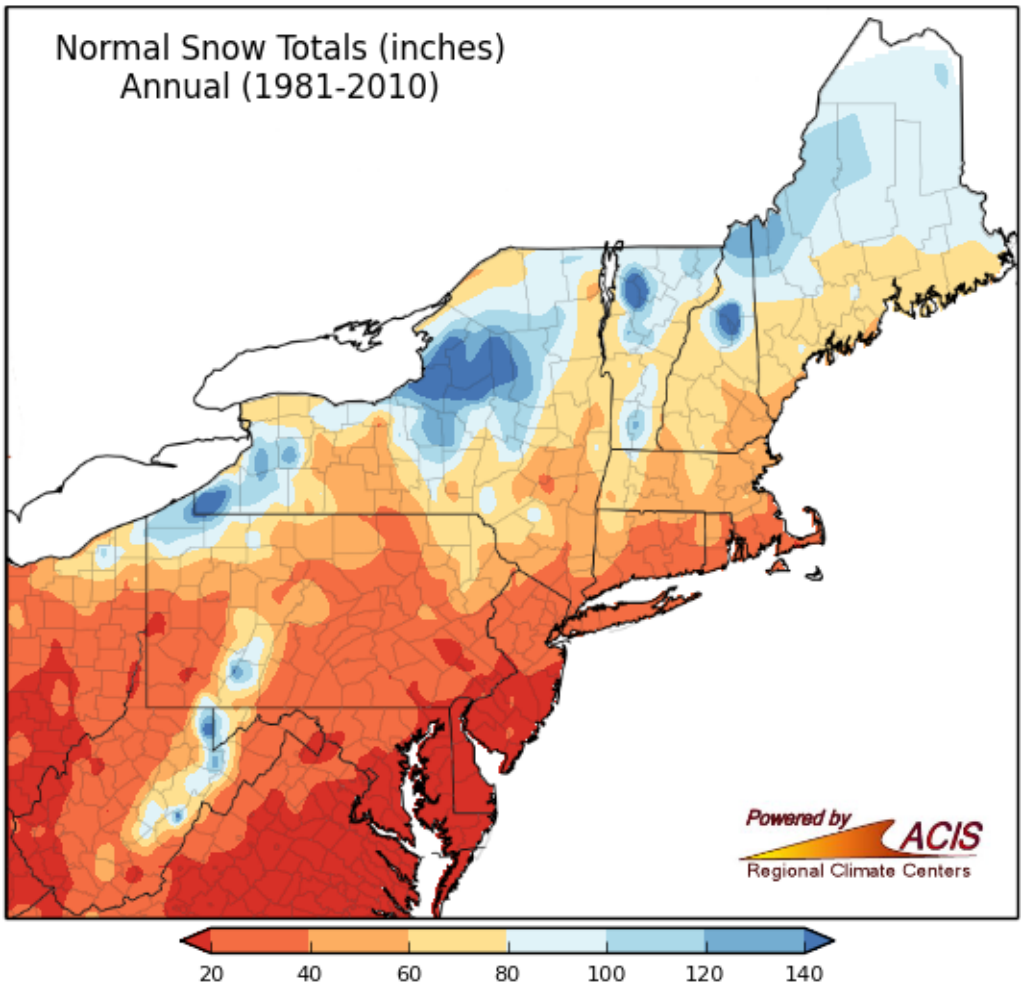

Figure 3.2. Average annual snowfall as in. of snow (1981-2010 normals) for the northeast region. (Source: NRCC 2019.)

Figure 3.4 shows the nationwide average AWSSI computed using 1980–2014 data. The AWSSI in itself provides little information; however, it is a useful measure to compare among winters at a given location, including the onset of winter and its length. The temperature and snow portions of the AWSSI can also be used to distinguish between how a particular winter progressed, as represented by temperature and snow accumulation, respectively. These indices can be useful in quantifying antecedent and transient conditions for regions where floods may result from rain-on-snow events.

are of limited record, AWSSI is also calculated using estimated snowfall from precipitation and temperature data. A degree-day approach is used to compute snowmelt and a compaction factor approach is used to estimate daily snow depths.

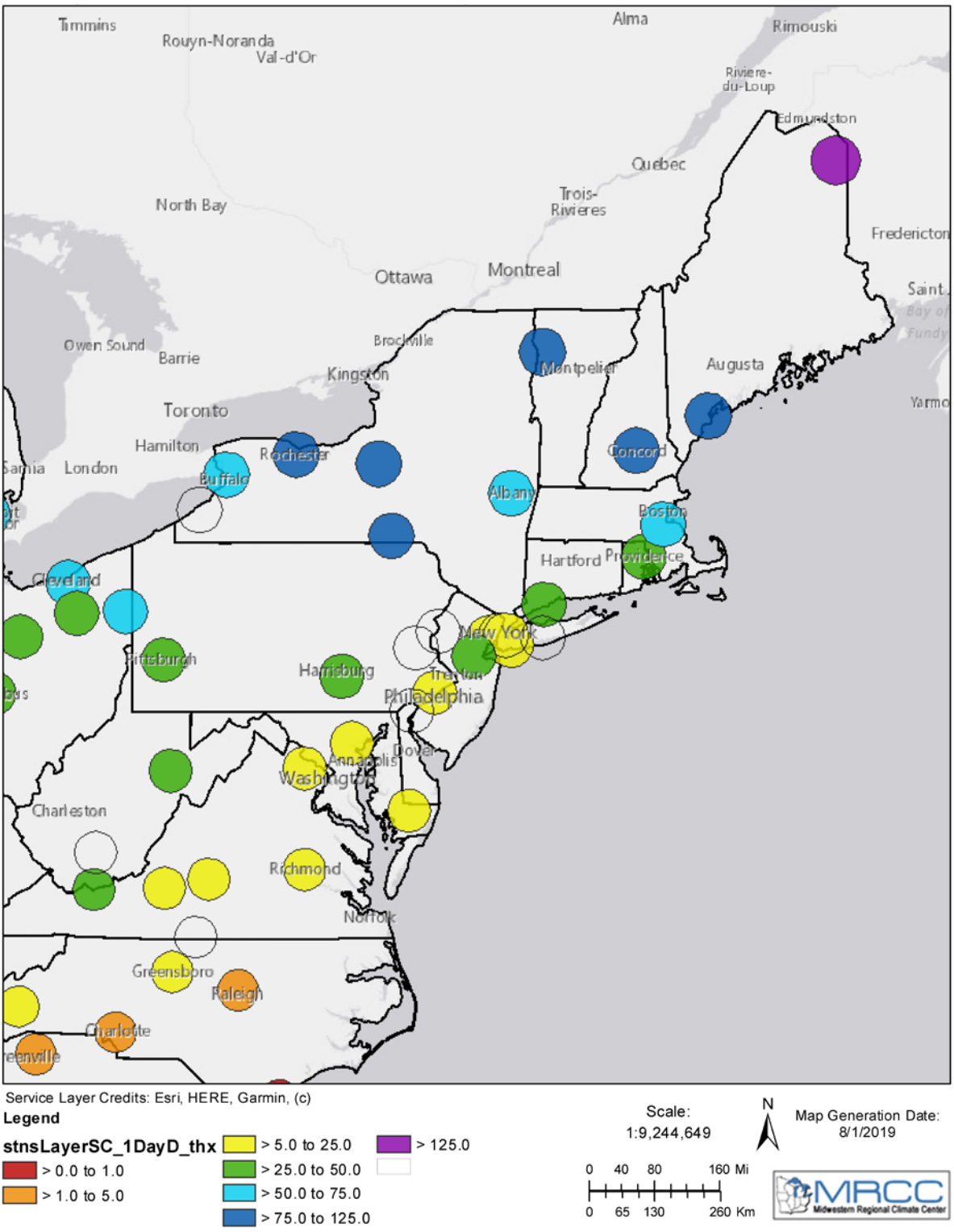

Figure 3.3. Average number of days with snow depth equal to or exceeding 1 in. based on the period 1961-2018. (Source: Midwestern Regional Climate Center.)

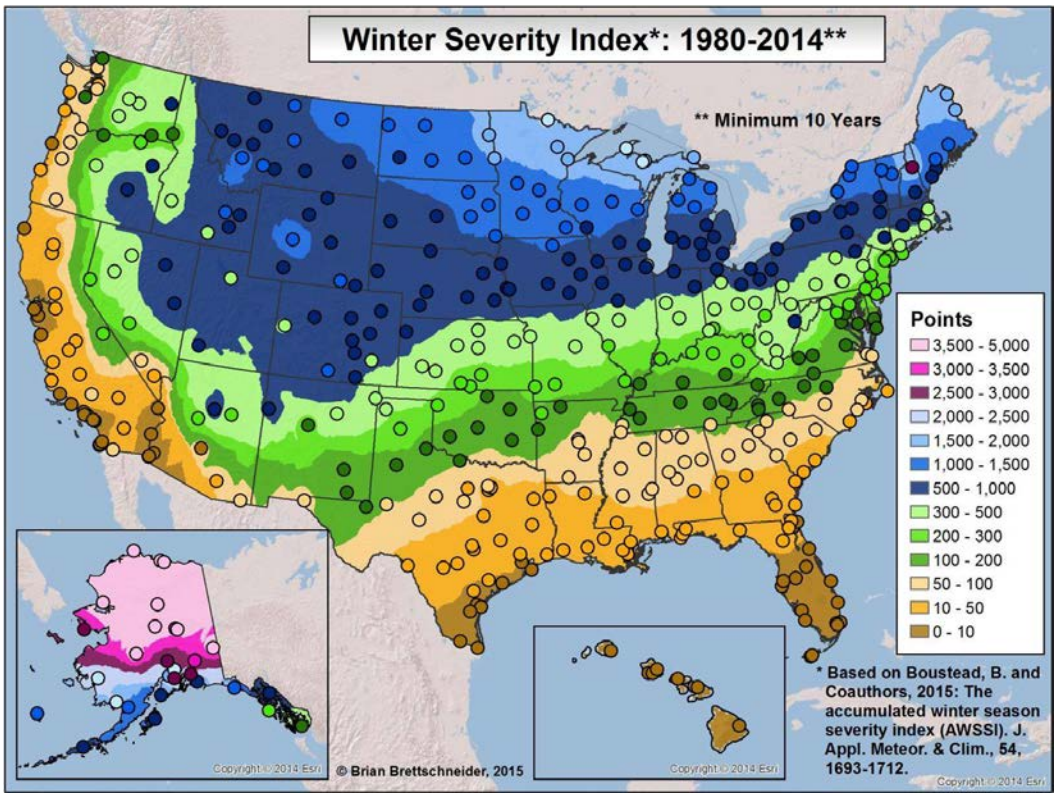

Figure 3.4. Average AWSSI computed for the 1980–2014 period. (Source: Midwestern Regional Climate Center.)

3.1.2 Observed Trends

- Mean annual precipitation shows a long-term increasing trend. Seasonally, increasing trends are statistically significant only for the fall season.
- Extreme precipitation frequency, as measured by occurrence of daily 0.2 annual exceedance probability (AEP) precipitation does not show a statistically significant trend. However, the number of 0.2 AEP, 2-day events shows significant increases, particularly in the last 50 years.
- The amount of precipitation falling in daily events that exceeds the 99th percentile of all non-zero precipitation days has increased significantly.
- The 0.05 AEP seasonal daily precipitation totals have increased, particularly in spring and fall seasons.
- Annual snowfall totals equal to or greater than the 90th percentile did not show statistically significant trend for the 1900-2006 period, but showed some statistically significant decreases for the 1950-2006 period.

Kunkel et al. (2013) reported that annual precipitation shows an increasing, statistically significant trend (0.39 in./decade) over the observed record (see Figure 3.5). A statistically significant trend in seasonal precipitation was found only for fall (0.24 in./decade). They also investigated a possible trend in extreme precipitation, represented by an extreme precipitation index. Using the Global Historical Climate Network

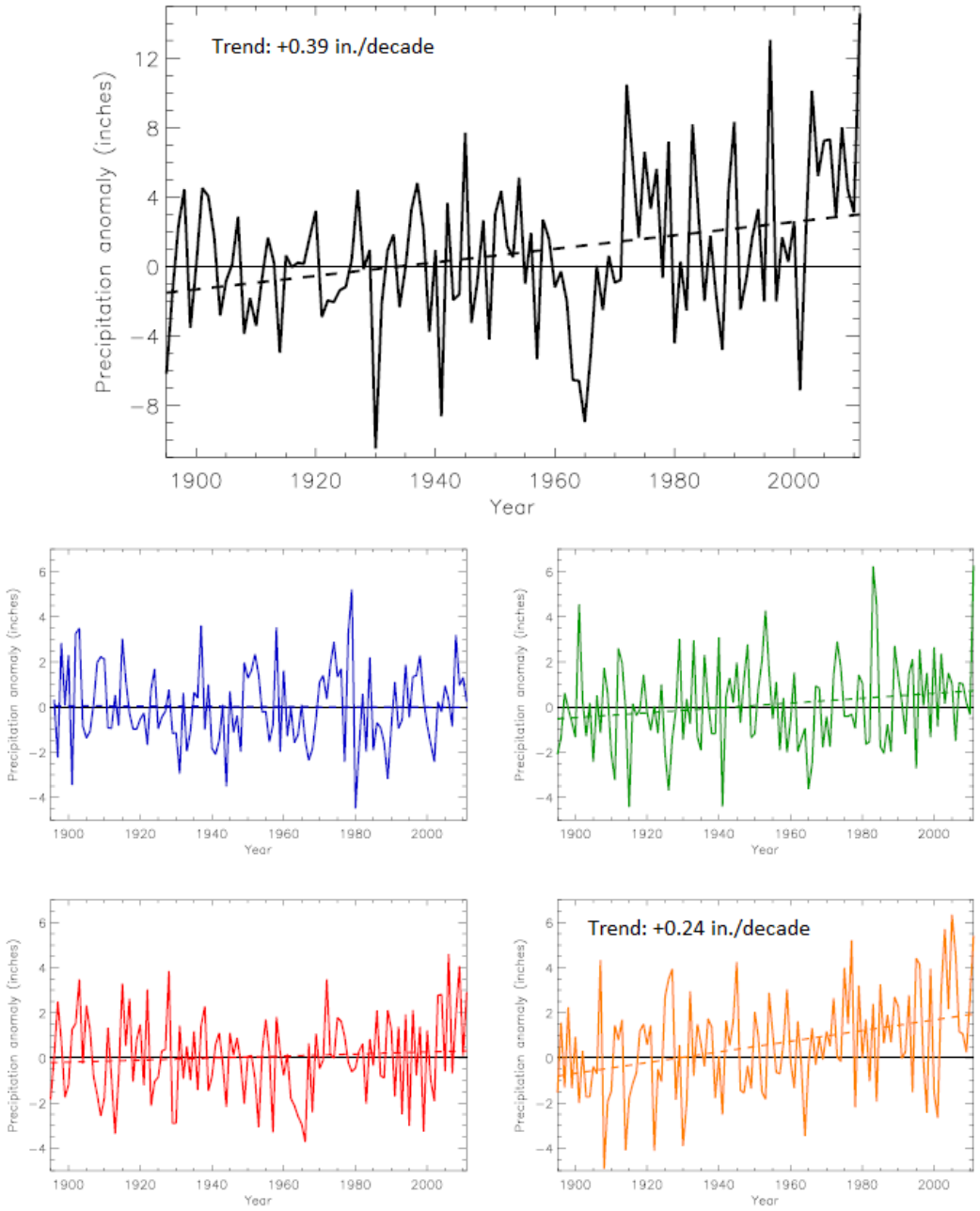

Figure 3.5. Trends in observed precipitation anomaly from 1895–2011 (deviations from 1901–1960 means) in the northeast region based on a gridded NOAA Cooperative Observer Network data. The top panel shows the annual precipitation anomalies, middle-left panel shows the winter precipitation anomalies, middle-right panel shows the spring precipitation anomalies, bottom-left panel shows the summer precipitation anomalies, and the bottom-right panel shows the fall precipitation anomalies. Values for statistically significant trends are shown. (Source: Kunkel et al. 2013.)

data for stations with less than 10 percent missing daily precipitation data for 1895-2011, events were ranked and the top one-fifth were selected. Numbers of selected events for each year for stations located inside a 1°x1° grid were averaged. Finally, the regional average for each year was calculated by averaging

the numbers of events across all grids; this regional average is called the extreme precipitation index. Figure 3.6 shows the time series of extreme precipitation index; the trend was not statistically significant (Kunkel et al. 2013).

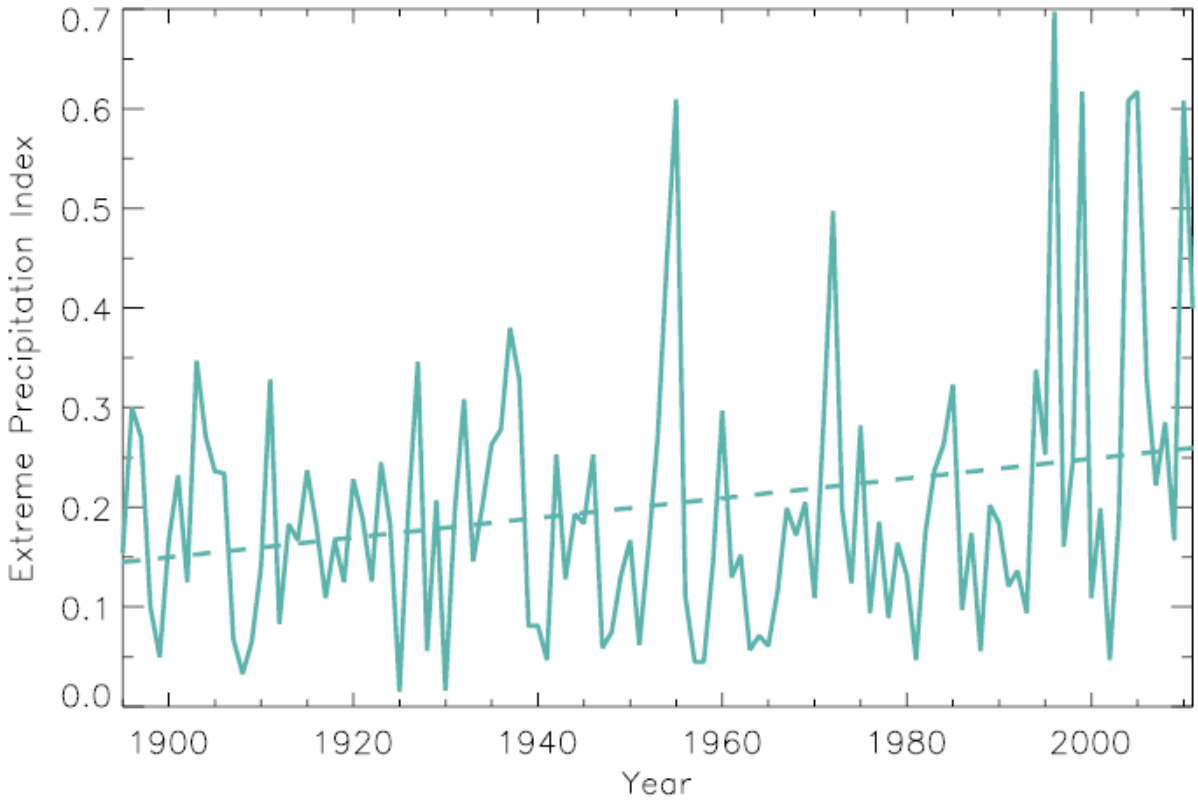

Figure 3.6. Time series of extreme precipitation index (see description in text) for the northeast region. The trend is not statistically significant. (Source: Kunkel et al. 2013.)

Figure 3.7 shows the observed change in the 0.05 annual exceedance probability (AEP) daily precipitation by season between 1948 and 2015. In the Northeast, larger changes are observed in spring (0.25 in.) and fall (0.23 in.), although a positive trend is seen in all seasons. Figure 3.8 shows the change in several metrics of extreme precipitation over the entire period of 1901–2016 or 1958–2016. The metrics include (1) the maximum daily precipitation in consecutive 5-year blocks from 1901 to 2016 calculated at individual stations, then averaged within each 2°x2° box, and then aggregated by region to calculate a trend; (2) daily precipitation in the top 1 percent of all days for 1958–2016; and (3) the number of 2-day events exceeding the 5-year recurrence interval threshold for 1958–2016 and 1901–2016. Changes over the Northeast are positive; the amount of precipitation falling in daily events that exceeds the 99th percentile of all non-zero precipitation days has increased 55 percent. The number of 2-day events exceeding the 0.2 AEP threshold shows an increase of 74 percent for the 1901–2016 period and of 92 percent for the 1958–2016 period (Figure 3.8).

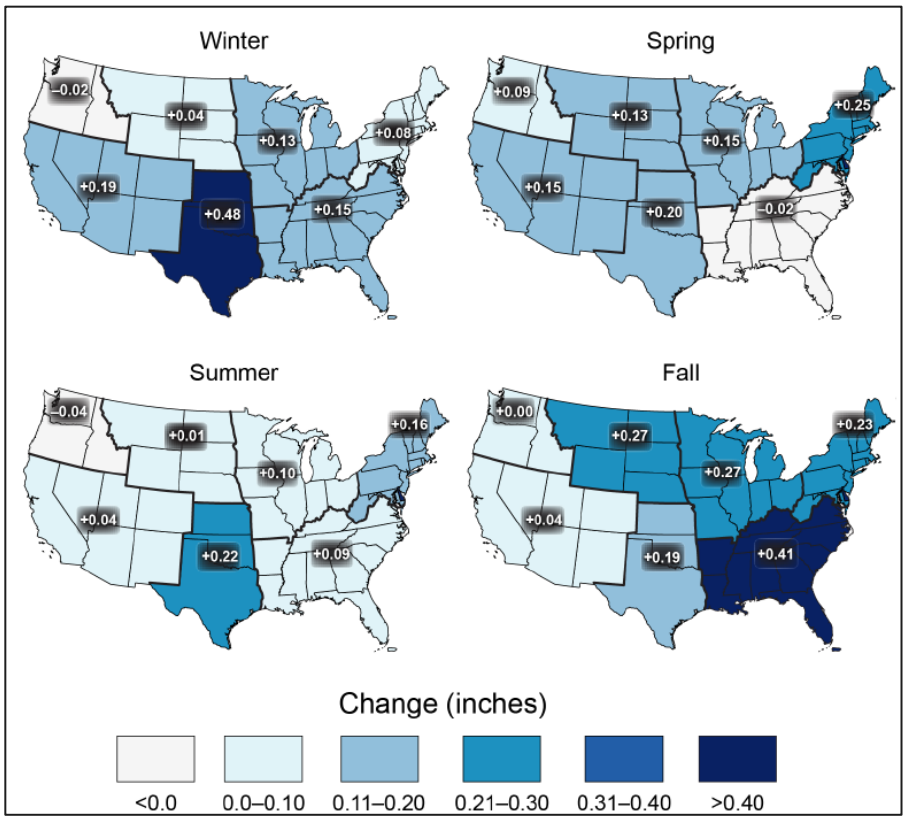

Figure 3.7. Observed changes in the 0.05 AEP seasonal daily precipitation totals over the period from 1948 to 2015 using data from the Global Historical Climatology Network data set. (Source: Easterling et al. 2017.)

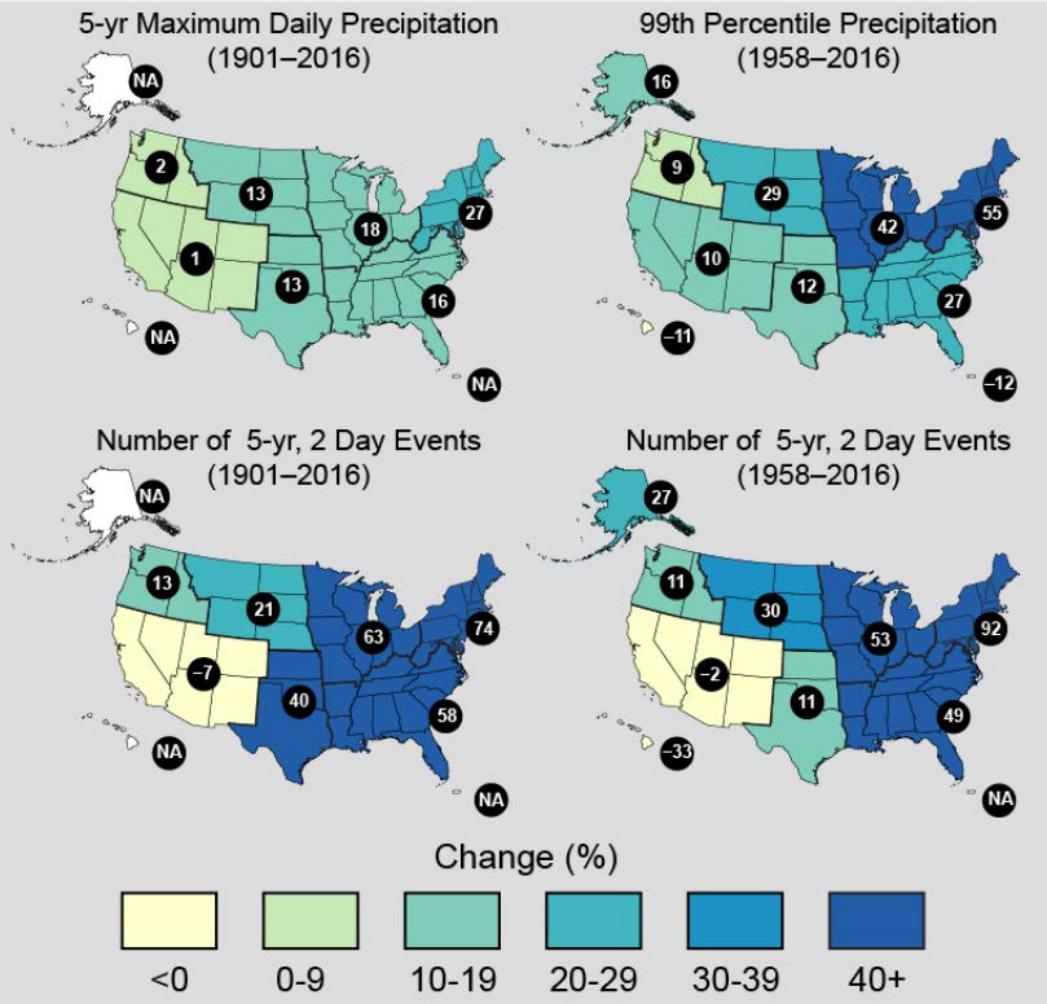

Figure 3.8. The change in several metrics of extreme precipitation by NCA4 region, including (upper left-hand panel) the maximum daily precipitation in consecutive 5-year blocks; (upper right-hand panel) the amount of precipitation falling in daily events that exceeds the 99th percentile of all non-zero precipitation days; (lower left-hand panel) the number of 2-day events exceeding the 5-year recurrence interval threshold, calculated over 1901–2016; and (upper right-hand panel) the number of 2-day events exceeding the 5-year recurrence interval threshold, calculated over 1958–2016. The numerical value is the percent change over the entire period, either 1901–2016 or 1958–2016. The percentages are first calculated for individual stations, then averaged over 2° latitude by 2° longitude grid boxes, and finally averaged over each NCA4 region. (Source: Easterling et al. 2017.)

Kunkel et al. (2009) analyzed the percentage of stations where winter-centered annual snowfall totals were equal to or greater than the 90th percentile (high-extreme snowfall) and were equal to or less than the 10th percentile (low-extreme snowfall) for National Climatic Data Center (NCDC) standard regions depicted in Figure 3.9; the time period used was 1937-38 through 2006-07 for this analysis. The whole northeast and a small portion of the central NCDC standard regions compose the northeast region as defined by NCA4. The estimated 1900–2006 trend for the high-extreme snowfall for the northeast region ranged from a decrease of 8.4 percentage frequency ($[100\ yr]^{-1}$) (central NCDC standard region) to a decrease of 2.2 percentage frequency (northeast NCDC standard region), but was not statistically significant. The estimated 1950–2006 trend for the high-extreme snowfall for the northeast region ranged

from a decrease of 19.4 percentage frequency (central NCDC standard region, statistically significant) to a decrease of 15.3 percentage frequency (northeast NCDC standard region, not statistically significant). The estimated 1900–2006 trend for the low-extreme snowfall for the northeast region ranged from an increase of 6.7 percentage frequency (central NCDC standard region, not statistically significant) to an increase of 12.7 percentage frequency (northeast NCDC standard region, statistically significant). The estimated 1950–2006 trend for the low-extreme snowfall for the northeast region ranged from an increase of 11.4 percentage frequency (central NCDC standard region, not statistically significant) to an increase of 21.7 percentage frequency (northeast NCDC standard region, statistically significant). The time series of the percentage of stations with high-extreme and low-extreme snowfall for the two NCDC standard regions that comprise the northeast region are shown in Figure 3.10. Since 1975, there seems to be a decreasing trend in the high-extreme snowfall frequency. The trends in the low-extreme since 1975 are less clear (northeast shows fluctuations and central shows a decreasing trend). However, taken together, they indicate a reduction in high-extreme snowfall frequency over the northeast. Kunkel et al. (2009) concluded that November-March air temperatures are key to the frequency of both metrics.

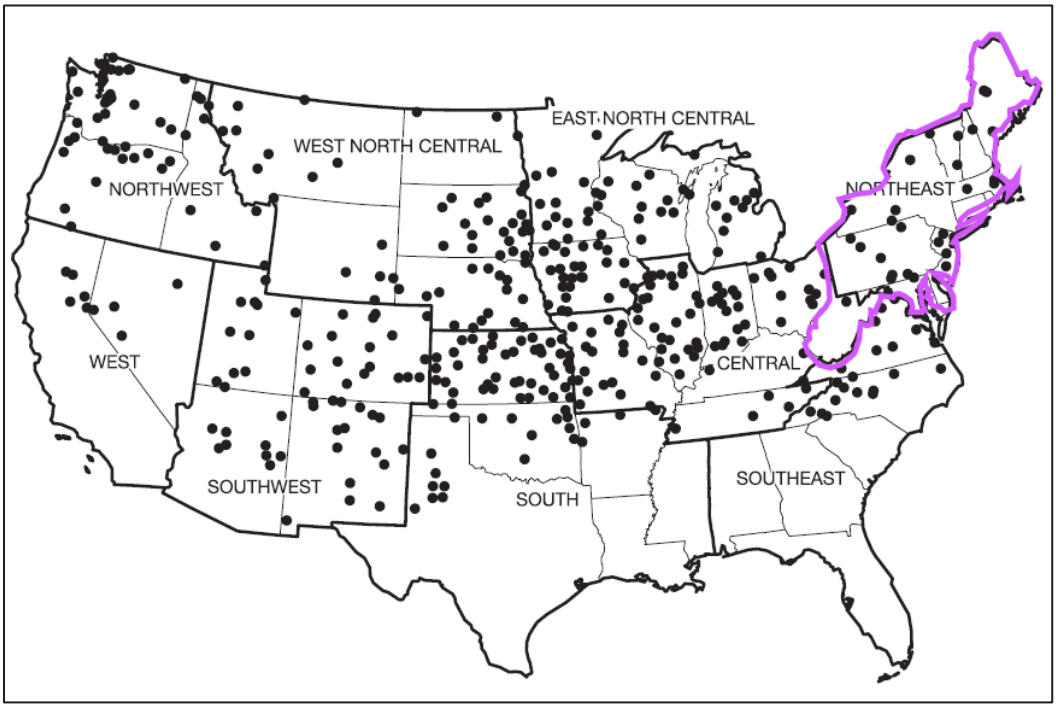

Figure 3.9. NCDC climate regions used by Kunkel et al. (2009).

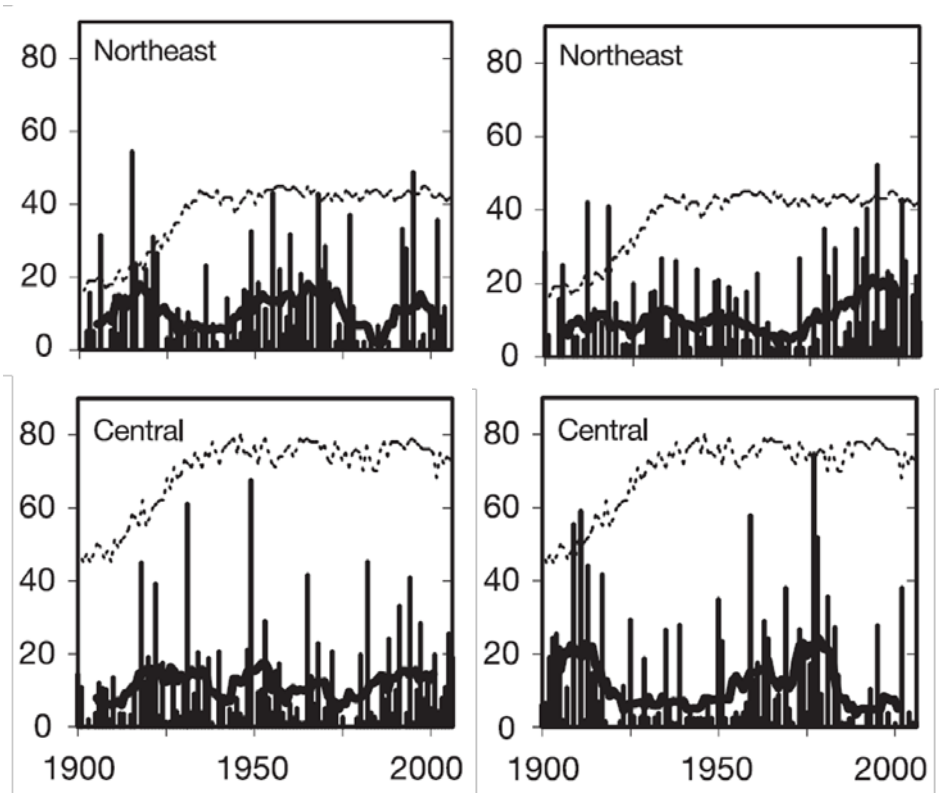

Figure 3.10. Regional average percentage of snowfall stations that are equal to or greater than the 90th percentile (left panel) and equal to or less than the 10th percentile annual snowfall. The percentile thresholds were estimated using data from 1937-38 through 2006-07. The thick black line is a moving 11-year average and the dashed line indicates the number of active stations. (Source: Kunkel et al. 2009.)

Since the 1960s, when snow cover data from satellites became available, northern hemisphere snow cover extent (SCE) has not changed significantly during winter but has increased in the fall and decreased in spring (Easterling et al. 2017). Partly due to higher temperatures, the decrease in spring SCE is larger than the increase in fall SCE. Since 2010, 7 of the 45 highest monthly SCE values occurred in fall or winter (November and December), while 9 of the 10 lowest monthly SCE values occurred in May and June, which indicates a trend toward earlier snowmelt, particularly at high latitudes (Kunkel et al. 2016). Using NOAA's Global Historical Climatology Network Daily data set to analyze northern hemisphere snow depths, Kunkel et al. (2016) also stated that while most of the trends in snow depths across the U.S. were not statistically significant, most grids exhibited negative trends (Figure 3.11).

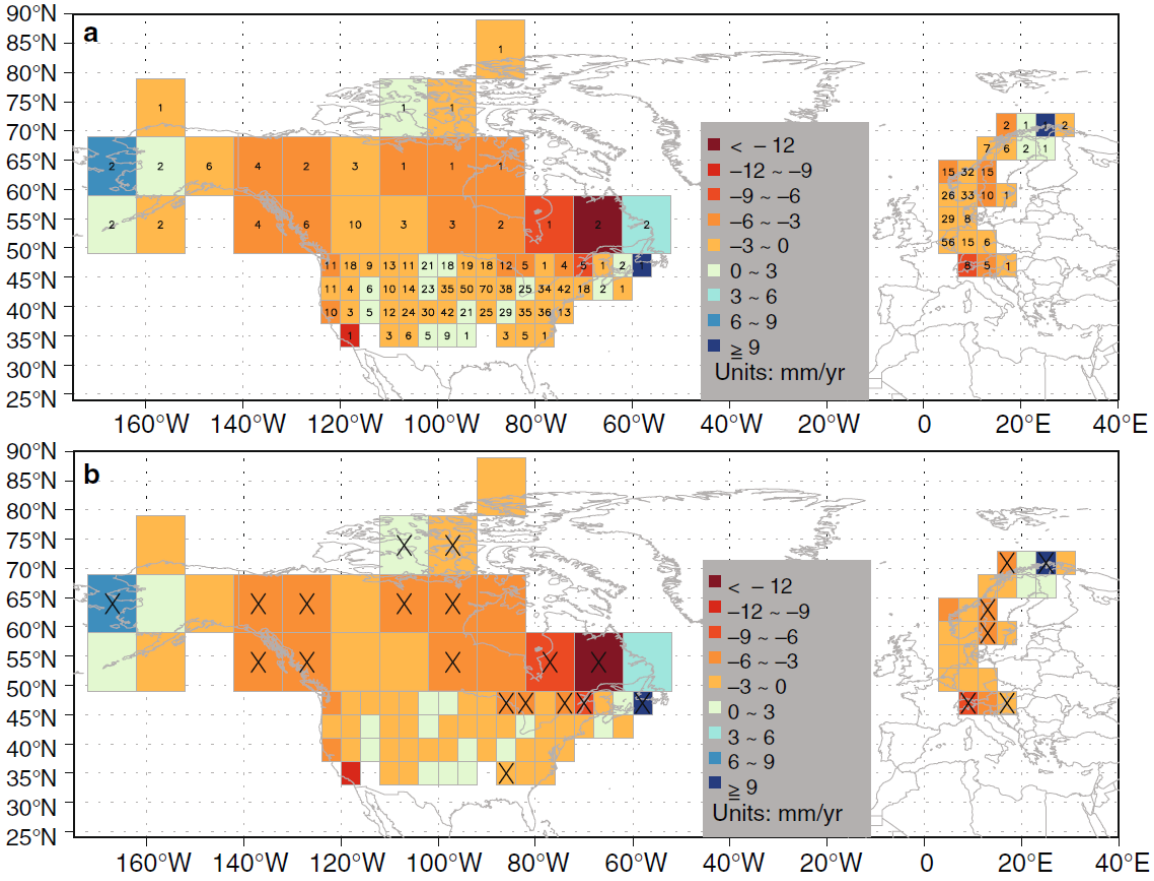

Figure 3.11. Trends in annual maximum snow depths for the period 1960-61 through 2014-15. The top panel indicates the number of stations available in the grid cell and the check marks in the bottom panel indicate statistically significant trends. (Source: Kunkel et al. 2016.)

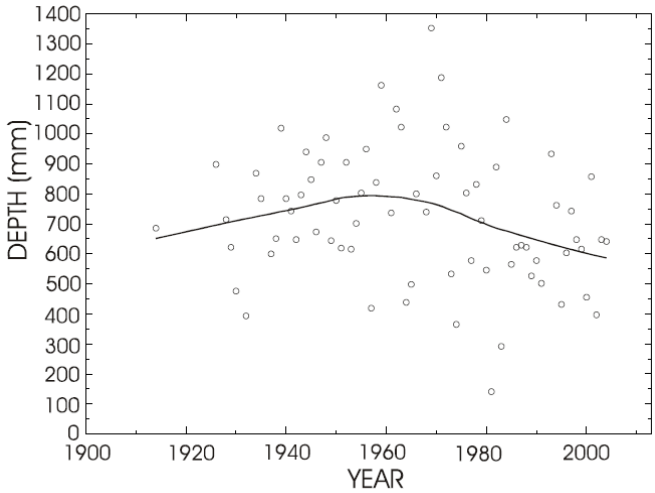

Figure 3.12. Changes in time for average annual snowpack depth for four snow course sites in western Maine-northern New Hampshire. The line depicts the smooth trend. (Source: Hodgkins and Dudley 2006.)

Snow depths at 18 of 23 long-term snow course sites in Maine and New Hampshire show statistically significant decreases (Hodgkins and Dudley 2006). The authors used observed records spanning at least 50 years through 2004. None of the snowpack time series data showed significant serial correlations and the authors used Mann-Kendall test to evaluate temporal trends. Figure 3.12 shows the data and smoothed trend for average annual snowpack depths for four snow course sites in western Maine-northern New Hampshire.

Huntington et al. (2004) evaluated changes in snow to total precipitation ratio at 21 U.S. Historical Climatology Network (USHCN) sites (Figure 3.13). Temperature and precipitation data from 1948-2001 was used. The authors compiled time series of snow-water equivalent (SWE), total precipitation, and SWE to total precipitation ratio (S/P ratio) for annual, winter (December-March), and monthly (October-April) periods. Temporal trends at individual sites, 21-site aggregate, and 4-site aggregate (sites in Maine and northwest New Hampshire) were tested using a nonparametric test for monotonic trend based on Kendall's tau statistic.

Eleven of 21 sites had significant decreasing trends in annual S/P ratios. All sites in northwest Maine and northernmost New Hampshire showed significant decreasing trends in annual S/P ratios. Five of eight sites located on or near the coast also showed significant decreasing trends in annual S/P ratios. Seven sites showed significant decreasing trends in winter S/P ratios. No site showed any significant or weak increasing trend. Analysis of aggregated data showed that the entire New England region and the northernmost region had significant decreasing S/P ratio trends, both for annual and winter periods.

Aggregated data for four northern New England sites showed that annual S/P ratios decreased from about 0.3 in 1949 to about 0.23 in 2000 (Figure 3.14). The locally weighted scatterplot smooth (LOWESS) curves in Figure 3.15 show that most of the decrease in S/P ratio occurred after 1975. Monthly trend analysis also revealed that the decreasing trends in S/P ratios at these four sites were significant for December and March, with the rate of decrease of S/P ratio being greater in December (Figure 3.15). The authors noted that the changes in S/P ratio occurs near the beginning and the end of winter when temperatures are more frequently near freezing and even small warming of temperatures can result in precipitation phase changes.

Huntington et al. (2004) noted that decreasing S/P ratios can be caused by (1) snowfall decreases larger than total precipitation decreases, (2) little change in snowfall with increases in rainfall, and (3) snowfall increases smaller than total precipitation increases. In their analyses, the authors found that neither total annual rainfall nor winter rainfall increased significantly for the New England region during 1949-2000. Annual rainfall showed a weak but insignificant increasing trend. The four northern New England sites also did not show significant trends in annual or winter rainfall. Total annual SWE, however, decreased significantly both for the entire New England region and the northern New England region. The authors concluded that the annual trends in S/P ratio are primarily due to decreasing snowfall and secondarily by increasing rainfall in non-winter periods.

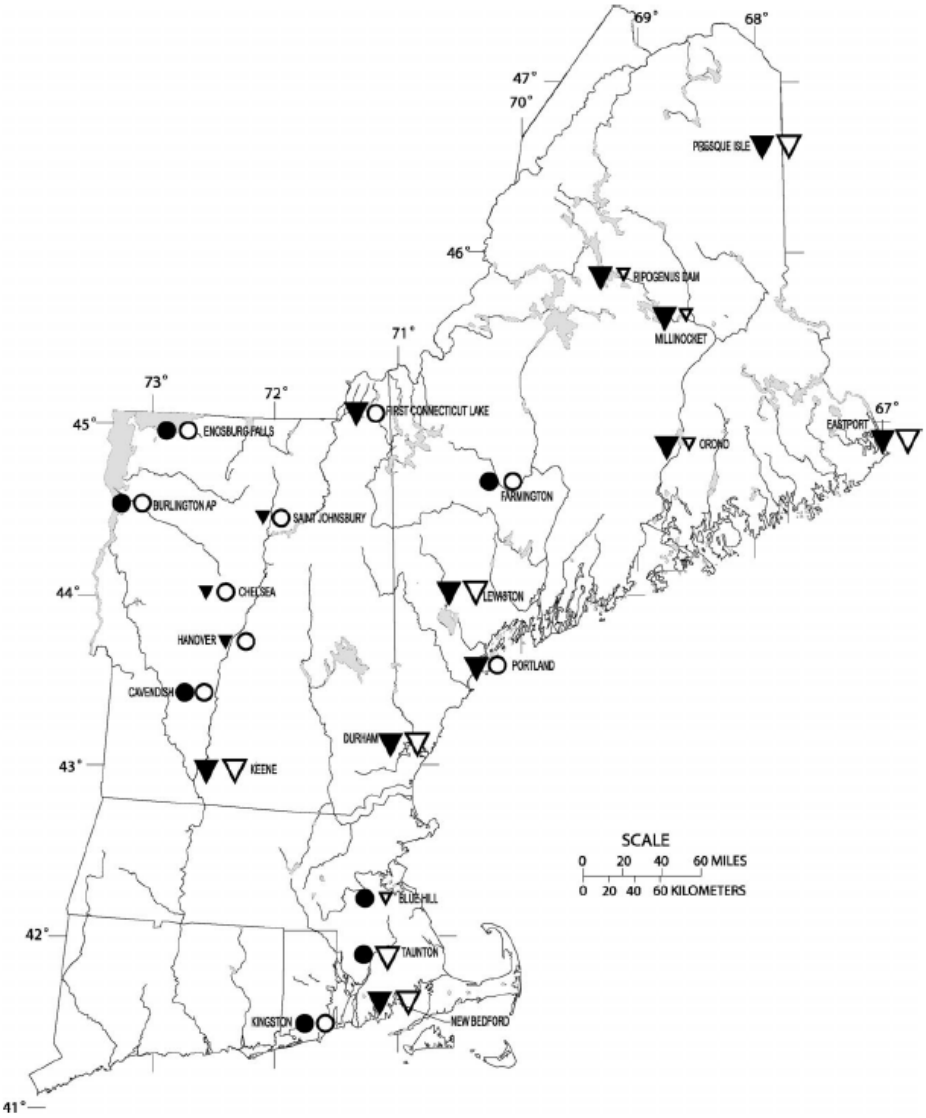

Figure 3.13. Locations of USHCN stations used by Huntington et al. (2004) for estimating trends in snow to total precipitation ratio. Annual trends are denoted by filled symbols and winter trends by open symbols. Upward (downward) pointing triangles indicate increasing (decreasing) trends and circles indicate no trend. Large triangles indicate significant trend (Kendall's tau p-value < 0.05) and small triangles indicate weak trends (Kendall's tau p-value from 0.05 to 0.20). (Source: Huntington et al. 2004.)

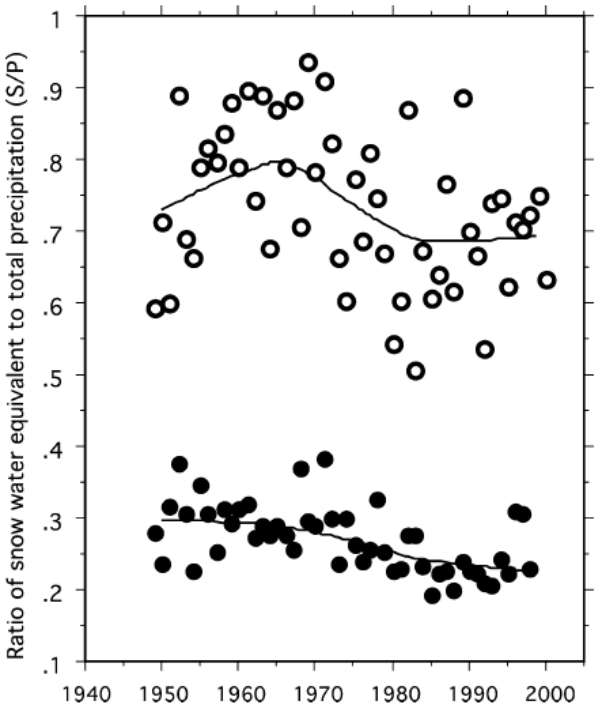

Figure 3.14. Snow to total precipitation ratio aggregated for four northernmost New England sites. The filled symbols represent annual ratios and open symbols represent winter ratios. The lines are the LOWESS curves. (Source: Huntington et al. 2004.)

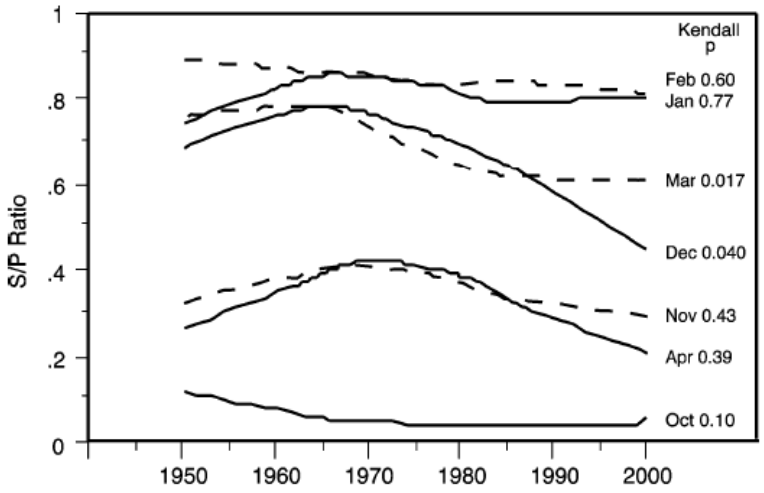

Figure 3.15. Monthly trends in snow to total precipitation ratio aggregated for four northernmost New England sites. March and December trends are significant. (Source: Huntington et al. 2004.)

3.2 Future Changes in Precipitation

- Based on CMIP3 model simulations, annual average precipitation is projected to increase over the northeast region with a south to north gradient. Greatest increases are projected for the northern parts of the northeast region, up to 9-12 percent under the A2 scenario during the last three decades of the 21st century, compared to the last three decades of the 20th century.
- Based on CMIP3 model simulations, winter precipitation is projected to increase the most, up to 20 percent, in the southwestern parts of the northeast region. Spring and fall precipitation is also projected to increase while summer precipitation is projected to decrease, although the changes are not significant, over most of the northeast region. CMIP5 model simulations and high-resolution, convection-permitting model simulations also show similar trends.
- Based on CMIP3 model simulations, number of days during a year with precipitation exceeding 1 in. are projected to increase with greatest increases, 25-30 percent, in the northern parts of the northeast region. Based on CMIP5 model simulations, the amount of daily precipitation corresponding to 0.05 AEP is also projected to increase, up to 22 percent during late 21st century for RCP8.5 scenario.

The projected changes in annual and seasonal mean precipitation from the CMIP3 global models and NARCCAP regional models are shown in Figure 3.16. From the CMIP3 models, there is a general south-north gradient in annual precipitation changes compared to the last three decades of the 20th century; the greatest increases are seen in the north by up to 9–12 percent under the A2 scenario by 2085. While the changes in parts of the northeast region are not statistically significant for the 2035 time period, models mostly agree on the precipitation increase under the high-emissions scenario. The downscaled projections by the NARCCAP models show increases of up to 7 percent in mean annual precipitation changes throughout the region. Increases in winter are the greatest, up to 20 percent in southwest portions of the region. Spring and fall show increases in most of the region with magnitudes varying from -4 to +12 percent. However, in more than half of the NARCCAP models, the simulated precipitation changes are not statistically significant for most of the northeast region.

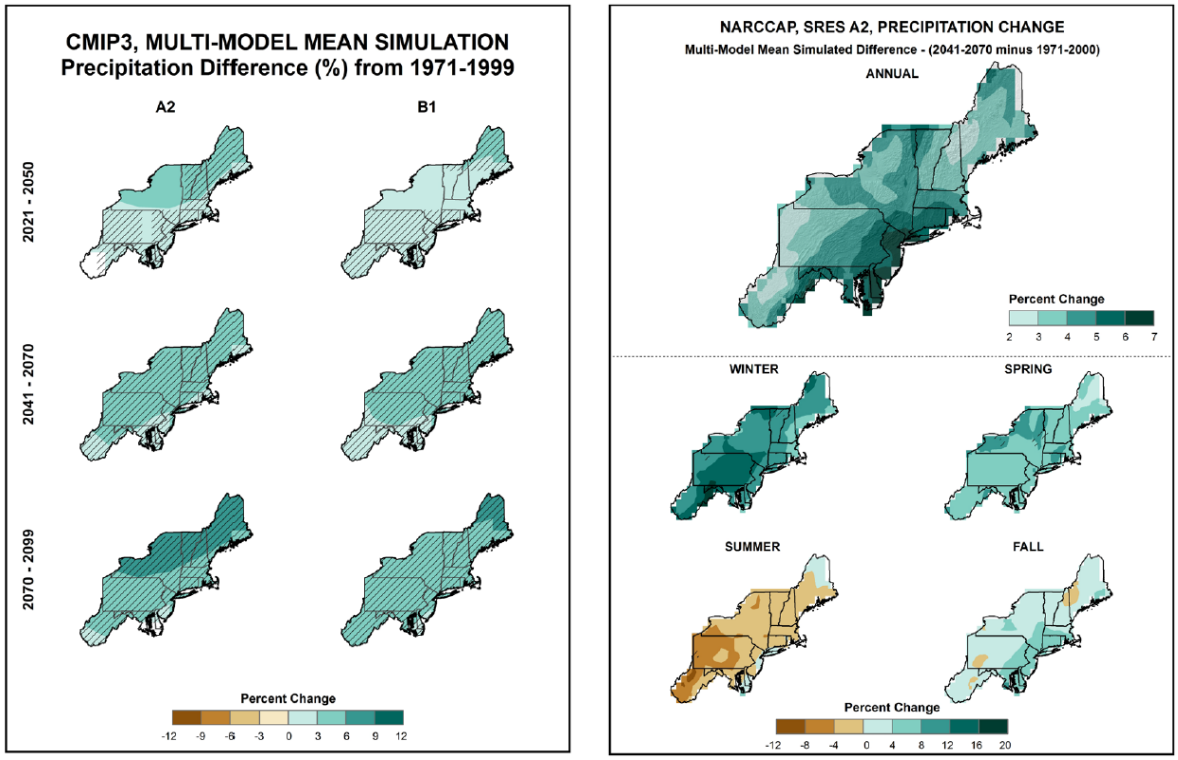

Figure 3.16. (Left) Simulated difference in annual mean precipitation (percent) for the northeast region, for 2021–2050, 2041–2070, and 2070–2099 with respect to the reference period of 1971–1999 from the CMIP3 global models for the A2 and B1 emissions scenarios. (Right) Simulated difference in annual and seasonal mean precipitation (percent) for 2041–2070 with respect to the reference period of 1971–2000 from the NARCCAP regional simulations for the A2 emissions scenario. In both panels, color with hatching indicates that more than 50 percent of the models show a statistically significant change in precipitation, and more than 67 percent agree on the sign of the change (source: Kunkel et al. 2013).

Lynch et al. (2016) investigated the changes in precipitation seasonality in the northeast region. In winter, cyclones form in the region of the midlatitude jet and storm tracks transport moisture from the North Atlantic to the northeastern U.S. In summer, the North Atlantic subtropical high directs meridional moisture transport poleward around its western flank into the region. Hence, climatologically the annual cycle of precipitation in the northeastern U.S. has a weak amplitude, with more precipitation in summer than winter. Using the historical and future (RCP8.5) simulations from 15 CMIP5 models, Lynch et al. (2016) analyzed the changes in monthly precipitation and found significant increases in precipitation in all seasons, particularly in winter and spring, but changes in summer precipitation are not significant due to large model disagreement (Figure 3.17). Hence model projections indicate a weakening of the precipitation annual cycle in the future, which is inconsistent with the observations (1951-2000) that show the largest positive trend in fall. The lack of precipitation increase projected for the future summer is a response to the westward extension of the North Atlantic subtropical high, which acts to reduce the amplitude of the quasi-stationary trough over the region and results in weak moisture divergence. During winter, moisture convergence increases although storm tracks are reduced in early winter (November-December) and increased in late early spring (March-April).

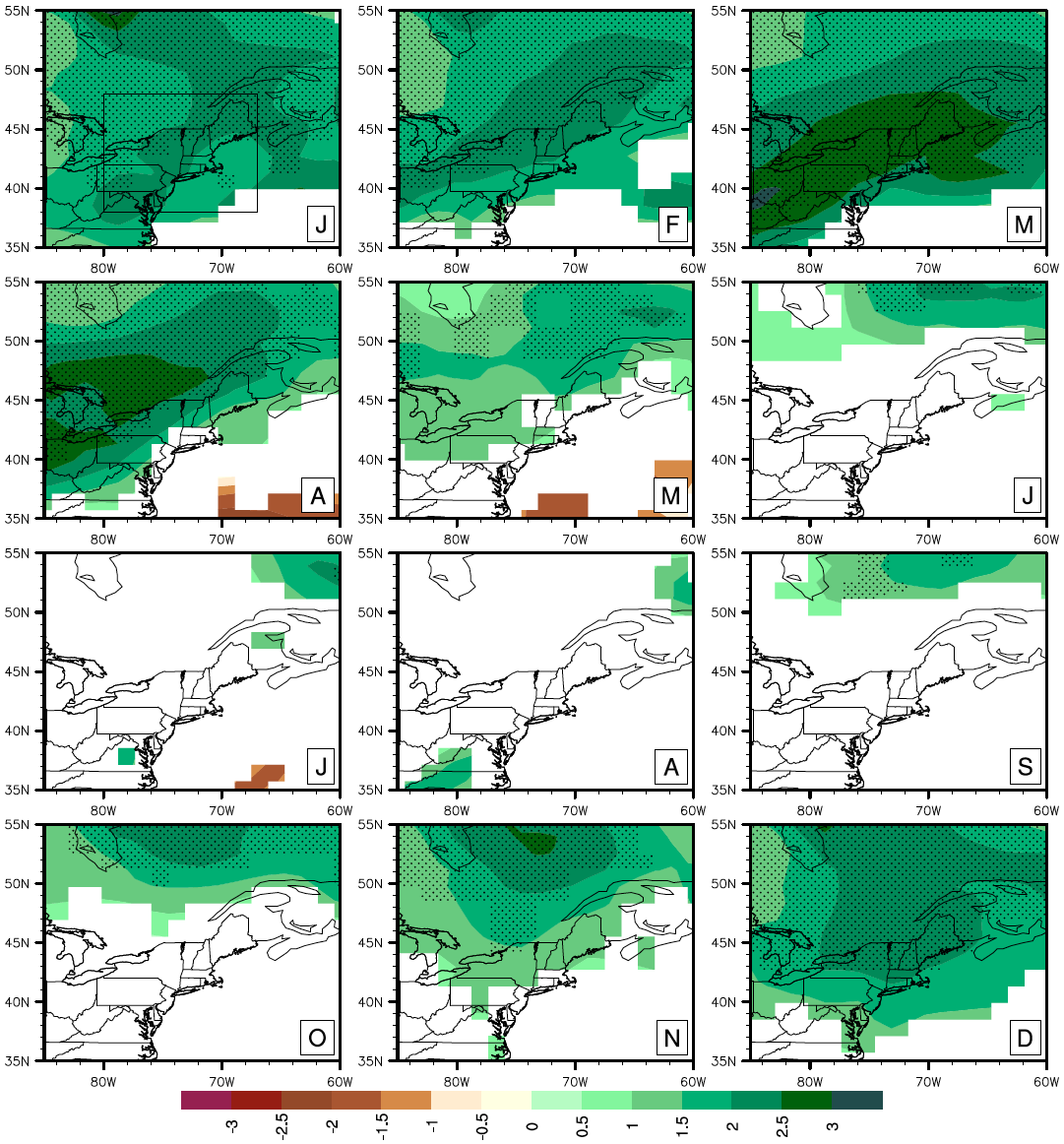

Figure 3.17. Future (2071–2100) minus present (1971–2000) monthly mean precipitation (cm) change from CMIP5 models. Rectangle in the top-left panel shows the greater northeast region that is used for area-averaged calculations. Colors indicate areas where the minimum model agreement on direction of change (70 percent) is met. Stippling indicates at least 50 percent of models show significant change at the 0.05 significance level. (Source: Lynch et al. 2016.)

Komurcu et al. (2018) used the Weather Research and Forecasting (WRF) convection-permitting model at 3 km grid spacing to dynamically downscale reanalysis and global climate simulations for the northeastern U.S. A historical simulation was first performed using boundary conditions from the European Center for Medium Weather Forecast (ERA-Interim) for 10 years (2006-2015) and compared with observations. The simulation (WRF-ERA) was able to capture the extreme precipitation associated with the nor'easter event in May 2006 in New England (Figure 3.18). Then the model was driven by the bias-corrected historical and future (RCP8.5) climate simulations produced by the Community Earth System Model (Bruyere et al. 2014) for three time slices representative of present day (PD; 2006–2020) (WRF-PD), mid-century (MC; 2041–2060) (WRF-MC), and end of century (EC; 2081–2100) (WRF-EC).

Figure 3.19 compares the change in seasonal mean precipitation projected by CESM with that downscaled using WRF, showing that the latter provides more detailed regional precipitation changes. Consistent with the CMIP5 projections analyzed by Lynch et al. (2016) discussed above, precipitation is projected to increase more significantly in winter while changes in summer are less spatially coherent.

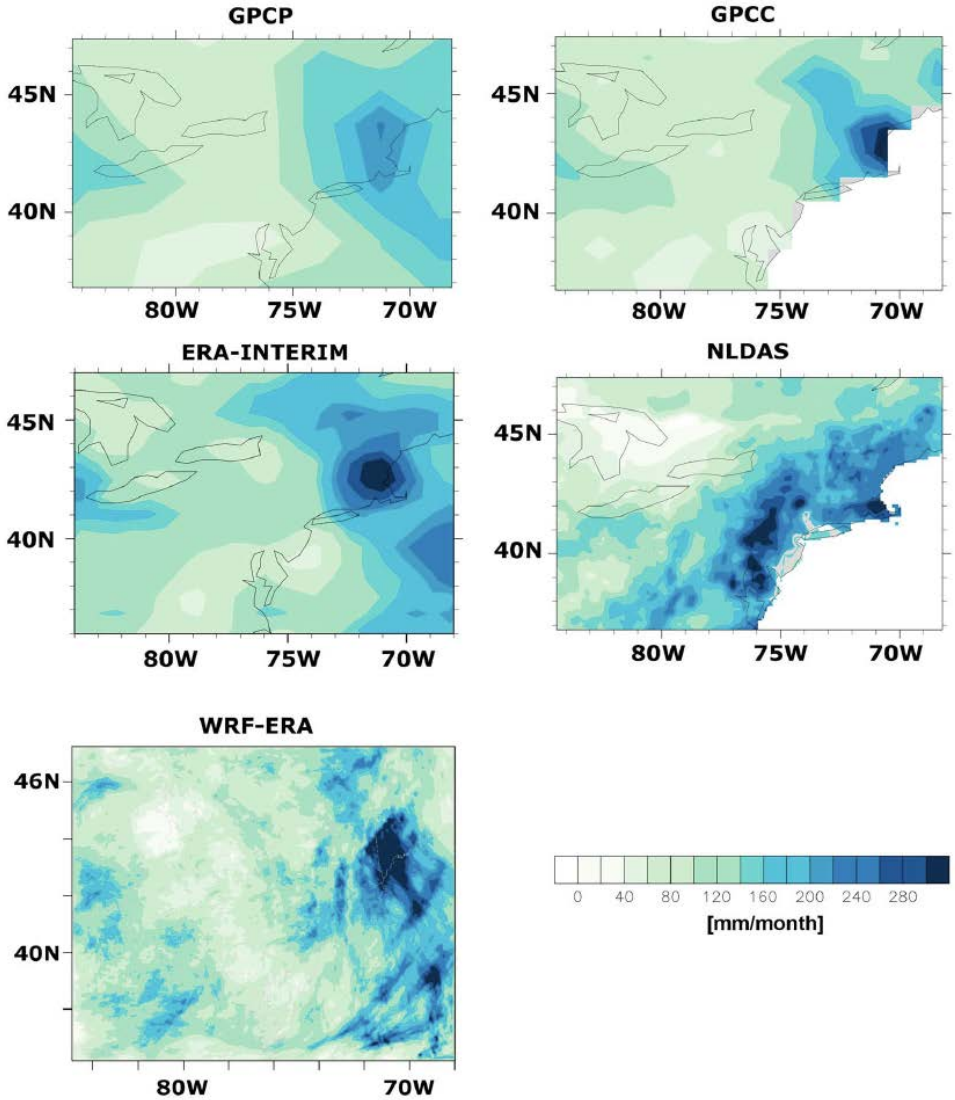

Figure 3.18. Monthly accumulated precipitation rate (mm/month) for May 2006 from GPCP, GPCC, ERA-Interim, NLDAS, and WRF-ERA. (Source: Komorcu et al. 2018.)

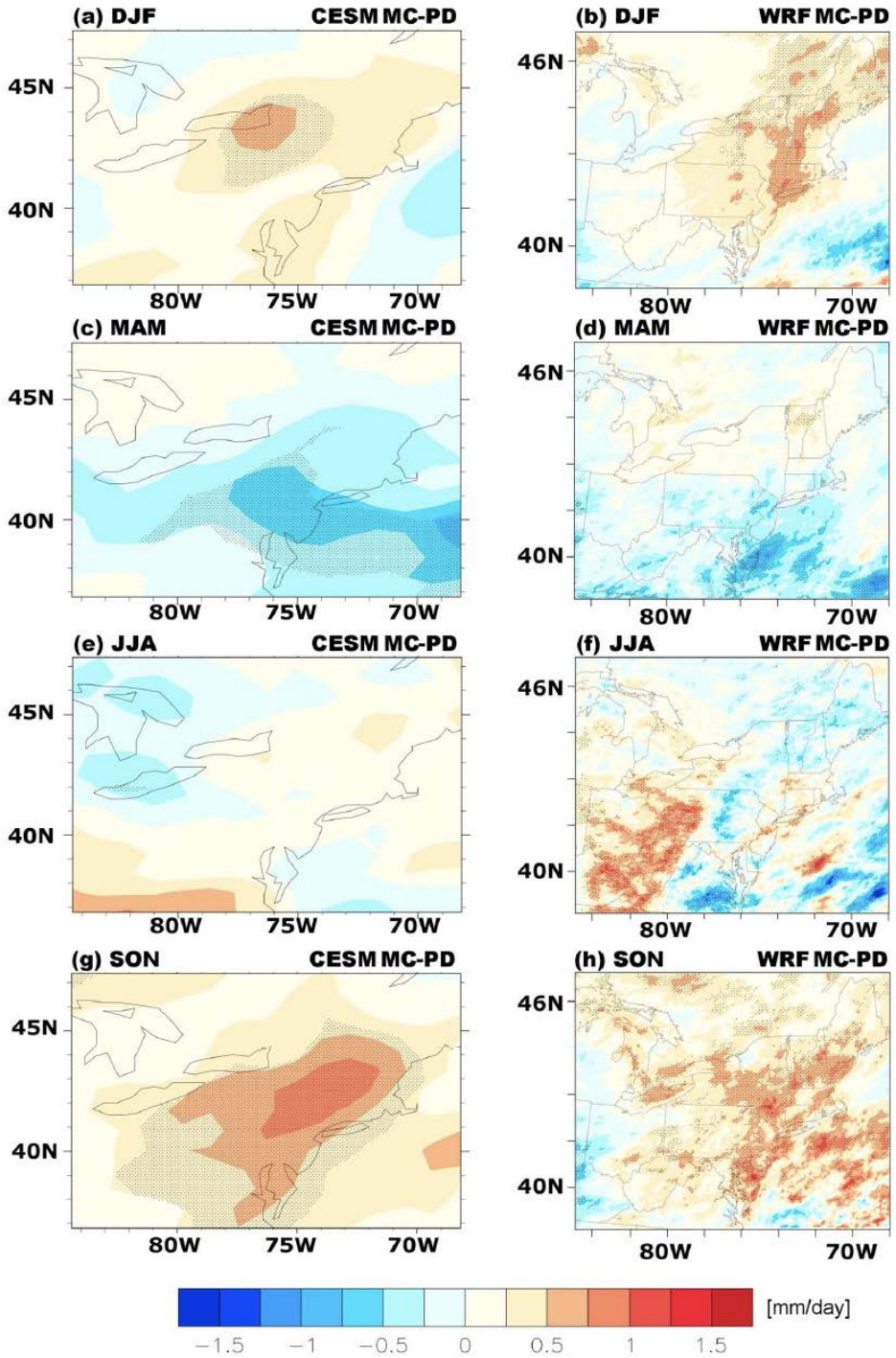

Figure 3.19. Seasonal differences (December-January-February [DJF], MAM, JJA, and SON) in daily precipitation rates [mm/day] between end of century and present day CESM projections CESM-MC–CESM-PD) (left column) and WRF projections (WRF-MC–WRF-PD) (right column). (Source: Komurcu et al. 2018.)

As the atmospheric water-holding capacity increases with warming following the Clausius-Clapeyron relationship, extreme precipitation is generally projected to increase even in the absence of changes in atmospheric large-scale circulation. In NCA3, extreme precipitation changes were assessed by comparing the annual number of days with precipitation greater than 1 in. using the NARCCAP regional climate

projections (Figure 3.20). Climatologically, there is a strong south-north gradient in extreme precipitation with the southern region showing 8 to 10 days per year with precipitation greater than 1 in. There are increases throughout the northeast region in the 2041–2070 period compared to the 1980–2000 period. The northern parts of the region featured increases up to 30 percent and the projected changes are statistically significant, particularly where the increases are larger.

The changes in extreme precipitation can also be summarized by depicting the changes in the value corresponding to 0.05 AEP daily precipitation (Figure 3.21). The value corresponding to 0.05 AEP was calculated based on statistically downscaled data obtained by the Localized Constructed Analogs method (Pierce et al. 2014) applied to the CMIP5 global climate model (GCM) outputs. The Localized Constructed Analogs method assumes that meteorological processes produce cyclostationary statistical relationships between large-scale and finer-scale values of a climatological field. By finding the day with observed values from fine-scale gridded observation data, and best matching the GCM simulation in the wider region as well as in the local neighborhood around a model grid point, the GCM value is downscaled to 1/16-degree resolution using the historical analog, scaled to match the amplitude of the model day being downscaled. The daily values corresponding to 0.05 AEP from the Localized Constructed Analogs data show increases everywhere in the U.S. in both the lower (RCP4.5) and higher (RCP8.5) emissions scenarios. Changes between 10 and 22 percent are found over the Northeast, depending on the period and emissions scenarios.

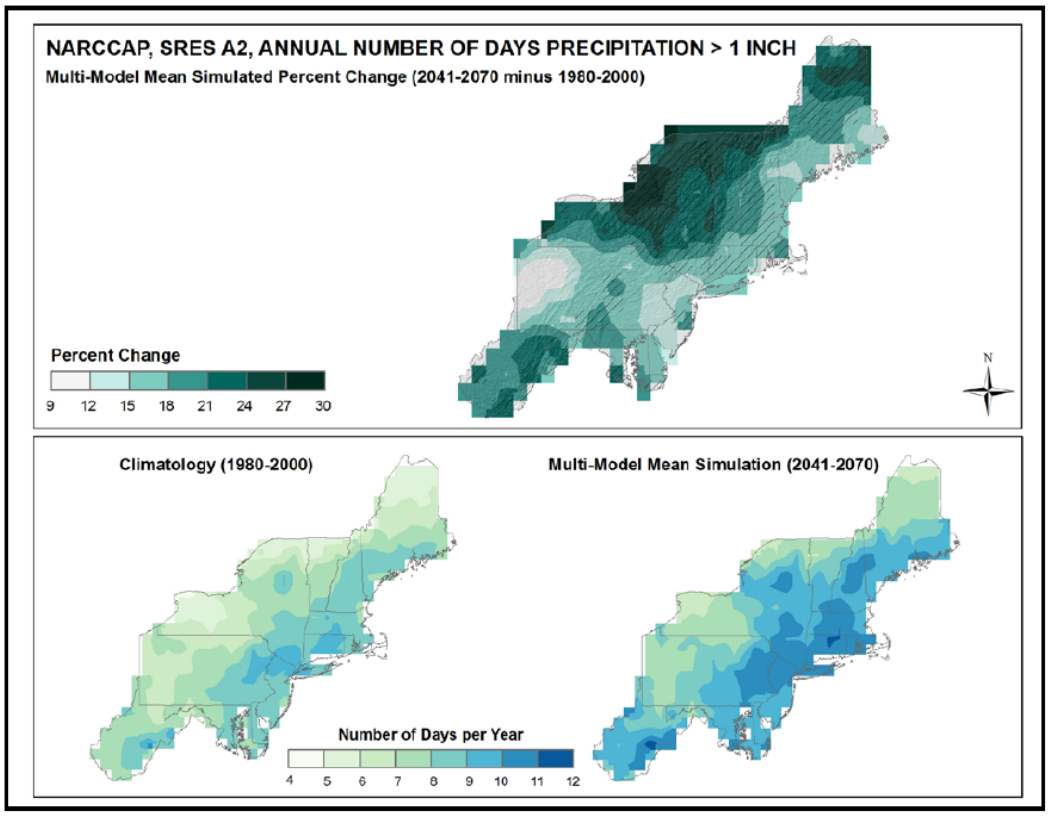

Figure 3.20. (Top) Similar to Figure 3.16, but for simulated differences in the annual number of days with precipitation >1 in. from the NARCCAP projections for the mid-century. Color and crosshatching have the same meaning as Figure 3.16. (Bottom) Climatological mean for the present (left) and future (right). (Source: Kunkel et al. 2013.)

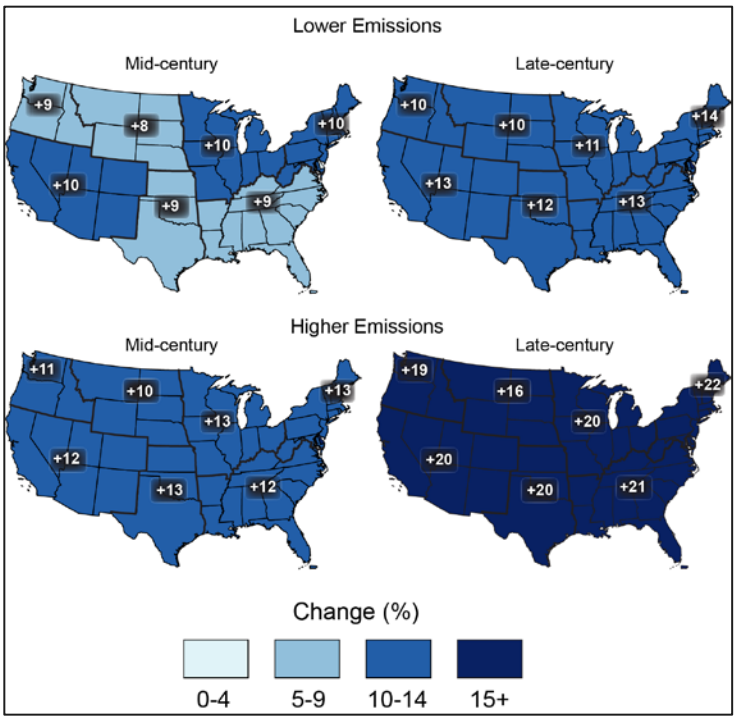

Figure 3.21. Projected change in the amount of daily precipitation corresponding to 0.05 AEP for mid- and late-21st century for RCP4.5 and RCP8.5 emissions scenarios using Localized Constructed Analog downscaled data. (Source: Easterling et al. 2017.)

4.0 Tropical and Extratropical Cyclones and Convective Storms in the Northeast Region

Extreme precipitation in the northeast region is generated by several physical and dynamical mechanisms in different seasons. Using daily precipitation data from 935 long-term National Weather Service Cooperative Observer (COOP) stations and the large-scale circulation (surface pressure and temperature) from the twentieth century reanalysis (Compo et al. 2006; 2011) for 1908-1948 and the NCEP-NCAR reanalysis (Kalnay et al. 1996) for 1949-2009, Kunkel et al. (2012) classified extreme precipitation events in the U.S. by their generation mechanisms. These include extratropical cyclones (ETCs), fronts (FRTs), North American monsoon (NAM), isolated thunderstorms occurring in convectively unstable air masses denoted as air mass convection (AMC), MCSs, upslope flow precipitation (USF), and tropical cyclones (TC). The latter were identified using an automated process based on the National Hurricane Center's hurricane database archive (HURDAT; Jarvinen et al. 1984; Neumann et al. 1999). A hierarchy was used to determine the primary causes starting with frontal systems at the largest scale, and ETCs as the second priority cause.

Figure 4.1 shows the percentage of extreme precipitation attributed by Kunkel et al. (2012) to different mechanisms for different regions of the U.S. for annual and seasonal mean. Mechanisms contributing to extreme precipitation in the northeast region include FRT, ETC, TC, and MCS. Since MCSs often occur in association with fronts, the latter would be selected as the primary causes so the hierarchical classification attributes only 2% of extreme precipitation to MCSs even in the summer. Feng et al. (2018) developed an algorithm to specifically track MCSs using gridded precipitation, radar reflectivity, and outgoing longwave radiation data to identify convective core and stratiform regions associated with MCSs. Using this method, Feng et al. (2019) developed a climatology of MCSs and their associated large-scale environments, showing MCSs produced between 20 to 35 percent of precipitation in the northeast region during spring and summer (Figure 4.2). Since MCSs are known to generally produce higher rain rates than fronts because of their convective cores, it is likely that a larger fraction of extreme precipitation in the northeast region is produced by MCSs in the warm season than classified by Kunkel et al. (2012).

Given the importance of tropical cyclones, extratropical cyclones, and fronts (with embedded MCSs) in producing extreme precipitation in the northeast region, this chapter summarizes findings reported in the literature on how these storm types may respond to warming in the past and/or future.

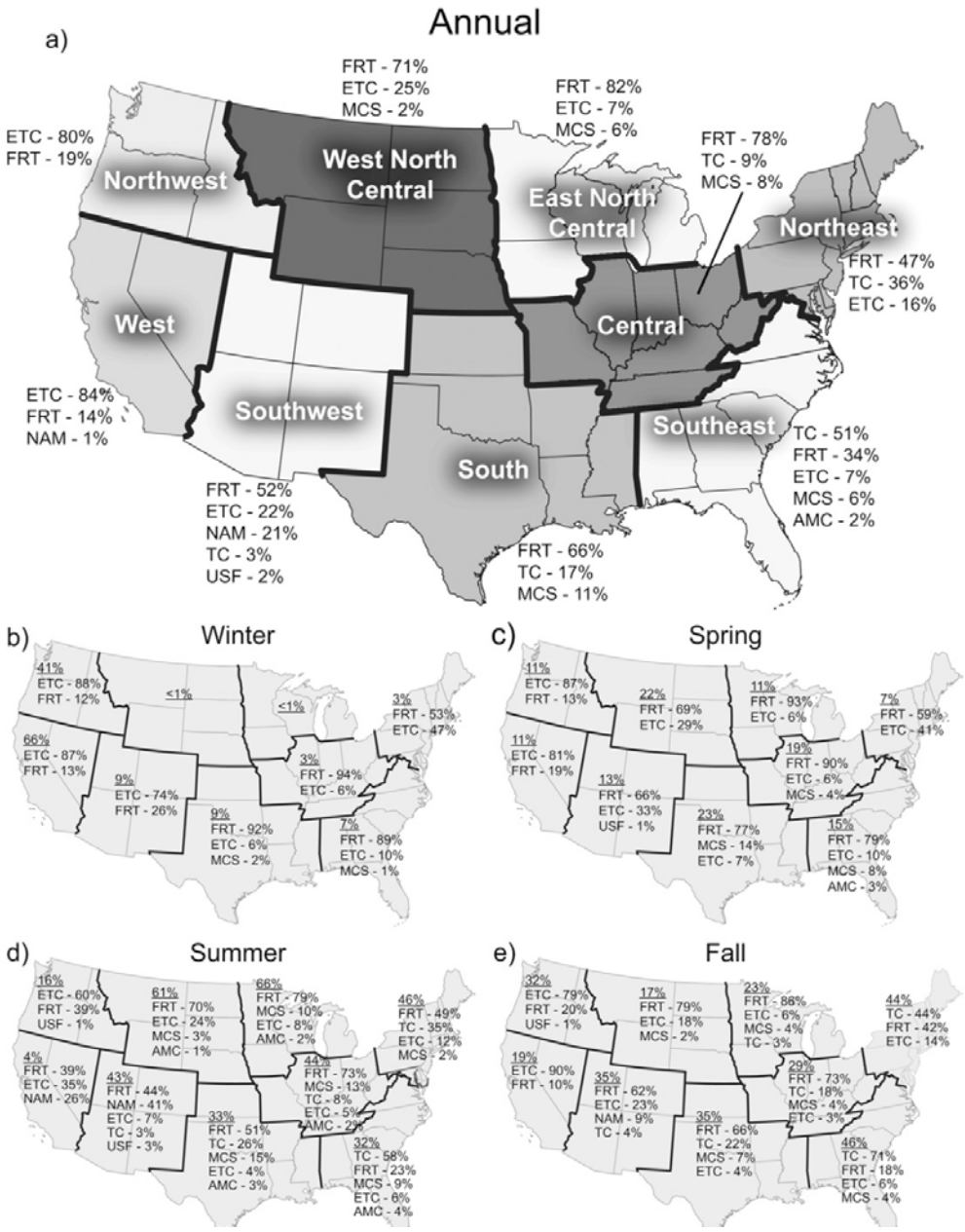

Figure 4.1. Maps of regional and seasonal contributions of major extreme event causes for (a) annual, (b) winter [December–February (DJF)], (c) spring [March–May (MAM)], (d) summer [June–August (JJA)], and (e) autumn [September–November (SON)]. In the seasonal maps, the underlined values are the percentages of total events occurring in that season; the values next to the causes are the percentages of total seasonal number of events. (Source: Kunkel et al. 2012.)

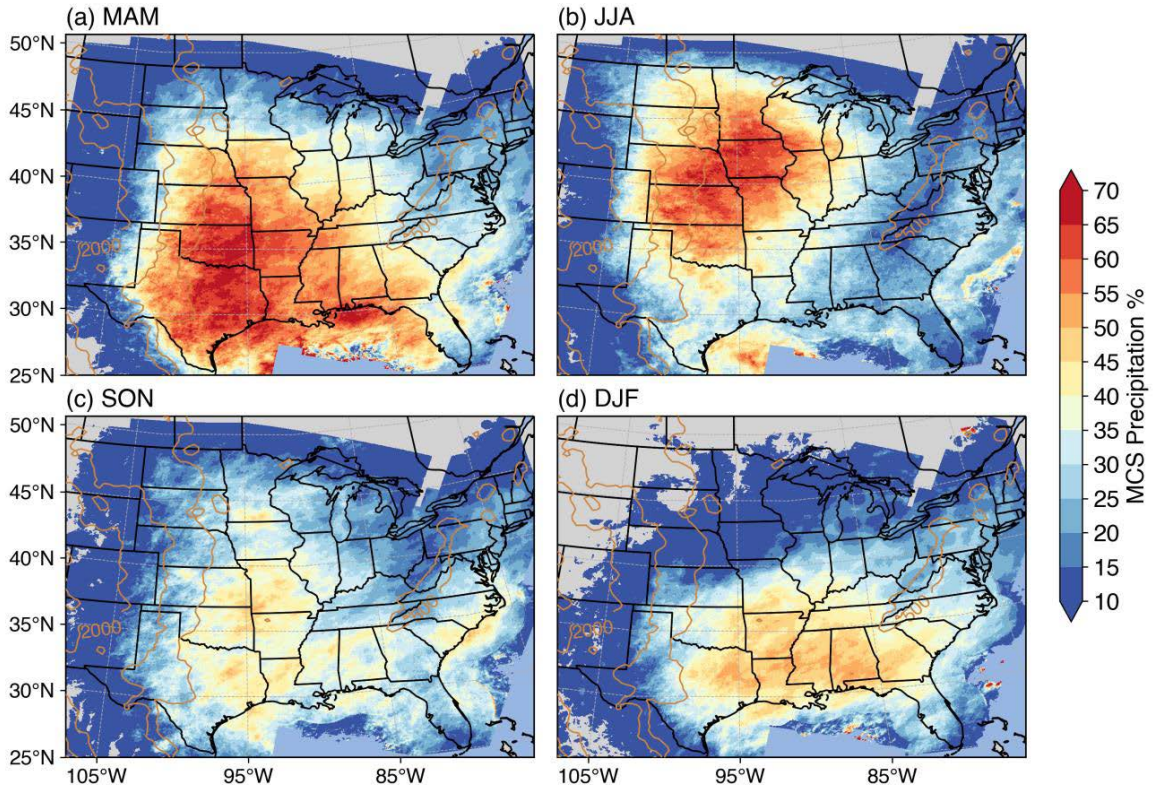

Figure 4.2. Spatial distribution of the fraction of MCS precipitation during the four seasons for 2004–2016: (a) March-April-May, (b) June-July-August, (c) September-October-November, and (d) DJF. Brown contours show the terrain height for 500 m, 1000 m and 2000 m, respectively. Note that areas over the ocean and north of the U.S.-Canada border have reduced radar coverage such that the results in those areas must be treated with caution. (Source: Feng et al. 2019.)

4.1 Tropical Cyclones

- Tropical cyclones (TCs) may change under global warming as more energy is supplied by the warmer oceans but other factors such as changes in atmospheric static stability, vertical wind shear, steering winds, upper ocean stratification, and increased moisture can cause diverse changes in TCs in different ocean basins.
- There are some observational evidences that the mean latitude where tropical cyclones reach their lifetime maximum intensity has migrated poleward in the last 30 years due to tropical expansion and the translational speed of tropical cyclones has decreased in 1949-2016 due to the slow down of tropical circulation.
- Climate models generally project an increase in tropical cyclone intensity (or the number of category 4-5 storms), rainfall rate, and storm size for Atlantic hurricanes due to warmer sea surface temperatures and increase in humidity. However, models do not project consistent changes in the total number of tropical cyclones in the Atlantic basin or globally.
- Changes in tropical cyclones characteristics in the North Atlantic are generally consistent with those projected for the global average, but the projected future changes can vary substantially across different ocean basins.
- Modeling experiments suggest that climate change since the pre-industrial period had not significantly changed tropical cyclone intensity, but continued warming in the future will significantly enhance tropical cyclone intensity as well as rain rate in the 21st century.
- Future changes in large-scale circulation are not favorable for a Sandy-like storm that went through (incomplete) transition from tropical cyclone to extratropical cyclone following an unprecedented track steered by anomalous circulation but warming and increased moisture may increase the intensity of the storm in the future for a Sandy-like storm following its observed track.

TCs derive their energy from the ocean so TC intensity is expected to increase with warmer sea surface temperatures (SSTs) in the future, although the frequency of all TCs may or may not increase because meteorological factors such as wind shear and atmospheric stability also play a role. This understanding is borne out in model projections reported in many studies, which show more consistency in the projected increase in TC intensity than change in TC frequency. An example based on a high-resolution modeling study is used here to illustrate the general finding regarding TC changes in a warmer climate. Knutson et al. (2015) used the Geophysical Fluid Dynamics Laboratory (GFDL) High-Resolution Atmospheric Model (HiRAM) at 50-km grid spacing with prescribed SSTs to simulate tropical cyclone genesis globally. Simulations were performed for 20 repeated seasonal cycles driven by the observed mean seasonal cycle of SSTs derived from 1982-2005 as a control run. Simulations were also performed for a late 21st century projection in which perturbations are added to the observed mean seasonal cycle of SSTs based on the difference between 2081-2100 and 2001-2020 derived from the CMIP5 multimodel ensemble following the RCP4.5 scenario. Then each storm simulated by HiRAM is downscaled using the GFDL hurricane model, with a horizontal grid spacing near the storm of 6 km, including ocean coupling to represent “cold wake” generation. The results shown below are those produced by the GFDL hurricane model. Various aspects of TCs simulated by the hurricane model were found to compare well with observations.

Figure 4.3 compares the tracks and intensity of category 4-5 storms in the present and future climate. The total number of cat 4-5 storms increases from 244 to 313 globally, corresponding to an increase of 28

percent. Consistent increases in cat 4-5 storms are found in all basins except the southwestern Pacific Ocean where Huang et al. (2015) found that changes in ocean subsurface environment may suppress TC intensification under global warming. Considering the changes in the duration of cat 4-5 storms, the number of cat 4-5 days increases by 35 percent globally. In the Atlantic Ocean, the number of cat 4-5 storms increases by 42 percent and the number of cat 4-5 days increases by 175 percent. While the increase in both the number of cat 4-5 storms and the number of cat 4-5 days is statistically significant globally at the 0.05 confidence level, the same cannot be said for the increase over the Atlantic Ocean.

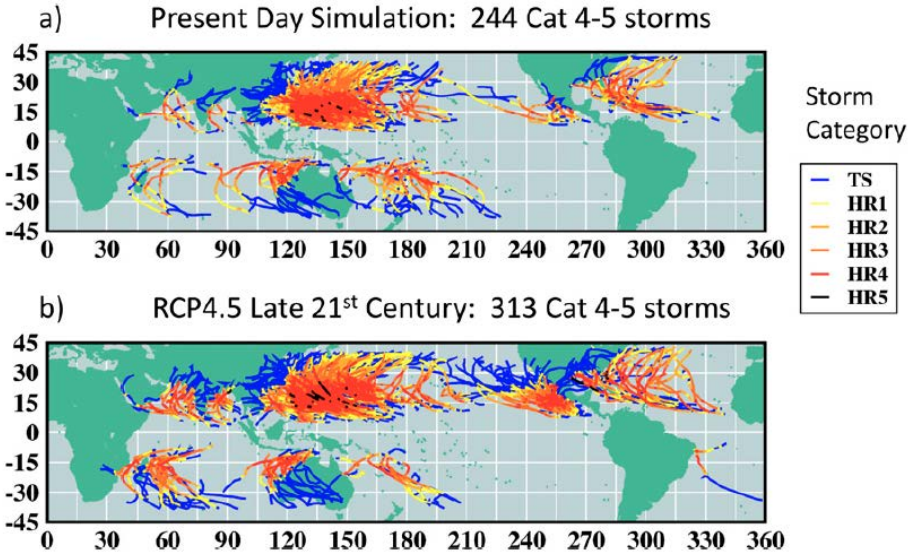

Figure 4.3. Tracks of simulated cat 4–5 tropical cyclones for (a) present day or (b) late-twenty first-century (RCP4.5; CMIP5 multimodel ensemble) conditions. Simulated tropical cyclone tracks were obtained using the GFDL hurricane model to resimulate (at higher resolution) the tropical cyclone cases originally obtained from the HiRAM C180 global mode. Storm categories or intensities are shown over the lifetime of each storm, according to the Saffir–Simpson scale. The categories are depicted by the track colors, varying from tropical storm (blue) to category 5 (black; see legend). (Source: Knutson et al. 2015.)

To contrast the occurrence of all tropical storms vs. the occurrence of cat 4-5 TCs, Figure 4.4 compares the spatial distribution of the changes in tropical storms occurrence and cat 4-5 storms occurrence. In the Atlantic basin, tropical storm occurrence decreases by 9 percent while the occurrence of cat 4-5 storms increases by 42 percent. Globally, the occurrence of all tropical storms decreases by 16 percent compared to the increase in cat 4-5 storms by 28 percent, both statistically significant at the 0.05 level.

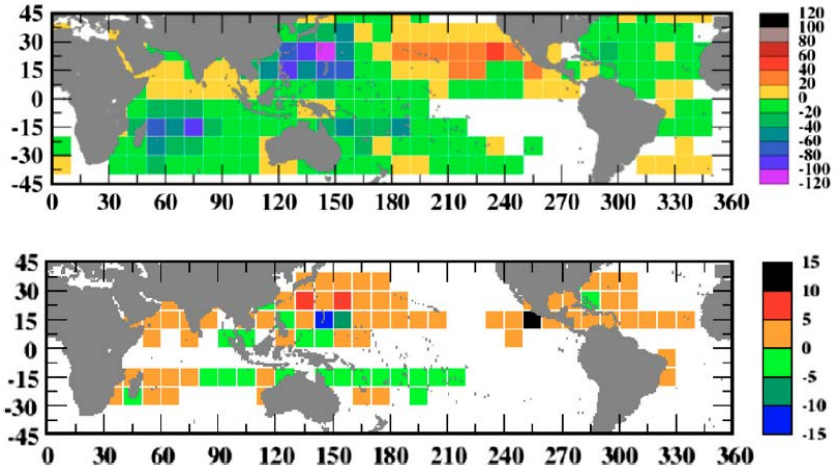

Figure 4.4. Simulated change in occurrence of (top) all tropical storms (tropical cyclones with winds exceeding 17.5 ms^{-1}) and (bottom) cat 4-5 storms (surface winds of at least 59 ms^{-1}) between the late-twenty-first-century (RCP4.5; CMIP5 multimodel ensemble) and the present-day conditions; unit: storms per decade. Simulated tropical cyclone tracks were obtained using the GFDL hurricane model to resimulate (at higher resolution) the tropical cyclone cases originally obtained from the HiRAM global model. Occurrence refers to the number of days, over a 20-yr period, in which a storm exceeding 17.5ms^{-1} intensity was centered within the 108 x 108 grid region. White regions are regions where the difference between the experiments is zero. (Source: Knutson et al. 2015.)

For storm sizes, Figure 4.5 compares the relative frequency of TCs of various sizes based on observations and the hurricane model simulations for the control and warming experiments. The control simulation compares well with observations both in terms of distribution shape, which is approximately lognormal (Chavas and Emanuel 2010), and variability. Globally, the median storm size stays nearly the same in the present day and future. Over the North Atlantic, however, the median storm size increases by 11 percent in the future, but changes in storm size are not consistent across the various basins, with both increases and decreases simulated.

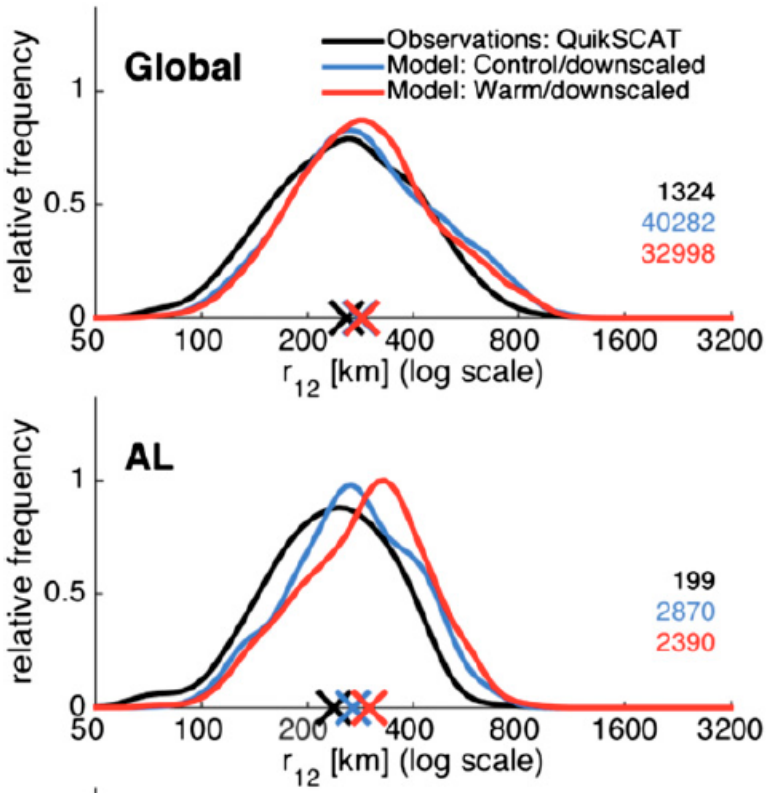

Figure 4.5. Relative frequency of tropical cyclone size, globally (a) and for North Atlantic (b). The size metric, r12, is the radius at which the azimuthal-mean azimuthal wind speed decreases to 12ms^{-1}. Black curves depict observed estimates based on QuikSCAT satellite measurements; blue and red curves depict distributions based on model simulations for control (present day; blue) or warm climate (late twenty-first century; red) conditions. The ‘‘X’’ marks on each diagram denote median values. The numbers listed on each diagram denote the number of cases analyzed. (Source: Knutson et al. 2015.)

Figure 4.6 shows the percent change in precipitation rate as a function of averaging radius (i.e., precipitation averaged over a disk of the given radius), considering all TCs globally and in the Atlantic Ocean. The dotted line in each panel gives an indication of the change in large-scale environmental water vapor in the basin, approximated as 7 percent times the average SST change in the basin. The percent change in precipitation rate is typically similar to the water vapor scaling (7 percent following the Clausius-Clapeyron [CC] scaling times the SST change), with notable exceptions in some ocean basins (not shown). Globally and in the Atlantic basin, precipitation rate is enhanced near the storm center, but this is not true for all the basins. In a study using a regional climate model to downscale global simulations, Wright et al. (2015) analyzed landfalling TCs in the eastern U.S. and found an increase of average TC rain rates by as much as the CC scaling over land within 500 km of the storm center. However, they found that the area-averaged rain rates from a given tropical cyclone in the warmer climate is greater for larger averaging radius (300–500km) than near the storm, which differs from the finding of Knutson et al. (2015) that the increase occurs within 200 km of the storm center.

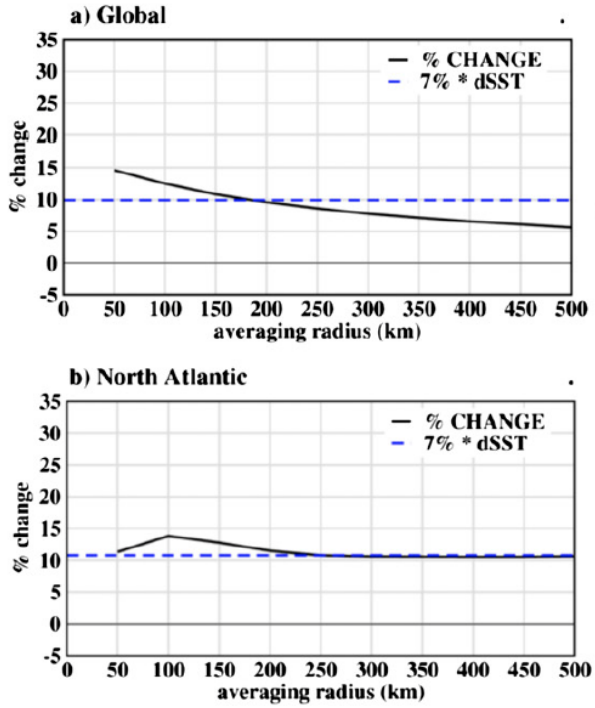

Figure 4.6. Percent change (warm climate minus control) in tropical cyclone precipitation as a function of averaging radius from the storm center, for all tropical cyclones globally (a) and in the Atlantic Ocean (b). The dotted line, computed as the SST change over the basin multiplied by 7 percent $^{o}C^{-1}$, approximates the increase in atmospheric water vapor content in the basin associated with the SST warming, assuming negligible change in relative humidity. (Source: Knutson et al. 2015.)

Since Hurricane Harvey made landfall on the coast of Texas and produced torrential rainfall and inland flooding, several studies have attempted to attribute the unprecedented rainfall from Harvey to anthropogenic warming and investigated how TC precipitation rate may change in the future. Risser and Wehner (2017) applied a covariate-based extreme value statistical analysis accounting for the external influence of global warming and the internal influence of El Niño Southern Oscillation to observed precipitation from the Global Historical Climatology Network. They found that human-induced climate change likely increased the chances of the observed precipitation accumulations during Hurricane Harvey in the most affected areas of Houston by a factor of at least 3.5. Furthermore, precipitation accumulations in these areas were likely increased by at least 18.8 percent, which is larger than the 6-7 percent associated with the attributable warming of 1^{o}C in the Gulf of Mexico according to the CC scaling.

Van Oldenborgh et al. (2017) also investigated the role of anthropogenic warming on the extreme rainfall produced by Harvey. They analyzed three ensembles (6 members) of simulations from the EC-Earth global atmospheric model at 25 km resolution (Haarsma et al. 2013), the GFDL HiFLOR fully coupled global climate model (Delworth et al. 2006, 2012) at 25 km resolution for the atmosphere, and the HadRM3P regional climate model, also at ~25 km resolution (Massey et al. 2015) for different time periods corresponding to different historical and future forcings. They found a 2xCC scaling and 1xCC scaling in two of the ensembles while one ensemble of simulations did not realistically represent the extreme rainfall on the Gulf Coast. They concluded that global warming made the precipitation of Hurricane Harvey about 15 percent more intense, or equivalently made such an event three times more likely. These results are in general agreement with those of Risser and Wehner (2017).

Lastly, Wang et al. (2018) used an ensemble of mesoscale atmospheric model simulations to attribute the long-duration intense rainfall of Harvey. From 60 simulations with constrained boundary and initial conditions to remove the long-term climate trends, they found that the post-1980 climate warming could have contributed to the extreme precipitation that fell on southeast Texas during 26–29 August 2017 by approximately 20 percent, with an interquartile range of 13–37 percent. Further analysis of a global climate model tracking Harvey-like stalling systems indicates an increase in storm frequency and intensity over southeast Texas through the mid-21st century. Overall, using different approaches, Risser and Wehner (2017), van Oldenborgh et al. (2017), and Wang et al. (2018) all identified some contributions of warming to the unprecedented rainfall of Hurricane Harvey and motivated further studies to determine and understand how extreme TC rainfall may scale with warming.

Another investigation of the anthropogenic influence on hurricanes is reported by Patricola and Wehner (2018) who analyzed both wind-speed intensity and rainfall changes. They used a convection-permitting regional climate model to simulate 13 intense TCs in the recent record to determine how these events would change if they had occurred in pre-industrial and in future (end of century in RCP4.5, 6.0, and 8.5) climates. To represent the pre-industrial and future climates, the thermodynamic component (relative humidity and geopotential height) of climate change is removed or added, respectively. The model reproduced the tracks and intensities of the 13 intense TCs reasonably well. More detailed analysis and sensitivity experiments were performed for Katrina, Irma, and Maria. As shown in Figure 4.7, they found that, relative to pre-industrial conditions, climate change so far did not change the wind-speed intensity of the three hurricanes, but future anthropogenic warming would robustly increase the wind speed as warming continues.

For TC rainfall, analysis was performed based on composites of the simulations of each storm. From Figure 4.8, climate change at present relative to pre-industrial enhanced rainfall rate of Katrina by 4-9 percent over an approximately $5x5^{o}$ box centered on the TC. For Irma and Maria, climate change at present increased rainfall by 6 and 9 percent, respectively, but the increase occurs over a smaller box of $1.5x1.5^{o}$. For Irma and Maria, the largest increase in rainfall tends to occur in the same location of the historical maximum and there is drying in the outer-TC radii. Extending the analysis to all 13 intense TCs simulated, a robust increase in wind speed and rainfall is apparent in 11 of the 13 storms. Lastly, this study found that the sign of projected changes in TC intensity and rainfall does not change between simulations with and without convective parameterizations, giving some confidence in projections from global models with parameterized convection and fine enough resolution to resolve TCs.

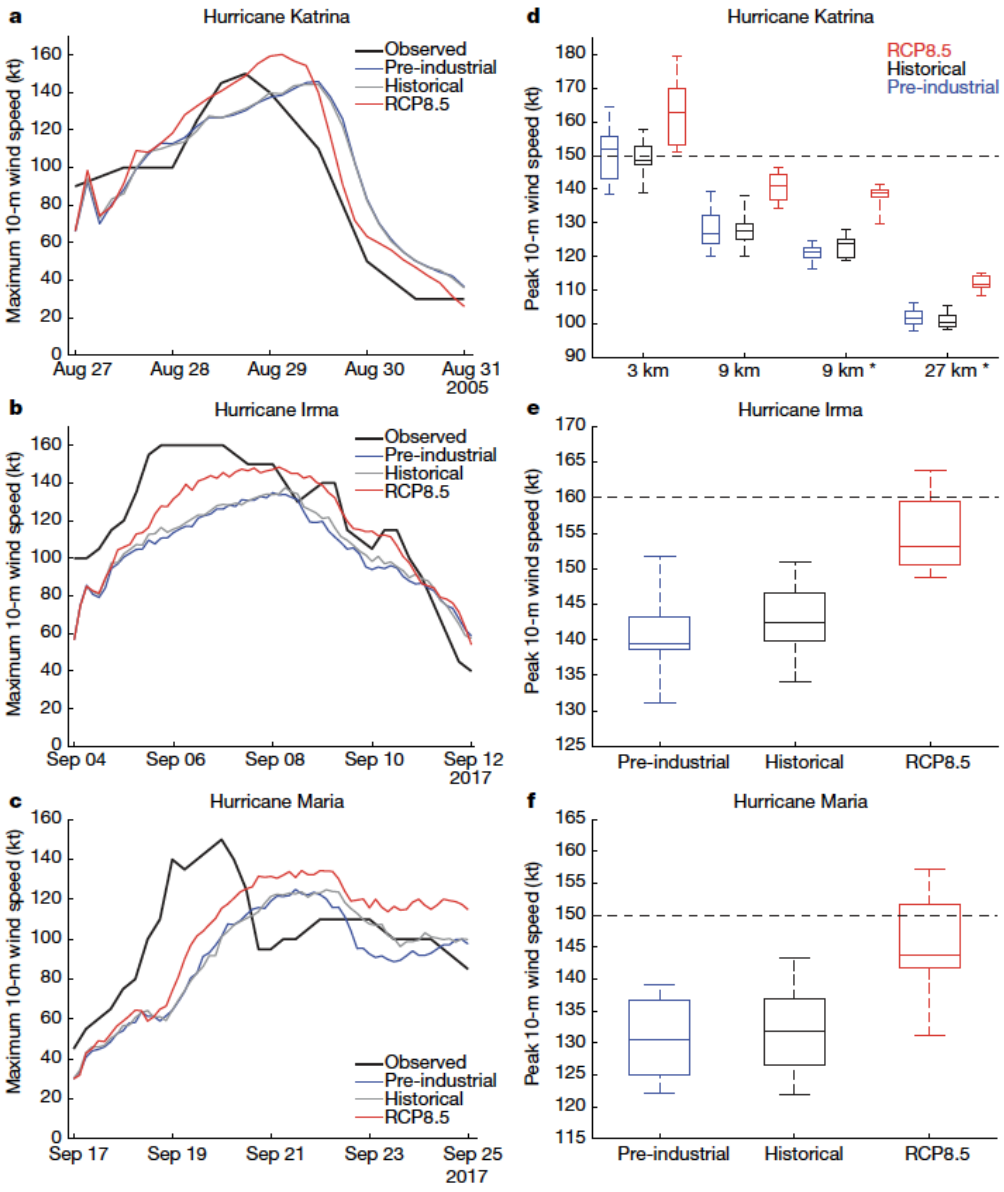

Figure 4.7. Time series and boxplots of tropical cyclone maximum 10-m wind speed. a–c, The time series of maximum 10-m wind speed (knots, kt) from observations (black) and the ensemble mean of the pre-industrial (blue), historical (gray) and RCP8.5 (red) simulations of hurricanes Katrina at 3-km resolution (a), Irma at 4.5-km resolution (b) and Maria at 4.5-km resolution (c). d–f, Boxplots of peak 10-m wind speed (kt) from the ten-member ensemble of pre-industrial (blue), historical (black) and RCP8.5 (red) simulations of hurricane Katrina at 3-km, 9-km (with and without convective parameterization) and 27-km resolution (d), and of hurricanes Irma (e) and Maria (f) at 4.5-km resolution. The center line denotes the median, box limits denote lower and upper quartiles, and whiskers denote the minimum and maximum. The observed peak intensity is marked with a horizontal dashed black line. Simulations that used convective parameterization are denoted by an asterisk. (Source: Patricola and Wehner 2018.)

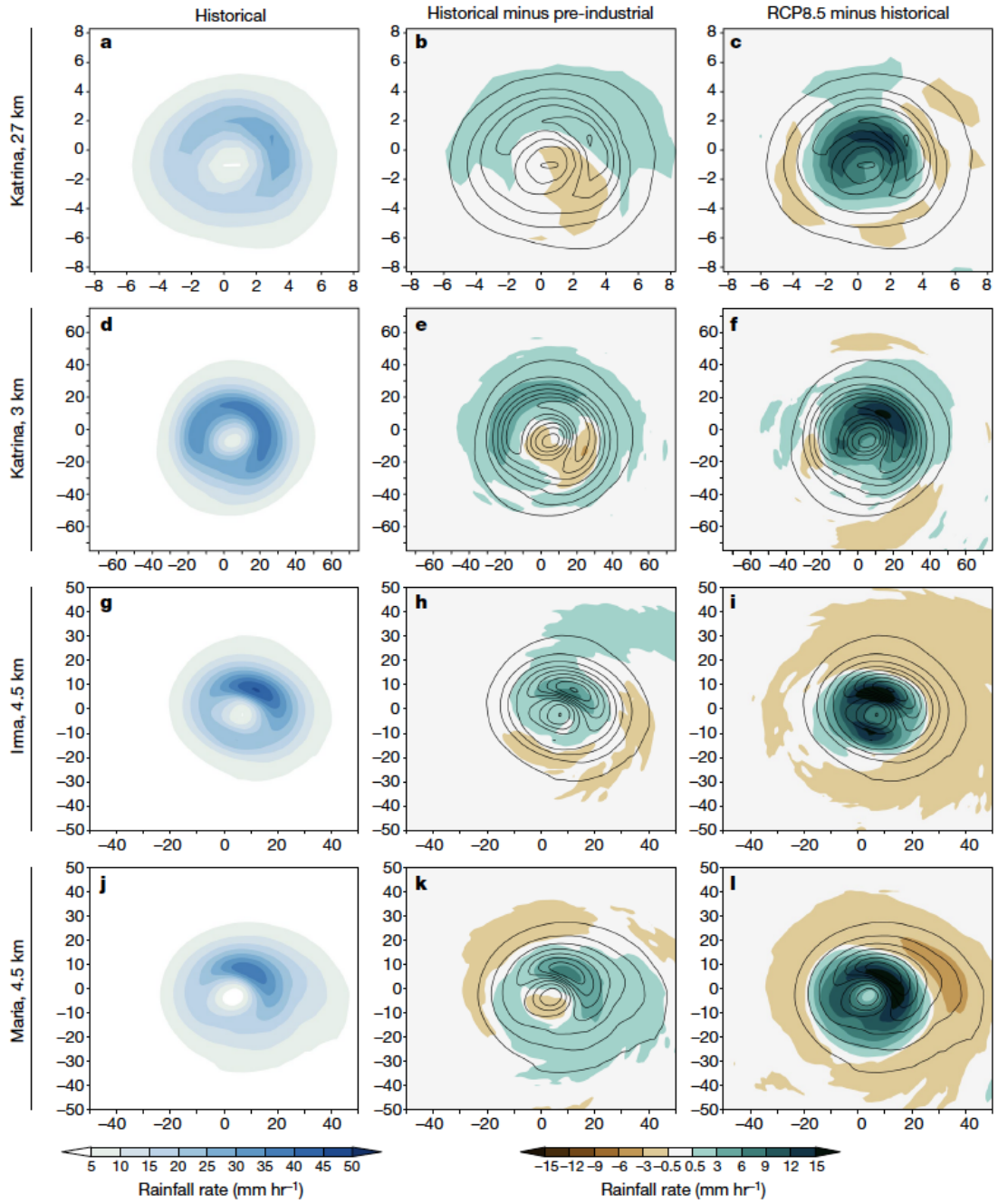

Figure 4.8. Tropical cyclone rainfall composites. a–c, Rainfall rate (color scale) relative to tropical cyclone center and throughout the simulated tropical cyclone lifetime from the ensemble mean of the historical (a), historical minus pre-industrial (b) and RCP8.5 minus historical (c) simulations of hurricane Katrina at 27-km resolution. d–l, As in a–c but for simulations of hurricane Katrina at 3-km resolution (d–f) and of hurricanes Irma (g–i) and Maria (j–l) at 4.5-km resolution. Contours denote the rainfall rate (in millimeters per hour) from the corresponding historical simulation. The x and y axes show the number of model grid points from the tropical cyclone center. (Source: Patricola and Wehner 2018.)

Besides TC frequency, intensity, and rainfall, other aspects of potential TC changes under warming have also been discussed in the literature. Kossin et al. (2014) found a poleward migration of the average latitude at which TCs have achieved their lifetime maximum intensity over the past 30 years. In both northern and southern hemispheres, they estimated statistically significant poleward migration rates of 53 and 62 km per decade, respectively. The migration away from the tropics is apparently linked to marked changes in the mean meridional structure of environmental vertical wind shear and potential intensity, and can plausibly be linked to tropical expansion, which is thought to have anthropogenic contributions (Lucas et al. 2014; Staten et al. 2018). Motivated by the weakening of summertime tropical circulation under warming (e.g., Vecchi et al. 2006), Kossin (2018) investigated possible changes in the TC translation speed, as TCs are carried along within their ambient environmental wind. Based on global tropical-cyclone 'best-track' data, Kossin (2018) found that TC translation speed has decreased globally by 10 percent over the period 1949-2016, with large variations regionally. Over land areas affected by North Atlantic TCs, the slow down of translation speed is 20 percent. As local TC rainfall is influenced not only by the rain rate but also by the TC translation speed, "stalling" of TCs such as Hurricane Harvey with the slow down of translation speed has important implications for the local rainfall totals after TCs make landfall in the future.

Tropical cyclones can transition to extratropical cyclones (ETCs) when connected with nearby fronts. Hurricane Sandy is a well-known example of a TC transitioning to an ETC, causing devastating damages in the U.S. east coast through storm surge and strong winds. Evans et al. (2017) and Keller et al. (2019) provided a comprehensive review of the dynamical and physical processes that govern ET and its impacts, how ET is diagnosed, and the prediction skill of ET forecast. Figure 4.9 shows tracks of TCs that completed the transformation stage of ET in various ocean basins. For the North Atlantic TCs, Evans et al. (2017) noted that slow transitioning TCs were more intense and larger as ET began than their fast-transitioning counterparts. Post-ET weakening was approximately twice as likely as post-ET intensification.

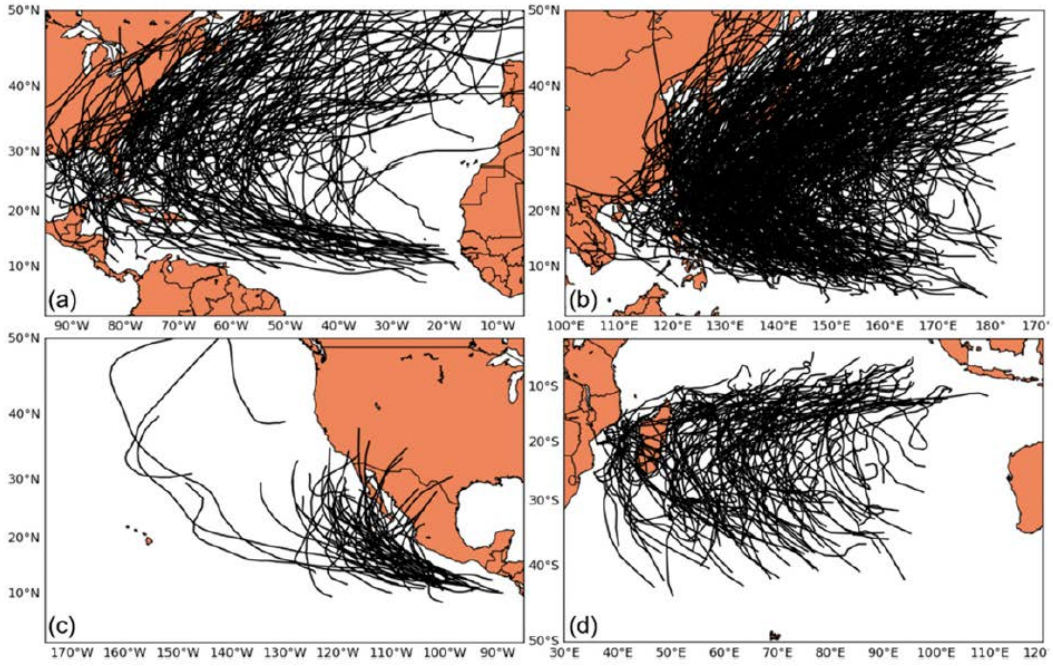

Figure 4.9. Tracks of TCs that completed the transformation stage of ET for the (a) North Atlantic [1981–2010; ET designations from HURDAT2 best-track data, described in Landsea and Franklin (2013)], (b) western North Pacific (1981–2010; ET designations from Japan

Meteorological Agency best-track data), (c) eastern North Pacific [1971–2012; reanalysis-derived cyclone phase space (CPS) ET designations by Wood and Ritchie (2014a)], and (d) southwestern Indian Ocean [1987–2013; reanalysis-derived ET designations subjectively determined by Griffin and Bosart (2014)]. No attempt is made to account for ET classification practice differences between operational centers or the historical evolution of ET classification practices at these centers. (Source: Evans et al. 2017.)

Barnes et al. (2013) investigated how a Sandy-like hurricane may change in a warmer climate by considering whether the persistent large-scale atmospheric patterns that steered Sandy onto the east coast will become more frequent in the coming decades. Three aspects of the atmospheric circulation that potentially contributed to Sandy's unprecedented track were considered and shown in Figure 4.10. These include: (1) an equatorward-shifted Atlantic midlatitude jet stream (Figure 4.10A), (2) a blocking anticyclone over the Atlantic (Figure 4.10B), and (3) a large-scale, cyclonic Rossby wave-breaking event off of the coast (Figure 4.10C). These aspects are in sharp contrast to the climatological westerly winds that advect TCs northeastward away from the coast as they enter the mid-latitudes (Figure 4.10D). The CMIP5 multimodel ensemble projects a robust poleward shift of the midlatitude jet (Barnes and Polvani 2013), which implies stronger westerlies at higher latitudes. Consistent with the fewer easterlies and a more poleward jet, the CMIP5 models also project a decrease in blocking in the western Atlantic basin in the August-October season. Lastly the CMIP5 models also project a decrease in the number of cyclonic wave breaking, consistent with the decrease in blocking frequency. Overall the CMIP5 projections do not favor the atmospheric circulation features experienced by Sandy that helped steer it toward the coast.

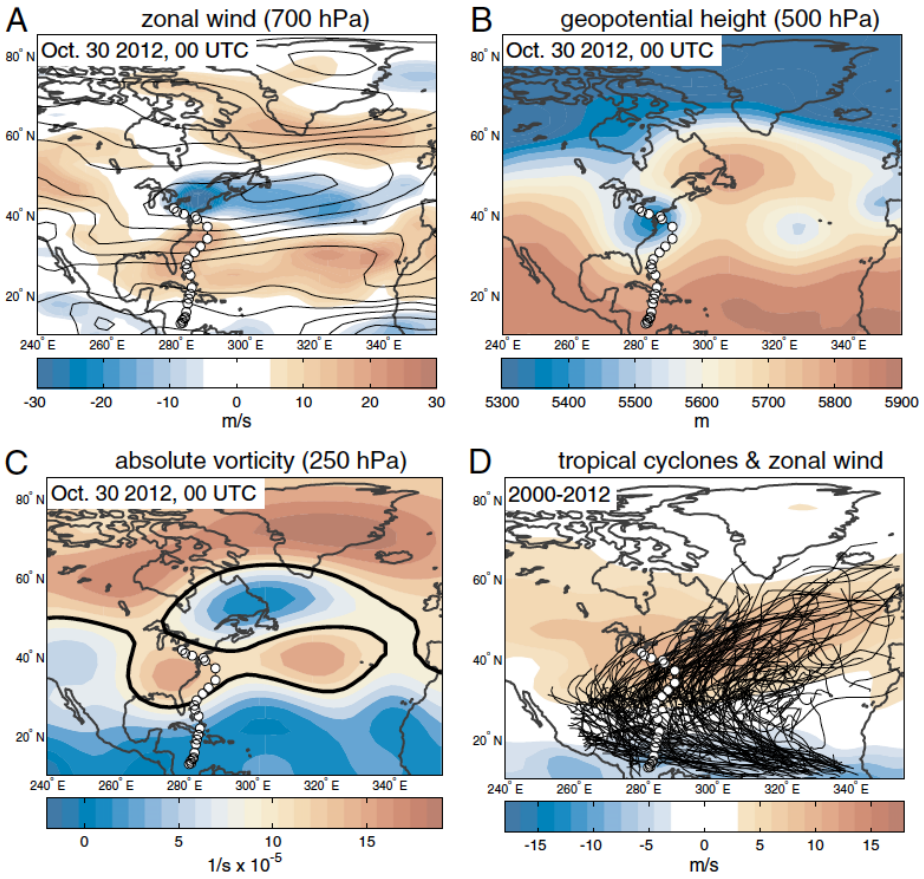

Figure 4.10. (A–C) October 20, 2012 (A) 700-hPa zonal wind, (B) 500-hPa geopotential height field, and (C) 250-hPa absolute vorticity field. Meteorological fields are from the NCEP/NCAR Reanalysis (National Centers for Environmental Prediction/National Center for

Atmospheric Research). (D) Tropical cyclone tracks from the National Hurricane Center HURDAT2 data and mean 700-hPa zonal winds over 2000–2012. Thin black contours in A denote the October climatology between 2000 and 2012. The thick black contour in C signifies the $11x10^{-5}$ s^{-1} overturning contour associated with a cyclonic Rossby wave-breaking event. The white circles denote the track of Sandy. (Source: Barnes et al. 2013.)

Lackman (2015) also investigated possible changes to Sandy if it were to occur in the past or the future. Unlike Barnes et al. (2013) who focused on the large-scale circulation changes simulated by GCMs, Lackman (2015) focused on the thermodynamic effects and performed numerical experiments using a regional model at 6 km grid spacing. Having successfully simulated the characteristics of Sandy based on the reanalysis boundary conditions, Lackman (2015) performed additional simulations corresponding to the past by imposing the mean thermodynamic changes simulated by a few GCMs from CMIP3 between 1880-1890 and 2000 to 2010 to the reanalysis boundary conditions. Another set of simulations were also performed for the future by imposing GCM simulated changes between the 1990s and 2090s to the reanalysis boundary conditions. These simulations show changes to Sandy's tracks Figure 4.11) due to imposed changes in the thermodynamic environment alone. Changes in the thermodynamics can influence the steering flow as changes in the latent heating released can generate potential vorticity that impact the lower and upper level circulation. Sandy makes landfall southward and northward of the observed landfalling location in the past and future. For intensity, Figure 4.12 shows that under the past climate conditions, there is no significant change in Sandy's intensity, but in the future, Sandy's intensity is significantly enhanced. This finding that climate change thus far did not change the intensity of Sandy is consistent with the finding of Patricola and Wehner (2018) based on a similar method but applied to other hurricanes, as discussed above.

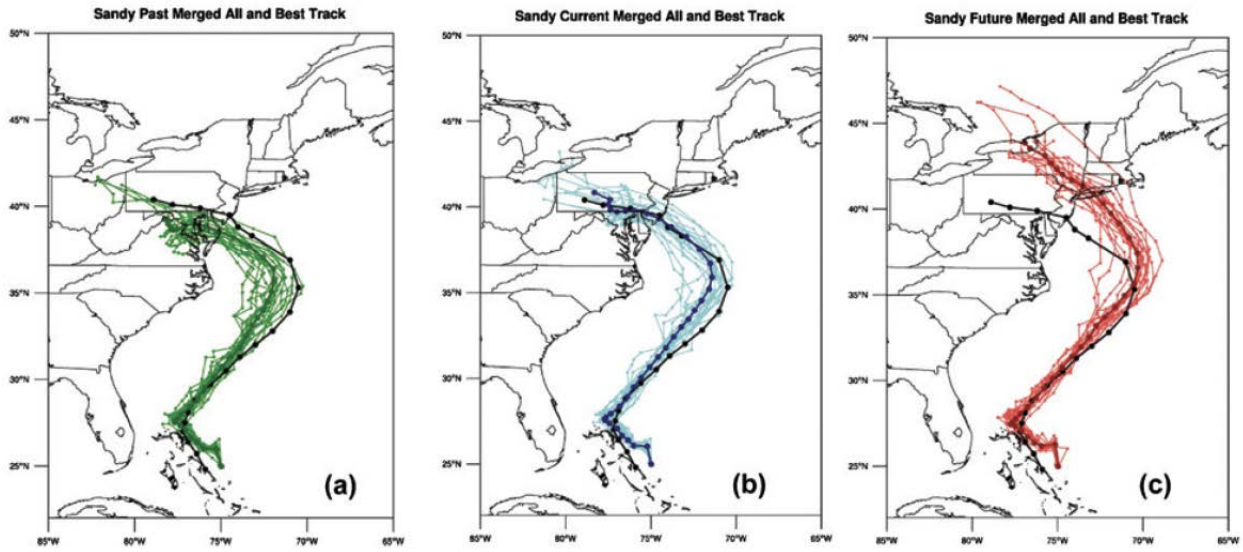

Figure 4.11. Track ensembles for (a) past, (b) current, and (c) future paths of Hurricane Sandy, derived from 6-day WRF simulations initialized 0000 UTC 26 Oct. The black line represents the National Hurricane Center best track; lighter colored lines represent ensemble members, and darker colored lines represent ensemble means for past (green), current (blue), and future (red). (Source: Lackman 2015.)

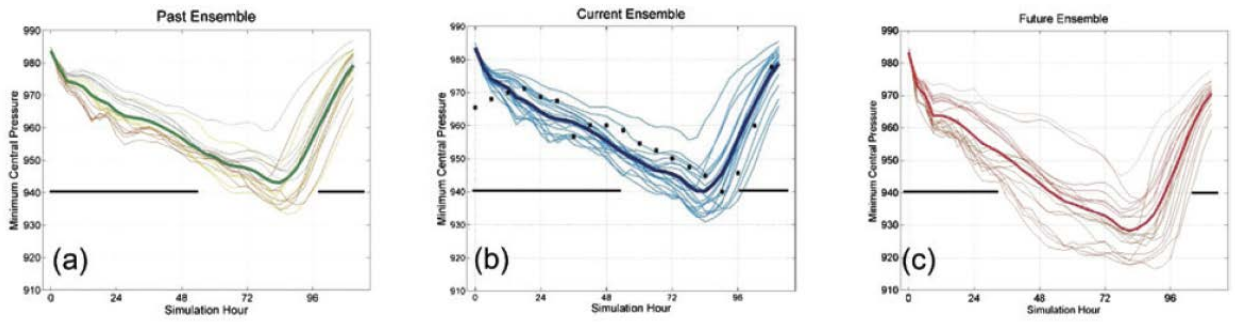

Figure 4.12. Time series showing ensemble intensity plots for (a) past, (b) current, and (c) future simulations. Enhanced horizontal line corresponds to landfall intensity of 940 hPa. (d) The ensemble means together to facilitate comparison. (Source: Lackman 2015.)

4.2 Extratropical Cyclones

- Extratropical cyclones (ETCs) frequency may change under global warming due to changes in the static stability of the atmosphere and meridional temperature gradients near the surface and in the troposphere. Competitions among these factors lead to large uncertainties in projecting future changes in ETCs.
- Mean available potential energy (MAPE) is a useful concept for understanding ETC changes. It correlates significantly with eddy kinetic energy (an indicator of ETC activity) in observations and models. Furthermore, model differences in projecting ETC frequency changes can be partly explained by model differences in projecting changes in MAPE.
- During summer in northern hemisphere, convection associated with ETCs may become more energetic due to mean surface warming, even as ETC activity may weaken due to weakening of meridional temperature gradient.
- Climate models projected a significant decrease in North American storm-track activity, with the largest decrease in summer and the smallest decrease in spring. Despite large differences among model projections, less than 20% of the models show an opposite sign of change.
- Analysis focusing on ETCs in eastern North America illustrates the regional nature of ETC changes such as the opposite changes in storm track density and storm intensity in western Atlantic and eastern U.S.
- Climate models projected broad declines in snowstorm frequency by the later 21st century but reduction in extreme snowfall is much less than the reduction in mean snowfall.

Extratropical cyclones (ETCs) are synoptic-scale, low-pressure weather systems that occur in the mid-latitudes. Forming along frontal zones of temperature and dewpoint gradient, ETCs are baroclinic. They develop through cyclogenesis along frontal zone near an upper-level jetstream or through extratropical transition of tropical cyclones that connect with nearby fronts. The latter type of ETCs has been discussed briefly in Section 4.1 so here the focus is on ETCs that develop through cyclogenesis along frontal zone. Global warming may influence ETCs and their storm tracks through several mechanisms. For example, enhanced temperature gradient in the upper troposphere/lower stratosphere due to warming in the upper troposphere and cooling in the lower stratosphere, a signature of increased greenhouse gases, may shift the storm tracks poleward (Yin 2005). Reduced meridional surface temperature gradient due to polar

amplification and increased static stability (i.e., buoyancy is less likely to induce turbulent motion and storm development) in the subtropics due to enhanced upper-tropospheric warming may reduce the frequency of midlatitude ETCs. Polar amplification refers to the larger surface warming in the polar region that results partly from surface albedo feedback, but also from melting of sea ice that exposes the warmer ocean to increase the surface heat fluxes to the atmosphere. Furthermore, increased moisture due to warming may increase the latent heat released by ETCs and enhance their intensity. Therefore, changes in ETCs have been generally summarized by a poleward shift of storm tracks and a decrease of ETC frequency but an increase in ETC intensity. However, regional changes may also influence storm activities differently in different regions. An example is the meridional shift of local storm track in the eastern U.S. and western Atlantic due to changes in the Gulf Stream sea surface temperature gradient (Joyce et al. 2009; Woollings et al. 2010).

Despite some general understanding of the thermodynamical and dynamical mechanisms for ETC changes in the future, model projections of poleward shift of storm tracks and reduced frequency but intensification of ETCs remain uncertain, partly due to the competing changes of upper- and lower-level meridional temperature gradients. At the upper level, cooling in the lower troposphere in the midlatitude and warming in the tropics, a result of the decrease in moist adiabatic lapse rate with temperature (Emanuel 1994), increase the meridional temperature gradient while at the lower-level, polar amplification reduces the meridional temperature gradient. Although Held and O'Brien (1992) and Lunkeit et al. (1998) showed that baroclinic wave activity is more sensitive to lower-level than upper-level changes, such sensitivity appears more complex in climate model projections.

The competing effect among meridional temperature gradients in the upper levels and near the surface and static energy (i.e., vertical temperature gradient) can be understood using concepts of energy. The total energy of the atmosphere consists of internal, latent, and gravitational potential energy but only a small part of the total energy associated with the mean state of the atmosphere is available for conversion to kinetic energy. This part of the energy of the mean state is called "mean available potential energy" (MAPE), which increases with increasing horizontal temperature gradients and decreasing static stability. MAPE is determined by the time-averaged and zonally averaged temperature and humidity fields. O'Gorman (2010) used the concept of MAPE to look at changes in ETCs under warming. He first confirmed using reanalysis data that the eddy kinetic energy (EKE), a measure of the intensity of storm tracks, is proportional to MAPE. Hence MAPE is a useful quantity for analysis of ETC changes. Although the total energy of the atmosphere is expected to increase in a warmer and moister atmosphere under global warming, the changes in MAPE depend on the changes in baroclinicity at different levels and latitudes and the changes in latent heat release. Hence consideration of only the surface meridional temperature gradient is inadequate for understanding changes in the intensity of the storm tracks. O'Gorman (2010) found a statistically significant correlation between the changes in EKE and dry MAPE (neglecting latent heating) across the CMIP3 multimodel ensemble, suggesting that the changes are mainly associated with large-scale circulation changes (dry MAPE) rather than changes in latent heating. Furthermore, uncertainty in the dry MAPE changes across the models is related to the competition between the meridional temperature gradients in the troposphere vs. near the surface and changes in static stability simulated by different models. Overall, for the northern hemisphere, the CMIP3 models showed a decrease in storm track intensity during summer and a small increase in storm track intensity during winter, resulting in an increased seasonal cycle of storm track intensity.

Extending the study of O'Gorman (2010), Gertler and O'Gorman (2018) used MAPE to study the changes in ETC activities in the northern hemisphere during summer. They decomposed MAPE into dry MAPE and convective MAPE, with the latter calculated simply as the difference between the moist MAPE and dry MAPE that includes and not includes latent heating, respectively. Note that convective MAPE is associated with the mean state of the atmosphere and generated primarily by the large-scale circulation driven by the meridional temperature gradient, so it is different from the convective available

potential energy (CAPE), which is calculated from instantaneous soundings and related to instability of the local atmospheric column. Using reanalysis data, Gertler and O'Gorman (2018) found that the non-convective MAPE decreased between 1979 and 2017 during summer, consistent with the decrease in EKE and ETC activity. However, the convective MAPE increased, implying an increase in the energy available for convection. They further found that non-convective and convective MAPE both increase with increasing mean surface temperature and decrease with decreasing meridional surface temperature gradient, but convective MAPE is relatively more sensitive to the increase in mean surface temperature. This suggests that even though ETC activity may weaken in the northern hemisphere summer, the convection associated with ETCs may become more energetic.

Using model output from CMIP3 and CMIP5, Chang (2013) analyzed the changes in ETC activity in North America to provide some insights on the similarities and differences between the projections from two generations of GCMs. Storm tracks were determined using two methods by compiling statistics of (1) ETCs identified by cyclone tracking (Hodges 1999) and (2) bandpass-filtered transient eddies based on sea-level pressure variance (Blackmon 1976). In both cyclone and sea-level pressure variance statistics, CMIP5 models projected a significant decrease in North American storm track activity, with the largest decrease in summer and the smallest decrease in spring. A poleward shift of storm track activity is apparent in the upper troposphere while in the lower troposphere, there is mainly a decrease in storm track activity with a maximum decrease south of the climatological storm track maximum for all seasons. CMIP5 models projected larger decrease in cyclone frequency for significant cyclones, defined as cyclones with perturbation amplitude of 20 hPa or larger in the cool seasons and 15 hPa or larger in summer. These storms represent the strongest 25 percent or few of all cyclones passing over North America in each season.

Although there are significant model-to-model differences in the magnitude of the changes projected by the CMIP5 models, less than 20 percent of the models show an opposite sign of change. Compared to CMIP3, CMIP5 models projected much larger decreases in storm track activity. Both the model-to-model differences within the ensemble of CMIP5 models as well as the differences between CMIP5 and CMIP3 projections can partly be explained by the differences in MAPE, an indicator of the baroclinicity of the mean flow. Seasonal differences in the changes of storm track activity were attributed partly to the strength of the polar amplification, which is weakest in spring compared to other seasons. Decrease in ETC activity may influence precipitation in the future. CMIP5 models that projected larger decrease in storm track activity in summer also projected a larger area of decrease in precipitation over the eastern U.S. and Canada. In winter, there are also indications that models projecting larger storm track decrease also projected a farther northward intrusion of the decreases in subtropical precipitation.

Colle et al. (2013) also analyzed CMIP5 simulations to study futures changes in ETCs, but they focused on the region of eastern North America and western Atlantic during the cool season. Cyclone tracking was used to identify ETCs to compile their statistics. Unlike Chang (2013) who analyzed all available CMIP5 models, Colle et al. (2013) selected only models that produced more realistic ETC track density and intensity compared to observations for their analysis. Six of the top seven CMIP5 models with the highest spatial resolution were ranked the best overall, suggesting that model resolution may be an important consideration for modeling ETCs. The best seven models showed a 10-30 percent decrease in cyclone track density and weakening of cyclones over the western Atlantic storm track (Figure 4.13a and b). In contrast, there is a 10-20 percent increase in cyclone density track over the eastern U.S. and 10-40 percent more intense cyclones (980 hPa) (Figure 4.13c and d) and 20-40 percent more rapid deepening rates (Figure 4.14. Same as Figure 4.13~~Figure 4.14. Same as Figure 4.13~~) just inland of the U.S. East Coast. From more detailed analysis of two of the best performing models, the increase in cyclone intensity along the East Coast may be related to increased latent heating, as there was little change in Eady growth rates, jet strength, and temperature gradient, but there was 5-30 percent more

precipitation associated with the storm track. Overall, these results illustrate the regional nature of ETC changes around eastern North America.

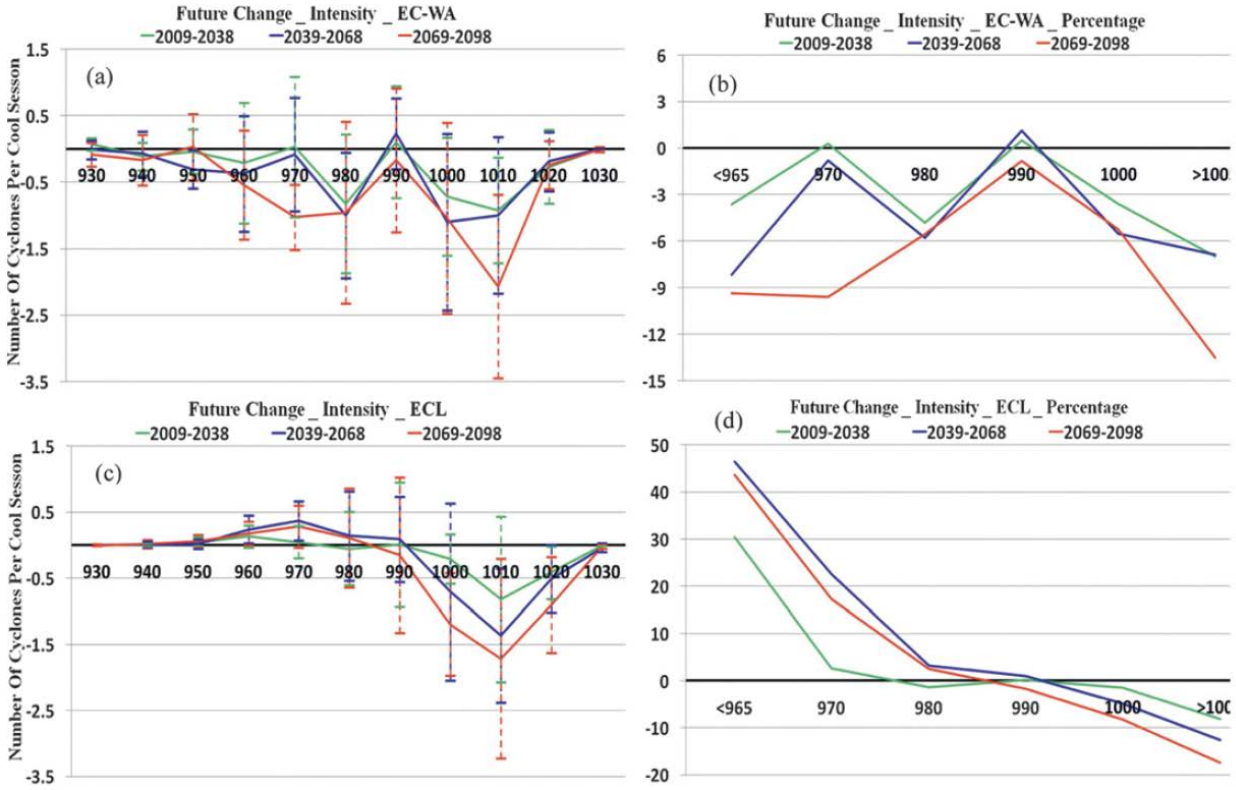

Figure 4.13. Difference in the number of cyclones per cool season reaching their maximum intensity (minimum pressure) for each 10-hPa bin between the three future periods and 1979-2004 for (a) East Coast western and central Atlantic (EC-WA) and (c) East Coast land (ECL). The difference for each future period is for the mean of the results of each Best7 model, with the one standard deviation range shown by the vertical bar. Similar for (b) and (d), but for percentage change. (Source: Colle et al. 2013.)

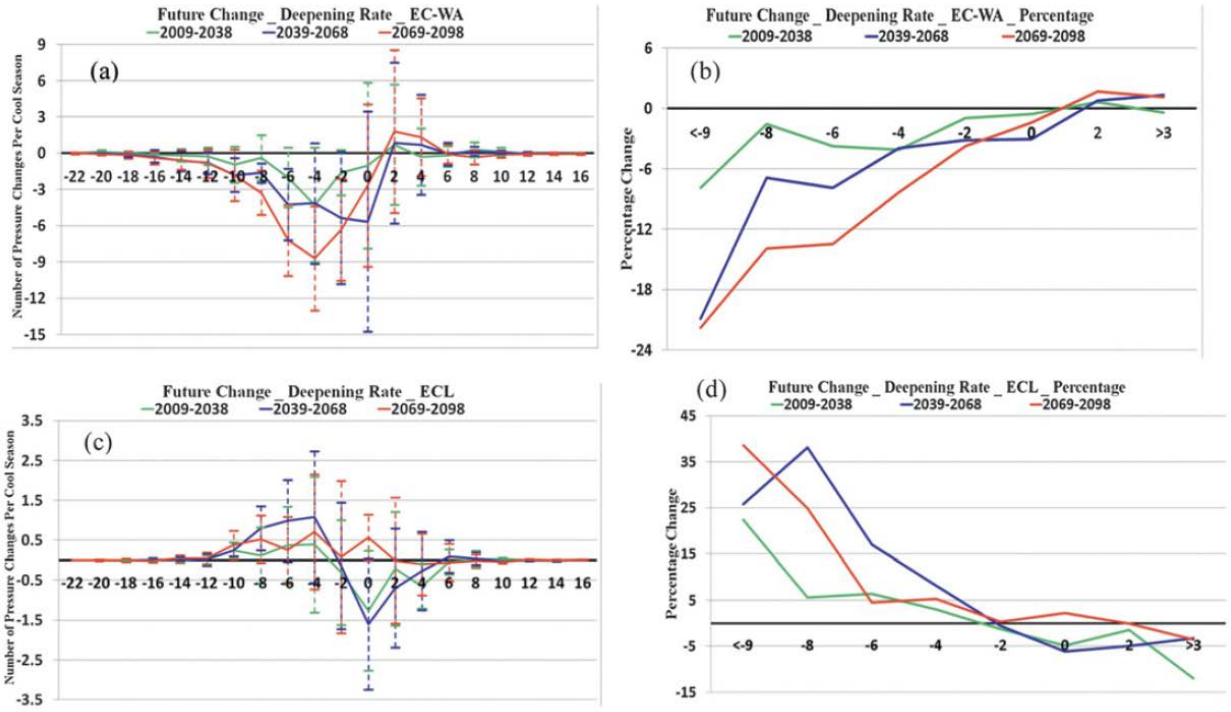

Figure 4.14. Same as Figure 4.13, but for cyclone deepening rates calculated as the 6-h central pressure changes for the full cyclone evolution. (Source: Colle et al. 2013.)

Focusing on snowstorms in the northeastern U.S., Zarcycki (2018) tracked ETCs in the Community Earth System Model Large Ensemble (CESM-LENS) (Kay et al. 2014) using an automated method similar to Hodges (1999). Precipitation type (rain, snow, rain/snow mix, ice pellets, and freezing rain) was derived by applying the Bourgouin algorithm (Bourgouin 2000), requiring model output of full vertical temperature sounding at each model grid point every 6 hr. Storm total snowfall was generated by summing all 6-hourly snowfall occurring within 12^{o} of each sea-level pressure minimum locations along the ETC track. A Regional Snowfall Index (RSI) was calculated by masking the northeast region for each tracked storm and applying the area and population weightings defined in Squires et al. (2014) to both the accumulated snowfall and population density to produce an RSI value and corresponding category ranging from Category 1 (notable) to Category 5 (extreme). An example of a detected Category 5 snowstorm is shown in Figure 4.15. Because the RSI metric collocates storm snowfall with population, it is more relevant to societal impacts. Analysis shows broad declines in snowstorm frequency by the later 21st century primarily because a warmer atmosphere is less conducive to produce snowfall as the predominant precipitation type. However, this effect is partially offset by increased precipitation so the reductions of major events (RSI of Category 3 or higher) are less significant (Figure 4.16i). The ensemble mean of the CESM-LENS shows a mean reduction of cyclone density (Figure 4.16c), but large differences are notable among ensemble members.

The contrasting broad declines in snowstorm frequency and the less significant reductions of major snowfall events discussed by Zarcycki (2018) is consistent with the theoretical analysis of O'Gorman (2014). For example, O'Gorman (2014) found that the 99.99th percentile of daily snowfall decreases by 8 percent in the CMIP5 multimodel median, compared to a 65 percent reduction in mean snowfall. O'Gorman argued that based on theory, extreme snowfall occurs within a narrow range of optimal temperature that is cold enough for precipitation to fall as snow rather than rain but warm enough for the atmosphere to hold enough moisture to produce an extreme amount of precipitation. As global warming

does not influence the optimal temperature for extreme snowfall, changes in extreme snowfall are expected to be much smaller than changes in mean snowfall, which is supported by climate model projections.

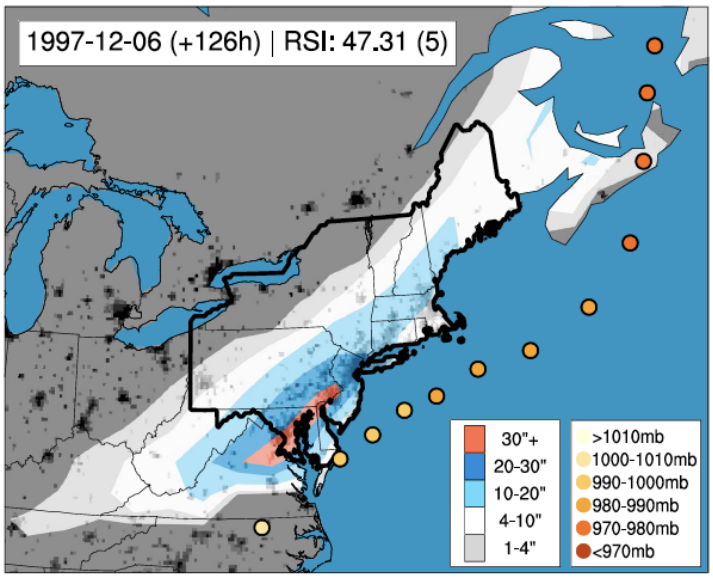

Figure 4.15. Example of a detected Category 5 snowstorm in the CESM-LENS. Minimum sea-level pressure (storm track) is marked at 6-hourly increments by circles, with inner coloring denoting storm intensity. Integrated snowfall (inches) is overlaid as color contours on population density (grayscale, lower[higher] density lighter[darker], with the northeast region (bold) masked for the RSI calculation. (Source: Zarcycki 2018.)

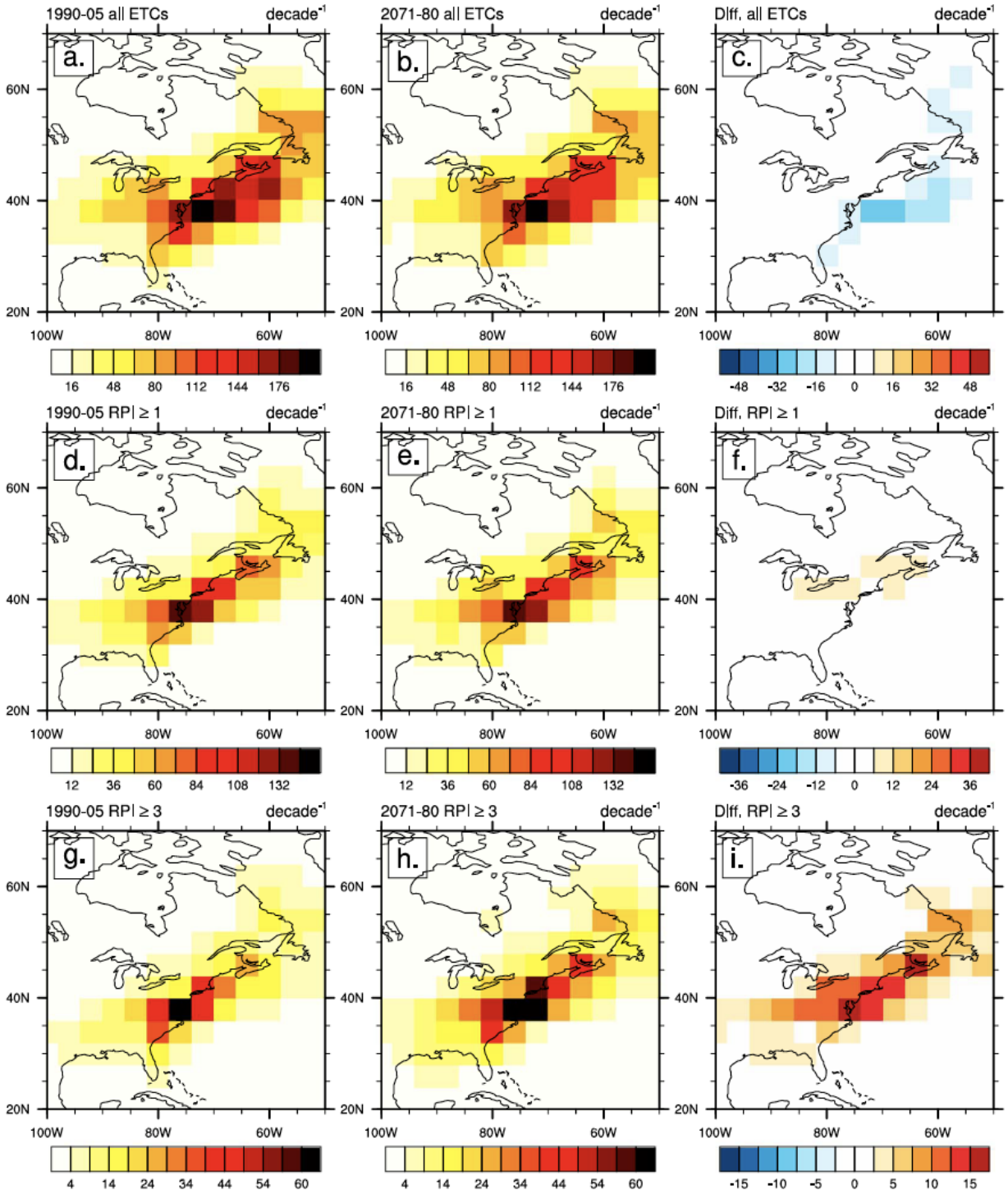

Figure 4.16. Ensemble average track density for all tracked ETCs (top), RPI ≥ 1 (middle), and RPI ≥ 3 (bottom) for present day (left) and end-of-century (middle) time slices. Track density is defined by number of times an ETC tracks over each 4 x 4° gridbox, normalized to number of occurrences per decade. End of century (2071–2080) minus present day (1990–2005) panels are shown on the right. Note the different scales for each row. ETCs = extratropical cyclones; RPI= Regional Precipitation Index. (Source: Zarcycki 2018.)

4.3 Convective Storms

- Convection permitting models capable of simulating mesoscale convective systems (MCSs) show an increase in MCS track density and intensity in the warmer future.
- In a warmer climate, MCSs have heavier rain rates spreading over larger area associated with more vigorous convection. Stronger updraft due to increased latent heat release in more humid atmosphere with warming produces more ice and snow above the freezing level.

As discussed in the Year 3 report on climate change in the midwest region, global climate models generally failed to simulate MCSs, as reflected in model biases in simulating the diurnal cycle of precipitation (van Weverberg et al. 2017) and rainfall intensity, resulting in large dry and warm biases in the central U.S. (Lin et al. 2017). In contrast, convection-permitting regional climate simulations are more skillful in capturing MCSs (Prein et al. 2017a; Yang et al. 2017) because deep convection is explicitly resolved rather than parameterized as in global and regional models applied at grid spacing between 10-100 km. Using a pseudo-global warming approach, Prein et al. (2017b) projected changes in MCSs over the contiguous U.S. with convection-permitting regional climate simulations at 4 km grid spacing. They compared a simulation for 2001-2013 driven by boundary conditions from a global reanalysis for the present climate with a simulation in which the reanalysis boundary conditions are perturbed by adding the mean monthly changes derived as the difference between the period 2071-2100 and 1976-2005 from the CMIP5 multimodel ensemble mean following the RCP8.5 scenario. MCSs were tracked as precipitation objects for analysis of their tracks and precipitation characteristics.

Figure 4.17 shows the MCS tracks simulated for the current and future climate. The simulations showed an increase in MCS track density and intensity over the mid-Atlantic region. Note that the mid-Atlantic region defined in the study includes part of the northeastern U.S. region defined by the National Climate Assessment. Compared to other U.S. regions, the increase in MCS frequency is higher in the northeastern U.S. Table 4.1 shows the number of hours with MCSs in the 13 summer seasons simulated for the present and future. Compared to other regions, the NE has the lowest number of hours with MCSs of 542, but this number is projected to double in the future. Figure 4.18 shows the changes in MCS macrophysical and microphysical properties in the mid-Atlantic region. In a warmer climate, MCSs have higher and colder cloud top (Figure 4.18B and C), indicative of more vigorous convection with stronger updraft (Figure 4.18F) over larger area (Figure 4.18G). Because of warmer temperature, the freezing level height increases in the future (Figure 4.18A). The stronger updraft produces more ice and snow above the freezing level (Figure 4.18E).

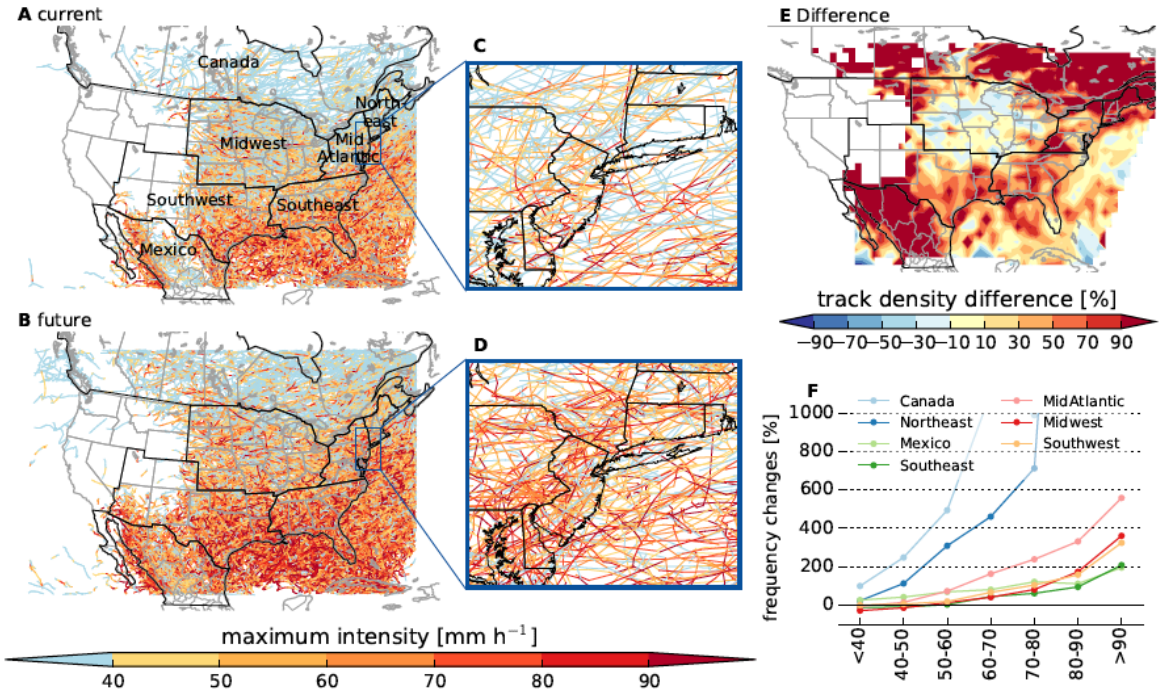

Figure 4.17. Changes in the frequency of MCSs. MCS tracks in the current (a) and future climate simulation (b) show a clear increase in MCS frequency and maximum precipitation (Pmax) (colors) in most regions. c,d, Inlays show a zoom on the Mid-Atlantic region. e, Future minus current relative track density differences. f, Relative frequency changes for different Pmax classes in subregions (a). (Source: Prein et al. 2017b Supplementary Information.)

Table 4.1. Total number of hours with MCSs in the 13 summer seasons for each region in the control and future climate simulation (rows) and in different Pmax classes in mmh^{-1} (columns). (Source: Prein et al. 2017b Supplementary Information)

Region	period	<40	40-50	50-60	60-70	70-80	80-90	>90	total
Canada	current	2,032	293	118	37	18	5	4	2,507
	future	4,050	1,020	701	445	196	109	66	6,587
Northeast	current	355	109	45	23	8	1	1	542
	future	435	232	184	129	65	40	25	1,110
Mexico	current	1,306	727	757	677	458	338	415	4,678
	future	1,645	1,030	1,279	1,221	1,013	714	1,227	8,129
Southeast	current	1,835	1,320	1,400	1,155	946	616	753	8,025
	future	1,630	1,183	1,441	1,666	1,525	1,199	2,322	10,966
MidAtlantic	current	953	462	316	186	104	57	43	2,121
	future	893	529	545	489	352	246	283	3,337
Midwest	current	3,368	1,392	932	569	284	114	69	6,728
	future	2,399	1,197	1,054	802	514	312	318	6,596
Southwest	current	1,462	865	851	675	469	281	319	4,922
	future	1,459	911	1,011	1,122	960	725	1,354	7,542

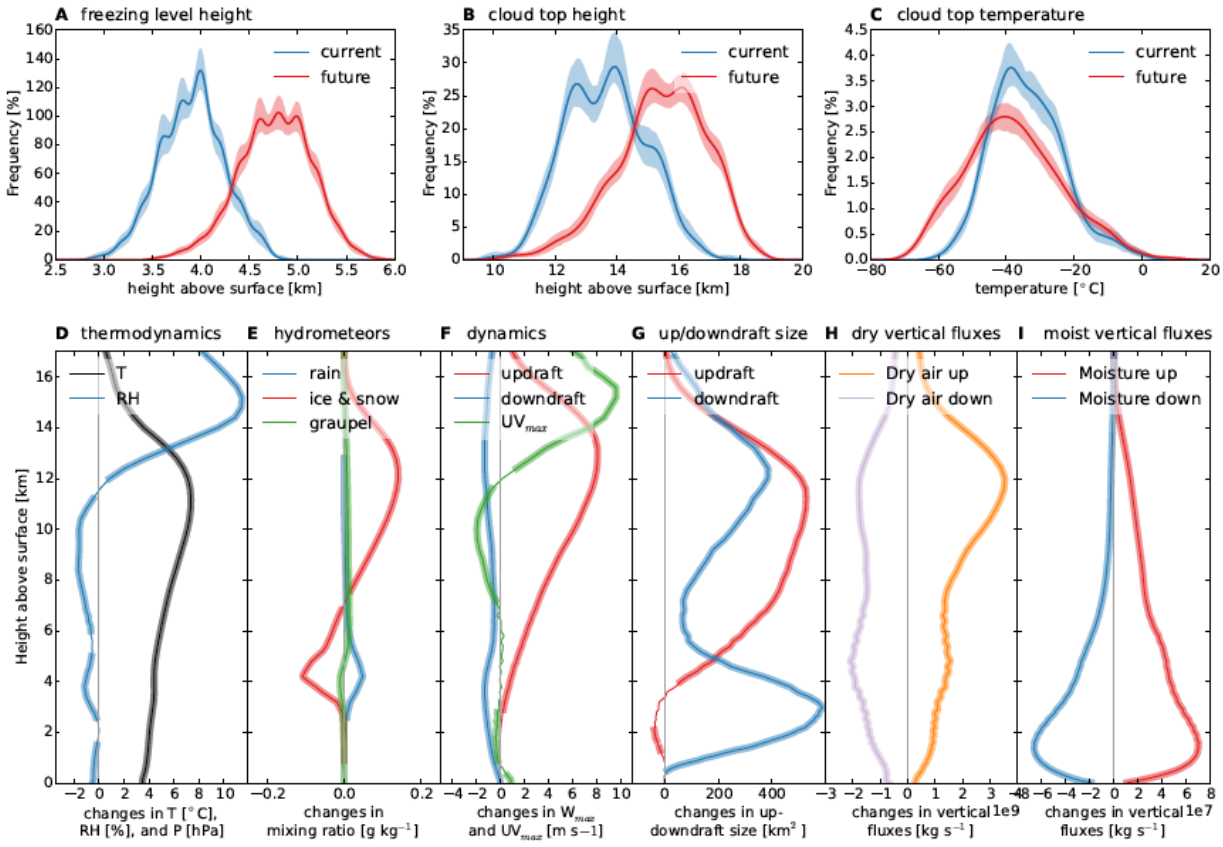

Figure 4.18. Changes in the average MCS environments in JJA Mid-Atlantic MCSs. Probability density functions of current and future MCS freezing level heights (a), cloud top heights (b), and cloud top temperatures (c). Absolute changes in thermodynamics (d), hydrometeors (e), maximum vertical and horizontal wind speeds (f), up and downdraft sizes (g), dry air vertical mass fluxes (h), and moist vertical mass fluxes (i). Thick lines in d–i show significant changes (alpha is 0.01) according to 100 bootstrap samples. Shadings in a–c show the 1–99 percentile range of the probability density functions according to 100 bootstrap samples. Changes in temperature and relative humidity are calculated in the MCS inflow region. (Source: Prein et al. 2017b Supplementary Information.)

5.0 Sea-Level Rise and Storm Surge in the Northeast Region

Sea-level rise poses significant threats to coastal infrastructures and ecosystems through inundation and increased frequency and severity of storm surge, which may also increase due to intensified storms under warming. The northeast region has large population and many infrastructures along the Atlantic coast so understanding how sea level and storm surge respond to climate change is important for long-term planning and adaptation. This chapter summarizes findings in the literature regarding sea-level rise and storm surge, including results that are particularly relevant to the northeast region.

5.1 Sea-Level Rise

- The mean global sea level has risen by 3.2 ± 0.4 mm/yr between 1993 and 2007. The northeastern U.S. has experienced higher-than-global increase in sea level since the 1970s.
- Between 1950-1979 and 1980-2009, sea-level rise in the northeastern U.S. was 3-4 times higher than the global average, making it a hotspot of accelerated sea level rise. The higher local sea level rise in the northeastern U.S. has been attributed to land subsidence induced by glacial isostatic adjustment and weakening of the Gulf Stream.
- In the RCP8.5 scenario, the likely range of local sea-level rise for New York City is 0.7-1.3 m between the 17th and 83rd percentile levels by 2100. Uncertainty in oceanographic processes contributes importantly to uncertainty in the projection.
- When integrated over the 21st century and under all RCP scenarios, the expected number of years with current 1-in-10 year flood events is at least five times larger than 10, the number predicted without sea-level rise.
- In the 21st century, cities like New York, Boston, and Portland in the northeastern U.S. stand out with the largest sea-level rise but decreasing variability over time compared to other cities around the world. A weakening of the Atlantic Meridional Overturning Circulation (AMOC) is responsible for the large sea-level rise as well as the decreasing variability in the northeast coast. Climate mitigation (RCP4.5) reduces the sea-level rise relative to the business-as-usual (RCP8.5) scenario.

As discussed in Kopp et al. (2014), future change in the mean global sea level (GSL) is controlled primarily by the thermal expansion of ocean water and by mass loss from glaciers, ice caps, and ice sheets. Changes in land water storage due to groundwater depletion and reservoir impoundment also played a role in the 20th century but such changes are expected to be relatively minor contributors compared to other factors in the 21st century. For adaptation planning and risk management, assessment of local sea-level (LSL) rise is critical, as it can deviate substantially from GSL rise due to several factors: (1) non-uniform changes in ocean dynamics, heat content, and salinity, (2) perturbations in the Earth's gravitational field and crustal height, together known as static-equilibrium effects, associated with the redistribution of mass between the cryosphere and the ocean, (3) glacial isostatic adjustment (GIA), ongoing adjustment of the solid Earth to the loss of the North American ice sheet at the end of the last ice age, and (4) vertical land motion due to tectonics, local groundwater, and hydrocarbon withdrawal, and natural sediment compaction and transport.

The mean GSL has increased gradually in the last century, driven mainly by thermal expansion of the ocean and addition of mass from melting of glaciers and the Greenland and Antarctic ice sheets. Satellite

and in situ measurements show that about one-third of the mean GSL rise since 2004 has been associated with thermal expansion, and about two-thirds has been primarily from the melting of land-based ice (USGCRP 2017) (Figure 5.1a). The rate of mean GSL rise has increased from 1.7 ± 0.3 mm/yr averaged over the 20th century to about 3.2 ± 0.4 mm/yr between 1993 and 2007 (Merrifield et al. 2009). The increase in mean GSL since 1900 can be largely attributed to global warming, as model simulations without greenhouse gas warming do not capture the rapid rise in GSL in the 20th century (Figure 5.1b).

Consistent with the mean GSL increase, the sea level across the northeastern U.S. coastline has risen gradually during the last century. The spatial pattern of sea surface height changes between 1993 and 2014 shows a higher-than-global increase in the U.S. Northeast since the 1970s (Figure 5.1c). The higher LSL rise has been attributed to land subsidence induced by GIA and weakening of the Gulf Stream that may be related to the weakening of the Atlantic meridional overturning circulation (AMOC) (Yin and Goddard 2013; Rahmstorf et al. 2015). The northeast U.S. as a hotspot of accelerated sea-level rise was investigated by Sallenger et al. (2012) and shown in Figure 5.2. Between 1950-1979 and 1980-2009, sea-level rise increases in the northeast hotspot, about 1,000-km along the highly populated North American Atlantic coast north of Cape Hatteras, were 3-4 times higher than the global average. Analysis of geological and historical sea-level records shows a significant rate of increase since the 19th century. In New Jersey, Miller et al. (2013) showed that it is extremely likely that sea-level rise in the 20th century was faster than during any other century in the last 4.3 thousand years.

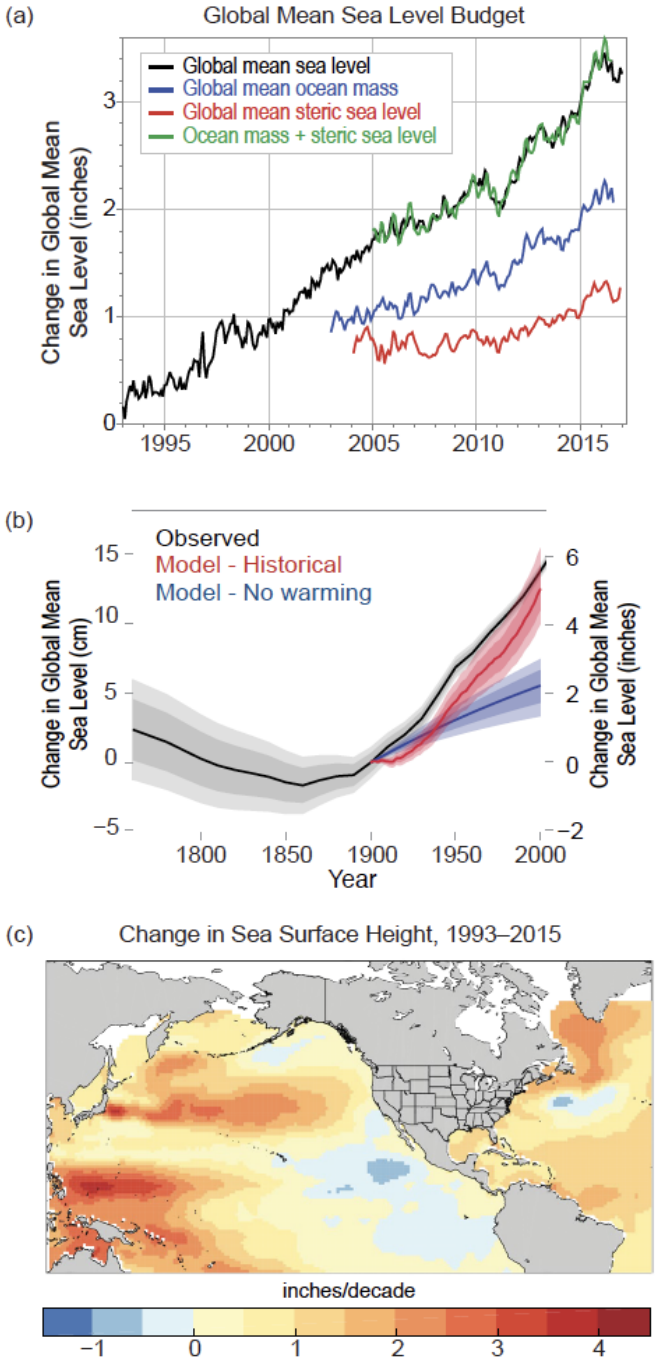

Figure 5.1. (a) Contributions of ocean mass changes from land ice and land water storage (measured by satellite gravimetry) and ocean volume changes (or steric, primarily from thermal expansion measured by in situ ocean profilers) and their comparison to global mean sea-level (GMSL) change (measured by satellite altimetry) since 1993. (b) An estimate of modeled GMSL rise in the absence of 20th century warming (blue), from the same model with observed warming (red), and compared to observed GMSL change (black). Heavy/light shading indicates the 17th–83rd and 5th–95th percentiles. (c) Rates of change from 1993 to 2015 in sea surface height from satellite altimetry data (adapted and updated from Kopp et al. 2015). (Source: USGCRP 2017.)

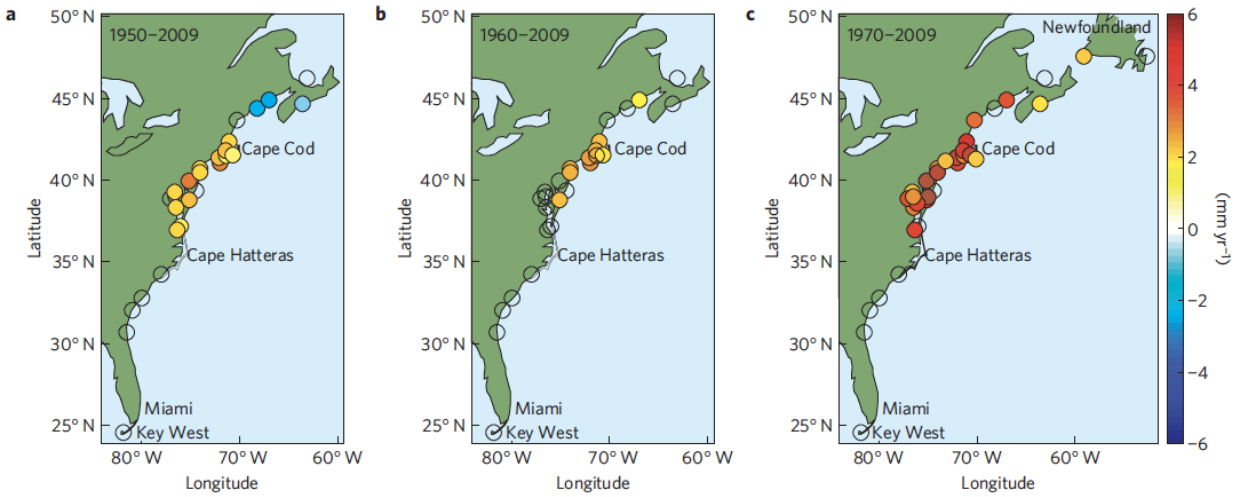

Figure 5.2. Spatial variations of sea-level rise difference (SLRD) on the North American east coast. Each circle represents a gauge location and is color-coded to reflect SLRD. Circles with no color fill are not statistically different from zero. Confidence limits are $\pm 1\sigma$ and account for serial correlation. More gauges were available for plots that show results from shorter time series. a, 1950–2009. b, 1960–2009. c, 1970–2009. (Source: Sallenger et al. 2012.)

Kopp et al. (2014) presented a global set of LSL projections on timescales ranging from the coming decades through the 22nd century, with complete probability distributions informed by a combination of community assessment, expert elicitation, and process modeling. The sources of information used to produce the probabilistic projections are summarized in Figure 5.3. Details of methods used to project LSL are described in Kopp et al. (2014).

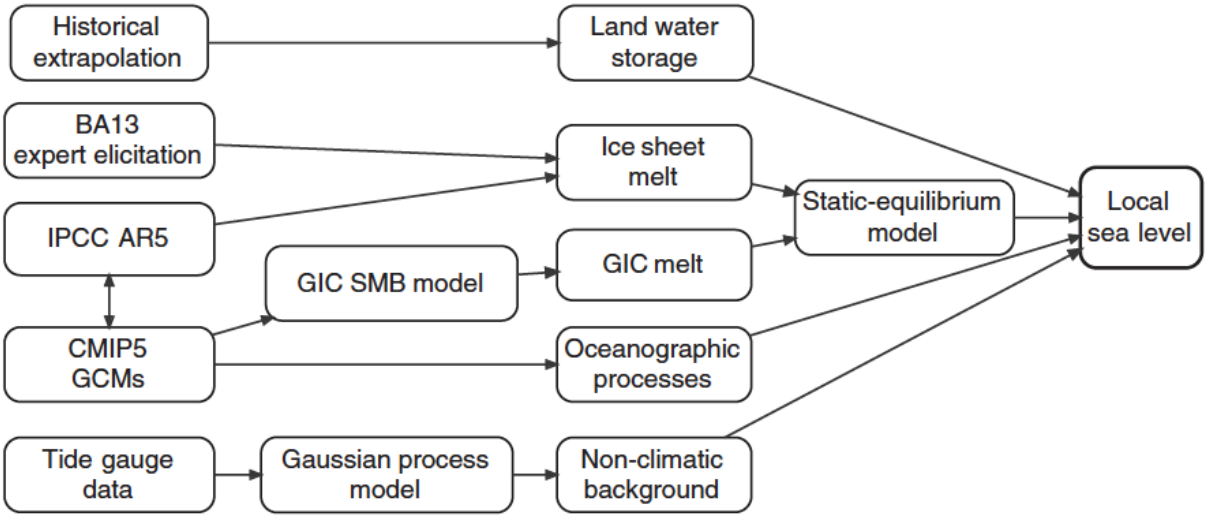

Figure 5.3. Logical flow of sources of information used in LSL projections. GCMs: global climate models; GIC: glaciers and ice caps; SMB: surface mass balance. (Source: Kopp et al. 2014.)

Using the framework shown in Figure 5.3, projections of mean GSL for RCP2.6, 4.5, and 8.5 through the end of the 22nd century are shown in Figure 5.4. Uncertainty from different components contributing to the mean GSL changes with time. Kopp et al. (2014) noted that in 2020, about two-thirds of the total variance in GSL is due to uncertainty in projections of thermal expansion. By 2050 in RCP8.5, changes in ice-sheet volume are responsible for more than half of the variance and by 2100, Antarctic ice sheet alone is responsible for half of the variance, while Greenland ice sheet is responsible for an additional 30%. Hence for long-term projections beyond 2100, uncertainty in projecting Antarctic and Greenland ice sheet has the largest contributions to uncertainty in projecting mean GSL. By 2100 following RCP8.5, the median mean GSL rise is 79 cm and by 2200, this increases to 200 cm. The GSL under RCP8.5 increasingly differs from that under RCP4.5 and RCP2.6 after 2100.

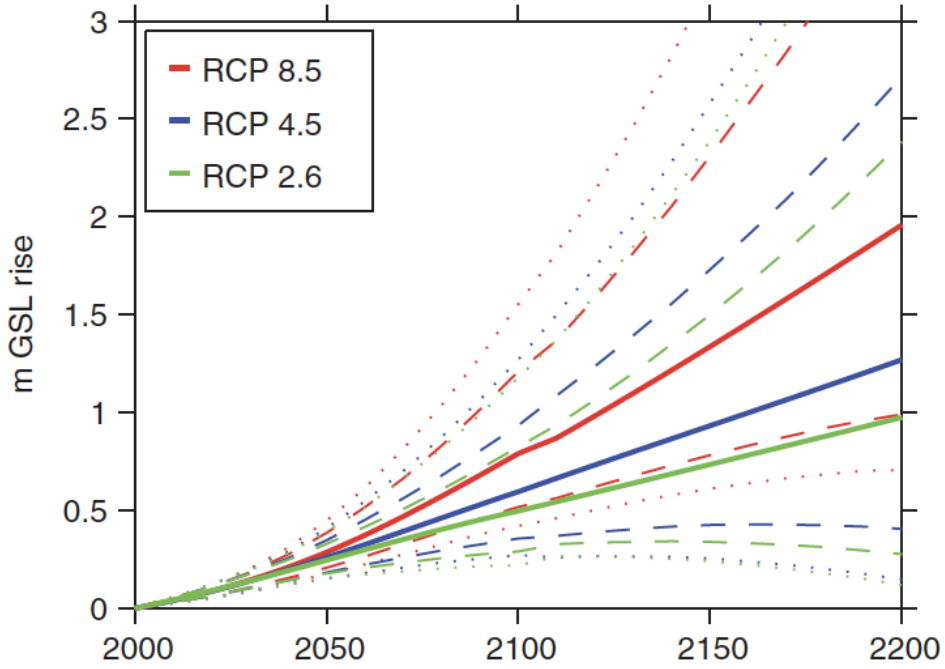

Figure 5.4. Projections of GSL rise for the three RCPs. Heavy=median, dashed=5th–95th percentile, dotted=0.5th–99.5th percentiles. (Source: Kopp et al. 2014)

The spatial distribution of LSL under RCP8.5 in 2100 is provided in Figure 5.5. The median projection for the NE region is close to 1 m, with a width of ~0.6 m between the 17th and 83rd percentile levels. Uncertainty in oceanographic processes contributes importantly to uncertainty in projecting LSL in northeastern North America. Tables Table 5.1 and Table 5.2 summarize the LSL projections for New York City for three RCP scenarios and the contributions from different factors, respectively. As discussed in Kopp et al. (2014), New York City experiences greater-than-global sea-level rise in all three scenarios. The likely range of LSL rise is 0.7-1.3 m by 2100 under RCP8.5. Three factors enhance the LSL rise in New York City relative to the GSL rise: (1) the site experiences GIA-related sea-level rise of 1.3±0.2 mm/yr because it is located on the subsiding peripheral bulge of the former Laurentide Ice Sheet; (2) the rotational effects of the West Antarctic Ice-Sheet mass loss adds 20% to the region's sea-level response to that mass loss, and (3) changes in the Gulf Stream may result in dynamic sea-level rise in the mid-Atlantic region. From Table 5.2, oceanographic processes including thermal expansion and dynamic processes have the largest contribution of 51 cm to the median LSL rise in New York City by 2100 under

RCP8.5. Of the 51 cm, ~10-15 cm is contributed by dynamic ocean processes, with a large 17th to 83rd percentile range of ~40 cm (Figure S4 of Kopp et al. 2014). Constraining the projection of the ocean component is thus important for reducing uncertainty in projecting LSL in northeastern U.S.

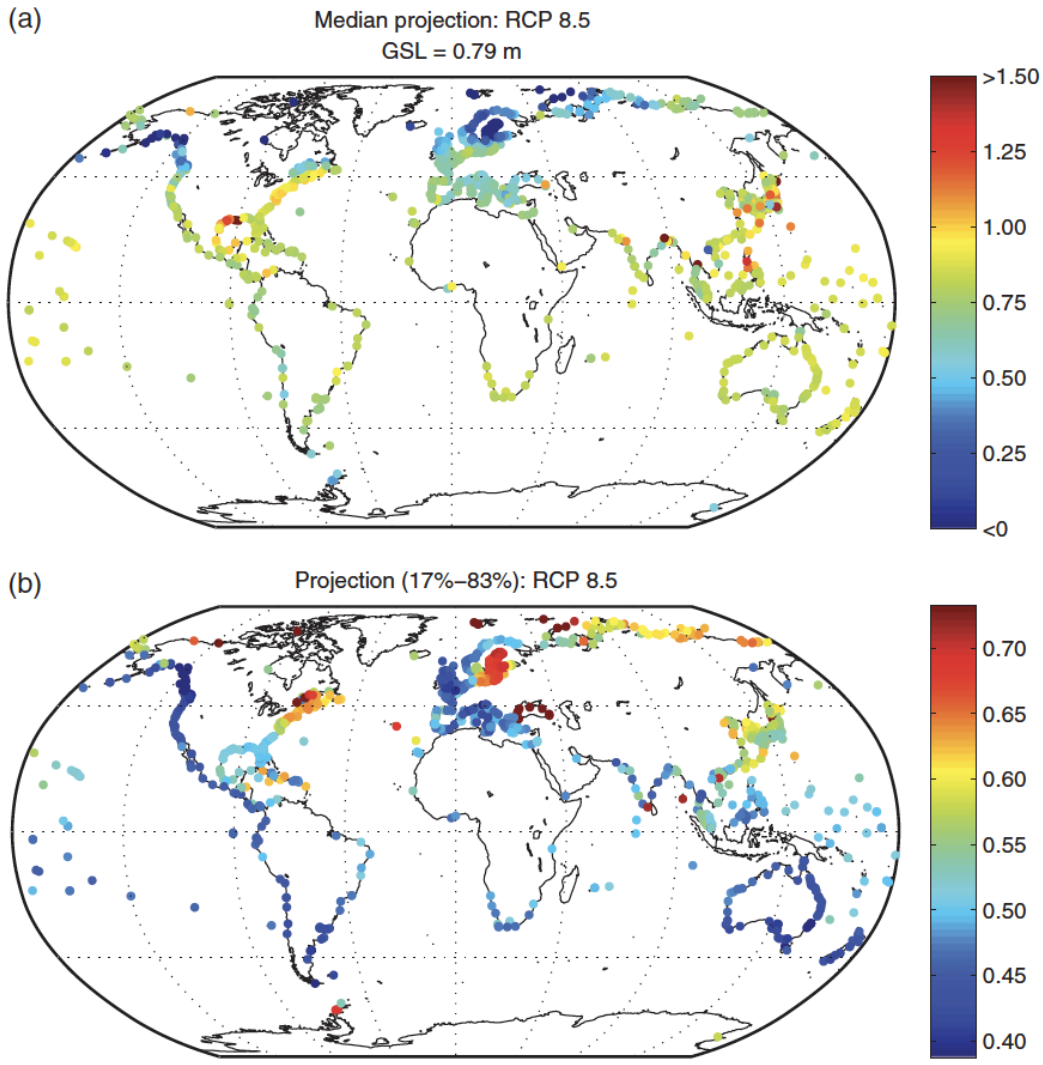

Figure 5.5. (a) Median projection and (b) width of likely range of LSL rise (m) in 2100 under RCP 8.5. (Source: Kopp et al. 2014.)

Table 5.1. LSL projections for New York, NY, USA. (Source: Kopp et al. 2014.)

	RCP 8.5					RCP 4.5					RCP 2.6				
cm	50	17–83	5–95	0.5–99.5	99.9	50	17–83	5–95	0.5–99.5	99.9	50	17–83	5–95	0.5–99.5	99.9
New York, NY, USA (Bkgd: 1.31 ± 0.18 mm/yr)															
2030	21	13–29	7–35	−1 to 44	<50	20	15–25	11–29	6–34	<40	20	14–26	9–31	2–38	<40
2050	38	27–50	19–59	8–73	<85	36	26–45	19–53	10–66	<75	35	24–45	16–53	6–67	<75
2100	96	65–129	44–154	15–212	<305	75	51–101	35–123	11–183	<255	62	41–85	27–106	7–170	<245
2150	150	110–200	90–250	60–420	<610	110	70–160	40–200	10–360	<520	90	60–120	40–170	30–340	<520
2200	210	150–290	120–370	70–690	<1020	140	80–220	50–300	−0 to 600	<890	110	60–180	40–260	20–580	<890

Table 5.2. Components of LSL rise in 2100 for New York, NY, USA. (Source: Kopp et al. 2014.)

	RCP 8.5					RCP 4.5					RCP 2.6				
cm	50	17–83	5–95	0.5–99.5	99.9	50	17–83	5–95	0.5–99.5	99.9	50	17–83	5–95	0.5–99.5	99.9
New York, NY, USA															
GIC	14	11–17	9–19	6–22	<25	11	8–13	6–15	3–18	<20	9	7–12	5–13	3–16	<20
GIS	6	3–11	2–17	1–31	<40	4	2–7	1–10	0–18	<25	3	2–5	1–8	1–14	<20
AIS	4	−8 to 17	−12 to 38	−15 to 108	<180	6	−5 to 19	−9 to 38	−12 to 104	<170	7	−4 to 20	−8 to 40	−11 to 110	<180
Oce.	51	24–78	5–98	−24 to 125	<140	35	15–55	1–70	−23 to 92	<100	23	6–41	−6 to 53	−25 to 71	<80
LWS	5	3–7	2–8	−0 to 11	<10	5	3–7	2–8	−0 to 11	<10	5	3–7	2–8	−0 to 11	<10
GIA/Tect.	13	12–14	12–15	11–15	<15	13	12–14	12–15	11–15	<15	13	12–14	12–15	11–15	<15
Total	96	65–129	44–154	15–212	<305	75	51–101	35–123	11–183	<255	62	41–85	27–106	7–170	<245

The LSL projections with the full probability distributions can be combined with extreme value distributions to estimate the expected number of years in which flooding exceeds a given elevation, integrated over a given interval of time. Figure 5.6 shows the expected fraction of years with flooding at the New York City tide gauge in excess of a given height above the mean higher high water (MHHW). When integrated over the 21st century and under all RCP scenarios, the expected number of years with current 1-in-10 year flood events is at least five times larger than would be predicted without sea-level rise.

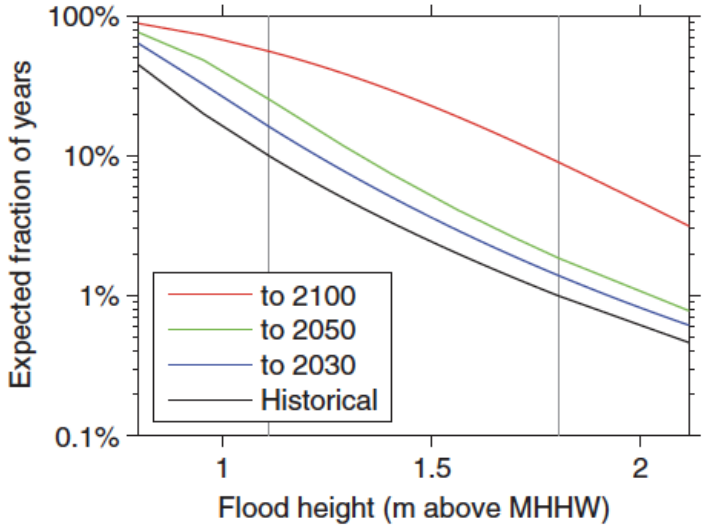

Figure 5.6. Expected fraction of years with flooding at the New York City tide gauge in excess of a given height under stationary sea level (black) and RCP 8.5 over 2001–2030 (blue), 2050 (green) and 2100 (red). Gray vertical lines indicate the current 1-in-10 and 1-in-100 year flood levels. Heights are relative to MHHW for New York City. (Source: Kopp et al. 2014)

Similar to the analysis reported by Kopp et al. (2014) with some specific examples for New York City, Kopp et al. (2016) produced an assessment of the regional sea-level rise in New Jersey for the New Jersey Climate Adaptation Alliance (NJCAA). Table 5.3 summarizes the findings of the report, which are concluded in the statements below in the executive summary of the report.

- New Jersey coastal areas are likely (about 67 percent probability) to experience SLR of 0.6 to 1.0 ft. between 2000 and 2030, and 1.0 to 1.8 ft. between 2000 and 2050. There is about a 1-in-20 chance (5 percent probability) that SLR will exceed 1.1 ft. by 2030 and 2.0 ft. by 2050.
- While differences in SLR projections under different emissions scenarios before 2050 are minor (<0.1 ft.), SLR projections after 2050 increasingly depend upon the evolution of future global greenhouse gas emissions over the current and future decades.

- Under a high-emissions scenario (RCP 8.5), coastal areas of New Jersey are likely (about 67 percent probability) to see SLR of 2.4 to 4.5 ft. between 2000 and 2100. There is about a 1-in-20 chance (5 percent probability) that SLR will exceed 5.3 ft.
- Under a low-emissions scenario (RCP 2.6), coastal areas of New Jersey are likely (about 67 percent probability) to see an increase in SLR of 1.7 to 3.1 ft. between 2000 and 2100. There is about a 1-in-20 chance (5 percent probability) that SLR will exceed 3.8 ft. by 2100.
- A worst-case SLR (defined as a 1 in 1000 chance) of 2.8 ft. by 2050 and 10 ft. by 2100 is physically possible in New Jersey.

Table 5.3. Projections of sea-level rise for New Jersey (ft.). Estimates are based on Kopp et al. (2014). Columns correspond to different projection probabilities. For example, the 'Likely Range' column corresponds to the range between the 17th and 83rd percentile; consistent with the terms used by the IPCC (Mastrandrea et al., 2010). All values are with respect to a 1991-2009 baseline. Note that these results represent a single way of estimating the probability of different levels of SLR; alternative methods may yield higher or lower estimates of the probability of high-end outcomes. (Source: Kopp et al. 2016.)

	Central Estimate	Likely Range	1-in-20 Chance	1-in-200 Chance	1-in-1000 Chance
Year	*50% probability SLR meets or exceeds…*	*67% probability SLR is between…*	*5% probability SLR meets or exceeds…*	*0.5% probability SLR meets or exceeds…*	*0.1% probability SLR meets or exceeds…*
2030	0.8 ft	0.6 – 1.0 ft	1.1 ft	1.3 ft	1.5 ft
2050	1.4 ft	1.0 – 1.8 ft	2.0 ft	2.4 ft	2.8 ft
2100 Low emissions	2.3 ft	1.7 – 3.1 ft	3.8 ft	5.9 ft	8.3 ft
2100 High emissions	3.4 ft	2.4 – 4.5 ft	5.3 ft	7.2 ft	10 ft

As discussed above, ocean processes have the largest contribution to the future LSL in New York City under all scenarios. Uncertainty in projecting changes in LSL due to ocean processes can be attributed to uncertainty in the projected warming that influences thermal expansion and uncertainty related to ocean dynamics (wind-driven and buoyancy driven circulation), both have important contributions from model uncertainty and internal variability. While model uncertainty may be reduced as understanding of the processes improves over time, uncertainty related to internal variability is not reducible because internal variability is intrinsic to the climate system. Hu and Bates (2018) investigated the steric (thermal expansion) and dynamic sea-level rise in two large ensembles of simulations from the Community Earth System Model version 1 (CESM1) (Kay et al. 2015) following the RCP4.5 and RCP8.5 scenarios to understand the role of mitigation (RCP4.5 vs. RCP8.5) and internal variability in LSL projections. More specifically, they investigated the internal variability associated with the AMOC, the Antarctic Circumpolar Current (ACC), the North Atlantic Oscillation (NAO), and the Pacific Decadal Oscillation (PDO) and their influence on LSL in the near term (2021-2040) and long term (2061-2080) with (RCP4.5) and without (RCP8.5) climate mitigation. Only the steric and ocean dynamic components of sea-level rise are studied.

From Figure 5.7, that displays the ratio of the ensemble averaged 20-year mean sea-level rise (a-d) and the decadal trend of sea-level rise to the global mean, LSL along the northeastern North America coast is consistently higher than the global mean in both scenarios and both the near-term and long-term periods. The GSL rise projected by CESM1 is comparable to the CMIP5 model projections. The difference in sea-level rise between the two scenarios is small in the near term because of the large inertia of the ocean but

in the long term, there is a difference of 4.6 cm in GSL between the two scenarios. Note that the spatial patterns of sea-level rise are similar between the two scenarios and the two time periods, suggesting that the underlying governing processes for LSL are similar between scenarios. Hu and Bates (2018) noted that except in the South Atlantic, the intra-ensemble variability (a measure of internal variability influence) of sea-level rise and decadal trends due to steric and dynamic contributions is larger in regions where the ensemble mean sea-level rise and decadal trends are higher than the global mean.

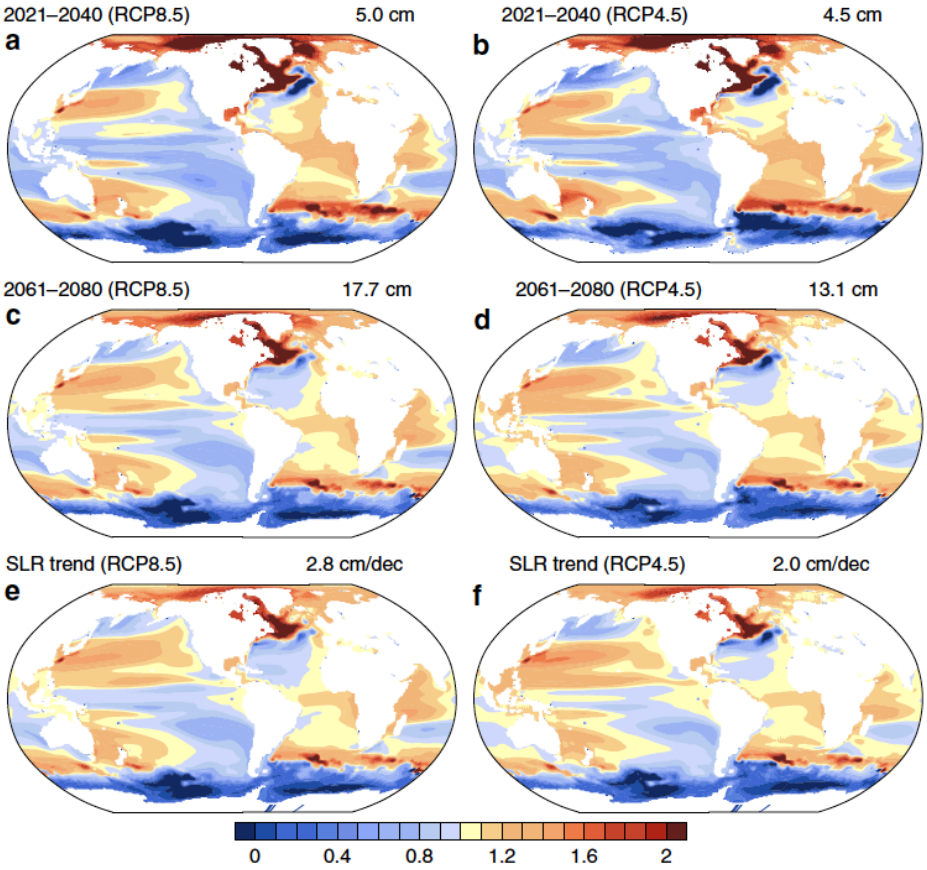

Figure 5.7. Ratio of ensemble averaged 20-year mean sea-level rise (a-d) and the decadal trend (e,f) of sea-level rise to the global mean, shown as the numbers on the top right of each panel. For a–d, the ensemble GMSL rise is relative to the ensemble mean sea level of 1986–2005. The decadal trend is the average 10-year trend over the period 2006–2080. The left panels are for RCP8.5 and right panels for RCP4.5. (Source: Hu and Bates 2018.)

The regional differences in LSL (related mostly to ocean dynamics) are shown more clearly in Figure 5.8 for major coastal cities worldwide. Consistent with the spatial distribution shown in Figure 5.7, cities along the northern West Atlantic stand out with the largest sea-level rise in both periods compared to other locations, with New York, Boston, and Portland, all within the Northeast U.S. region at the top. Compared to other cities, the northeastern U.S. also stands out in terms of the changes in variability over time. Together with the equatorial west coast of Africa and the west coast of India, the northeastern U.S. coast (apparent in Boston and Portland comparing the variance in the near term and long term in Figure 5.6) shows reducing variability over time while nearly all other cities have an opposite trend in variability. On average, the ensemble mean steric and dynamic LSL decadal trends from 2006 to 2080 in RCP4.5 are 20 to 50 percent less than that in RCP8.5. By 2061–2080, the reduction of sea-level rise of RCP4.5

relative to RCP8.5 is statistically significant at the 95 percent level almost everywhere in the global ocean.

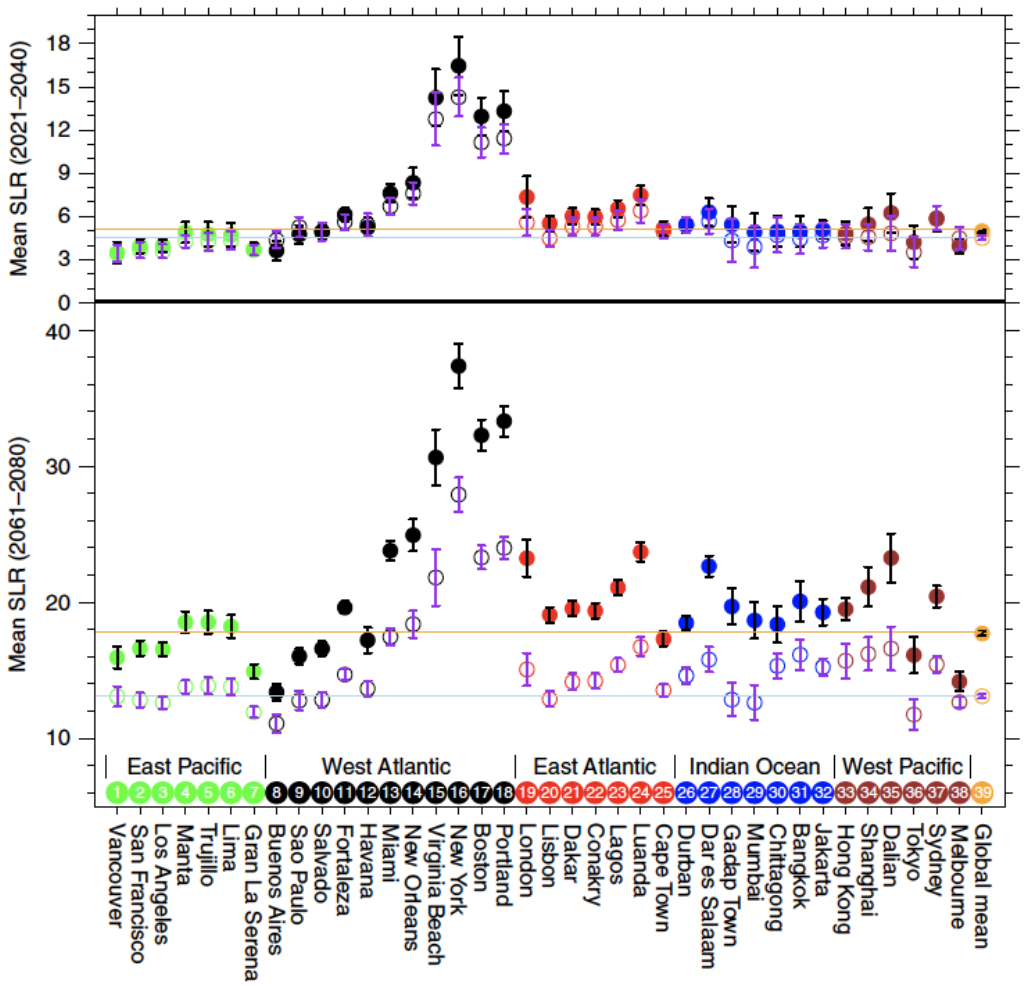

Figure 5.8. Twenty-year mean sea-level rise for selected cities. This mean sea-level rise is relative to the mean of the 1986–2005. The top is for the mean of 2021–2040 and the bottom for 2061–2080. The solid dots are the ensemble mean sea-level rise for RCP8.5 and open circles the ensemble mean sea-level rise for RCP4.5. The bars indicate ensemble variability (±1 standard deviation). The units are in centimeters. The brown and light blue line represent the ensemble global mean SLR for RCP8.5 and RCP4.5, respectively. The color-coded dots/open circles represent east (green) and west (brown) Pacific coasts, west (black) and east (red) Atlantic coasts, and Indian Ocean coast (blue). (Source: Hu and Bates 2018.)

To understand the spatial distribution of LSL and the change in variability over time, Hu and Bates (2018) analyzed how the various modes of variability change over time and differ between the two scenarios. Both AMOC and NAO have important effects on ocean processes in the subpolar North Atlantic that influence sea level along the northeastern U.S. coast. In CESM1, under global warming, AMOC weakens as the larger precipitation increases than evaporation increases causes warming and freshening, and warming increases sea ice meltwater export from the Artic. The weakening of AMOC is larger in RCP8.5 than RCP4.5 due to the larger warming in the former scenario (Figure 5.9). With the weaker AMOC, the northward transport of upper ocean water weakens and the Gulf Stream is less vigorous. The latter relaxes the slope of the sea surface to increase sea level more north and west of the Gulf Stream. Therefore, the

larger LSL rise along the northeastern U.S. coast is due to the enhanced warming and freshening and a weaker AMOC, both effects increase over time and are larger in RCP8.5 than RCP4.5. Hence the intra-ensemble variance is smaller in RCP8.5 than RCP4.5 and decreases in the 21st century relative to the 20th century, contributing to the more significant difference between the two scenarios over time. In contrast to AMOC, CESM1 simulated no robust changes in magnitude, position, or timescale of NAO in either scenario (Figure 5.8) but on interannual timescale, NAO contributes importantly to the variance of LSL due to its influence on ocean stratification, affecting the water mass density and the associated ocean currents. In summary, the sea-level rise projections are well separated between the two scenarios toward the end of the century but internal variability is large in the near term. Any policy limiting greenhouse gas emission will not immediately reduce the overall impact of climate change in coastal regions experiencing sea-level rise, but the impact will be significant on multi-decadal or longer timescales.

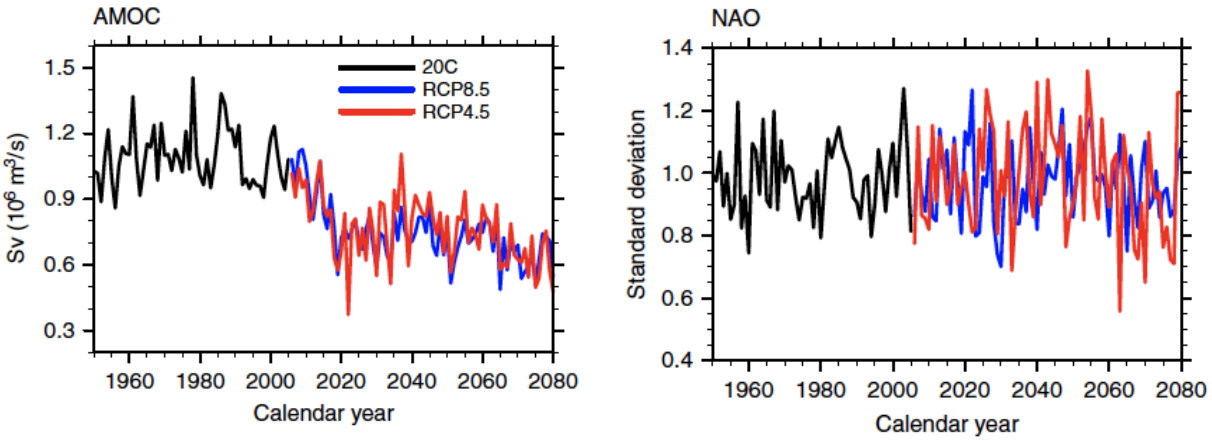

Figure 5.9. Time evolving intra-ensemble standard deviation for AMOC (left) and NAO (right). Black lines represent the intra-ensemble standard deviation for the twentieth century (1920–2005); blue lines are the intra-ensemble standard deviation for RCP8.5 (2006–2080); and red lines the intra-ensemble standard deviation for RCP4.5 (2006–2080). (Source: Hu and Bates 2018.)

5.2 Storm Surge

- At the Battery tide gauge in New York City, the present-day 100-yr storm surge is estimated to be about 1.74 m. Considering the changes in hurricane climatology may increase the 100-yr and 500-yr storm tide levels by about 0.7 – 1.2 m by the end of this century, which is comparable to the sea-level rise of 0.5 – 1.5 m projected for the region.
- One study using hurricane/hydrodynamics models driven by CMIP3 models estimated the storm surge height and return period of Sandy to be 2.8 m and 398 y in 2000. Considering only the effect of sea-level rise, the return period (flood height) of Sandy is estimated to be ~1,200 y (2.3 m) in 1800 and ~90 y (3.7 m) in 2100. Considering both sea-level rise and storm climatology change, the return period in 2100 becomes ~23-130 y (3.5-4.3 m).
- Using a similar methodology but driven CMIP5 models, another study projected little change in storm surge in the future because of a compensation between increased storm intensity and reduced tropical cyclone track density impacting New York City due to a shift of storm track towards offshore.
- Analysis of observations has identified an increased correlation between storm surge and heavy precipitation in New York City and Boston in the past few decades due to changes in weather patterns favoring the compound flooding events.

Coastal flooding in the northeastern region can be caused by nuisance or tidal flooding and storm surge due to the strong winds associated with extratropical cyclones and tropical cyclones. Global warming can exacerbate coastal flooding through all these processes by increasing sea level and intensifying storms. Nuisance or tidal flooding is more predictable; it increases with sea-level rise and causes inconvenience but not significant threats to infrastructures and properties. Wind is the primary factor governing storm surge. According to Orton et al. (2019), of the top 22 known historical storm tide events in New York City history, 15 have been caused by extratropical cyclones, which impact the region far more often than hurricanes (Booth et al. 2015; Catalano and Broccolo 2018). However, ETCs appear to have a lower maximum storm tide potential because their observed maximum wind speeds are much lower than those for hurricanes or hybrid storms such as Sandy (Orton et al. 2016). Hence this section focuses on storm surge related to TCs, while noting that global warming is likely to increase nuisance and tidal flooding and storm surge induced by ETCs.

To estimate how storm surge associated with TCs may change in the future, Lin et al. (2012) used a hurricane model driven by GCMs and a hydrodynamics model to simulate storm surge in New York City (NYC). The hurricane model is a combined statistical/deterministic approach based on a statistical model of TC synthetic tracks and a deterministic model of TC intensity, both driven by the GCM large-scale atmospheric and oceanic environments. This approach is used because the horizontal resolution of GCMs is typically too low to simulate intense TCs and dynamical downscaling approach is too computationally expensive to be used to provide probabilistic information for risk assessment. A set of 5,000 New York-region storms (storms within a 200-km radius from the Battery (74.02W, 40.9N) were produced under the observed climate (1981-2000) based on reanalysis large-scale conditions. To study the impact of climate change, two additional sets of 5,000 New York-region storms were produced for the present (1981-2000) and future (2081-2100) conditions under the A1B emission scenario, which is comparable to RCP4.5 for each of 4 GCMs chosen to span the range of the 7 CMIP3 models that provide the required data for hurricane modeling. The storm frequency derived from each GCM is calibrated to the observed value of 0.34 for NY-region storms estimated from the best-track Atlantic hurricane data. From the 4 GCMs, the change in storm frequency ranges from a decrease of 15 percent to an increase of 290 percent. Two

hydrodynamics models are used: the Advanced Circulation (ADCIRC) model (Luettich et al. 1992) and the Sea, Lake, and Overland Surges from Hurricanes (SLOSH) model (Jelesnianski et al. 1992). The SLOSH simulation (~ 1 km resolution) is used to select the extreme surge events, which are further analyzed with higher-resolution (~10 m) ADCIRC simulations to estimate the probability distributions of NYC surges.

Driven by the reanalysis for the present conditions, Figure 5.10 shows examples of storm surge simulated around the NYC area for two worst-case scenarios at Battery driven by a northeastward moving storm (Figure 5.10a) and a weaker but larger storm with a northwestward translation (Figure 5.10b). The estimated present 50-yr storm surge is about 1.24 m, the 100-yr surge is about 1.74 m and the 500-yr surge is about 2.78 m. For simulations driven by the GCMs for the present and future climate, Figure 5.11 shows the diverse storm tide return levels at Battery associated with each GCM projecting increase, decrease, and no change in the storm tide return levels. These discrepancies can be attributed to the models' different estimations of the change of the storm frequency and the surge severity, which depends not only on storm intensities that are projected to increase by the hurricane model driven by all GCMs, but also other aspects of storms. Uncertainty is noted by Lin et al. (2012) regarding the storm's radius of maximum wind (R_m) and storm's outer radius (R_o, which was assumed to be constant in the simulation). For the CNRM and GFDL models, the 100-yr and 500-yr storm tide levels will increase by about 0.7 – 1.2 m by the end of the century, which is comparable to the sea-level rise of 0.5 – 1.5 m projected for the region, so changes in storm climatology play an important role in increased storm surge in the future. Figure 5.12 shows the flood height simulated by the hurricane/hydrodynamic models driven by each GCM when sea-level rise of 1 m is considered. Adding sea-level rise, flood height is projected to increase in all simulations and the combined effect of storm climatology change and sea-level rise will greatly shorten the surge flooding return periods. For example, the present New York 100-yr surge flooding may occur every 20 yr or less and the present 500-yr surge flooding may occur every 240 yr or less.

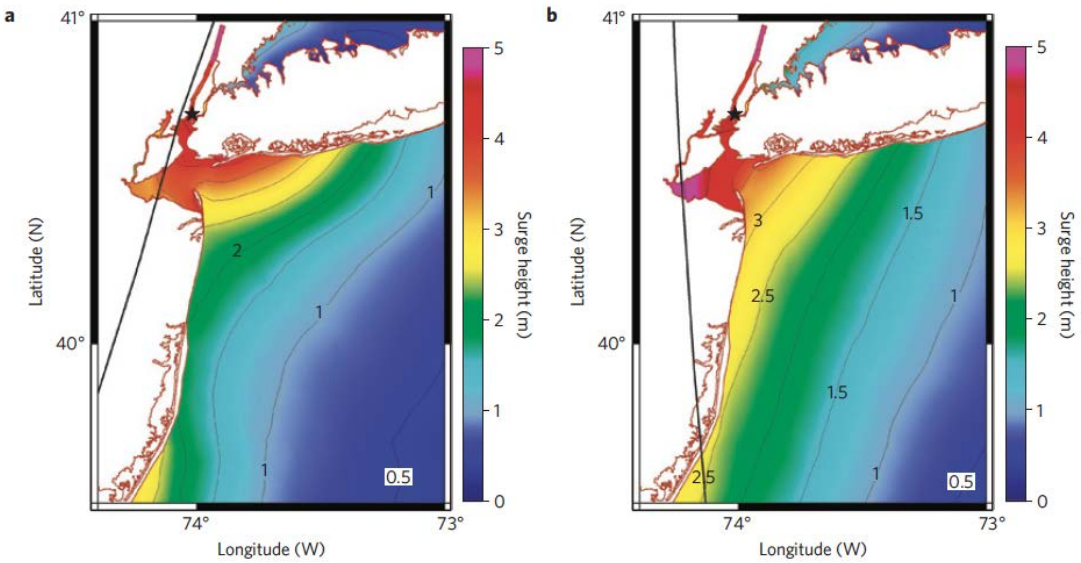

Figure 5.10. Two worst-case surge events for the Battery, under the reanalysis climate. The contours and colors show the surge height (m). The black curve shows the storm track. The black star marks the location of the Battery. The storm parameters when the storm is closest to the Battery are as follows. a, Storm symmetrical maximum wind speed V_m = 56.6 ms^{-1}, minimum sea-level pressure P_c = 960.1 mb, radius of maximum wind R_m = 39.4 km, translation speed U_t = 15:3ms^{-1} and distance to the site d_s = 3.9 km. b, V_m = 52.1 ms^{-1}, P_c = 969.2 mb, R_m = 58.9 km, U_t = 9.7ms^{-1} and d_s = 21.1 km. (Source: Lin et al. 2012.)

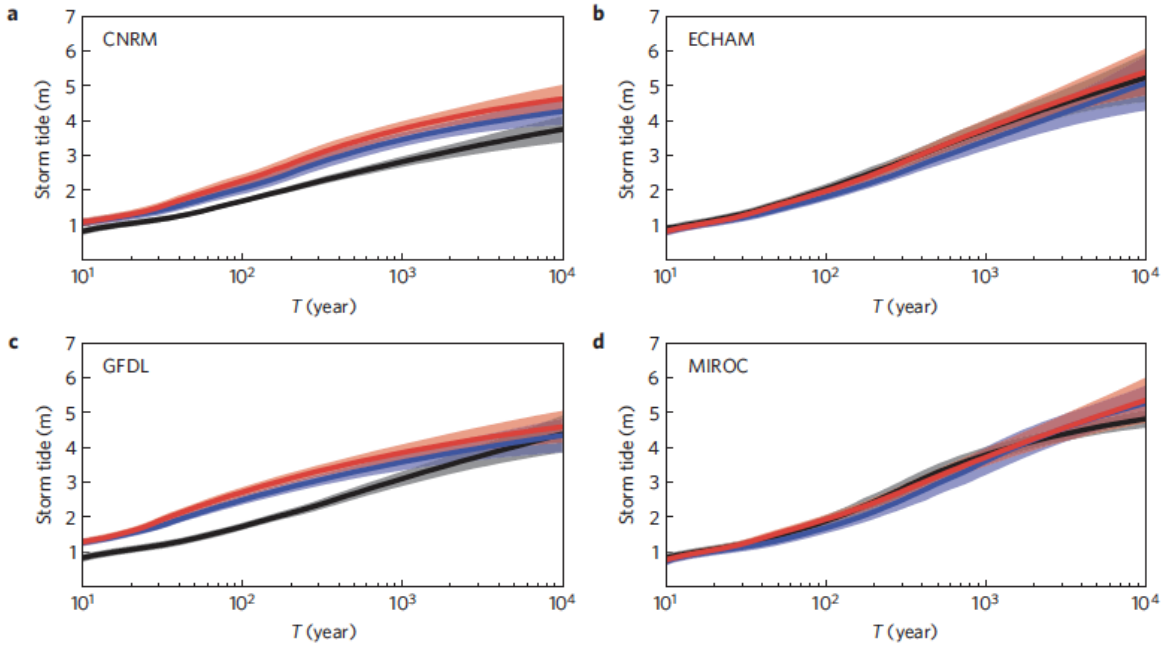

Figure 5.11. Estimated storm tide return levels for the Battery, predicted with each of the four climate models. The black is for the present climate, the blue is for the IPCC A1B climate and the red is for the IPCC A1B climate with R_o increased by 10 percent and R_m increased by 21 percent. The shade shows the 90 percent confidence interval. (Source: Lin et al. 2012.)

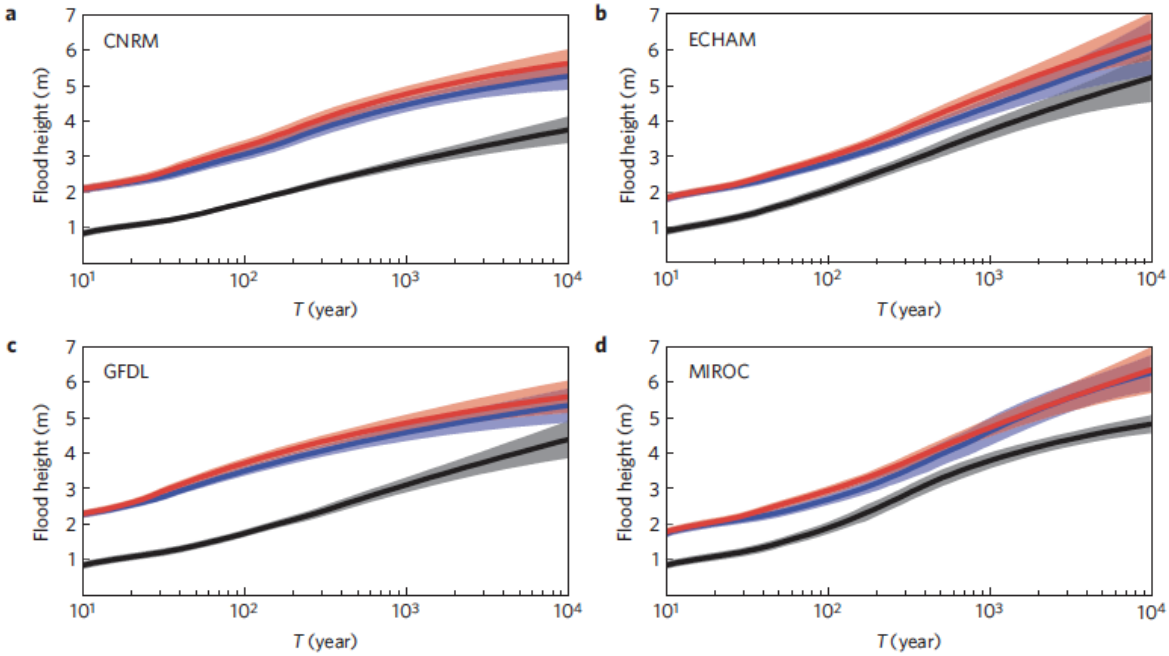

Figure 5.12. Estimated flood return levels for the Battery, predicted with each of the four climate models. The black is for the present climate, the blue is for the IPCC A1B climate and the red is for the IPCC A1B climate with R_o increased by 10 percent and R_m increased by 21 percent. The shade shows the 90 percent confidence interval. The sea-level rise for the A1B climate is assumed to be 1 m. (Source: Lin et al. 2012.)

Hurricane Sandy generated the highest recorded water level (3.4 m) at New York Harbor in at least 300 years, due to sustained strong easterly winds and a storm surge maximum (2.8 m) coinciding with high tide (Colle et al. 2015; Orton et al. 2016). Hence Sandy has been used as in many case studies to anticipate that may happen in the future if a Sandy-like hurricane happens again. Using a similar methodology of Lin et al. (2012), Lin et al. (2016) investigated how Hurricane Sandy's flood frequency varies in response to the sea level and storm activities due to climate change between 1800 and 2100. More specifically the simulations produced by Lin et al. (2012) with the hurricane/hydrodynamic models driven by reanalysis and 4 GCMs were again utilized, except that the GCM estimates of storm frequency for the same period as the reanalysis (1981-2000) were bias-corrected, and the same bias-correction was applied to the projections for 2081-2100. This way, the reanalysis driven simulation was used to represent the period of 2000 and the GCM driven simulations were used to represent the period of 2100. Assuming no change in storm climatology between 1800 and 2000, another simulation was performed using the reanalysis storm climatology and the sea level of 1800 to represent the period of 1800. The year 2000 was set as the baseline with regional sea level (RSL) set to 0. Sea-level projections were produced following the RCP4.5 (similar to A1B) scenario every decade from 2000 to 2100. Past RSL from 1800 to 2000 for NYC was estimated based on a spatiotemporal empirical model. Astronomical tide was not considered in this study. Different from Lin et al. (2012), statistical storm size variation was considered in the analysis.

Figure 5.13 compares the flood height for different return periods for three periods: 1800, 2000, and 2100. With the reanalysis (National Center for Environmental Prediction - NCEP) storm climatology, results are shown for three periods that differ only due to sea-level changes. For 2100, results are shown for the 4 GCMs discussed in Lin et al. (2012). The return period of a storm surge of a Sandy-like storm (2.8 m) is 398 y in 2000, which is lower than the estimate in Lin et al. (2012) that neglected storm size variation. There is a substantial shift of the flood return period curve from 1800 to 2000, and the shift is even larger to 2100. Considering only the effect of RSL rise, the return period of Sandy's flood height is estimated to be ~ 1,200 y in 1800 and ~ 90 y in 2100. Considering both RSL rise and storm surge climatology change, the return period of Sandy's flood height in 2100 becomes ~ 23 y to 130 y, depending on the GCMs. The Sandy flood height is estimated to be about 2.3 m in 1800 and 3.7 m in 2100 if only RSL rise is considered, but the flood height becomes 3.5 to 4.3 m in 2100 if the change in storm climatology is also accounted for.

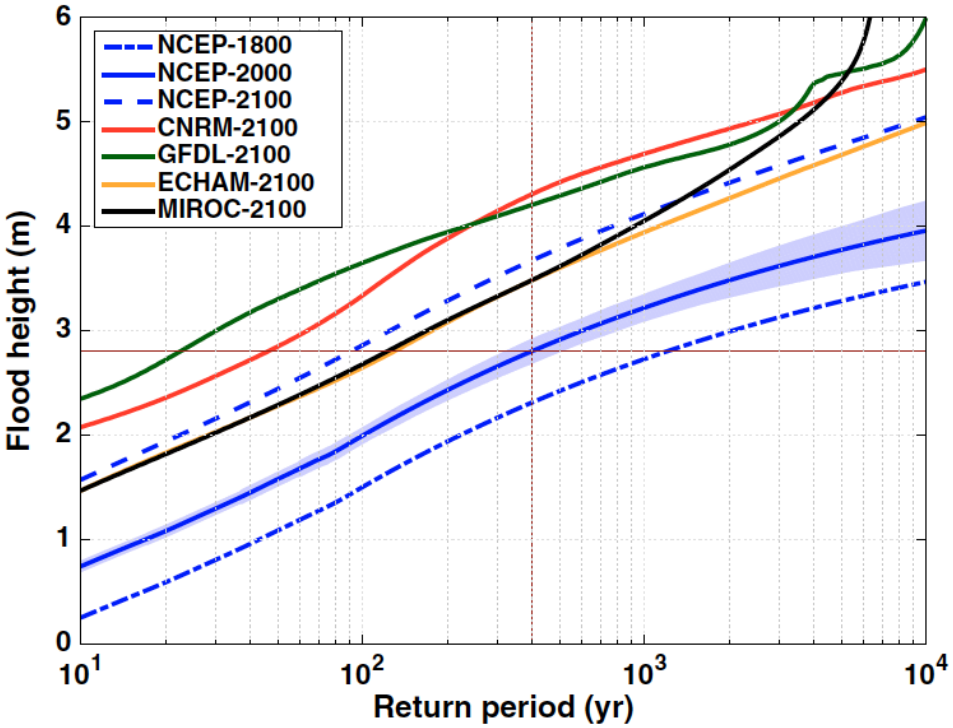

Figure 5.13. Return periods of flood heights (relative to the mean sea level of the baseline year 2000) in NYC, estimated for years 1800, 2000, and 2100. The solid blue curve shows the return period of flood heights (also storm surges as RSL = 0 m) for year 2000, estimated based on NCEP reanalysis. Other solid curves show the return period of flood heights for 2100, based on the projected RSL distributions and surge climatology projected by the various climate models (CNRM-CM3, GFDL-CM2.0, ECHAM5, and MIROC3.2). The dashed blue curve shows the return period of flood heights for 2100 based on the projected RSL of 2100 and the NCEP surge climatology (of 2000, neglecting the change of surge climatology from the baseline). The dash-dotted blue curve shows the return period of flood heights for 1800 based on the estimated RSL of 1800 and the NCEP surge climatology (of 2000, neglecting the change of surge climatology). The blue shading shows the 90 percent confidence interval of the 2000 NCEP curve (the statistical confidence interval for the other curves is similar). The red dashed lines highlight Sandy's flood height of 2.8 m (horizontal) and Sandy's estimated return period in 2000 of 398 y (vertical). (Source: Lin et al. 2016.)

Evolution of the return period (398 y) and flood height (2.8 m) of Sandy from 1800 to 2100 is shown in Figure 5.14. Estimated temporal evolution of Sandy's return period and flood height and of RSL from year 1800 to 2100 (relative to the sea level of the baseline year 2000). (Top) Return period of Sandy's flood height of 2.8 m. (Middle) Flood height with Sandy's estimated return period of 398 y (in 2000). As in Figure 5.13~~Figure 5.14. Estimated temporal evolution of Sandy's return period and flood height and of RSL from year 1800 to 2100 (relative to the sea level of the baseline year 2000). (Top) Return period of Sandy's flood height of 2.8 m. (Middle) Flood height with Sandy's estimated return period of 398 y (in 2000). As in Figure 5.13~~, based on RSL values (RSL = 0 at 2000) also shown in the same figure. As RSL increased by 50±8 cm between 1800 and 2000, the mean GSL rose by about 13 cm to 18 cm. As discussed in Section 5.1, the higher-than-GSL in NYC is related to GIA and ocean dynamics. The projected RSL rise in NYC is higher than the mean GSL. Figure 5.14. Estimated temporal evolution of Sandy's return period and flood height and of RSL from year 1800 to 2100 (relative to the sea level of the baseline year 2000). (Top) Return period of Sandy's flood height of 2.8 m. (Middle) Flood height with

Sandy's estimated return period of 398 y (in 2000). As in Figure 5.13~~Figure 5.14. Estimated temporal evolution of Sandy's return period and flood height and of RSL from year 1800 to 2100 (relative to the sea level of the baseline year 2000). (Top) Return period of Sandy's flood height of 2.8 m. (Middle) Flood height with Sandy's estimated return period of 398 y (in 2000). As in Figure 5.13~~ shows that the frequency and magnitude of NYC's extreme floods may increase dramatically over time, due to the compound effects of sea-level rise and storm climatology change. The authors noted that the absolute value of the return period of Sandy-like storm may be overestimated because the hurricane model does not account for the effect of extratropical transition. Since a significant portion of TCs moving into the high latitudes of the U.S. Atlantic coast undergo extratropical transition (Hart et al. 2001), improving understanding of extratropical transition is important for projecting future changes in storm surge in the northeast region.

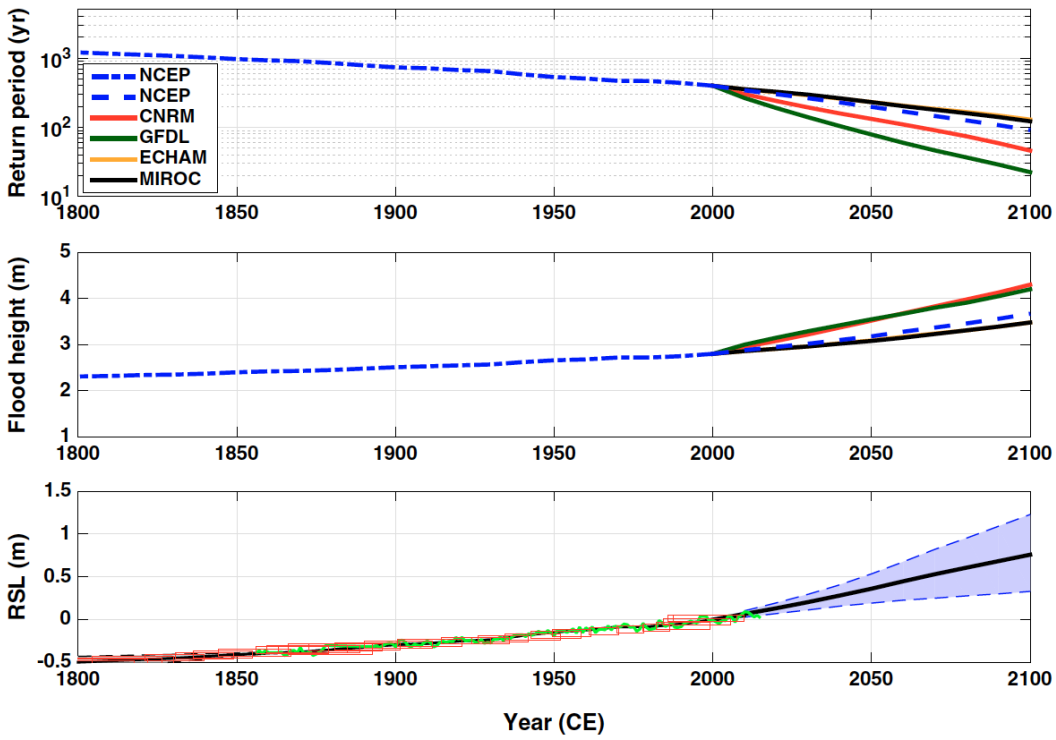

Figure 5.14. Estimated temporal evolution of Sandy's return period and flood height and of RSL from year 1800 to 2100 (relative to the sea level of the baseline year 2000). (Top) Return period of Sandy's flood height of 2.8 m. (Middle) Flood height with Sandy's estimated return period of 398 y (in 2000). As in Figure 5.13, solid curves show the estimates accounting for the change in both RSL and surge climatology, and dashed and dash-dotted blue curves show the estimates accounting for only the change in RSL. (Bottom) Estimated past and projected future RSL (black solid curve, mean; shading, 5 to 95 percent quantile range). Annual mean sea level observed at the Battery tide gauge is shown by the green curve, and the proxy reconstruction from Barnegat Bay is represented by the red rectangles, showing 2σ vertical and geochronological uncertainties. (Source: Lin et al. 2016.)

Using a similar methodology of Lin et al. (2012, 2016) involving a hurricane model and a hydrodynamics model, Reed et al. (2015) studied the increased threat of TCs and coastal flooding to NYC during the anthropogenic era (1975-2005) compared to the pre-anthropogenic era (850-1800). Three CMIP5 models

were used to drive the hurricane/hydrodynamics models. With sea-level rise from 850 to the anthropogenic era, storm flood heights in NYC increased by ~1.24 m. With changes in sea level and TC characteristics, flood risk has greatly increased from the 500-y return period for a ~2.25 m flood height during the pre-anthropogenic era decreasing to ~24.4 y return period in the anthropogenic era. Interestingly, ignoring the storm surge height simulated by the hurricane/hydrodynamics models driven by the three GCMs does not show noticeable change between the pre-anthropogenic and anthropogenic eras, except for a longer tail in the probability distribution of storm surge height in the anthropogenic era, which is related to an increase in the radius of maximum winds, lower minimum pressures, and higher maximum winds than storms in the tail of the pre-anthropogenic era.

Garner et al. (2017) extended the analysis of Reed et al. (2015) by including more CMIP5 models, looking at coastal flooding out to 2300, and including analysis that considered the potential partial collapse of the Antarctic ice sheet in the future. Based on the same three GCMs used in Reed et al. (2015), they found that the return periods of storm surge in NYC have little change or even slight increase from the present (1970-2005) to the future (2010-2300). This is consistent with the finding of Reed et al. (2015) that the storm surge height changes little between the pre-anthropogenic era and anthropogenic era. Including more CMIP5 models did not change the conclusion. Further analysis showed that storm intensity was projected to increase from the present to the future; however, the CMIP5 GCMs projected changes in the density of TC tracks shifted offshore (Figure 5.15). Hence the effect of increased storm intensity was compensated by the change in TC tracks. The latter is consistent with the changing patterns of sea-level pressure, favoring an eastward shift of TC tracks, away from NYC (Figure 5.16A). For one of the models (IPSL) that included simulation out to 2300, the pressure differences are found to intensify by the end of the 23rd century (Figure 5.16B). Hence, different from Lin et al. (2012, 2016) who found an increase in storm surge height due to changes in TC climatology projected by CMIP3 models for the future, Garner et al. (2017) found little change in the storm surge height using CMIP5 models that projected a compensation between increased storm intensity and reduced TC track density impacting NYC.

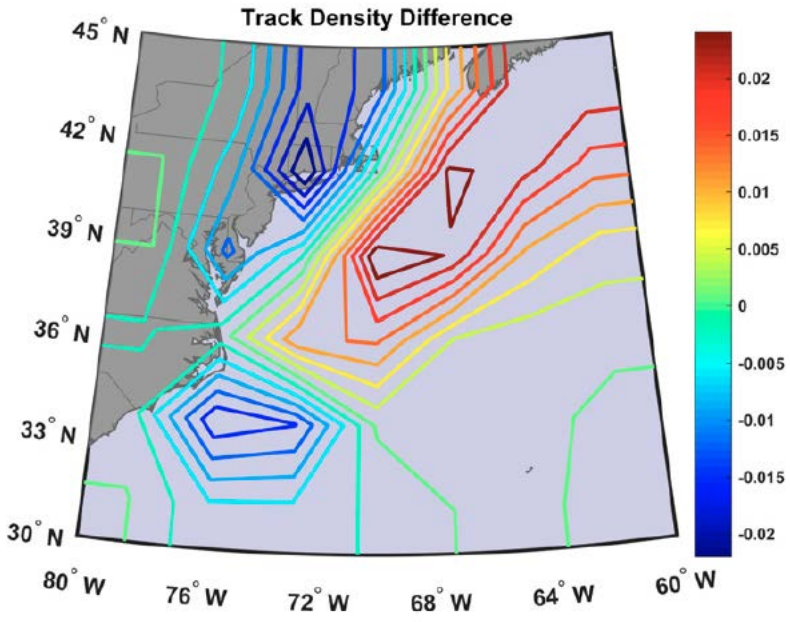

Figure 5.15. Multimodel mean difference between future and modern synthetic TC track densities from the MPI, CCSM4, and IPSL models. Track densities are determined by the sum total of tracks crossing through each grid box over 20-y periods from 2080–2100 and 1980–2000,

divided by the area of that grid box and the number of years (21). Here the grid box latitude–longitude scales are determined by the output resolution of the model in question. (Source: Garner et al. 2017)

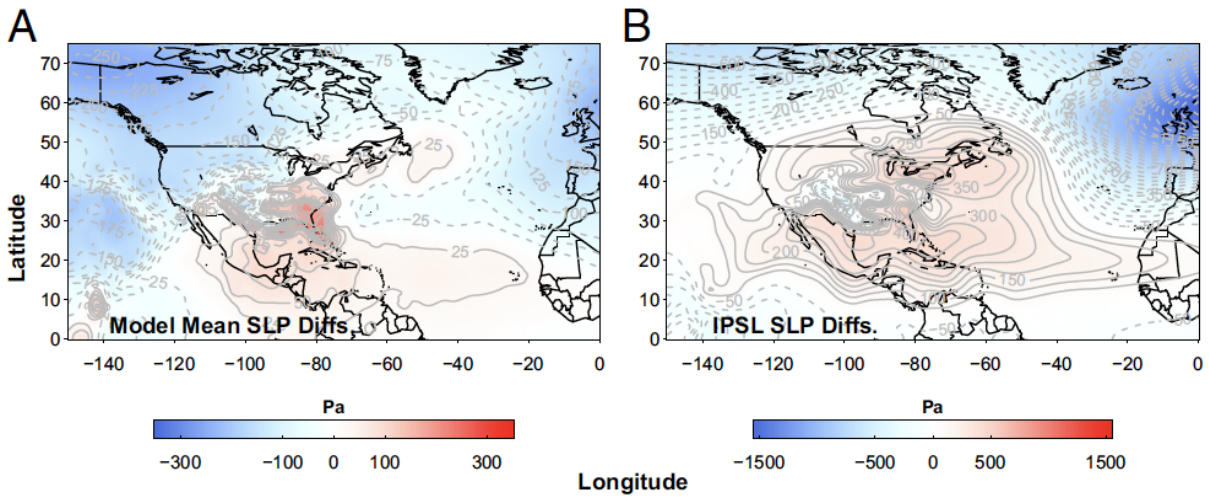

Figure 5.16. Mean August and September sea-level pressure (SLP) differences. Pressure differences (pascals) are between (A) 2080–2100 and 1980–2000 for all three models and (B) 2280–2300 and 1980–2000 for the IPSL model. Color bars show the range of SLP differences. (Source: Garner et al. 2017.)

Figure 5.17 shows the probability density function of flood height at the Battery tide gauge in NYC in 2100 (Figure 5.17A-C) and 2300 (Figure 5.17D) under both RCP4.5 and RCP8.5. These projections used two future SLR probability distributions – those based on Kopp et al. (2014) discussed in Section 5.1, and replacing the Antarctic ice-sheet (AIS) projections of Kopp et al. (2014) with a small ensemble generated by DeConto and Pollard (2016) that incorporated marine ice-sheet instability, ice-cliff collapse, and ice-shelf hydrofracturing mechanisms. With SLR, flood height shifts significantly to higher values in 2080-2100 (mean = 0.7-1.4 m higher than present) and 2280-2300 (mean = 2.4-13 m higher than present).

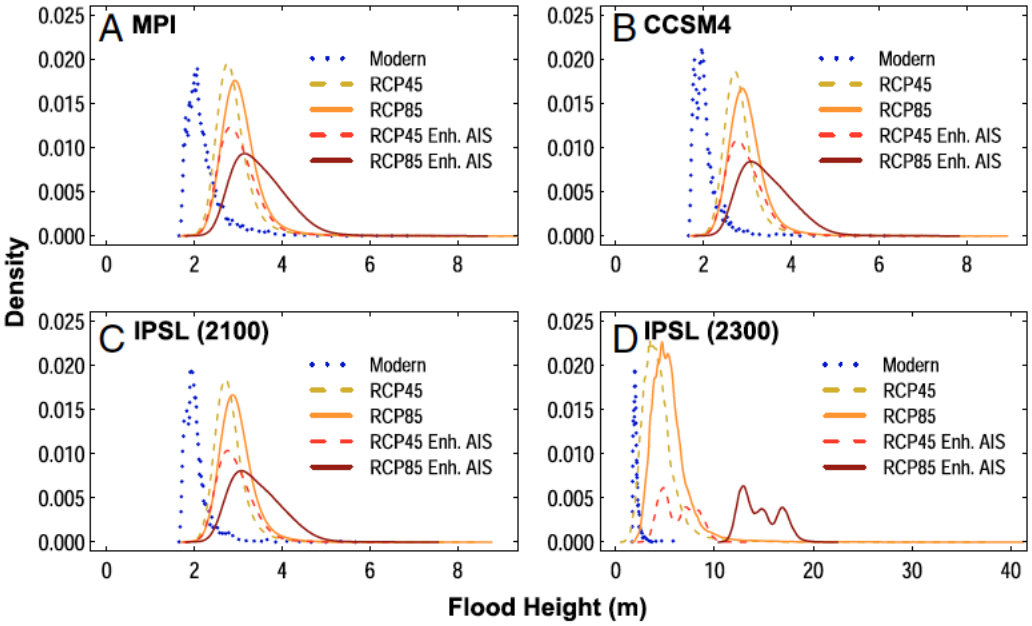

Figure 5.17. Normalized distributions of flood heights at the Battery tide gauge in NYC. Distributions are for the modern (1970–2005) and future eras for flood heights calculated using the RCP4.5 and RCP8.5 SLR projections (Kopp et al. 2014) and for flood heights calculated by combining enhanced AIS contributions (DeConto and Pollard 2016) with the RCP4.5 and RCP8.5 SLR projections (Kopp et al. 2014). Results are shown for future scenarios for (A) the MPI model, (B) the CCSM4 model, (C) the IPSL model, and (D) the IPSL model to 2300. (Source: Garner et al. 2017.)

The studies summarized above focused on coastal flooding resulting from TC-induced storm surges combined with SLR. Wahl et al. (2015) investigated the potential of flooding related to co-occurrence of storm surge and heavy precipitation in major U.S. cities. They considered three mechanisms for flooding due to the compound events: (1) joint occurrence of storm surge and heavy precipitation in estuarine regions may elevate water levels to initiate or exacerbate flooding; (2) a destructive storm surge already causes widespread flooding so any significant rainfall on top of this event increases flood depth and/or flood extent; (3) a moderate storm surge does not directly cause flooding but is high enough to fully block or slow down gravity-fed storm water drainage, such that precipitation is more likely to cause flooding. These mechanisms were investigated in two cases by searching for the highest annual storm surge and then take the highest precipitation within a time range of ± 1 day of this event (covers mechanisms 1 and 2) for Case I, and searching for the highest annual precipitation, and then take the highest storm surge within a time range of ± 1 day (covers mechanism 3) for Case II.

Figure 5.18 shows the correlation coefficient between storm surge and heavy precipitation for Case I and Case II. For Case I, significant correlation (τ) between storm surge and heavy precipitation associated with a higher likelihood of compound flooding for all sites along the Gulf and east coast (Figure 5.18b). For Case II, significant correlation is confined to the Gulf and southeast coast, NYC, and three sites on the west coast. Calculating the temporal changes in τ using 50-year moving windows, an increasing trend of τ for Case I is identified for several cities including NYC and Boston in the northeastern U.S. Much of the observed increasing trend of τ is due to higher incidence of joint events in the upper tail region of their probability distribution so they are highly relevant for flood risk and design.

More analysis of the data from NYC revealed that most compound flooding events from the past three to four decades lie close to the diagonal (high correlation between storm surge and heavy precipitation) but many of the earlier events are widely scattered (Figure 5.19a and b). TC events were identified and marked as solid squares, which exhibit strong concordance between high storm surge and heavy precipitation. An exception is Hurricane Sandy (red square in the upper left of Figure 5.19a), which induced flooding mainly by storm surge due to the unusual impact angle, with small rainfall amount. Compositing the sea-level pressure and winds of storm surge events with high and low precipitation amount shows that storm surges in NYC are accompanied by heavy precipitation when a high-pressure system stretches from Newfoundland south over the North Atlantic from where moist air is transported into the low-pressure system causing the storm surge (Figure 5.19c and d). Similar synoptic patterns can also be found for storm surge events in Boston with heavy precipitation (not shown). Using the synoptic patterns of Figure 5.19c and d as the reference environments favorable for compound events (storm surge and heavy precipitation), a pattern correlation can be calculated for the events in Case I and Case II to determine if they occurred in an environment favorable for compound events. The ratio of compound to non-compound events increases from 2.7 to 5 in the first and last 30-year periods for Case I and from 2.8 to 3.5 for Case II. This analysis confirmed that weather patterns favoring co-occurrences of storm surge and heavy precipitation have dominated the storm surge climate in NYC over the past few decades.

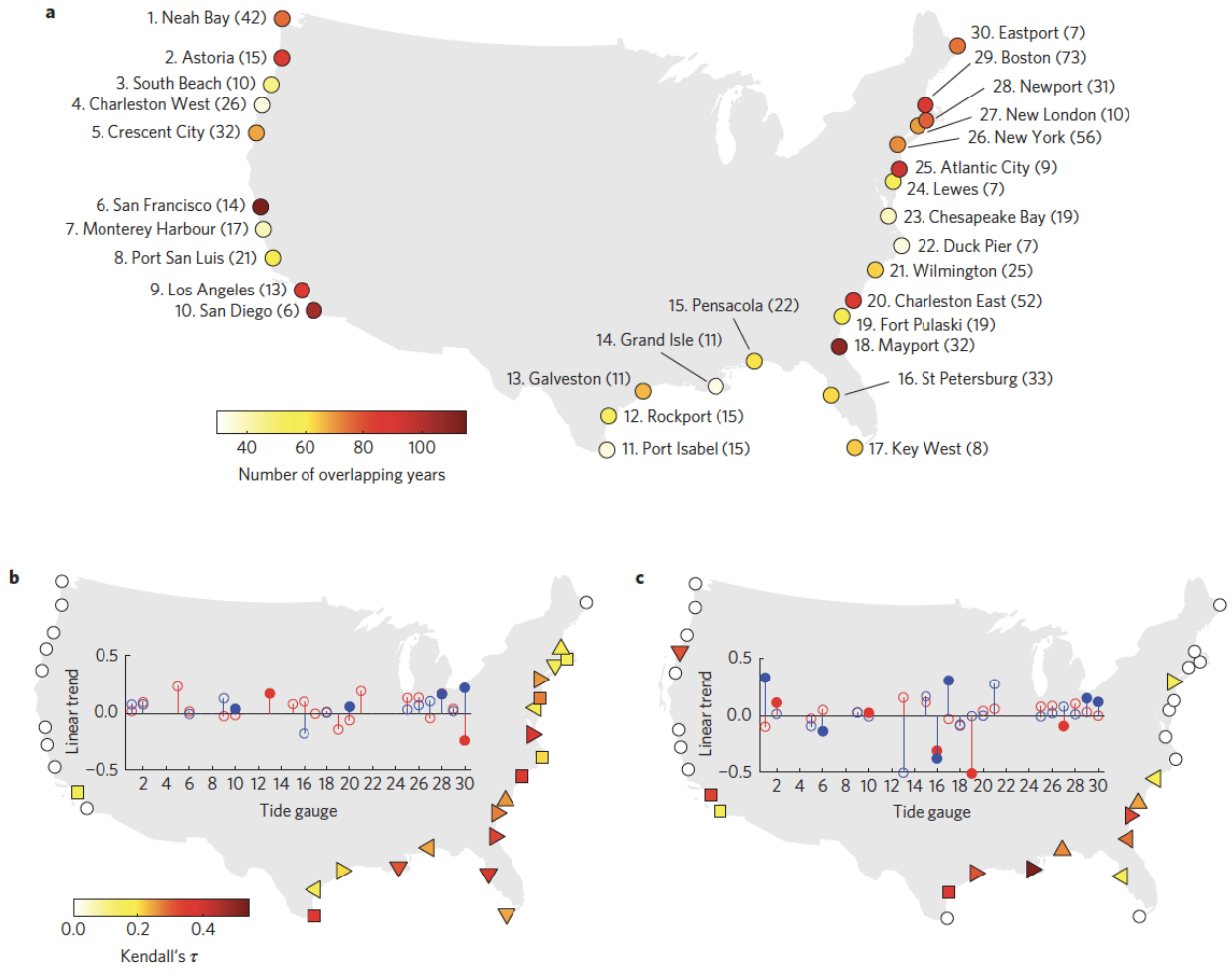

Figure 5.18. a, Tide gauge (TG) locations; color represents the number of overlapping years between storm surge and precipitation time series, numbers in brackets denote the number of precipitation stations in a radius of 25 km around the TGs. b,c, correlation coefficient (τ)

for Cases I (b) and II (c); markers denote the selected copula type (square is Frank; triangles pointing right, left, up and down are Gumbel, Clayton, Galambos and Hüsler-Reiss, respectively). Insets show linear trends for the storm surge (red; unit is cm yr^{-1}) and precipitation (blue; unit is $mmyr^{-1}$) time series for Cases I (b) and II (c) for all sites used in the non-stationary analysis. Open circles denote insignificant correlations or trends (90 percent confidence). (Source: Wahl et al. 2015.)

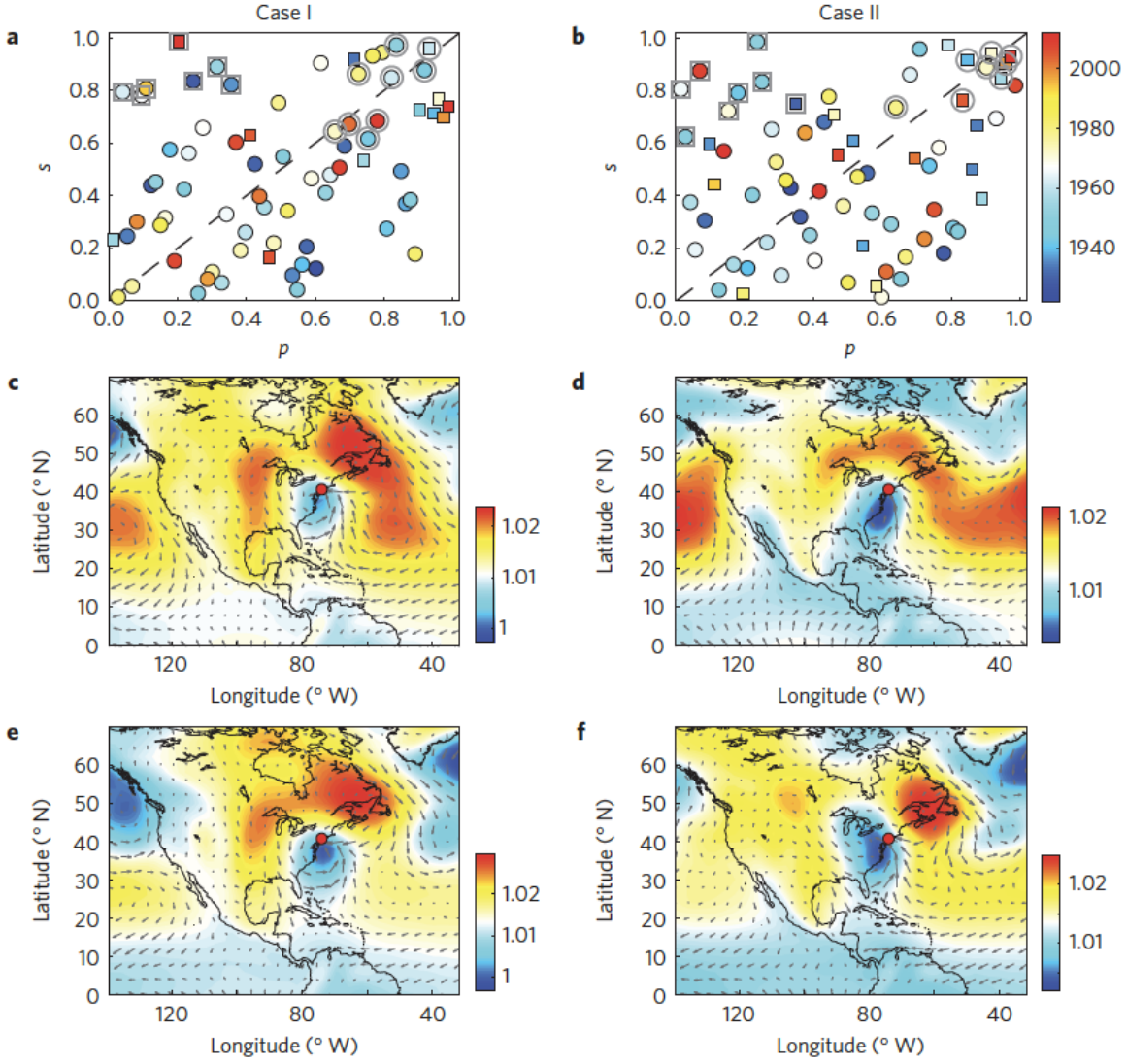

Figure 5.19. a,b, Rescaled pairs of ranks of storm surge (s) and precipitation (p); filled squares are tropical events; framed events were used for the composite plots; color denotes the year of occurrence. c–f, Composite plots of SLP (unit is $Pax10^5$) and wind for events with high storm surge and high precipitation (c,d; circle frames in a,b) and high storm surge and low precipitation (e,f; square frames in a,b). Case I (a,c,e); Case II (b,d,f). The NYC tide gauge location is shown by the red dot. (Source: Wahl et al. 2015.)

6.0 Great Lakes

Great Lakes water levels, including observed and projected changes in them were described in the Year 3 report that focused on the midwest region. In this chapter, we add to the Year 3 report discussion by describing water levels in Lake Ontario as it is affected by hydroclimatology of its contributing watersheds.

6.1 Hydrologic Characterization of Lake Ontario Watershed

Lake Ontario is the fifth largest of the Great Lakes with a water surface area of 7,340 mi^2 (GLERL 2019). Lake Ontario has a volume of 393 mi^3 and its retention time is estimated to be 6 years. Its shoreline length is 712 mi. The drainage area that contributes to Lake Ontario is about located both in the United States and Canada (Figure 6.1).

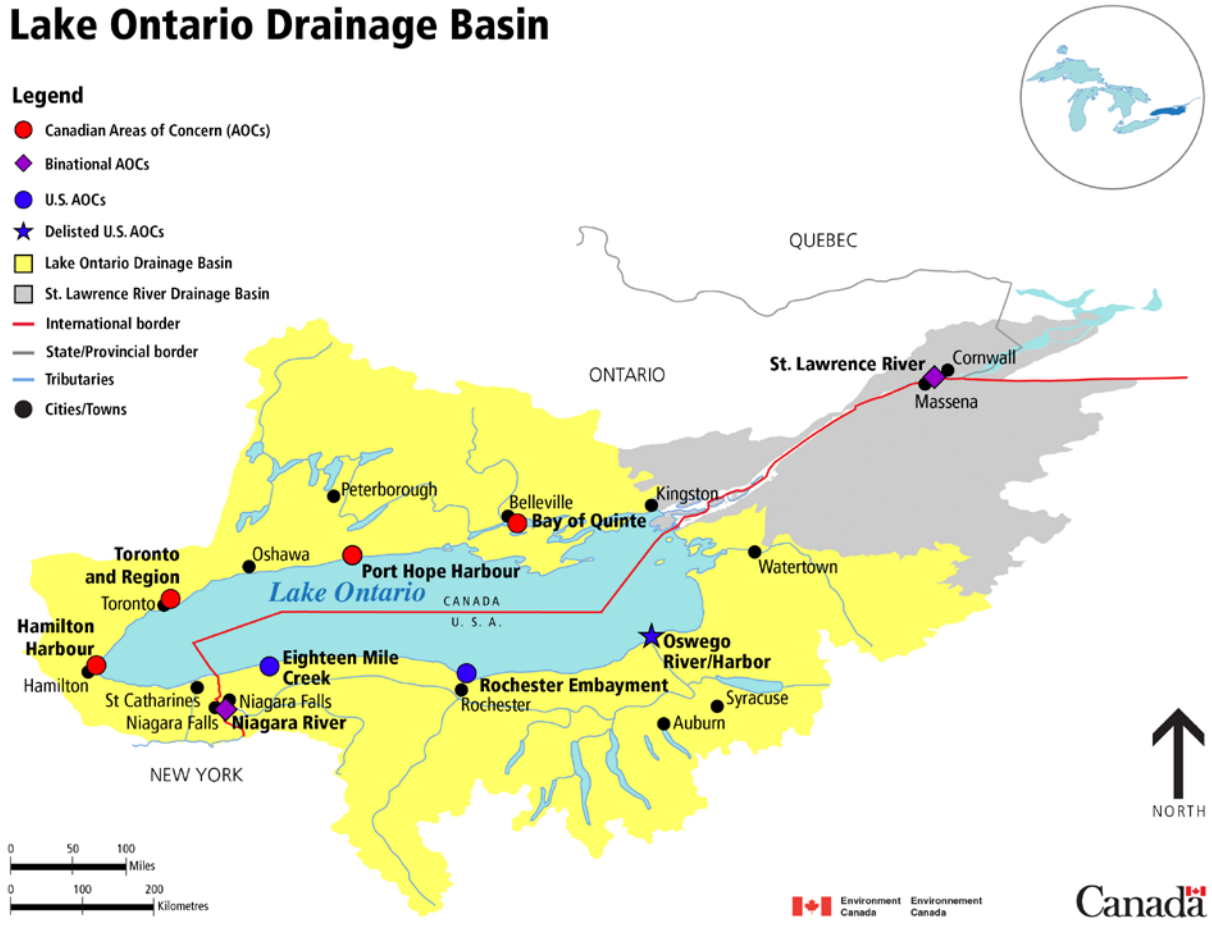

Figure 6.1. Lake Ontario drainage basin. (Source: Environment Canada.)

The Great Lakes Runoff Inter-Comparison Project for Lake Ontario (GRIP-O) was described by Gaborit et al. (2017a). The GRIP-O experiment used a time period from June 1, 2004 to September 26, 2011. The goal of GRIP-O was to compare different hydrologic models in their ability to estimate runoff for the

Lake Ontario watershed. Many of the tributaries that contribute to Lake Ontario have regulated flows. A significant part of the watershed is ungauged (Figure 6.2).

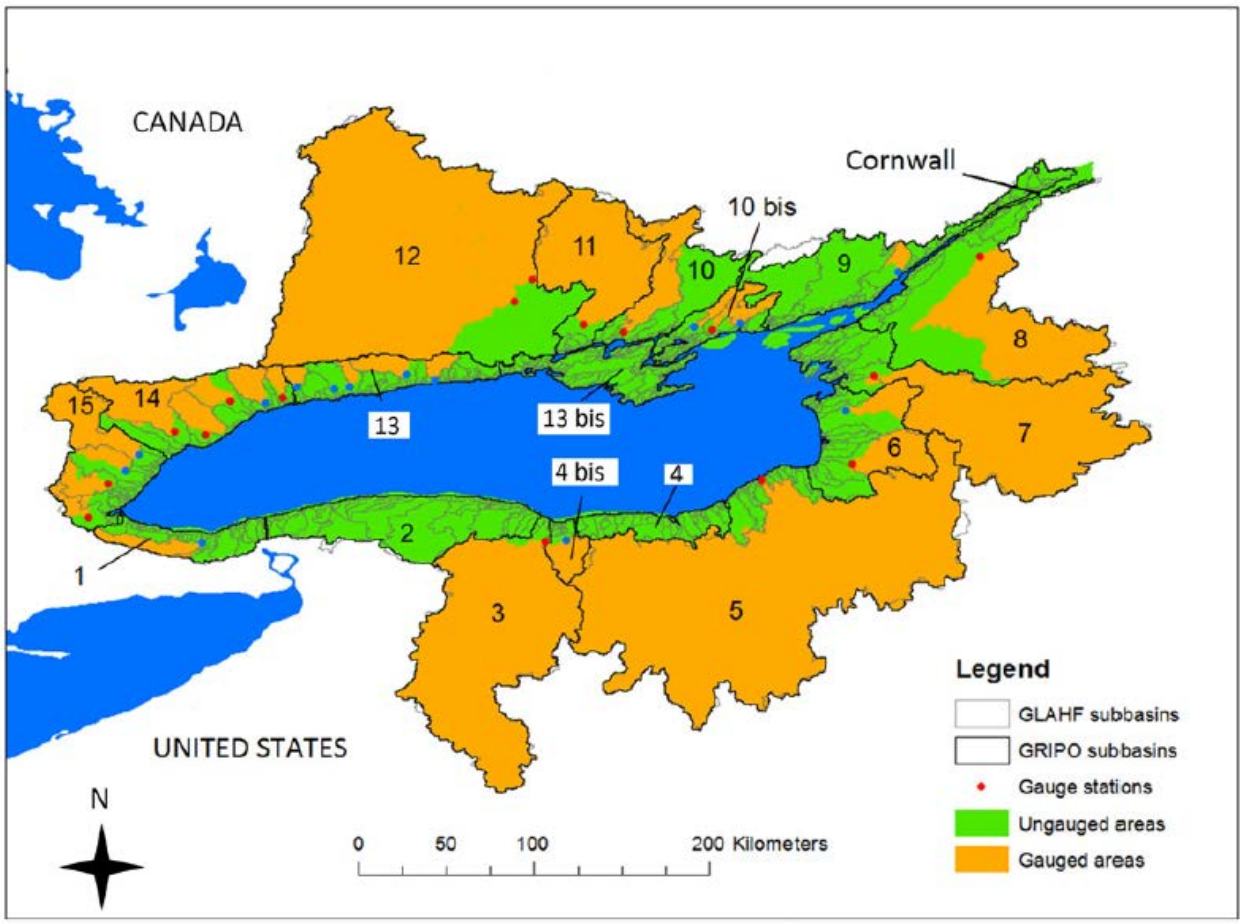

Figure 6.2. Gauged and ungauged areas of the Lake Ontario watershed. GRIP-O subbasins and the Great Lakes Aquatic Habitat Framework (GLAHF) subbasins are also shown. Th outlet of the Lake Ontario watershed is located at Cornwall, Ontario, Canada. (Source: Gaborit et al., 2017a.)

GRIP-O used two sources of precipitation data: (1) Canadian Precipitation Analysis (CaPA) and (2) Global Historical Climatalogy Network – Daily (GHCND). Two lumped hydrologic models were used: (1) GR4J (modèle du Génie Rural à 4 paramètres Journalier; Perrin et al. 2003) and (2) LBRM (Large Basin Runoff Model; Croley and He 2002). GR4J is a daily continuous model with four free parameters and consists of two reservoirs that represent the soil storage and basin routing. Runoff is estimated using unit hydrograph approach. A two-parameter snow model is also used with GR4J. LBRM is also a daily continuous model and includes a snow model. LBRM has nine free parameters. Both models use daily watershed average precipitation, minimum and maximum temperatures, and watershed area as input. GR4J also needs mean watershed latitude, which is used in the evapotranspiration estimation and mean watershed elevation. The snow model used with GR4J can use up to five elevation classes. Gaborit et al. (2017a) used a 4.5-year period starting June 1, 2007 as the model calibration period. The models were validated using 2 years of data starting June 1, 2005. Out of the four combinations of models and data sources (the two models intput with the two data sources), the GR4J model input with GHCND dataset performed the best (Gaborit et al. 2017a).

To determine the best approach for estimating runoff for the entire Lake Ontario drainage basin, Gaborit et al. (2017a) implemented a GR4J model for the entire drainage area represented as a single watershed. This model was input using weighted average precipitation and temperature of all subbasins and model output was compared with the sum of local subbsins' discharges. The authors reported that this model performed very well—better than the performances of the local subbasin models (Figure 6.3). The authors attributed this observation to local model biases being compensated in the aggregated model.

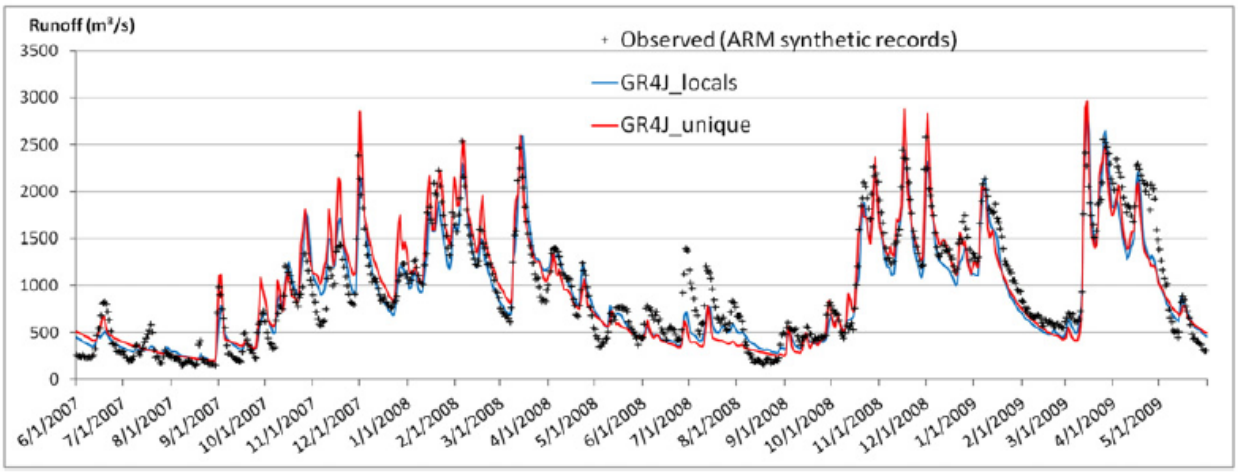

Figure 6.3. Comparison of model predictions with observed runoff data. GR4J_locals refers to basinwide runoff estimated by summing the GR4J local subbasin model predictions and GR4J_unique refers to basinwide runoff estimated by the GR4J model implemented for the entire Lake Ontario watershed. ARM stands for area-ratio method. (Source: Gaborit et al. 2017a.)

Gaborit et al. (2017b) described the development of a methodology to perform reliable streamflow simulations with a spatially distributed model, Global Environmental Multi-Scale (GEM)-Hydro, for the Lake Ontario drainage basin. GEM-Hydro contains the Soil, Vegetation, and Snow (SVS) land-surface scheme and the WATROUTE routing scheme. The authors compared three models in the study: GEM-Hydro, Modélisation Environnementale – Surface and Hydrology (MESH), and WATFLOOD. All three models have the same routing scheme, WATROUTE. However, they differ in land-surface schemes. MESH relies on the Canadian Land-Surface Scheme, in which each grid cell is subdivided into a number of tiles with each tile assigned one of five grouped response units (GRUs) based on land use and soil type combination. GEM-Hydro uses SVS. WATFLOOD does not solve energy balance, just the water balance and is therefore not considered to have a land-surface scheme. GEM-Hydro used a 10-arcminute (~20 km) resolution for its land-surface scheme and a 0.5-arcminute (~1 km) resolution for routing. MESH and WATFLOOD were implemented with a 10-arcminute resolution. Because GEM-Hydro was computationally demanding another version, in which WATROUTE was replaced by a unit hydrograph formulation. The version of the model was called GEM-Hydro-UH. The authors reported that simulated hydrographs from GEM-Hydro and GEM-Hydro-UH were very similar.

Gaborit et al. (2017b) used the study area shown in Figure 6.2. Physiographic data required by the models and respective sources and resolutions are shown in Table 6.1. The models were calibrated using the June 1, 2007 to September 26, 2011 time period with a one-year model spin-up period. Validation was performed using the June 1, 2005 to June 1, 2007 time period, also with a one-year spin-up period. The dynamically dimensioned search algorithm (Tolson and Shoemaker 2007) was used for calibrating all models.

Table 6.1. Physiographic data, sources, and resolutions used by Garborit et al. (2017b).

Dataset/origin	Type of data	Coverage	Resolution/scale
GSDE	Soil texture	Global	~1 km (30″)
GLOBCOVER 2009	Land cover	Global	300 m (10″)
HydroSheds	Flow directions	Global	~1 km (30″)
SRTM	DEM	Global	90 m (3″)
HyDAT	Gauge stations	CAN	NAm
NWIS	Gauge stations	US	NAm
CaPA v2.4b8	Precipitation	n/a	~15 km
RDPS	Atmospheric forcings	NAm	15/10 km

GEM-Hydro-UH was calibrated using multipliers that adjust parameters spatially but together, resulting in a set of 16 free parameters. MESH was calibrated with 12 free parameters for each of the 5 GRUs, resulting in a set of 60 free parameters. WATFLOOD had 14 free parameters. Because of high computational cost, GEM-Hydro-UH, MESH, and WATFLOOD were only calibrated for seven, two, and three GRIP-O subbasins, respectively. Gaborit et al. (2017b) reported that WATFLOOD showed a flashy behavior, MESH underpredicted flows, and GEM-Hydro-UH was somewhere in the middle of the other two models. The authors concluded that GEM-Hydro-UH outperformed the other two models both in calibration and in validation.

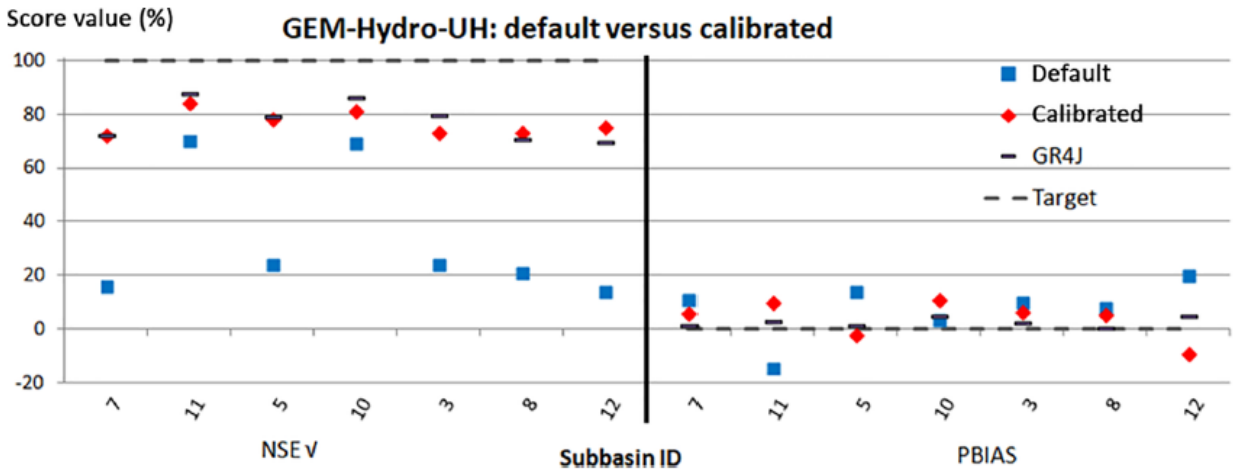

Figure 6.4. Performance of uncalibrated (default parameter values) and calibrated GEM-Hydro-UH. "NSE √" represents the Nash-Sutcliffe efficiency calculated using the logarithm of discharges and PBIAS is computed using observed and simulated flow values. Both measures are reported in percentages. GR4J refers to the model used in Gaborit et al. (2017a). (Source: Gaborit et al. 2017b.)

Calibration of GEM-Hydro-UH provided substantial improvements to model prediction (Figure 6.4). The performance of calibrated GEM-Hydro-UH also came very close to that of GR4J model driven with CaPA precipitation on the same subbasins. Gaborit et al. (2017b) performed a global calibration of GEM-Hydro-UH. In the global calibration, a unique SVS parameter set for the whole Lake Ontario watershed was obtained. The authors then used this global parameter set with GEM-Hydro, along with standard Manning's roughness coefficients in WATROUTE. The authors noted that globally calibrated GEM-Hydro provided good performance (Figure 6.5).

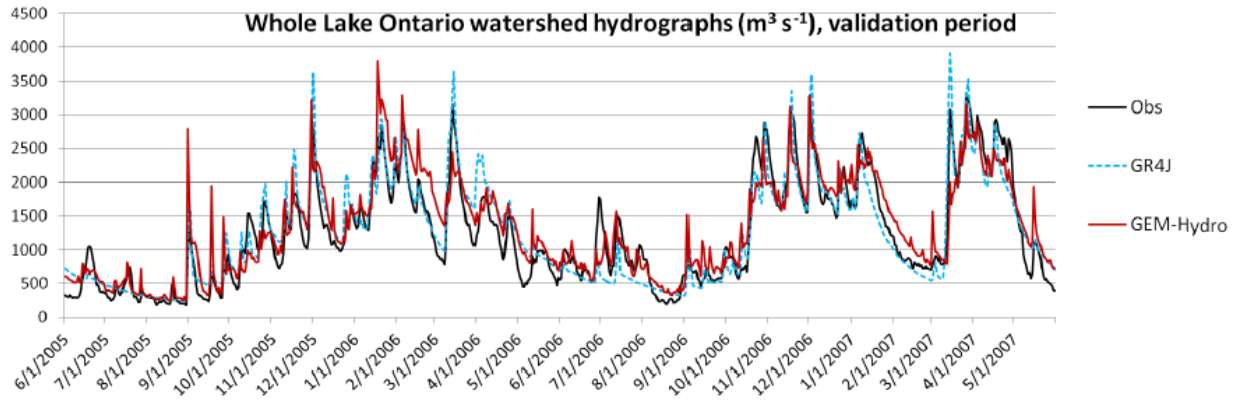

Figure 6.5. Observed and modeled (GR4J and GEM-Hydro) runoff during the validation period for the whole Lake Ontario watershed. (Source: Gaborit et al. 2017b.)

Carter and Steinschneider (2018) investigated the hydroclimatological drivers of floods on Lake Ontario in context of the 2017 flood (Figure 6.6). Lake Ontario a peak daily lake level of 75.88 m in late May 2017, which was the highest lake level in a century.

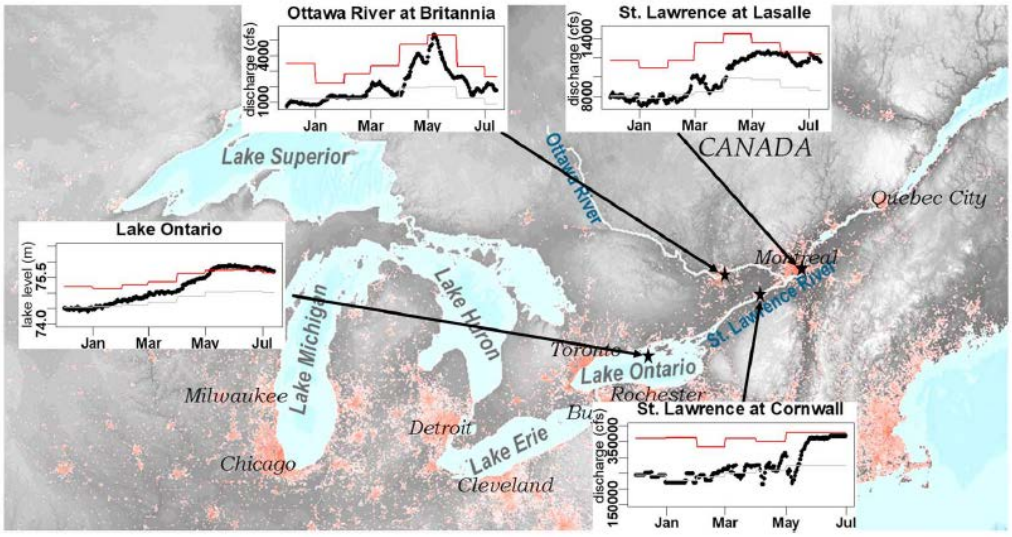

Figure 6.6. Water level on Lake Ontario and streamflow discharges at three locations during the 2017 flood event. Dots on the plots denote 2017 observed levels and discharges, the red line represents the respective maximum daily values per month, and the gray line represents the respective long-term monthly means. (Source: Carter and Steinschneider 2018.)

The extensive flooding across the Lake Ontario and St. Lawrence River drainage area was linked to large-scale anomalies across the region (Figure 6.7~~Figure 6.7~~). Flooding in the Ottawa River began in the first week of April, 2017 while flooding along St. Lawrence River at Montreal began in early may, 2017. During the 2016-2017 winter, wet and warm conditions caused higher than average net basin supply (NBS) into the upper Great Lake, which had higher than average water level entering the 2016-2017 winter. These conditions caused higher than average outflows from Lake Erie into Lake Ontario throughout the winter. Temperatures were well above average (4-8°C) in January and February 2017 that caused higher than average snowmelt from January through March, 2017 (Figure 6.7~~Figure 6.7~~). In March 2017, cooler temperatures in the east resulted in unstable ice formation on the St. Lawrence river,

precluding greater releases from Moses-Saunders dam which would have resulted in flooding at Montreal. In April 2017, an extensive snowmelt anomaly in southern Québec combined with above average precipitation resulted in flooding of the Ottawa and St. Lawrence Rivers. The precipitation anomaly strengthened in May and above average precipitation across the region extended into June.

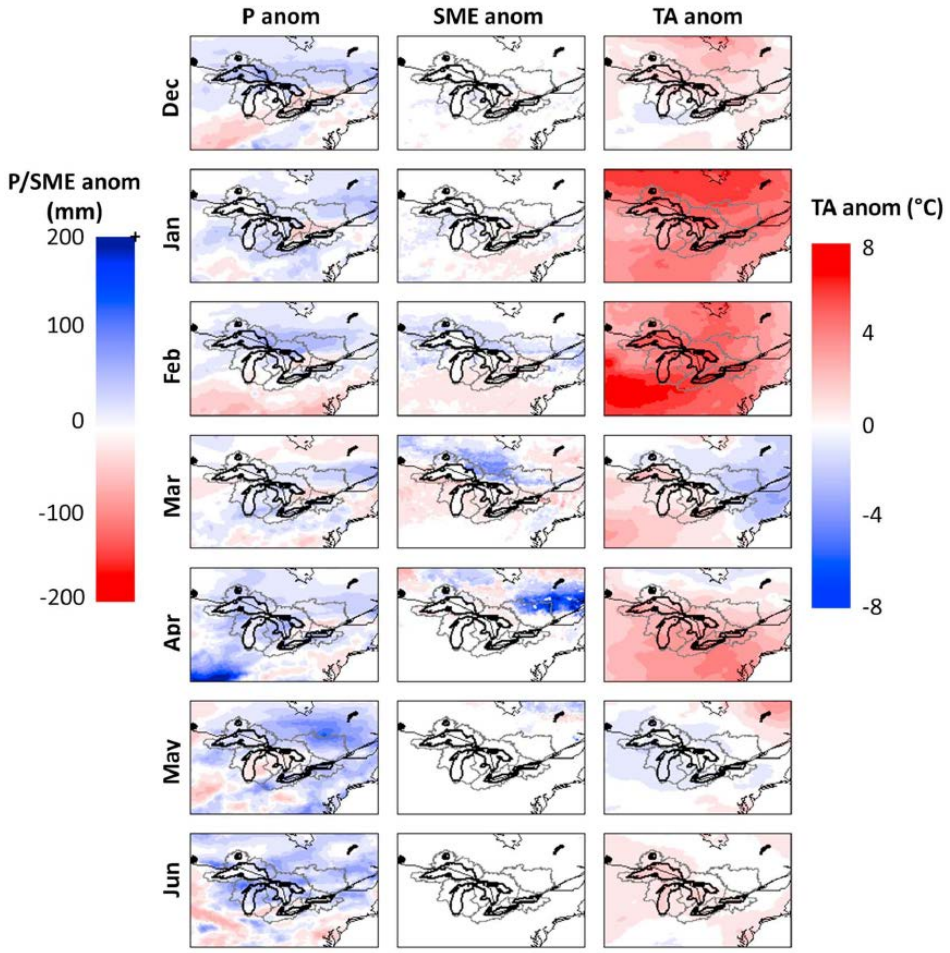

Figure 6.7. Monthly anomalies in precipitation (P), snowmelt water equivalent (SME), and air temperature (TA) from December 2016 through June 2017. (Source: Carter and Steinschneider 2018.)

While inflow from Lake Erie into Lake Ontario was 18 percent above mean and NBS was 35 percent above mean in April 2017, May 2017 NBS into Lake Ontario was more than twice its long-term mean (Carter and Steinschneider 2018). This large anomaly in NBS was the main cause of lake level rise in May 2017. Over the December 2016-June 2017 period, the anomalous inflow from Lake Erie into Lake Ontario was larger than NBS, indicating that the initial water-level conditions and hydroclimatology of upper Great Lakes during Spring 2017 contributed significantly to the 2017 flood.

Figure 6.8 shows precipitation anomalies and integrated water vapor transport (IVT) during December-March for seven flood years since 1949 in the Great Lakes area (Carter and Steinschneider 2018). In six of the seven flood years, winter precipitation was above average, in 1951, 1973, and 1974 at least one standard deviation greater than mean and in 1976 more than two standard deviations above the mean. Four of the seven flood years were La Niña years and one was a strong El Niño year. During the La Niña

years, wet anomalies over northern U.S. and Canada resulted from a northward shift in the jet in eastern Pacific and enhanced IVT over Pacific Northwest. During the El Niño year, the precipitation anomaly had a southern U.S. origin. Wet winters were also enhanced by IVT from the Gulf of Mexico, supplying warm and moist air that increased precipitation over the Great Lakes region. The 1993 flood year did not have these anomalies.

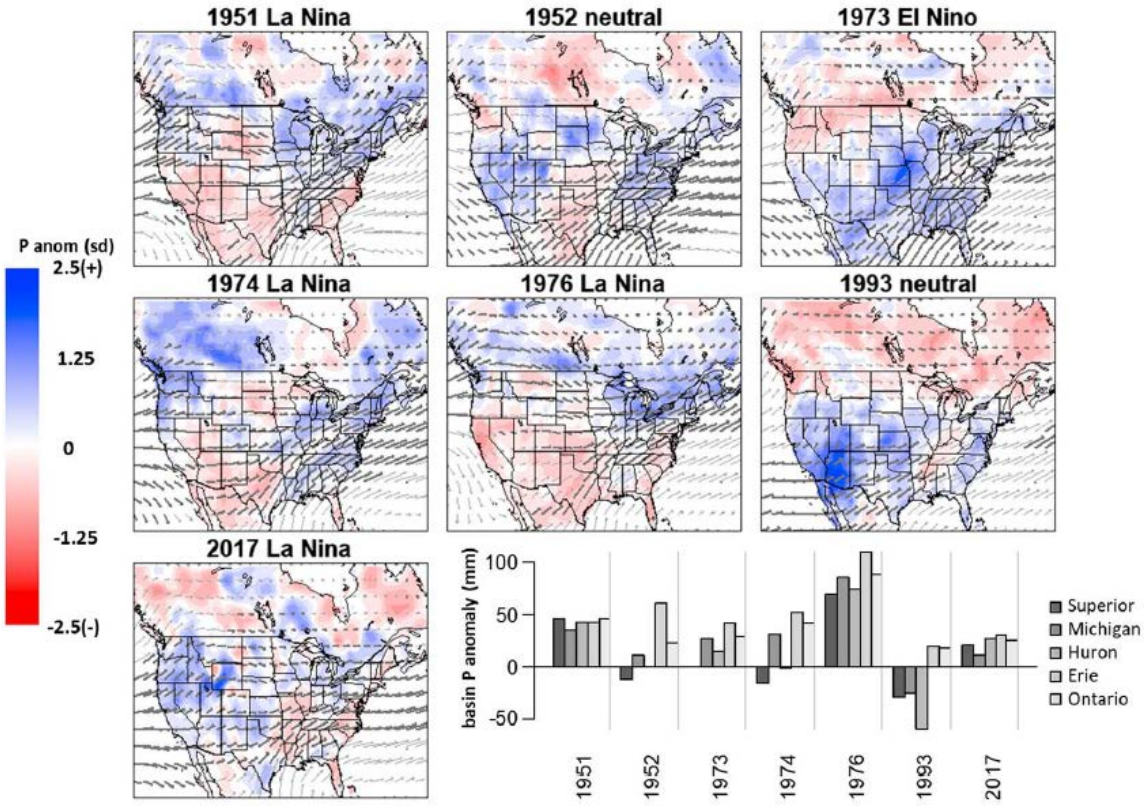

Figure 6.8. December-March cumulative precipitation anomalies and IVT; 10-254 $kg \cdot m^{-1} \cdot s^{-1}$) prior to seven Lake Ontario floods. Black arrows indicate IVT magnitude exceedance over mean seasonal value. The bar chart shows December-March precipitation anomaly for each Great Lake. (Source: Carter and Steinschneider 2018.)

In four of the seven flood years (1951, 1952, 1973, and 1993), winter and spring water levels in Lake Ontario were very high (Figure 6.9~~Figure 6.9~~). Winter water levels in some or all of the upper Great Lakes were also above average in all seven flood years. Two successive La Niña-influenced wet winter in 1949-1950 and 1950-1951 contributed to the high water-levels in years 1951 and 1952, respectively. Another La Niña-influenced wet winter occurred in 1970-1971 and contributed to above average water levels in upper Great Lakes at the start of 1971-1972 winter, which itself was a La Niña year. Hurricane Agnus contributed anomalous precipitation in late June 1972 that delayed the usual late summer decline in 1972 leading to anomalously high water-level at the start of 1972-1973 winter.

Springtime climate anomalies for the seven flood years are shown in Figure 6.10 (Carter and Steinschneider 2018). In four of the seven flood years (1973, 1974, 1993, and 2017), springtime precipitation was significantly above average. For all seven flood years, but particularly in 1973, 1974, and 2017, the precipitation anomaly covered the eastern half of the U.S., increasing precipitation input to the Great Lakes, particularly Lake Ontario. The authors noted that during these years the anticyclonic circulation around the western ridge of the North Atlantic Subtropical High caused IVT from the Gulf of

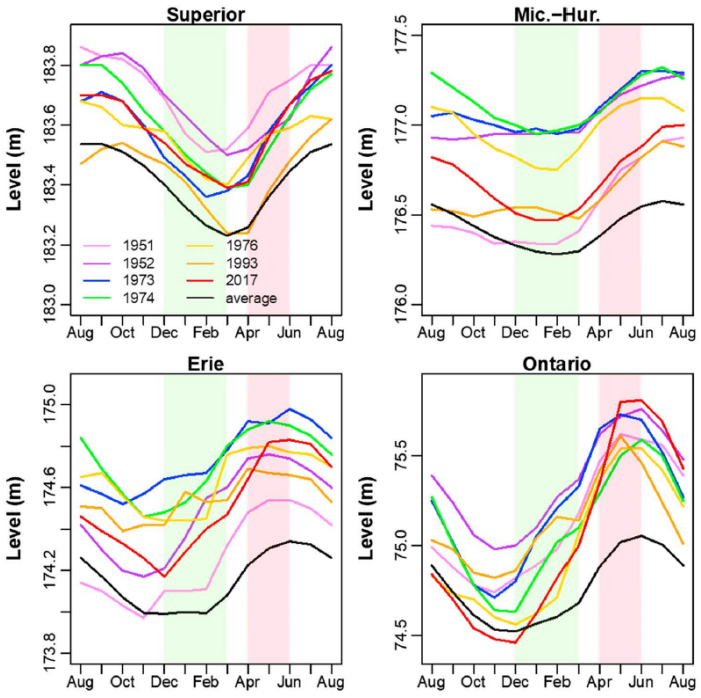

Figure 6.9. Mean monthly water level in the Great Lakes leading into the seven flood year shown with the long-term mean monthly water levels. Green shading indicates winter and red shading indicates spring. (Source: Carter and Steinschneider 2018.)

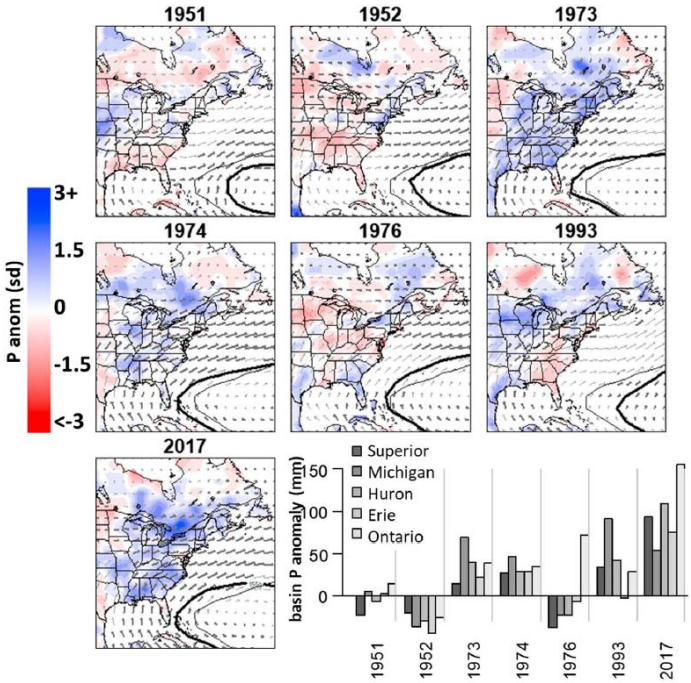

Figure 6.10. April–June cumulative precipitation anomalies and IVT; 0-358 $kg \cdot m^{-1} \cdot s^{-1}$) prior to seven Lake Ontario floods. Black arrows indicate IVT magnitude exceedance over mean seasonal value. The bar chart shows April-June precipitation anomaly for each Great Lake. (Source: Carter and Steinschneider 2018.)

Maxico to strengthen over the eastern U.S., causing above average precipitation across the region including the Great Lakes basin.

Carter and Steinschneider (2018) postulated that the expected maximum monthly average water level of Lake Ontario between April and August is a function of November water level in each of the Great Lakes, the December–February None 3.4 index, and April-May precipitation over the Lake Ontario drainage basin. The postulated function was of the following generalized additive model (GAM) form:

$$E[Ont_{max}] = \beta_0 + \beta_1 Sup_{Nov} + \beta_2 MH_{Nov} + \beta_3 Erie_{Nov} + \beta_4 Ont_{Nov} + f(Niño3.4) + \beta_5 LO.Prcp_{AM}$$

where Ont_{max} is the maximum (April-August) Lake Ontario water level, β's are regression coefficients, Sup_{Nov}, MH_{Nov}, $Erie_{Nov}$, and Ont_{Nov} are the November water levels in Lakes Superior, Michigan-Huron, Erie, and Ontario, $f(\cdot)$ is a regression spline with two degrees of freedom, and $LO.Prcp_{AM}$ is the April-May precipitation over Lake Ontario basin. The authors compared this postulated model with three linear variants: (1) a model using only November water levels, (2) a model using November water levels and Niño 3.4 index, and (3) a model using all three predictors but excluding nonlinear effects.

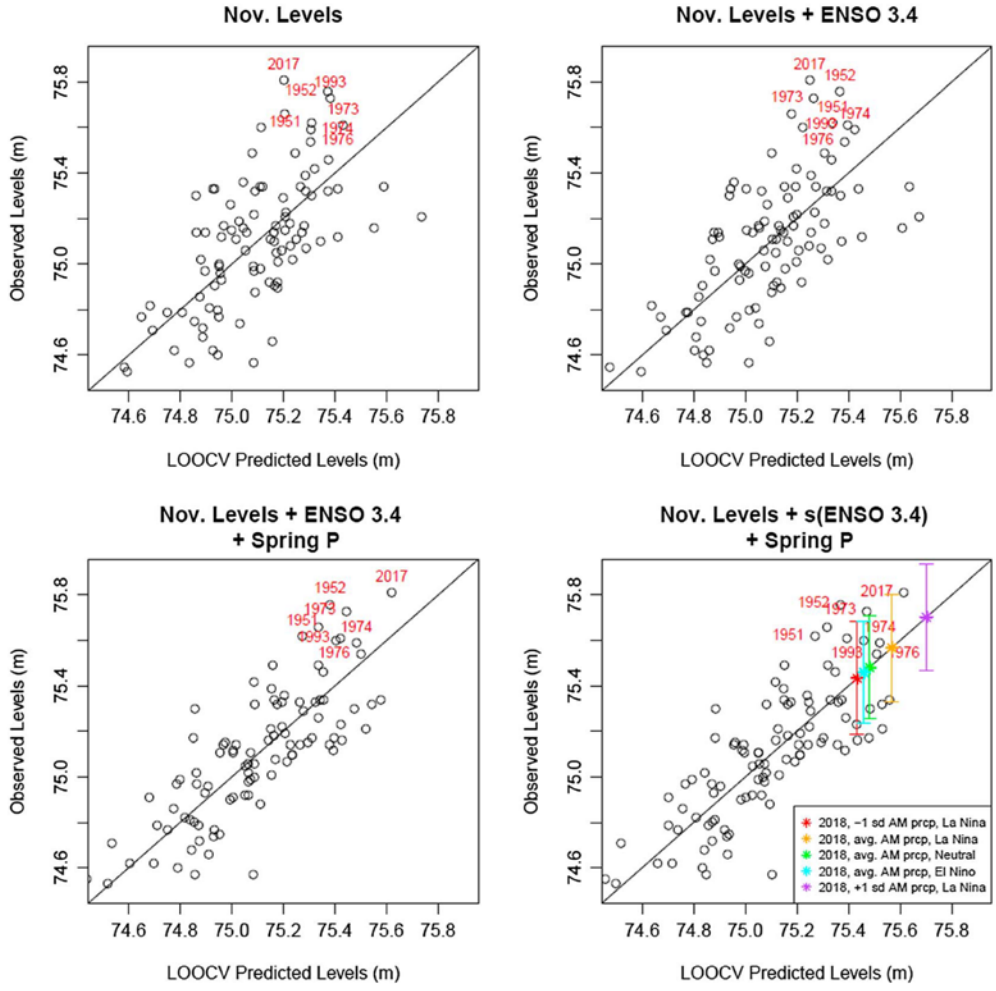

Figure 6.11. Observed and model predicted maximum monthly average April-August Lake Ontario water levels. Red year labels indicate flood years. Predictions for the 2018 maximum Ontario water levels are shown with ±1σ bounds for five scenarios of ENSO phase and spring precipitation (bottom-right panel). (Source: Carter and Steinschneider 2018.)

Figure 6.11 shows the observed and leave-one-out predicted maximum levels by the GAM model and the three simpler models. The authors noted that using only November water levels for the Great Lakes as predictors of following spring/summer Lake Ontario water levels provides some predictive capacity. Predictions improve when the Niño 3.4 index is added as a predictor and improve substantially when sprint precipitation on Lake Ontario basin is included in the model.

7.0 Hydrologic Impacts of Climate Change in Northeast United States

This chapter describes the hydrological impacts of climate change in the northeast region. The focus is on two metrics—floods and seasonality, resulting from precipitation and/or snowmelt events under climate change scenarios. Because both of these metrics are manifestations of runoff from precipitation and/or snowmelt influenced by springtime temperatures, conditions other than just precipitation and snowmelt are also important to consider. For example, precipitation or snowmelt events that are similar in magnitude can differ in the amount of runoff from the drainage area because of differences in antecedent soil moisture conditions or differences in the degree of imperviousness. The duration of the precipitation event is also important (e.g., a stalled storm system producing a low-intensity but longer-duration precipitation event can result in significantly greater flood magnitude compared to a higher-intensity shorter-duration storm for the same antecedent and physiographic conditions). Other factors that affect runoff include land use and cover, water-supply management, and urbanization. Some of these hydrometeorological parameters are not directly addressed in the NCAs.

7.1 Historical Flood Events

Floods in the Northeast Region can be produced by several mechanisms. These mechanisms include regionally persistent rainfall, locally heavy precipitation (e.g., thunderstorms and MCSs), extratropical cyclones, remnants of tropical cyclones during summer and fall, and late spring rainfall on snowpack. Some historical floods are briefly described below. The reason these flood events are highlighted is that they resulted from unusual combinations of hydrometeorological conditions and exceeded the previously recorded historical maximums. In general, the climate research community has not focused on evaluating trends and impacts of meteorological (and by extension, flooding) events of exceedance probabilities that are of interest to the NRC in a PFHA for permitting and licensing. Current climate models have significantly larger uncertainties for events whose exceedance probabilities approach those of interest to the NRC. The following events highlight some unusual combinations of hydrometeorological conditions that open a potential avenue to identifying similarly unusual combinations in climate simulations and how their frequencies are affected under various climate scenarios. This information could inform the NRC of combinations of hydrometeorological conditions relevant to PFHA.

7.1.1 June 1972 Floods from Hurricane Agnes

Hurricane Agnes was one of the largest hurricanes to occur in June (USGS 1975). A weak disturbance over the Yucatan Peninsula on June 14 intensified rapidly and moved east into the Caribbean Sea (Figure 7.1). Large amounts of moisture were fed into Agnes as a result of warm tropical waters and a second well-developed circulation system east of Agnes. On June 16, it reached tropical storm intensity and turned north toward the Florida panhandle. Agnes became a hurricane on June 18 as it moved north in the Gulf of Mexico. On June 19, Hurricane Agnes made landfall in the Florida panhandle near Port St. Joe, about halfway between Apalachicola and Panama City. As it moved inland, Agnus weakened to a tropical storm over Georgia and South Carolina. However, it started strengthening as a result of energy release from baroclinic sources associated with an extratropical trough approaching from the west. The strengthening was not strong enough to make Agnes a tropical storm, but likely resulted in development of a secondary low on June 21, about 80 mi north of the primary center (Figure 7.1). These two centers appeared as one on satellite images and moved along nearly parallel tracks through June 22. On June 21, Agnes strengthened into a tropical storm and crossed into the Atlantic Ocean off the coast of North Carolina, the original center of the storm passing about 35 mi north of Cape Hatteras. On the morning of

June 22, Agnes was about 210 mi east of Baltimore and reached its lowest central pressure, 977 mb, and turned northwest. It made landfall in the vicinity of New York City. On the afternoon of June 22, the further weakened original center of Agnes was absorbed into the now dominant extratropical, secondary low center. This new low stagnated over western Pennsylvania for about a day before slowly moving northeast and entering the North Atlantic.

Precipitation over the northeast U.S. during May 1972 was between 100 and 150 percent of normal and precipitation during the first half of June was also above normal in New York, Pennsylvania, New Jersey and Maryland leading to wet antecedent conditions (USGS 1975). From June 19 through June 24, Tropical Storm Agnes, stalled over the Susquehanna River Basin, produced 10-19 in. of rain over the mountainous areas of Pennsylvania and western New York and 6-10 in. elsewhere (Figure 7.2). Tropical Storm Agnes caused extensive flooding in the northeast U.S., particularly in the Susquehanna River Basin, as described below.

Schuylkill River at Philadelphia, Pennsylvania recorded a stage of 14.65 ft on June 23, 1972 and came close to its previous record stage of 14.7 ft on August 24, 1933. Only two previous stages, 17.0 and 14.8 ft, on October 4, 1869 and March 1, 1902, respectively were greater. Chemung River at Chemung, New York recorded a stage of 31.62 ft on June 23, 1972, over 7.5 ft higher than the previous record stage of 23.97 ft recorded on May 28, 1946. Susquehanna River at Wilkes-Barre, Pennsylvania recorded a stage of 40.91 ft on June 24, 1972, exceeding the March 18, 1865 stage of 33.1 ft. The peak stage at the same location was exceeded on September 9, 2011 (42.66 ft) during floods caused by Tropical Storm Lee although the discharge during the Agnes flood was greater (345,000 cfs compared to 310,000 cfs). West Branch Susquehanna River at Willamsport, Pennsylvania recorded a peak stage of 34.75 ft on June 23, 1972, exceeding the previously recorded peak stage of 33.57 ft on March 18, 1936. Susquehanna River at Sunbury, Pennsylvania recorded a peak stage of 35.8 ft on June 24, 1972, exceeding the previous peak stage of 34.6 ft on March 19, 1936. The recorded stage at this location during Tropical Storm Lee, 31.66 ft on September 8, 2011, came close to that during the Agnes flood, but did not exceed it. Susquehanna River at Harrisburg, Pennsylvania recorded a peak stage of 32.57 ft on June 24, 1972, exceeding the previously recorded peak stage of 29.23 ft on March 19, 1936. Allegheny River at Olean, New York recorded a peak stage of 24.3 ft on June 23, 1972, exceeding the previously recorded peak stage of 21.3 ft in 1942. Allegheny River at Salamanca, New York, a few miles downstream from Olean, also exceeded its previously recorded peak stage (16.24 ft on September 29, 1967) by nearly 7.8 ft (recorded stage on June 23, 1972 was 24.01 ft, which is still the maximum stage on record). Figure 7.3 shows the locations of selected streamflow gauges and drainage basins that experienced floods from Tropical Storm Agnes.

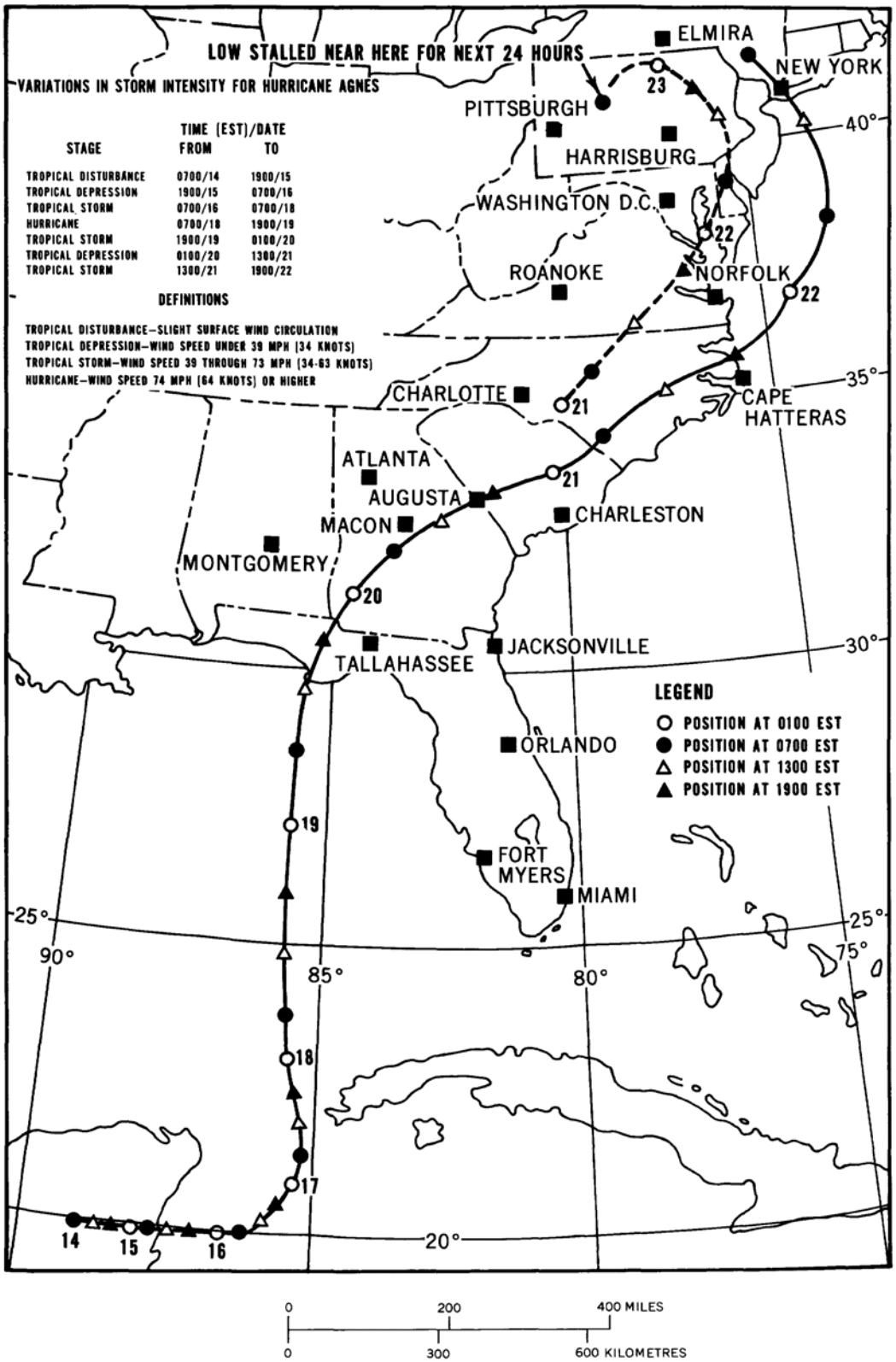

Figure 7.1. Track of Hurricane Agnes June 14-23, 1972. Also shown is the track of the extratropical system that moved nearly parallel to Agnes starting June 21. (Source: USGS 1975.)

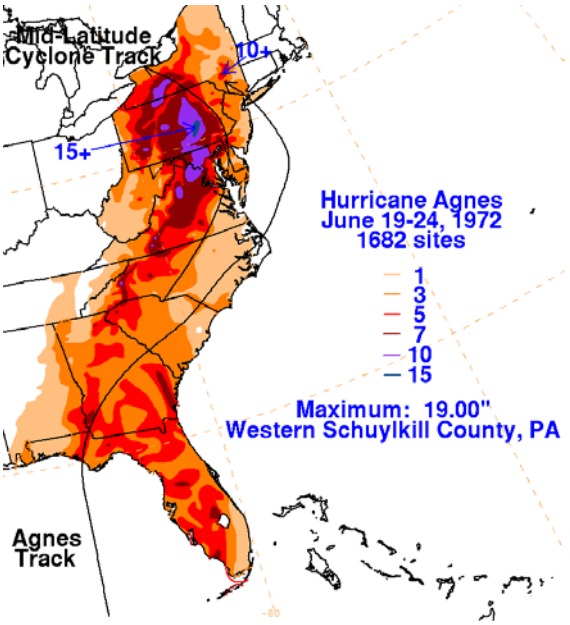

Figure 7.2. Total precipitation depth (in.) during June 19-24, 1972 from Hurricane Agnes and its remnants. (Source: NCEP 2019.)

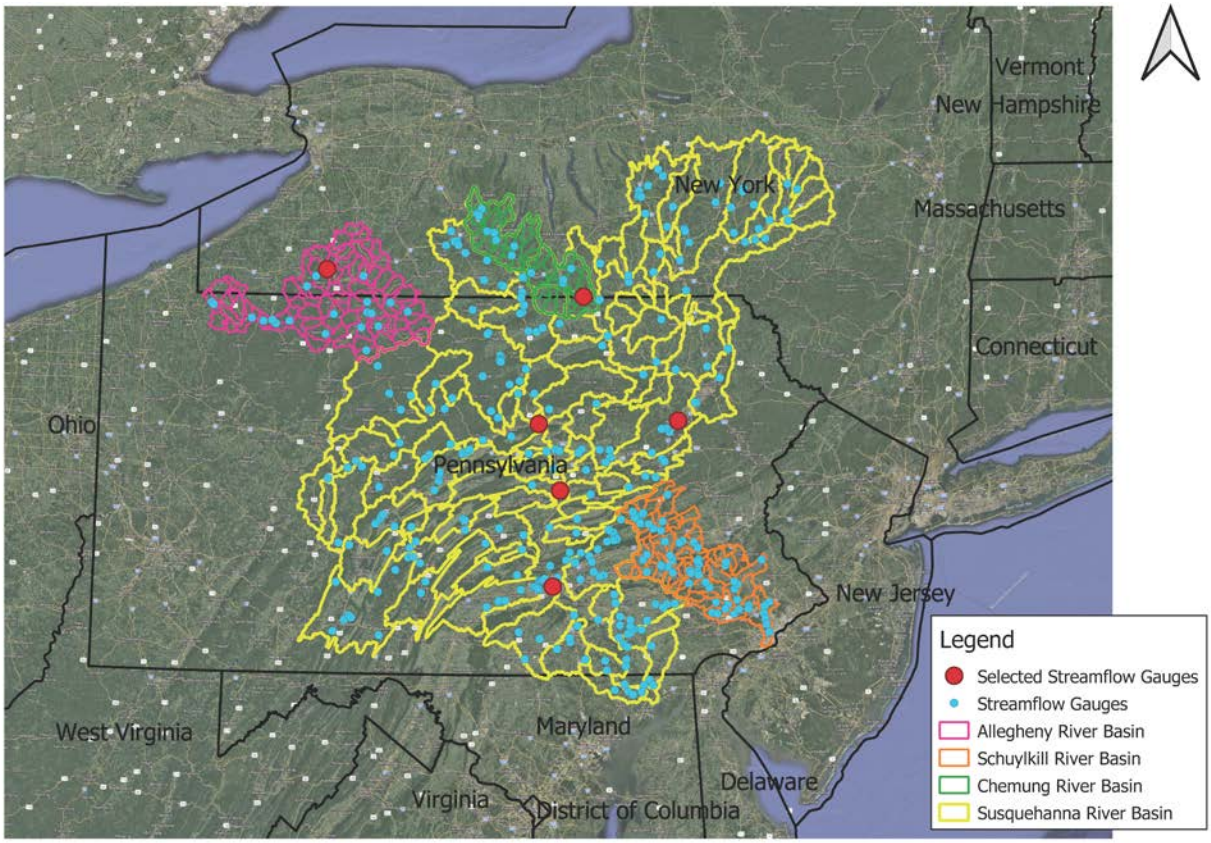

Figure 7.3. Locations of selected streamflow gauges in the northeast U.S. that experienced major flooding during Tropical Storm Agnes.

7.1.2 April 2005 Floods

USGS (2006) described floods in the Neversink River, a major tributary of the Delaware River, from the April 2-3, 2005 heavy rainfall amounts (3 to 6 in. within 36 hours) that caused major flooding in East and West Branches of the Delaware River and their tributaries. The rainfall was produced by a storm system that moved up the Appalachian Mountains and produced heavy rain in southeastern New York (Figure 7.4). The rainfall intensities were not high (about 0.5 AEP for 24-hour total at Claryville). The rainfall frequencies were also not low (generally frequencies at selected locations within the Neversink Basin were about 0.2 or more). However, a previous storm system during March 28-29 had already caused rivers and streams at greater than normal discharge; on April 1, 2005, the USGS streamflow gauge on the Neversink River at Claryville, NY, was at a level that is only exceeded 20 percent of the time or less. The April 2-3, 2005 rainfall on existing snowpack with daytime temperatures of 50°F or greater resulted in significant runoff. Snowmelt of nearly 8 in. was reported at Slide Mountain located near the headwaters of West Branch of Neversink River.

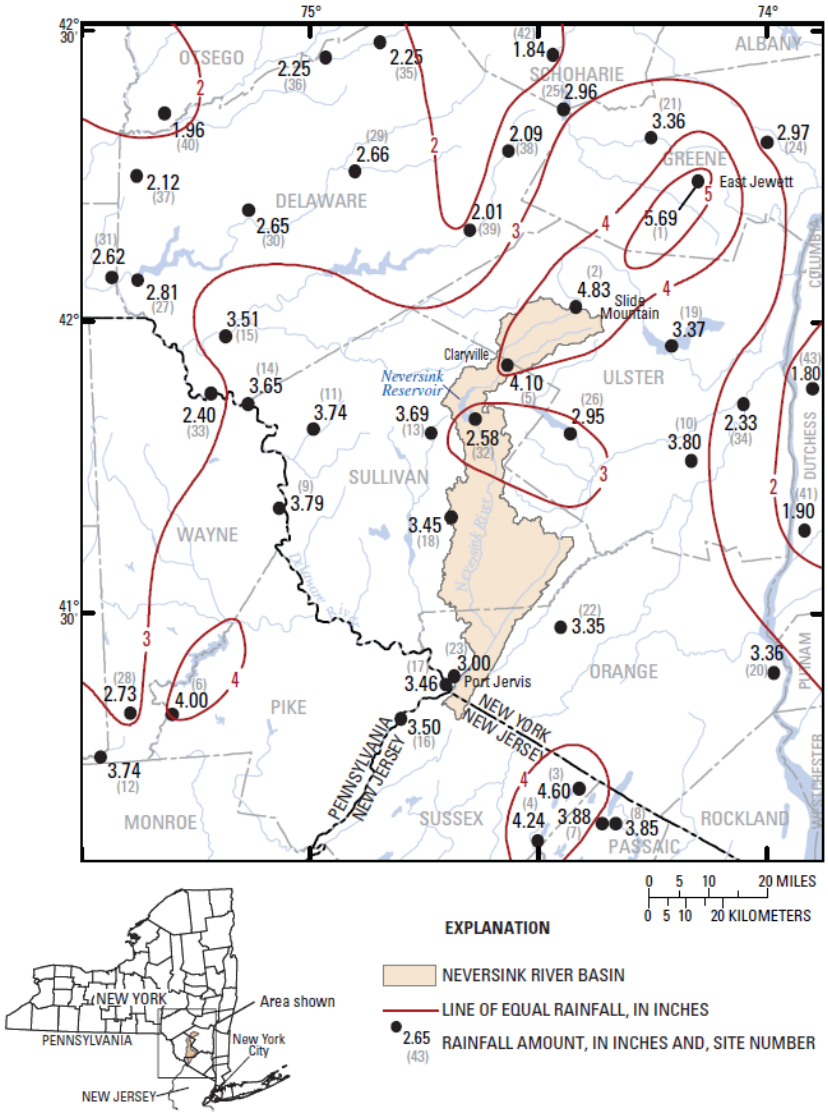

Figure 7.4. Rainfall amounts over southeastern New York from the April 2-3, 2005 storm. (Source: USGS 2006.)

USGS (2006) reported discharges and associated frequencies at 26 USGS streamflow gauges in the Delaware River Basin (Figure 7.5). At 11 (8 regulated, 3 unregulated flows) of the 26 streamflow gauges, both previous peak stage and peak discharge were exceeded during the April 2-3, 2005 flood. The estimated AEPs at two of the three streamflow gauges recording unregulated flows were 0.1 and 0.04 and between 0.01 and 0.002 at the third. The estimated AEPs at the streamflow gauges recording regulated flows were between 0.04 and 0.002.

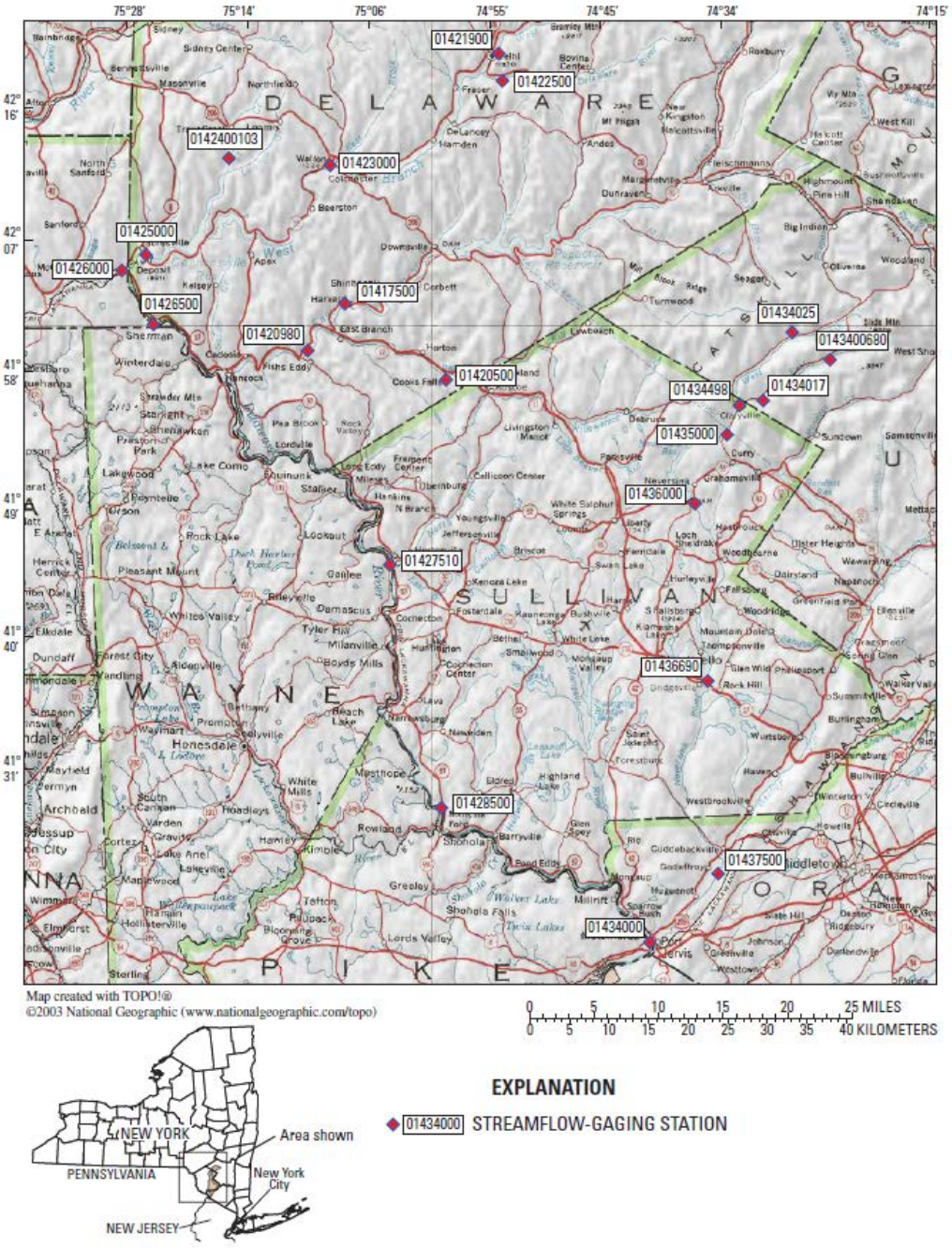

Figure 7.5. Selected USGS streamflow gauges in the Delaware River Basin analyzed by USGS (2006). (Source: USGS 2006.)

7.1.3 April 2007 Floods

USGS (2009) described the floods measured during April 15-18, 2007 nor'easter at 10 streamflow gauging stations in Massachusetts. Heavy rains from the storm (Figure 7.6), combined with seasonal high flows and wet soil moisture conditions resulted in extensive flooding in Massachusetts and neighboring states. USGS performed a peak flow analysis at 10 streamflow gauges to characterize the magnitude of the April 2007 flood (Figure 7.7). Peak discharges recorded or estimated for the April 2007 flood were among the highest since 1936. Of the 10 streamflow gauges, three reflect streamflow affected by regulation. To account for the effects of regulation, USGS used estimated discharges affected by regulation to perform peak flow analyses. Short streamflow records at several gauges were extended using surrogate streamflow gauges using maintenance of variance extension method (Hirsch 1982). For streamflow gauges where a surrogate gauge could not be used, regional flood flow equations were used to estimate the magnitude of the floods corresponding to selected AEPs.

Flood frequency analyses were performed using Bulletin 17B procedures. The estimated AEPs of peak flows at the 10 streamflow gauges for the April 2007 flood were generally between 0.04 and 0.02. Discharge in Merrimack River at Lowell, MA approached an AEP of 0.01.

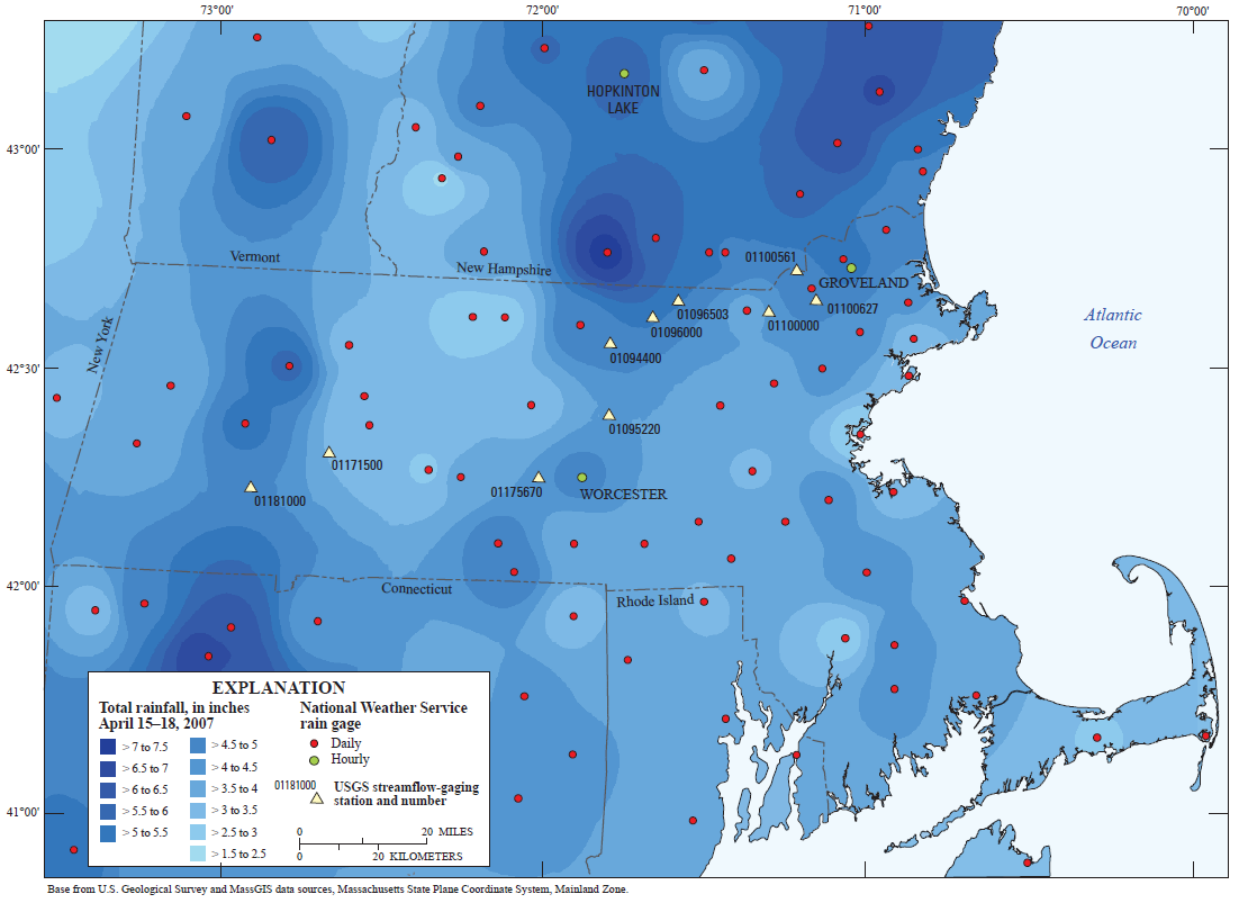

Figure 7.6. Total precipitation depth during April 15-18, 2007 storm in and around Massachusetts. (Source: USGS 2009.)

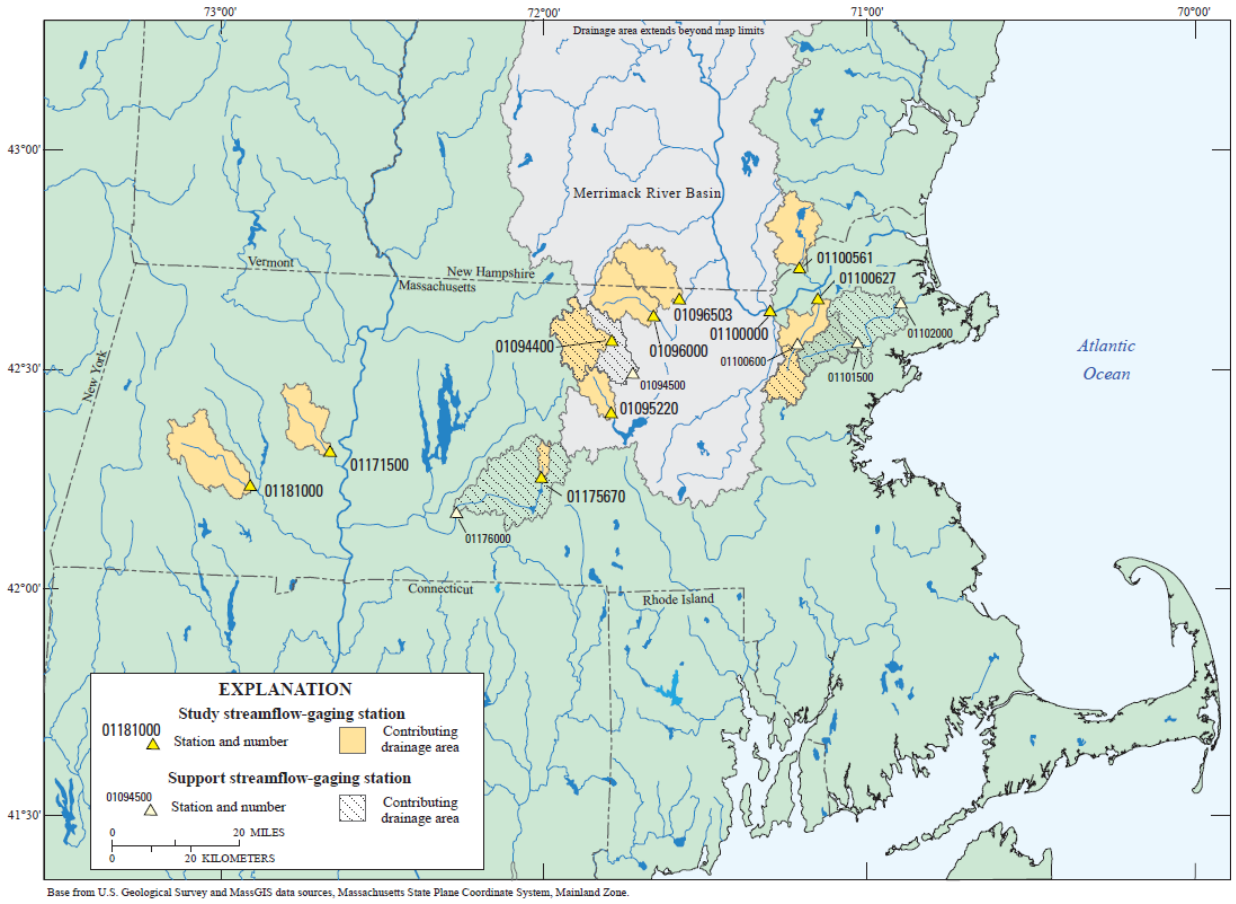

Figure 7.7. Locations of USGS streamflow gauges used to characterize the April 2007 flood. The Merrimack River at Lowell, MA streamflow gauge is numbered 01100000. Data from support streamflow gauges were used to support peak flow analyses in addition to the 10 study streamflow gauges. (Source: USGS 2009.)

7.1.4 February-March 2010 Floods

USGS (2012) described the floods resulting from heavy persistent rains from late February through March 2010 in Rhode Island, estimated the magnitude of flood flows for selected AEPs at streamflow gauges in Rhode Island, and developed statewide regional equations for estimating flood discharges at ungauged locations. At 18 of 21 active streamflow gauges in Rhode Island in 2010, peak discharge during mid-March to early April exceeded the previously recorded peak discharge.

The study used 43 streamflow gauges from Rhode Island (20), Connecticut (14), and Massachusetts (9) for the regional flood frequency analysis (Figure 7.8). Streamflows from only the unregulated portion of the record were used. Streamflow records were extended using the maintenance of variation extension (Hirsch 1982), but was limited to 22 streamflow gauges so as not to use surrogate streamflow stations too many times. Seven of the streamflow gauges also had historic peaks (discharges or stages or both, outside the period of continuous record). Flood frequency analyses were performed using Bulletin 17B procedures and the expected moments algorithm; the latter method allowed incorporation of interval data. Generalized regional skew was determined following recommendations of Bulletin 17B. Weighted skew was estimated using extended streamflow records at 40 streamflow gauges; three streamflow gauges were excluded because of regulation, large negative at-site skew, and redundancy with a downstream gauge.

The estimated AEPs of 2010 peak discharges at the 18 streamflow gauges that set new period-of-record highs, ranged from 0.04 to 0.002 (USGS 2012). The regional regression equations were developed by weighted multiple linear regression using drainage basin characteristics; three drainage basin characteristics were found statistically significant – drainage area, drainage density, and storage (total area of wetlands and water expressed as a percentage of drainage area).

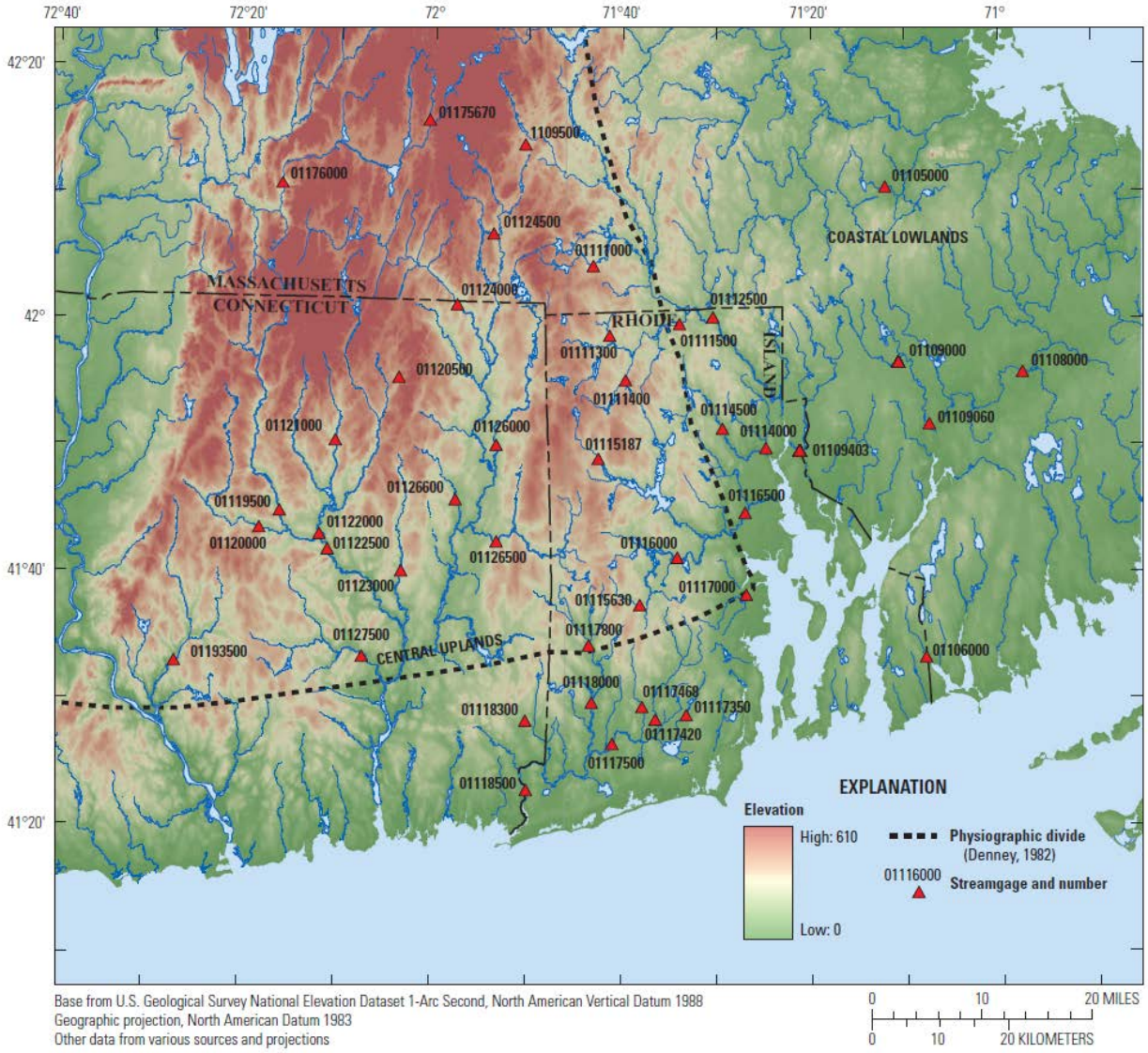

Figure 7.8. Streamflow gauges used in the Rhode Island flood frequency study. (Source: USGS 2012.)

7.1.5 February-September 2011 Floods

USGS (2015a) described the widespread flooding in the northeast U.S. during 2011 (Figure 7.9). Flooding occurred in the months February through May and July through September. During the floods of 2011, new period-of-record peak streamflow discharges were recorded at 180 streamflow gauges in the northeast U.S. During February 2011, monthly streamflows ranged between 25 and 75 percent of normal over the northeast U.S. while 2010-11 snowfall was above average. The AEPs of these flood discharges were estimated using procedures of Bulletin 17B.

Figure 7.9. Drainage area in northeast U.S. associated with flooding during 2011. (Source: USGS 2015a.)

During spring, persistent precipitation combined with snowmelt resulted in flooding in Connecticut and Massachusetts (Figure 7.10). At the start of this event (March 5, 2011), southern parts of New England had 10 in. or more of snow-water equivalent. By March 8, 2011 almost all of the snow had melted. Saugatuck River near Redding, CT recorded a new peak-of-record discharge of 2,900 cfs, which was assessed to have an AEP of 0.015. The widespread rainfall combined with snowmelt contributed to increased soil moisture in the northeast U.S.

During April 26-29, 2011, above-normal temperature-caused snowmelt in the upper elevations (SWE of 10 in. or more) combined with bands of rainfall and thunderstorms resulted in flooding in northern areas of New Hampshire, New York, and Vermont (Figure 7.11). Of the streamflow gauges shown in Figure 7.11, 17 recorded new peak-of-record discharges, with estimated AEPs ranging from 0.04 to less than 0.002.

During the months March through May, total precipitation in New York (16.7 in.), Pennsylvania (19.1 in.), and Vermont (17.1 in.) were the greatest in 117 years of record (USGS 2015a). This record rainfall contributed to flooding in Lake Champlain, with a period-of-record high water level of 103.3 ft observed at the Burlington gauge (Figure 7.12). An isolated weather system that passed through northern Vermont on May 26-27, 2011 produced localized thunderstorms, hail, and heavy rainfall (USGS 2015a). Flooding during this event was limited to smaller drainage areas (less than 100 mi^2); a peak-of-record streamflow discharge, with an estimated AEP of 0.017, was observed at Sleepers River near St. Johnsbury, VT on May 27, 2011.

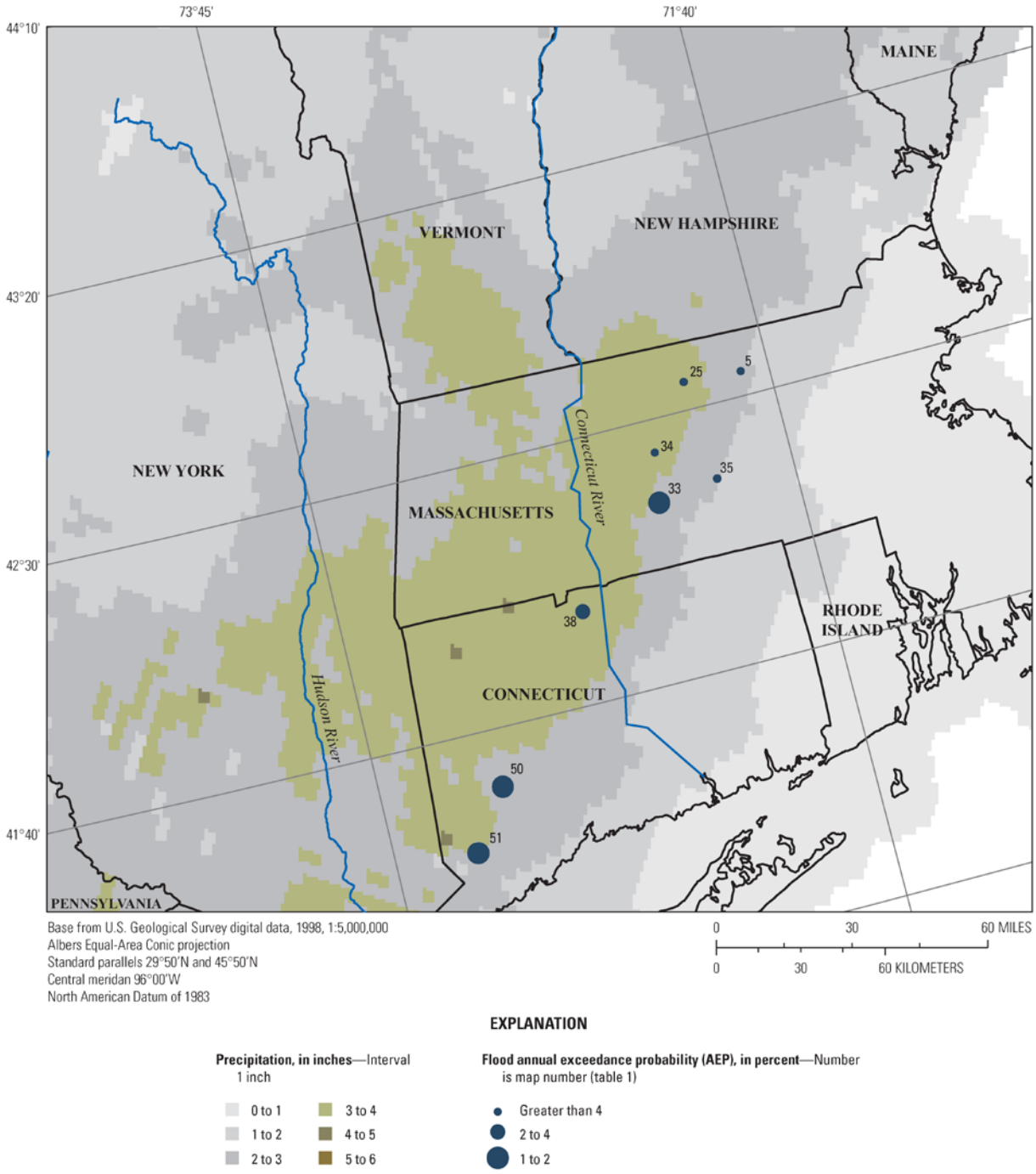

Figure 7.10. Cumulative precipitation during March 6-7, 2011 over parts of northeast U.S. and locations of streamflow gauges where flood discharge AEP was estimated. (Source: USGS 2015a.)

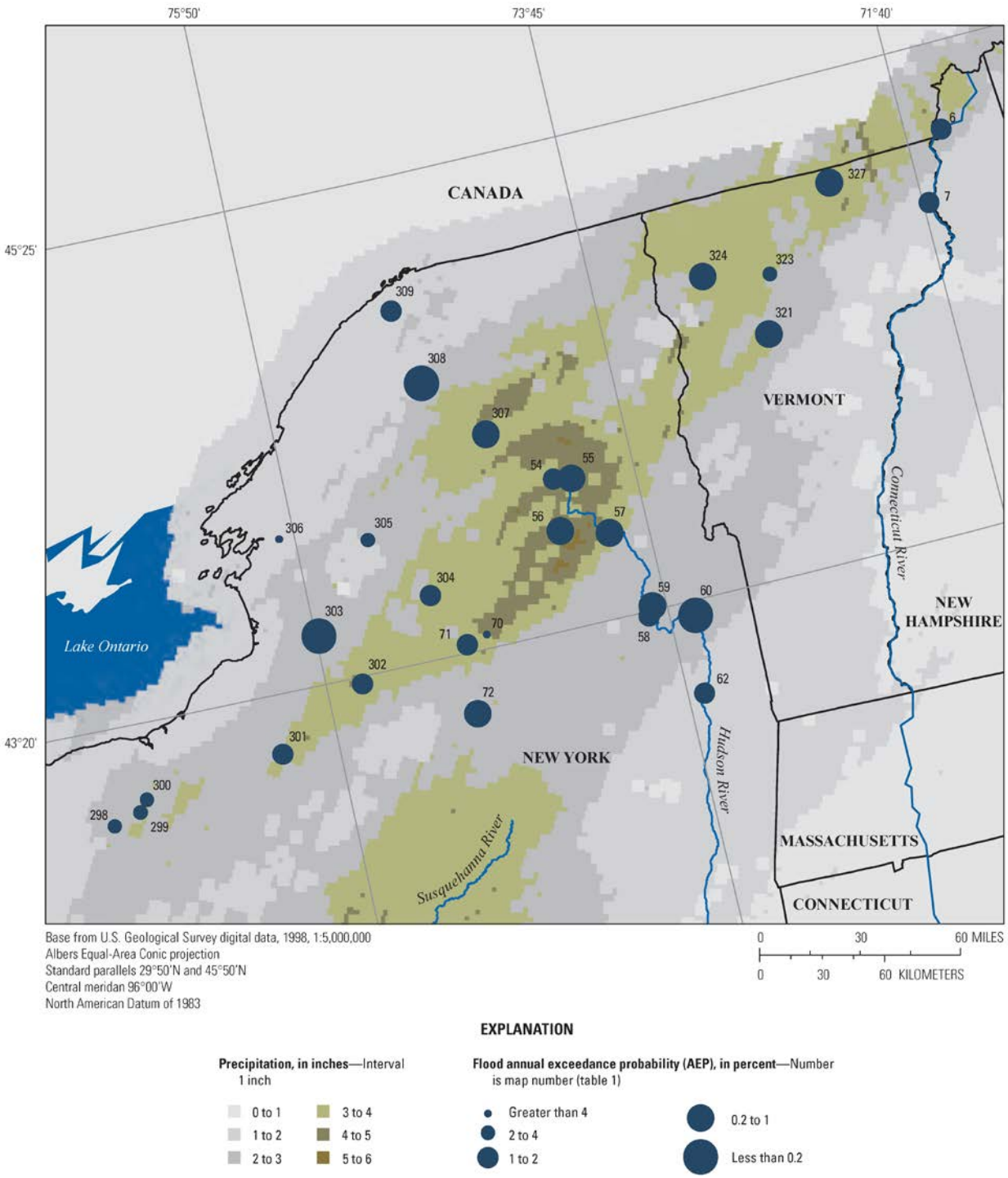

Figure 7.11. Cumulative precipitation during April 26-27, 2011 over parts of northeast U.S. and locations of streamflow gauges where flood discharge AEP was estimated. (Source: USGS 2015a.)

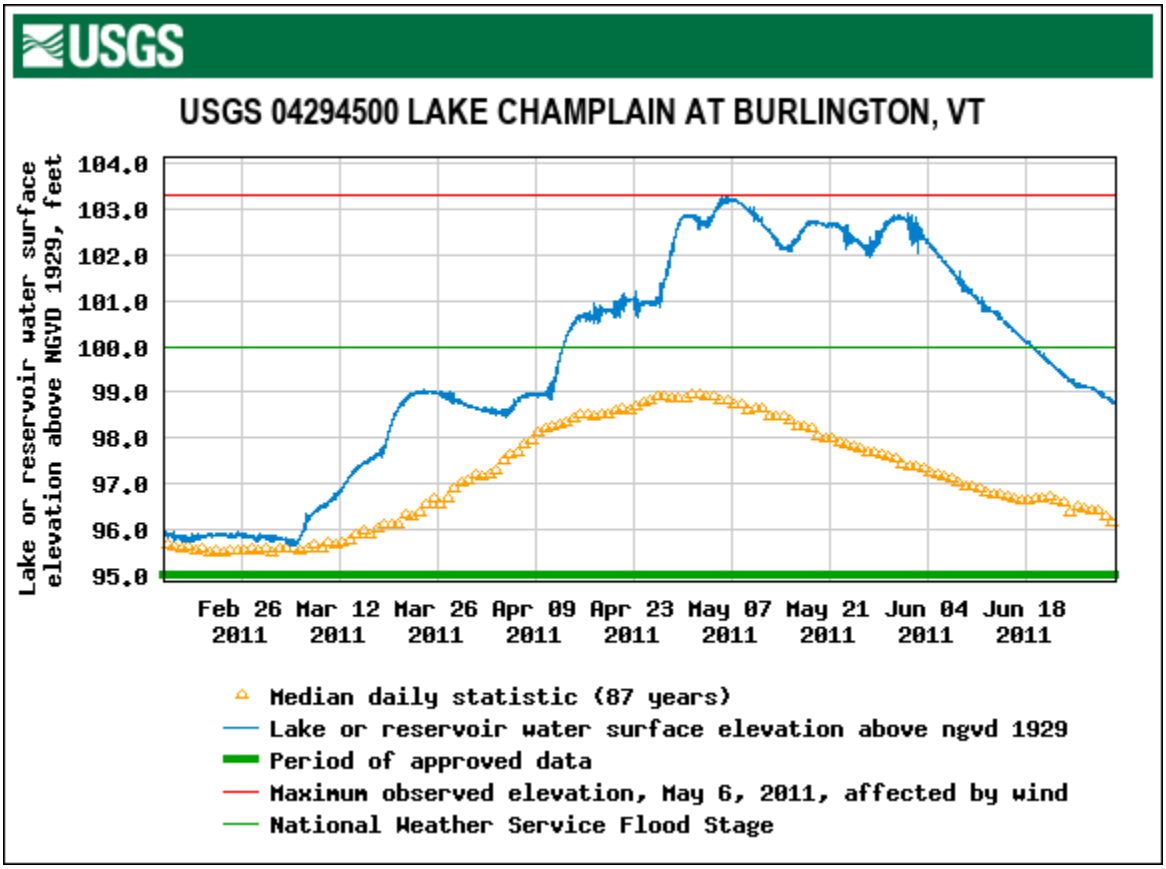

Figure 7.12. Observed lake levels in Lake Champlain at Burlington, VT during February-June, 2011. (Source: USGS National Water Information System.)

Hurricane Irene, on August 28, 2011, weakened to a tropical storm, made its third landfall near Little Egg Inlet, New Jersey (Figure 7.13; NWS 2012). Due to prior rainfall, antecedent soil moisture conditions over the northwest U.S. were very wet (Figure 7.14). Accumulated precipitation for August 27-29, 2011 over the northeast U.S. adjacent to Hurricane Irene's track is shown in Figure 7.15. The intense rainfall from Hurricane Irene resulted in new period-of-record maximums for August total precipitation amounts in New Hampshire, New Jersey, New York, and Vermont. Streamflow discharges at 186 USGS streamflow gauges were estimated to have an AEP of 0.04 or lower; at 23 of these streamflow gauges (located in the states of Delaware, Maine, New Hampshire, New Jersey, New York, and Vermont), the AEP was estimated to be 0.002 or less.

On September 6-9, 2011, remnants of Tropical Storm Lee moved across the northeast U.S. producing additional precipitation of 6-14 in. in Maryland, Pennsylvania, and New York (Figure 7.16; USGS 2015a). Discharges during early September 2011 at 29 streamflow gauges located in Maryland, New Jersey, New York, and Pennsylvania exceeded the previous historical peaks. At three of these gauges, estimated AEP was less than 0.002.

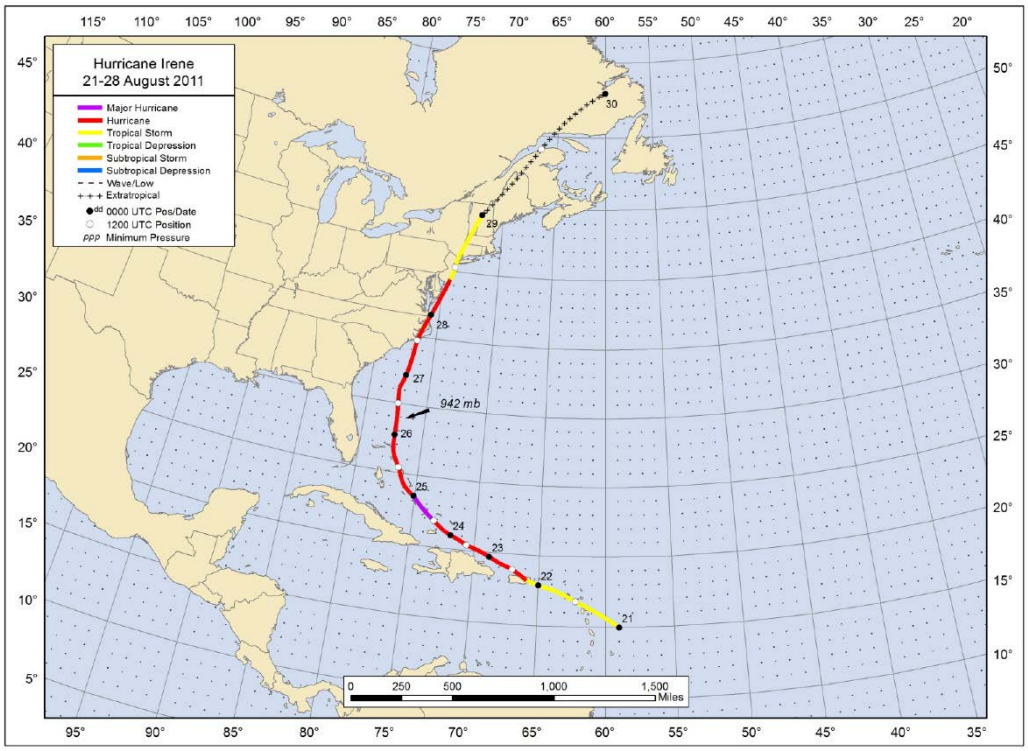

Figure 7.13. Post-storm best-track estimate of Hurricane Irene. (Source: NWS 2012.)

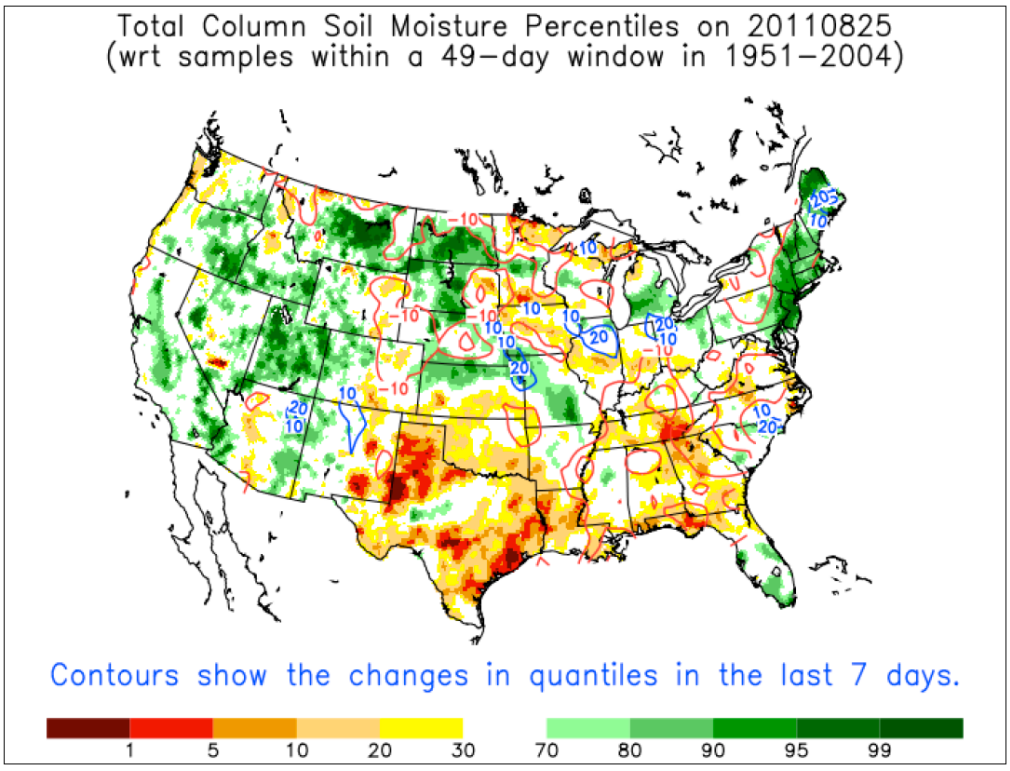

Figure 7.14. Soil moisture percentiles on August 25, 2011. The northeast U.S. along Hurricane Irene track had very wet soils. (Source: NWS 2012.)

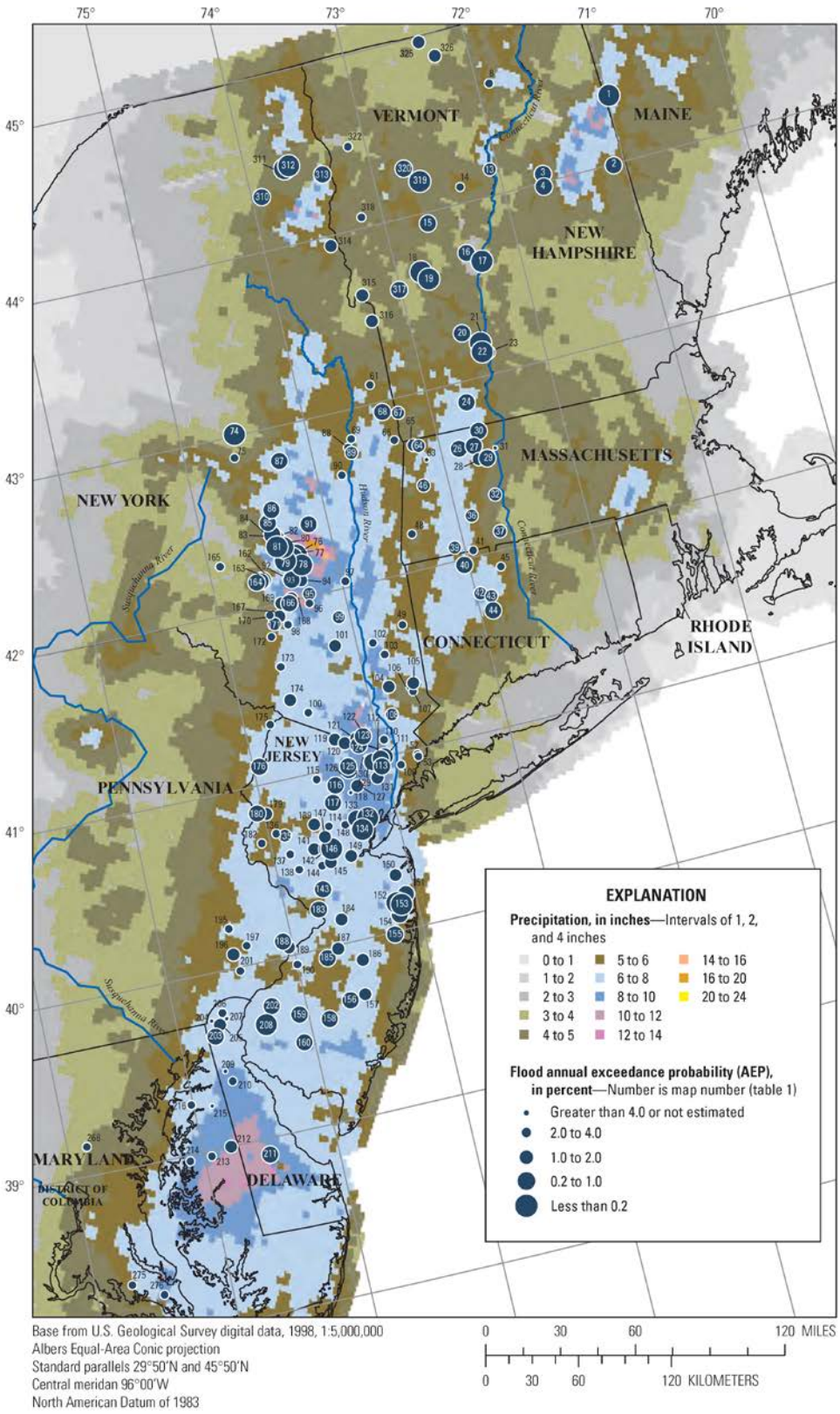

Figure 7.15. Cumulative precipitation during August 27-29, 2011. (Source: USGS 2015a.)

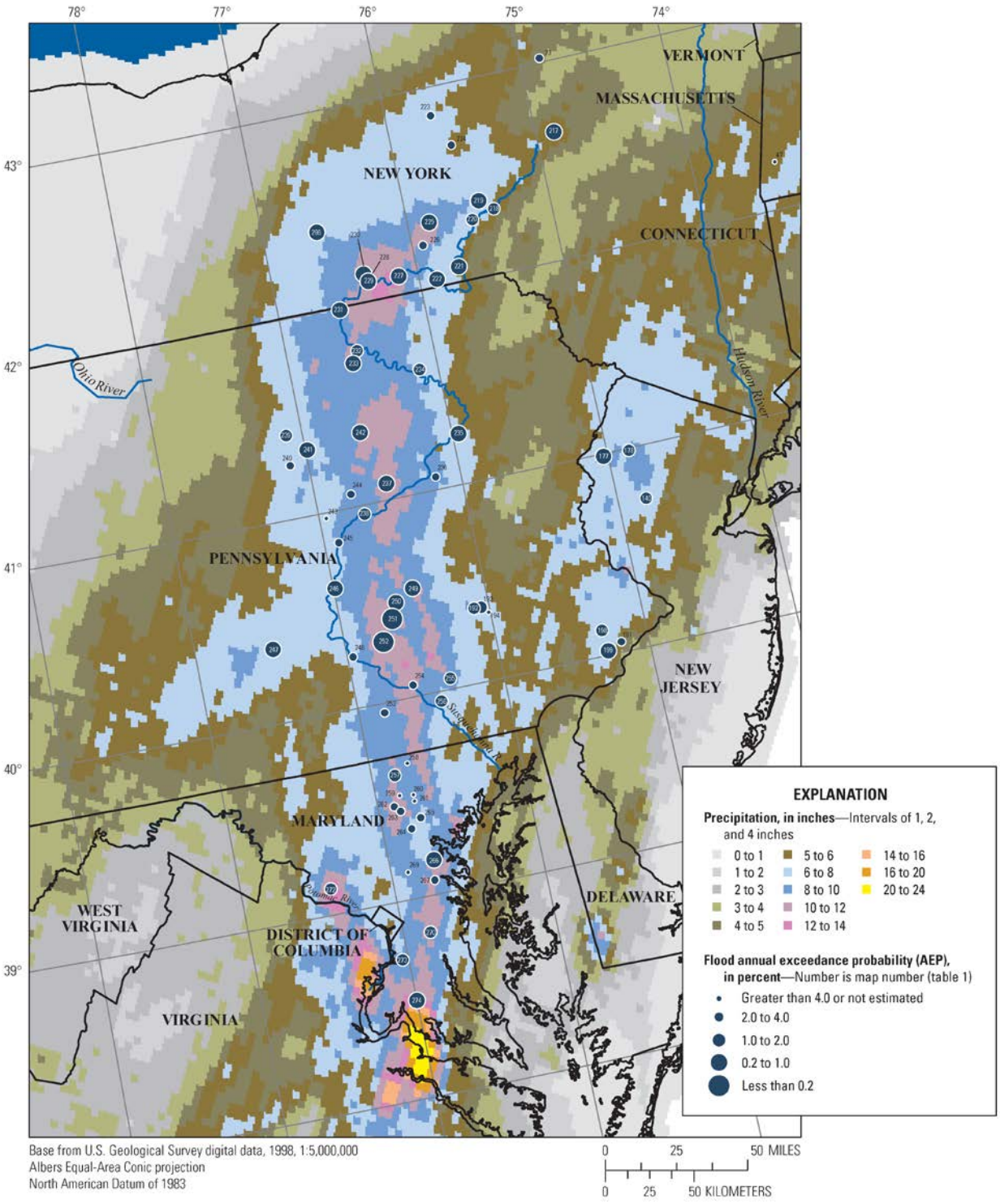

Figure 7.16. Cumulative precipitation during September 6-9, 2011. (Source: USGS 2015a.)

7.1.6 October 2012 Floods from Hurricane Sandy

Hurricane Sandy was a late-season tropical cyclone that made landfall as a Saffir–Simpson Category 1 hurricane in Jamaica and as a Category 3 hurricane in Cuba before moving through the Bahamas as a

Category 1 hurricane (Figure 7.17; Blake et al. 2013). As the storm moved northeast along the U.S. coastline, it grew considerably in size. As it turned northwest, it strengthened into a hurricane again. The storm made landfall near Brigantine, New Jersey as a post-tropical cyclone (a closed low-pressure system that is no longer a tropical cyclone; Blake et al. 2013).

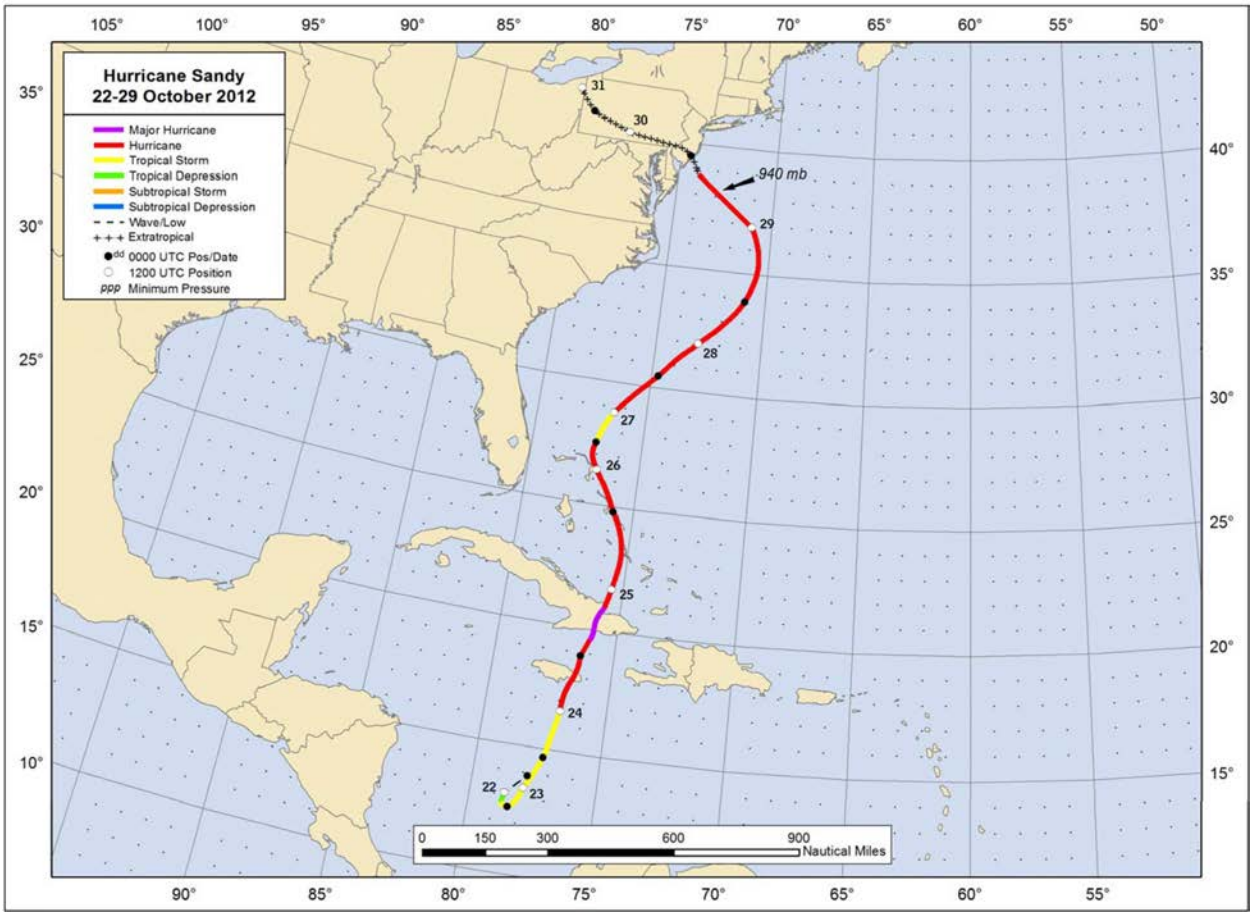

Figure 7.17. Post-storm best-track estimate of Hurricane Sandy. (Source: Blake et al. 2013.)

Hurricane Sandy was an extraordinarily large hurricane (Blake et al. 2013). Its size grew as it moved from the Bahamas to its landfall in New Jersey. The storm interacted with an upper-level trough over the northwestern Caribbean Sea and eastern Gulf of Mexico. As the storm moved north along the U.S. coast, its environment changed and initiated its transition into an extratropical storm aided by a warm front a few hundred miles northeast of its center and a weak stationary front on its northwest side. These interactions, while weakening the storm, also caused its wind and pressure fields to grow. As Sandy moved further north, the incomplete transition to an extratropical storm combined with its passage over the warm waters of the Gulf Stream, caused it to redevelop central convection and retain its tropical cyclone status. At the same time, well away from the core, frontal structures remained in the outer circulation, giving it hybrid characteristics. The storm never lost its large size and retained its hybrid characteristics through landfall.

Storm surge from Hurricane Sandy was the major cause of flooding in the coastal areas. USGS deployed 162 supplemental water-level and wave-height sensors (145 storm tide sensors [at 30-second intervals], 9 wave-height sensors [at 2-second intervals], and 8 real-time, rapid-deployment streamflow gauges) at 147 locations during October 26-29, 2012, prior to Sandy's landfall in New Jersey (Figure 7.18; USGS

2013). In addition, 62 sensors were deployed to measure barometric pressures at 30-second intervals. USGS also collect 950 high-water marks following Sandy.

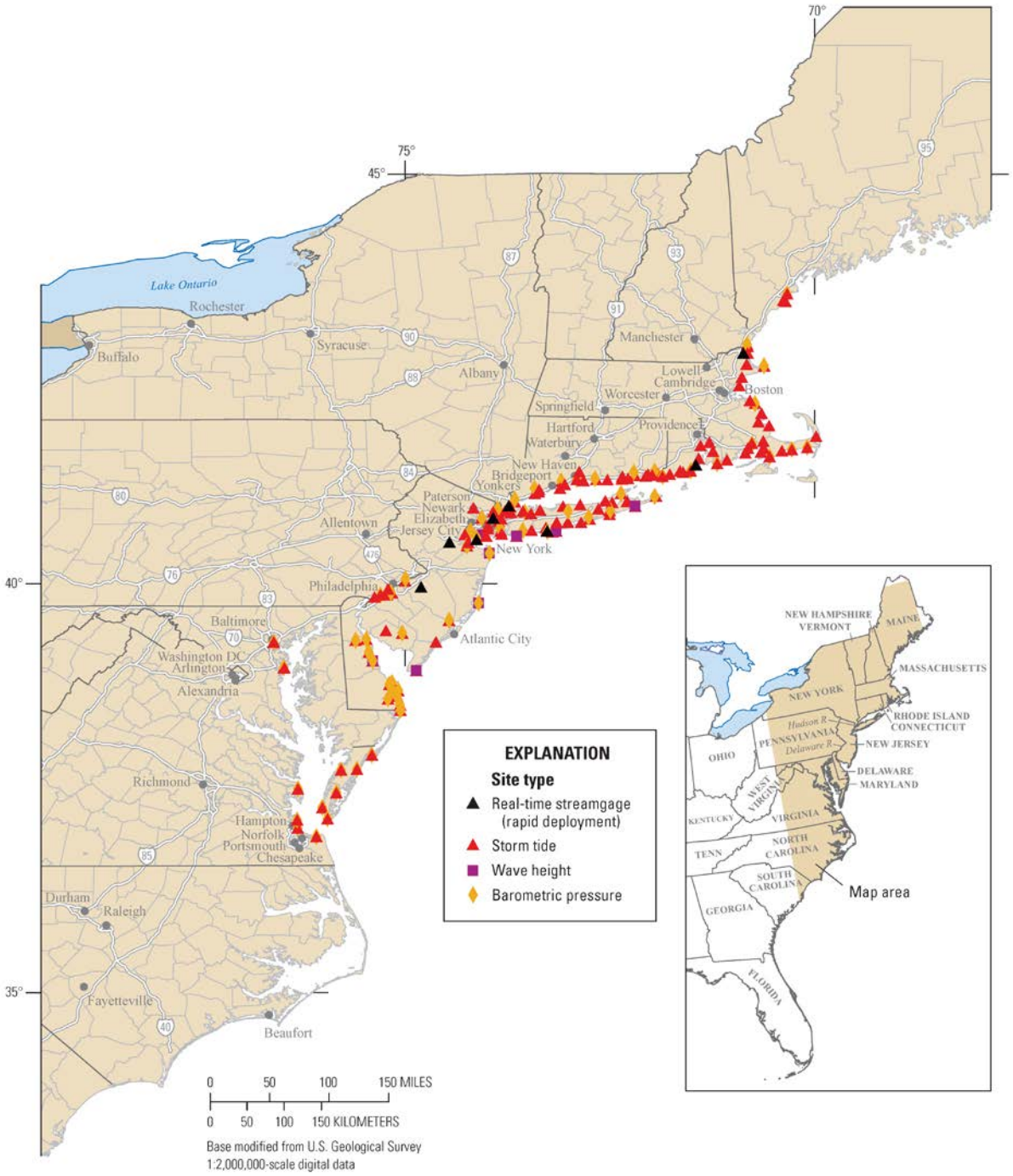

Figure 7.18. Locations of water-level, wave-height, and barometric-pressure sensors, and real-time streamflow gauges deployed for Hurricane Sandy. (Source: USGS 2013.)

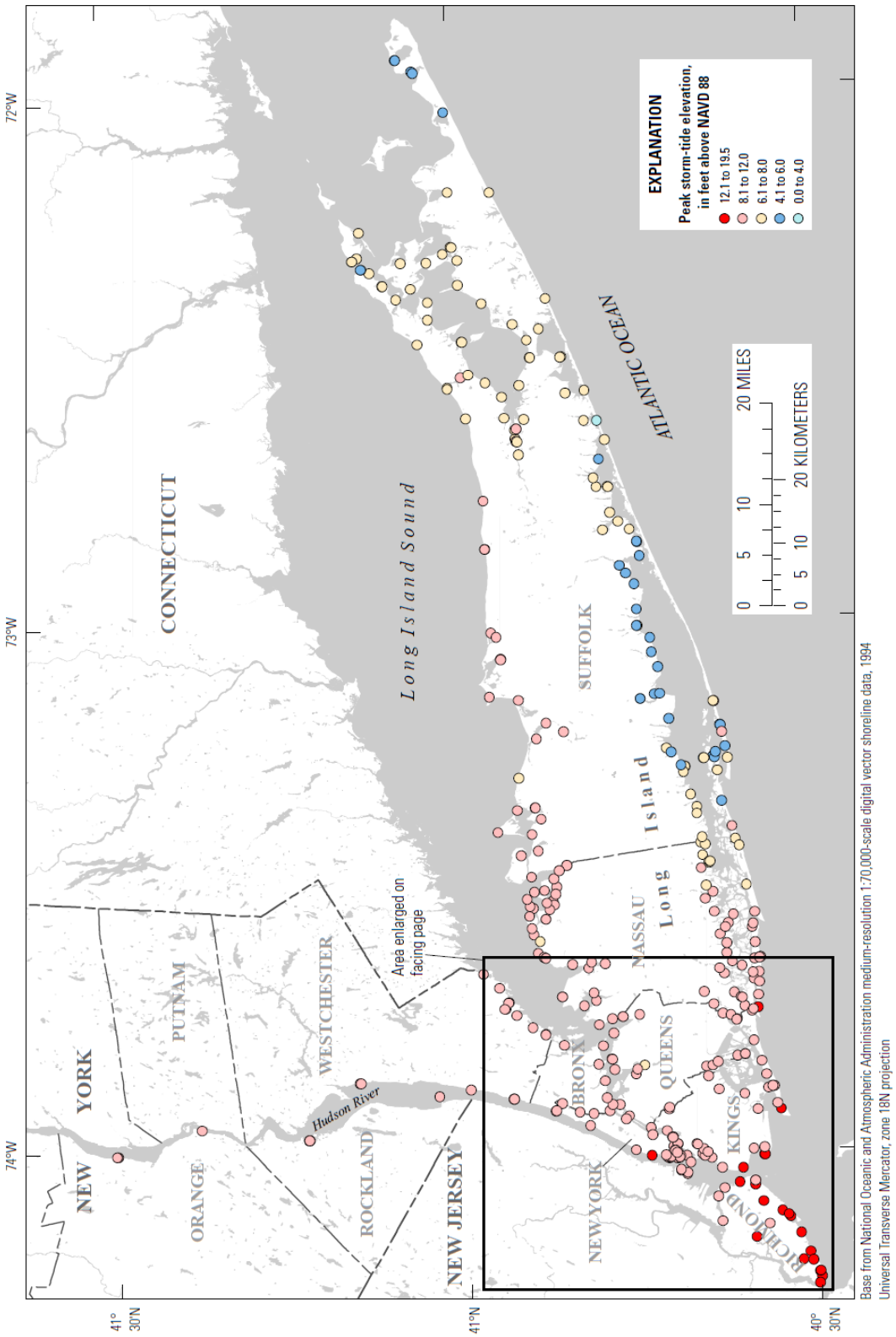

Figure 7.19. Peak storm tide elevations (ft. above NAVD88) in and near New York City. (Source: USGS 2015b.).

USGS (2015b) analyzed data collected at the supplemental monitoring locations. Peak storm tide elevations from Hurricane Sandy were (Figure 7.19) higher than those recorded during the December 1992 nor'easter at 24 of 27 nearly co-located sites and higher than those recorded during Tropical Storm Irene at all of 52 nearly co-located sites. Peak storm tide elevations from Hurricane Sandy also exceeded historical peak water-level elevations at 16 of 19 permanent monitoring sites.

USGS (2015b) also compared the peak storm tide elevations with the best available FEMA flood insurance studies, flood insurance rate maps, and preliminary work map data. Figure 7.20 shows the approximate AEPs of Hurricane Sandy storm tide stillwater elevations. Wind-wave effects, where expected to be greater than 3 ft, were removed using 3-minute mean peak elevations rather than observed water levels recorded at 30-second intervals. The AEPs of stillwater elevations during Hurricane Sandy were less than 0.002 east of New York City in Nassau and Suffolk Counties and at several locations up the Hudson River (Figure 7.20).

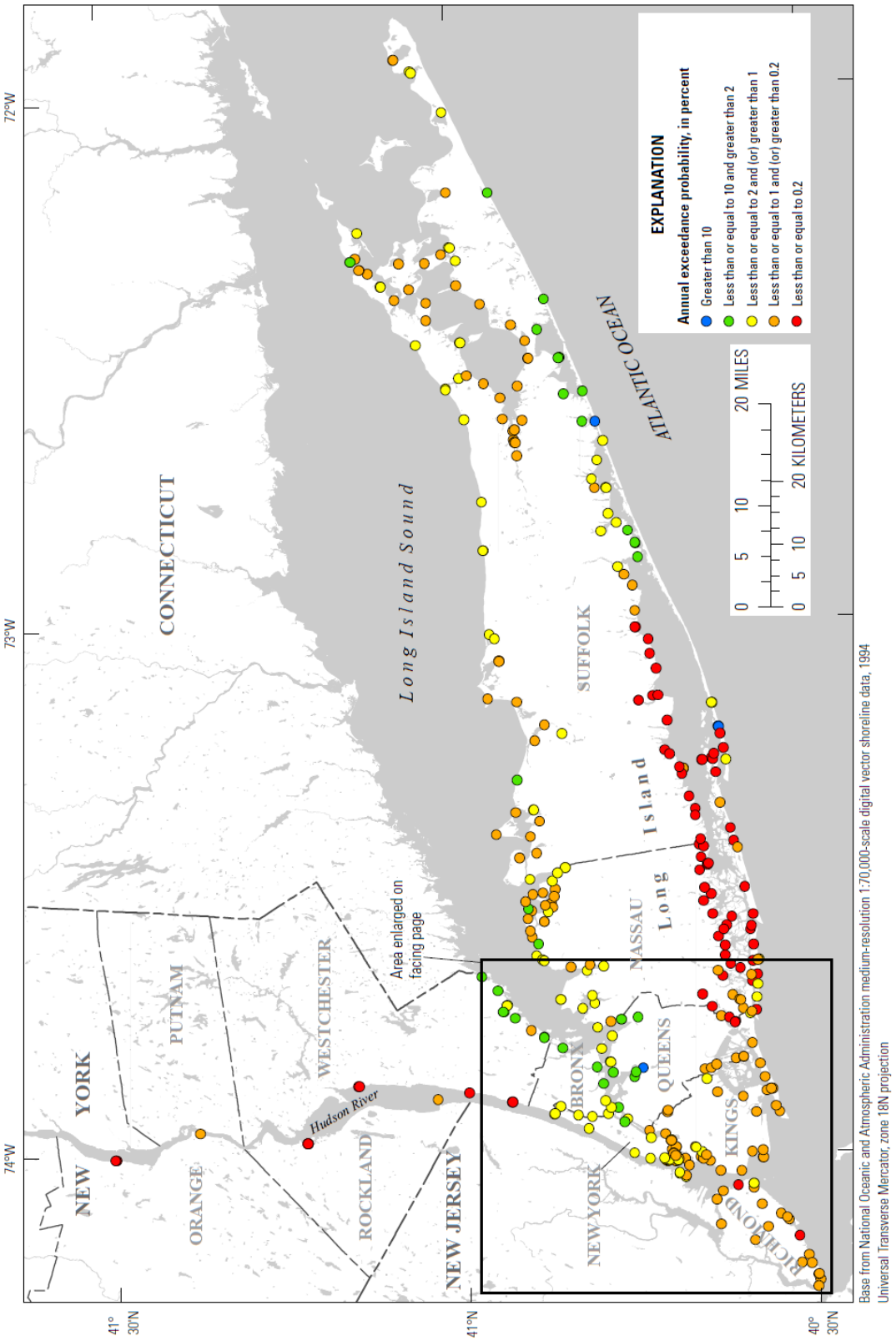

Figure 7.20. Annual exceedance probabilities (AEPs) for peak stillwater storm tide elevations from Hurricane Sandy. (Source: USGS 2015b.)

7.2 Hydrologic Cycle, Streamflow, and Floods

7.2.1 Observed Changes in Streamflow

Schulte et al. (2016) analyzed the influence of climate modes (NAO, Atlantic Multi-Decadal Oscillation [AMO], ENSO, PDO, and North Pacific Oscillation [NPO]) on Susquehanna, Delaware, and Hudson Rivers' streamflow from monthly to decadal scales. They used eight climate indices to represent the climate modes (Table 7.1). They investigated the relationships among streamflow, precipitation, temperature, and climate indices at monthly, seasonal, and annual timescales.

Table 7.1. Climate Indices Data (Schulte et al. 2016).

Climate Mode	Climate Index	Data	
		Source	Record Length
North Atlantic Oscillation	NAO	NCAR	1900-2010
Atlantic Multi-Decadal Oscillation	AMO	CPC	1900-2010
Polar Vortex Oscillation	AO	CPC	1950-2010
El Niño Southern Oscillation	ENSO	NCAR	1900-2010
	Niño 3.4	NCAR	1900-2010
Pacific Decadal Oscillation	PDO	UW	1900-2010
North Pacific Oscillation	NPO	NCAR	1900-2010
Pacific North American Teleconnection	PNA	CPC	1950-2010

NCAR – National Center for Atmospheric Research
CPC – Climate Prediction Center
UW – University of Washington

Mean monthly streamflows were obtained for Delaware Rive at Trenton, New Jersey (for the period 1913-2010), Hudson River above Lock 1 near Waterford, New York (for the period 1900-2010), and Susquehanna River at Harrisburg, Pennsylvania (for the period 1900-2010; Schulte et al. 2016). Streamflow at all of these gauges is influenced by regulation related to water supply, flood control, power plant uses, and interbasin diversions. Streamflow anomalies were computed by subtracting the climatological mean monthly streamflow from the monthly time series, which also results in the removal of the mean annual cycle of streamflow. Monthly precipitation and temperature data at stations above the streamflow gauges in the respective drainage basins were averaged and then also converted to anomalies. The streamflow anomalies and the annual cycles of precipitation and streamflow for the three river basins is shown in Figure 7.21.

Seasonal and annual linear Pearson correlation coefficients between streamflow and climate indices, precipitation and climate indices, and temperature and climate indices were computed (Schulte et al. 2016). The water year (October-September) was used as the annual time period and seasons were defined as winter (December–February or DJF), spring (March–May or MAM), summer (June–August or JJA), and fall (September–November or SON). Correlation analysis was also performed to estimate the influence of precipitation and temperature on streamflow. Because precipitation dominates the streamflow signal, a partial correlation coefficient was used to assess the influence of temperature on streamflow by removing the precipitation-streamflow dependence.

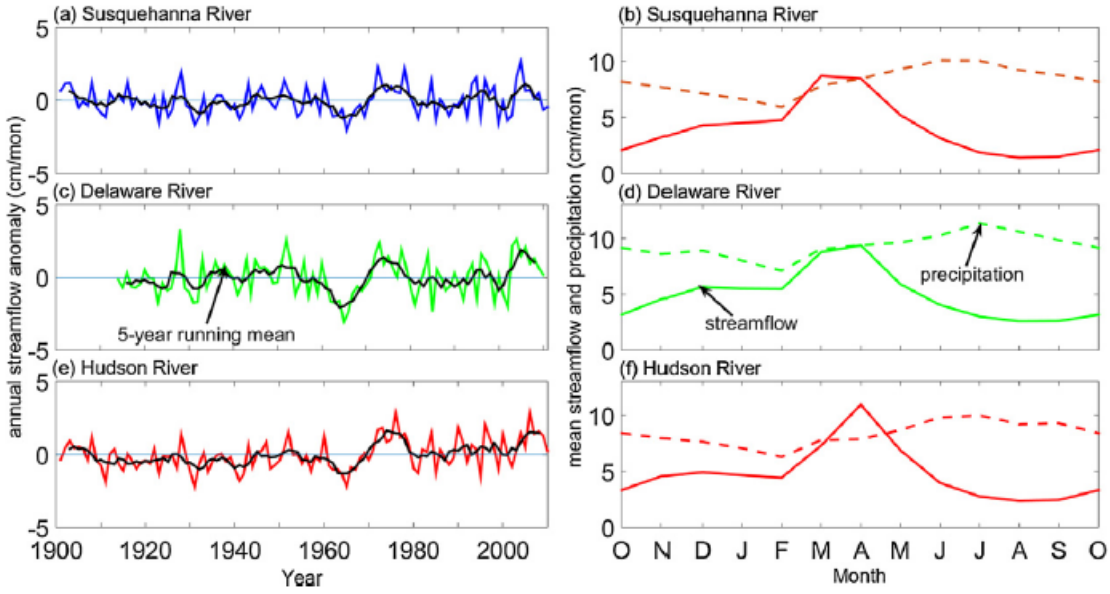

Figure 7.21. Left panels: 1900-2010 time series of annual average (colored lines) and five-year moving mean (black line) of streamflow anomalies. Right panels: mean annual cycle of streamflow (solid lines) and precipitation (dashed lines) for 1900-2010. (Source: Schulte et al. 2016.)

Schulte et al. (2016) noted that all river basins' streamflow in the 1900-1940 time period exhibited high-frequency variability. During 1950-1980, low-frequency variability became evident. The 1960s drought and the 1970s and 2000s wet periods are also seen in the streamflow anomalies time series for the three river basins. The mean annual cycles of streamflow for the three river basins show maxima in spring (MAM), minima in summer (JJA), and secondary maxima in fall (SON). The authors noted that these extrema are caused by the annual cycle of evapotranspiration and snowmelt, not precipitation. Precipitation has a weak annual cycle in all three river basins.

Figure 7.22 shows the ordinary and partial (lag 1) correlation coefficients between mean monthly precipitation and streamflow. All correlations were significant at the 5 percent level. The correlations are relatively low in the months of February, March, April, July, and November and relatively high in the month of May, June, August, September, October, and December. The authors suggested that some of the precipitation falling as snow may be responsible for streamflow being nearly equal to precipitation in the Delaware and Susquehanna River Basins during March and April, yet the streamflow-precipitation correlation remains low in those months. The authors attributed the low July streamflow-precipitation correlations to contributions from lagged baseflow and high evapotranspiration.

Figure 7.23 shows the partial correlation coefficients (with the dependence of streamflow on precipitation removed) between mean monthly maximum temperature and streamflow for the three river basins. The partial correlations were significant and positive during the cold season for all three river basins. The authors noted that this behavior is consistent with higher cold season temperatures generating greater streamflow. They also noted that the negative partial correlations during summer are physically consistent with higher temperatures promoting higher evapotranspiration and consequently, lower streamflow amounts.

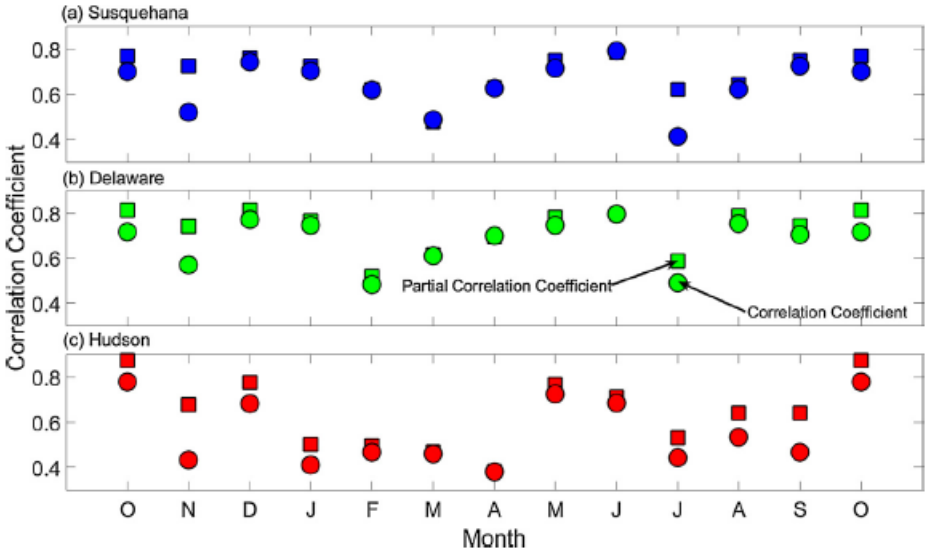

Figure 7.22. Ordinary and partial (lag 1) correlation coefficients between mean annual streamflow and precipitation in the Susquehanna, Delaware, and Hudson River Basins. (Source: Schulte et al. 2016.)

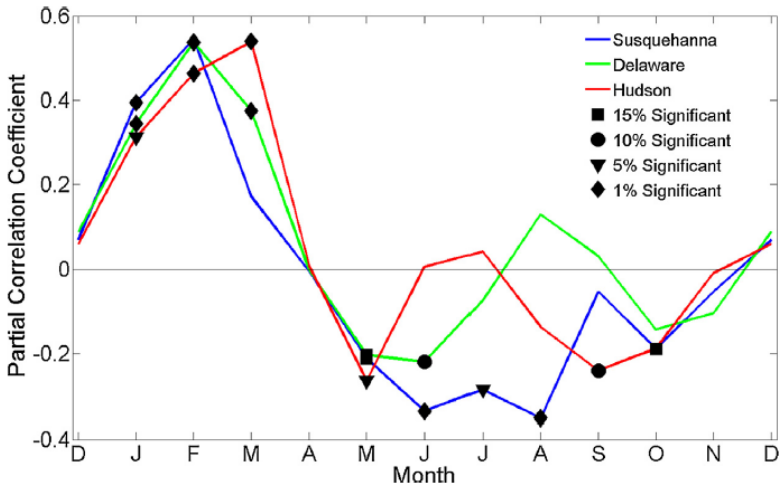

Figure 7.23. Partial correlation coefficients (with the effects of dependence of streamflow on precipitation removed) between mean monthly maximum temperatures and streamflow for the Susquehanna, Delaware, and Hudson River Basins. (Source: Schulte et al. 2016.)

Schulte et al. (2016) found some correlations between climate indices and streamflow, precipitation, and temperatures in the three river basins (Table 7.2). Generally, correlations seem to be weak; however, some interesting commonalities were observed. In all three river basins, winter temperature anomalies seemed to be moderately and positively correlated with NAO and AO while the fall temperature anomalies seemed to be weakly and positively correlated with AMO. AMO showed weak and positive correlation with fall precipitation anomalies in Delaware River Basin, but no correlation in the other two river basins. In the Delaware River Basin, NPO showed weak and positive correlation with fall precipitation anomalies and weak and negative correlation with spring precipitation anomalies. PNA also showed a weak and positive correlation with spring precipitation in the Delaware River Basin. In the Susquehanna River Basin, winter streamflow anomalies were weakly and negatively correlated with AMO while fall streamflow anomalies were weakly and positively correlated with NPO and weakly and

negatively correlated with PNA. In the Delaware River Basin, fall streamflow anomalies were weakly and positively correlated with AMO and NPO while spring streamflow anomalies were weakly and positively correlated with PNA. In the Hudson River Basin, fall streamflow anomalies were weakly and negatively correlated with PNA.

Table 7.2. Correlations between selected climate indices and hydrometeorological parameters. All shown correlations are significant at 5 percent level. (Source: Schulte et al. 2016.)

Climate Index	River Basin	Hydro-meteorological Parameter	Months (correlation coefficients significant at 5 percent)	Seasons (correlation coefficients significant at 5 percent)	Annual correlation coefficient significant at 5 percent
NAO	SRB	Q			
		P			
		T	Jan, Feb, Mar, Apr, Oct, Dec (0.38, 0.43, 0.34, 0.33, 0.31, 0.50)	DJF (0.49)	
	DRB	Q	Oct (-0.32)		
		P	Aug (0.25)		
		T	Jan, Feb, Mar, Apr, Oct, Dec (0.37, 0.41, 0.32, 0.30, 0.28, 0.53)	DJF (0.50)	
	HRB	Q	Jan (0.26)		
		P	Jan (0.26)		
		T	Jan, Feb, Jul, Oct, Dec (0.38, 0.40, 0.32, 0.30, 0.49)	DJF (0.51)	
AMO	SRB	Q	Jun, Oct (-0.26, 0.26)	JJA (-0.26)	
		P	Jun, Oct, Nov (-0.26, 0.49, -0.30)		
		T		SON (0.28)	
	DRB	Q	Jun, Oct (-0.30, 0.44)	SON (0.31)	
		P	Jun, Oct (-0.31, 0.45)	SON (0.26)	
		T	Sep (0.30)	SON (0.30)	
	HRB	Q	Oct (0.31)		
		P	May, Oct, Nov (-0.31, 0.48, -0.39)		
		T	Sep (0.28)	SON (0.28)	
AO	SRB	Q	Sep (0.34)		
		P			

Climate Index	River Basin	Hydro-meteorological Parameter	Months (correlation coefficients significant at 5 percent)	Seasons (correlation coefficients significant at 5 percent)	Annual correlation coefficient significant at 5 percent
		T	Jan, Feb, Mar, Apr, Oct, Nov, Dec (0.42, 0.37, 0.32, 0.28, 0.35, 0.36, 0.58)	DJF (0.53)	
	DRB	Q	Sep (0.34)		
		P			
		T	Jan, Feb, Mar, Oct, Nov, Dec (0.41, 0.36, 0.31, 0.39, 0.36, 0.56)	DJF, JJA (0.53, 0.28)	
	HRB	Q	May, Sep (0.30, 0.32)		
		P	May (0.32)		
		T	Jan, Feb, Jul, Oct, Nov, Dec (0.41, 0.27, 0.37, 0.42, 0.40, 0.53)	DJF, JJA, SON (0.52, 0.37, 0.31)	
ENSO	SRB	Q	Feb, Nov (0.27, -0.30)		
		P	Apr, Nov (-0.30, -0.30)		
		T			
	DRB	Q	May (0.30)		
		P	Apr, May (-0.26, 0.33)		
		T			
	HRB	Q			
		P	Feb, Nov (0.27, -0.30)		
		T	Mar (-0.30)		
Niño 3.4	SRB	Q	Feb (-0.30)		
		P	Apr (0.38)		
		T	Oct (-0.28)	SON (-0.25)	
	DRB	Q	Feb, Apr (-0.28, 0.27)		
		P	Apr (0.37)		
		T	Oct (-0.26)		
	HRB	Q			
		P	Feb (-0.32)		
		T	Mar, Aug (0.29, -0.27)		

Climate Index	River Basin	Hydro-meteorological Parameter	Months (correlation coefficients significant at 5 percent)	Seasons (correlation coefficients significant at 5 percent)	Annual correlation coefficient significant at 5 percent
PDO	SRB	Q			
		P	Apr (0.33)		
		T	Jan, Oct, Nov (-0.30, -0.38, -0.39)	SON (-0.43)	
	DRB	Q	Apr, Aug (0.27, -0.25)		
		P	Apr (0.29)		
		T	Jan, Oct, Nov (-0.24, -0.39, -0.36)	SON (-0.42)	
	HRB	Q			
		P	Feb (-0.28)		
		T	Oct, Nov (-0.40, -0.37)	SON (-0.47)	
NPO	SRB	Q	Jun, Sep, Nov (0.26, 0.26, 0.41)	SON (0.35)	
		P			
		T	Jan, Nov, Dec (0.29, 0.32, 0.33)		
	DRB	Q	Apr, Sep, Nov (-0.34, 0.25, 0.28)	MAM, SON (-0.37, 0.36)	
		P	Apr (-0.29)	MAM, SON (-0.31, 0.30)	
		T	Jan, Nov, Dec (0.25, 0.33, 0.27)		
	HRB	Q	Sep (0.29)	SON (0.29)	
		P			
		T	Oct, Nov, Dec (0.27, 0.34, 0.26)		
PNA	SRB	Q	Nov (-0.34)	SON (-0.30)	-0.26
		P	Apr (0.27)		
		T	Jan, May, Sep, Nov (-0.30, -0.26, 0.34, -0.29)		
	DRB	Q	Apr (0.39)	MAM (0.36)	
		P	Apr (0.38)	MAM (0.34)	
		T	Jan, Sep, Nov (-0.25, 0.30, -0.31)		
	HRB	Q	Sep (-0.27)		

Climate Index	River Basin	Hydro-meteorological Parameter	Months (correlation coefficients significant at 5 percent)	Seasons (correlation coefficients significant at 5 percent)	Annual correlation coefficient significant at 5 percent
		P			
		T	Sep, Oct, Nov (0.37, -0.25, -0.30)		

SRB – Susquehanna River Basin, DRB – Delaware River Basin, HRB – Hudson River Basin
Q – streamflow anomaly, P – precipitation anomaly, T – temperature anomaly

Berton et al. (2017) investigated the relationships between climate indices AMO and NAO and streamflow and precipitation anomalies in the Merrimack River Basin (Figure 7.24). Streamflow data from eight small undisturbed catchments in the Hubbard Brook Experimental Forest and 13 USGS streamflow gauges were used in the study; the median record length was 55 years. In addition to the undisturbed catchments in the experimental forest, two Merrimack subbasins had minimal land disturbance. Eleven Merrimack subbasins have undergone streamflow regulation, land use and cover changes, and/or urbanization. Streamflow discharge data from all 21 gauges were divided by the respective drainage areas and expressed in depth per unit area. The correlation analysis was performed at annual timescale (water year) as well at seasonal timescales (winter – DJF, spring – MAM, summer – JJA, and fall – SON). Anomalies were computed as standardized monthly values.

AMO and NAO data were obtained from NCAR. The authors defined positive phase of the climate indices as those greater than or equal to mean plus half the standard deviation and negative phase as those less than or equal to mean minus half the standard deviation; this resulted in the positive and negative phases of AMO being greater than 0.2 or less than -0.2, respectively. The resulting positive and negative phases of NAO were greater than 0.5 or less than -0.5, respectively.

First, Berton et al. (2017) performed a t-test to determine if the standardized annual and seasonal discharges were different between the positive and negative phases of the two climate indices. When the mean standardized discharge was found to be statistically different between the two phases, Pearson's correlation coefficients were determined between the discharge and the two climate indices. The authors classified the annual and seasonal discharges into dry, average, and wet classes based on deviations from the long-term mean. Finally, the relative frequencies of the occurrences of dry, average, and wet conditions were estimated. The estimated correlations of precipitation and discharge showed that three scenarios corresponding to AMO were significantly ($p \leq 0.2$) predictive of discharge throughout the Merrimack River Basin: (1) current year's discharge conditions predicted by previous year's AMO, (2) fall streamflow conditions predicted by previous summer AMO, and (3) winter discharge conditions predicted by previous spring AMO. These three scenarios are labeled "Annual -1 Lag," "Fall-1 Lag," and "Winter-2 Lag" in Figure 7.25. The authors found that only summer discharge was predicted significantly by previous winter NAO, i.e., at a 2-season lag. The correlations for the selected subbasins of Merrimack River Basin are shown in Figure 7.25.

Berton et al. (2017) noted that regulated subbasins were not treated differently than unregulated ones in their study. Also, when AMO was greater than or equal to 0.2, the magnitudes of annual correlation coefficients were affected by regulation and other changes. As shown in Figure 7.25, for the small, undisturbed, experimental forest subbasins, the annual 1-year lag correlation coefficients were 0.8 and 0.6, respectively. However, for larger subbasins affected by regulation, the correlation coefficients declined to about 0.5 (Figure 7.25, top-left panel). When AMO was in its positive phase, NAO's showed negative correlation with precipitation and discharge in the experimental forest subbasins, but was not predictive otherwise (Figure 7.25, top-left panel). When AMO was in its negative phase, NAO showed

negative correlations with annual 1-year lag precipitation and streamflow in large subbasins and positive correlations with discharge in experimental forest subbasins (Figure 7.25, top-right panel). Correlations with NAO in both its phases were generally weak, except for summer 2-season lag precipitation in experimental forest subbasins (Figure 7.25, bottom panel).

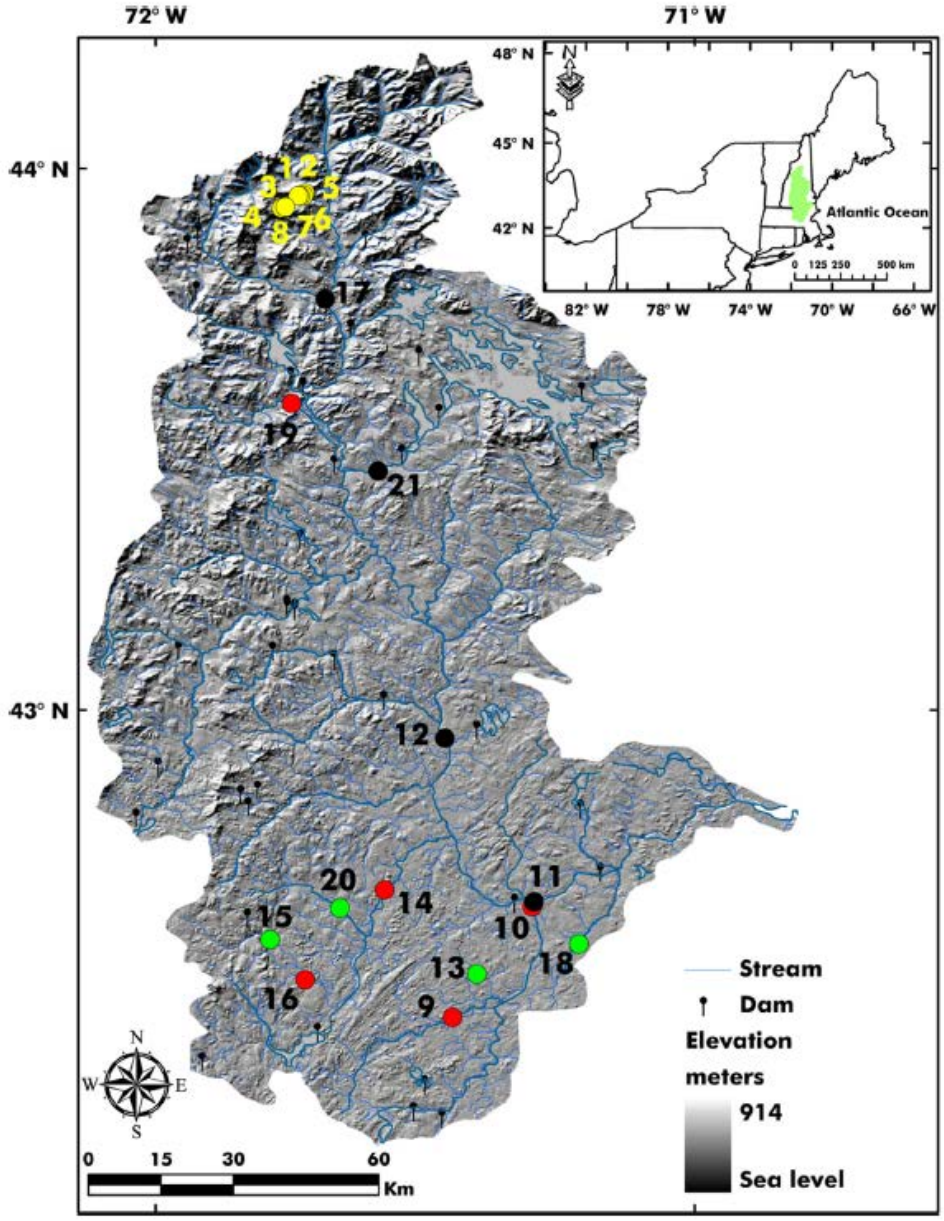

Figure 7.24. The Merrimack River Basin showing topography, streams, dams, and streamflow gauges. Yellow dots represent streamflow gauges in the Hubbard Brook Experimental Forest (drainage areas less than 1 km^2), green dots represent small drainage area streamflow gauges (drainage areas less than 200 km^2), black dots represent medium drainage area streamflow gauges (drainage areas less than 1,000 km^2), and red dots represent large drainage area streamflow gauges (drainage areas greater than 1,000 km^2). (Source: Berton et al. 2017.)

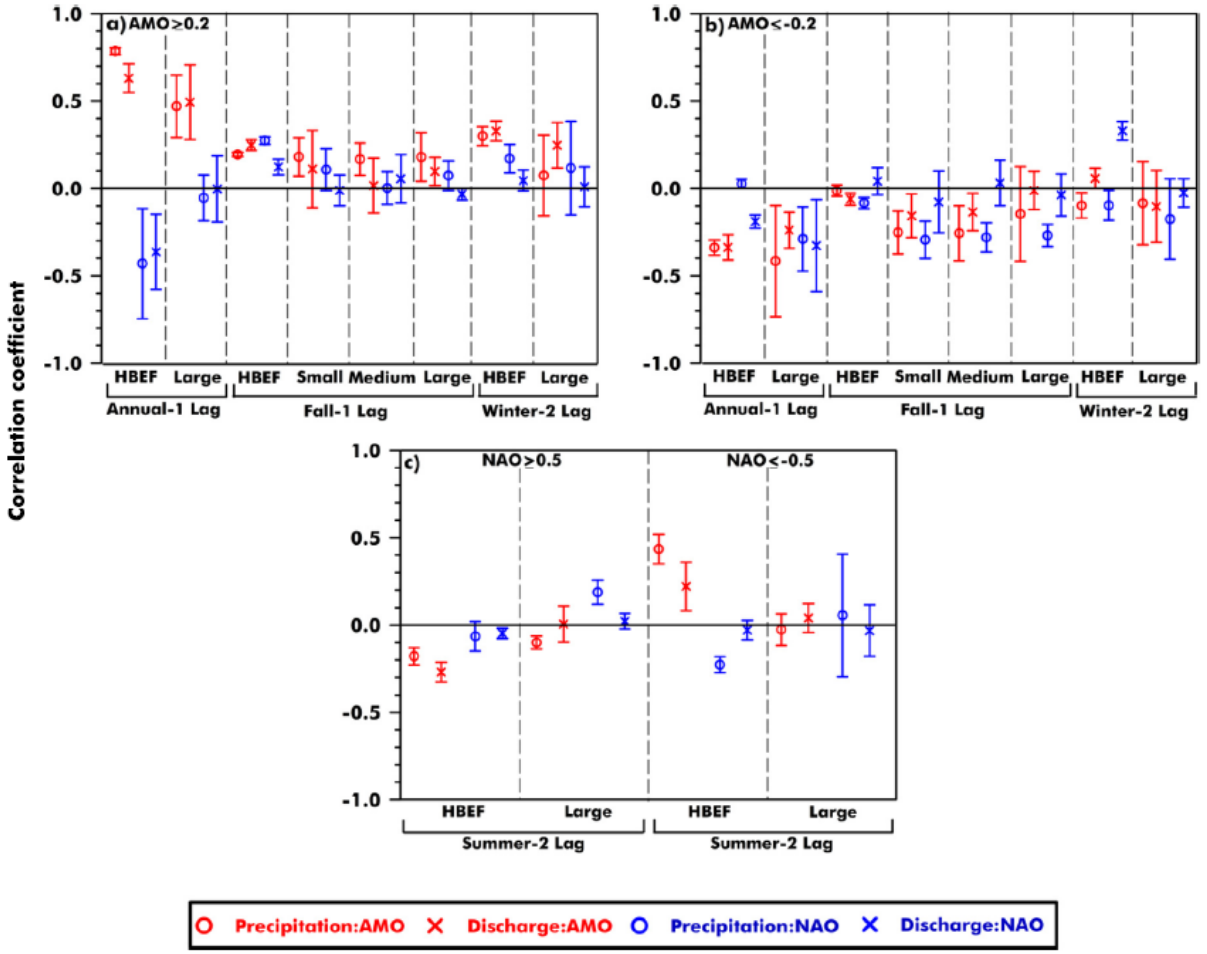

Figure 7.25. Statistically significant correlations between precipitation and discharge anomalies with AMO and NAO in various subbasins of the Merrimack River Basin. (Source: Berton et al. 2017.)

Dudley et al. (2017) evaluated historical changes in snowmelt-related streamflow timing using the winter-spring center volume date (WSCVD). Winter-spring period is defined as January 1 through May 31 for eastern U.S. The WSCVD is defined as the date when half of the total streamflow volume during the winter-spring period was recorded at the streamflow gauge. From among the reference streamflow gauges that have minimal human disturbance or alteration included in the Geospatial Attributes of Gages for Evaluating Streamflow (GAGES II) dataset (Falcone 2011), the authors selected those streamflow gauges from the Hydroclimatic Data Nework-2009 (Lins 2012) that had a minimum of 20 years of daily streamflow discharge data and whose drainage areas received an average of 30 percent or more of total precipitation as snow. The authors also selected USHCN meteorological stations nearest the chosen streamflow gauges. The study used 75 streamflow gauges and 58 USHCN stations (Figure 7.26).

Dudley et al. (2017) estimated trends in the WSCVD for three time periods—1920-2014 (15 gauges), 1940-2014 (54 gauges), and 1960-2014 (75 gauges). WSCVD trends indicated earlier dates at most (80-91 percent) of the streamflow gauges (Figure 7.27). The WSCVD trends in the northeast U.S. indicate earlier occurrence of WSCVD, particularly in the more recent time periods. The median advancement of WSCVD for eastern gauges was estimated to be 8.2 days for the 1940-2014 period and 8.6 days for the 1960-2014 period. Many gauges in the northeast U.S. show significant advancement of WSCVD by nearly 10 days (Figure 7.27).

Dudley et al. (2017) noted that March and April mean air temperatures significantly correlated with WSCVD at all eastern streamflow gauges, explaining about 39 percent of the variability of WSCVD in the eastern U.S. However, precipitation had little correlation with WSCVD, indicating that snowmelt timing in spring is the main driver for WSCVD trends. The authors also found that earlier WSCVD in the 1960-2014 period was correlated with positive phase of May AMO.

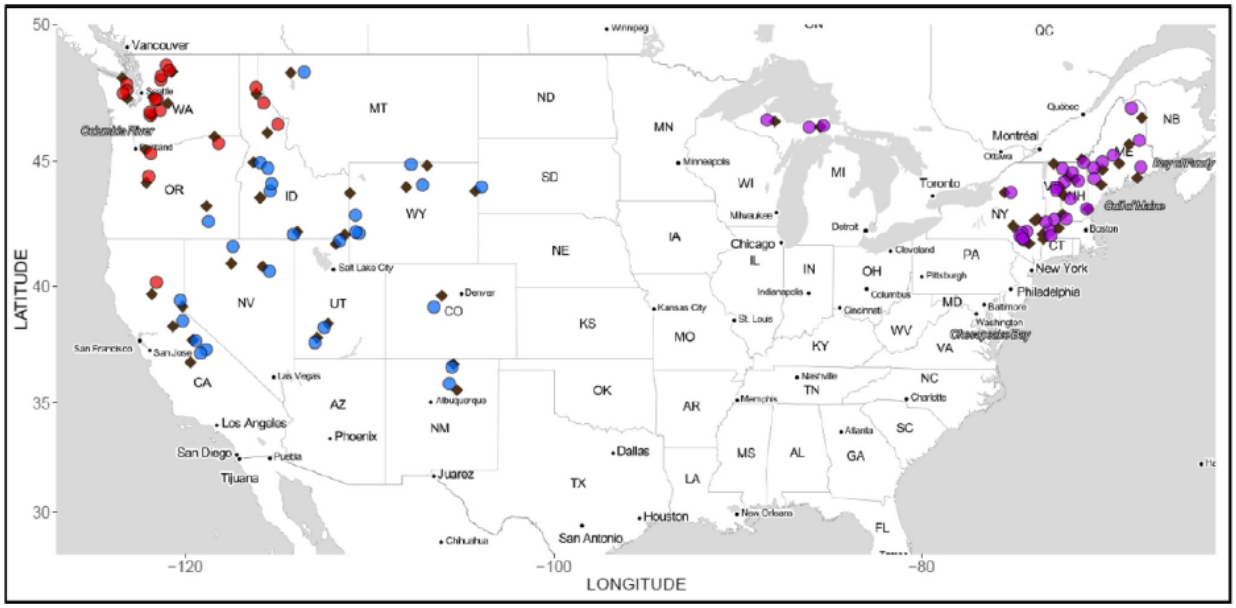

Figure 7.26. The 75 streamflow gauges (circles) and 58 meteorological stations used by Dudley et al. (2017).

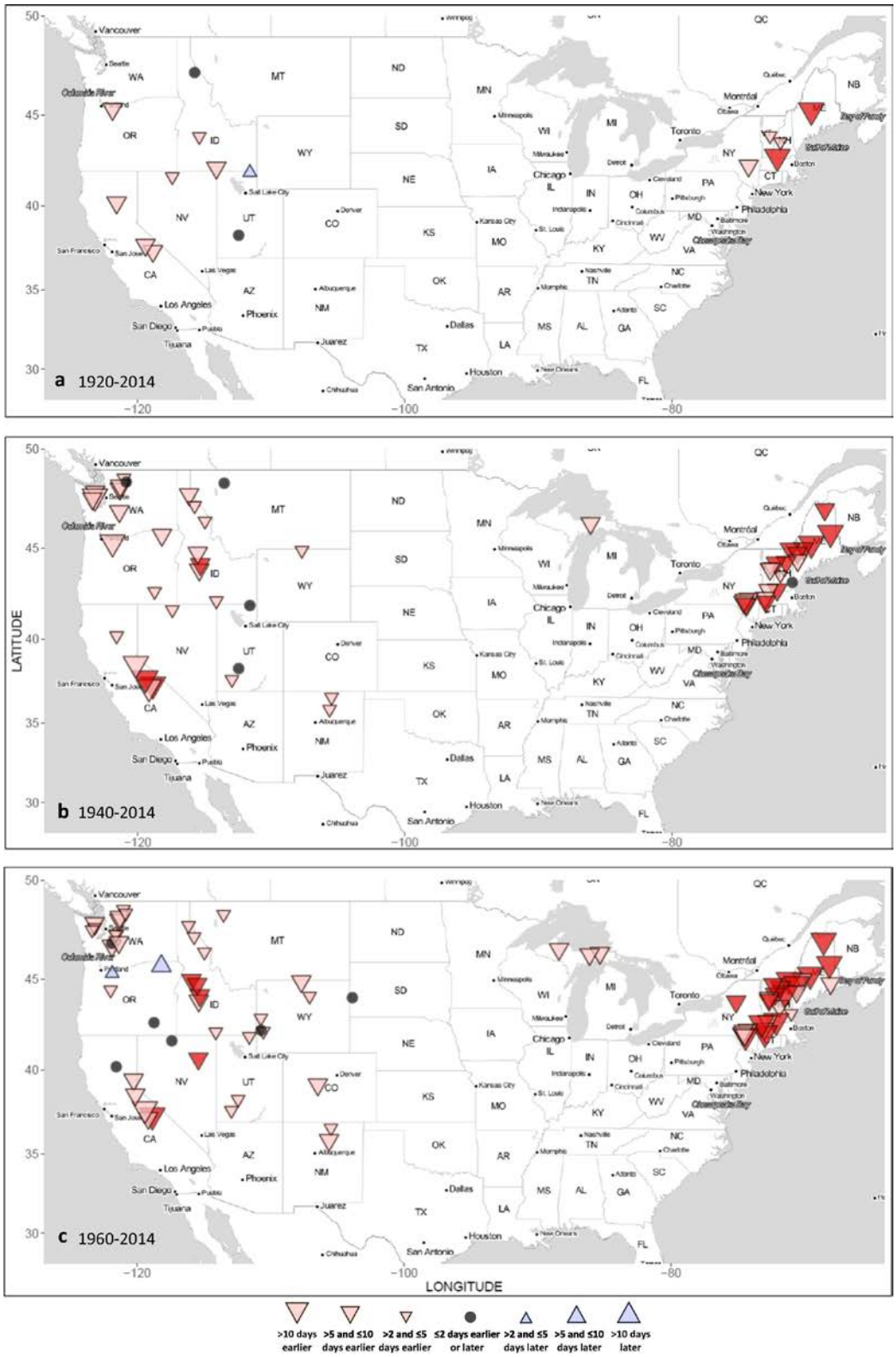

Figure 7.27. Trends in WSCVD for three selected time periods. Red shading indicates earlier WSCVD dates and blue shading indicates later WSCVD dates. Darker colors indicate significant ($p < 0.05$) trends. (Source: Dudley et al. 2017.)

Collins (2019) evaluated the change in flood seasonality over the New England and Mid-Atlantic regions of the northeast U.S. (Figure 7.28). The study used streamflow data from 90 gauges whose drainage basins are minimally disturbed. A peaks-over-threshold analysis was performed with flood records that on average, had 85 years of data and three peaks per year.

Collins (2019) grouped floods at each streamflow gauge by month and computed monthly relative frequencies adjusted such that all months were nominally 30 days. Significant flood seasons were then identified by comparing the observed monthly relative frequencies with the theoretical variability of a nonseasonal model (a circular uniform distribution function used to generate synthetic records). Observed monthly relative frequencies were then categorized into five possible classes (Figure 7.29).

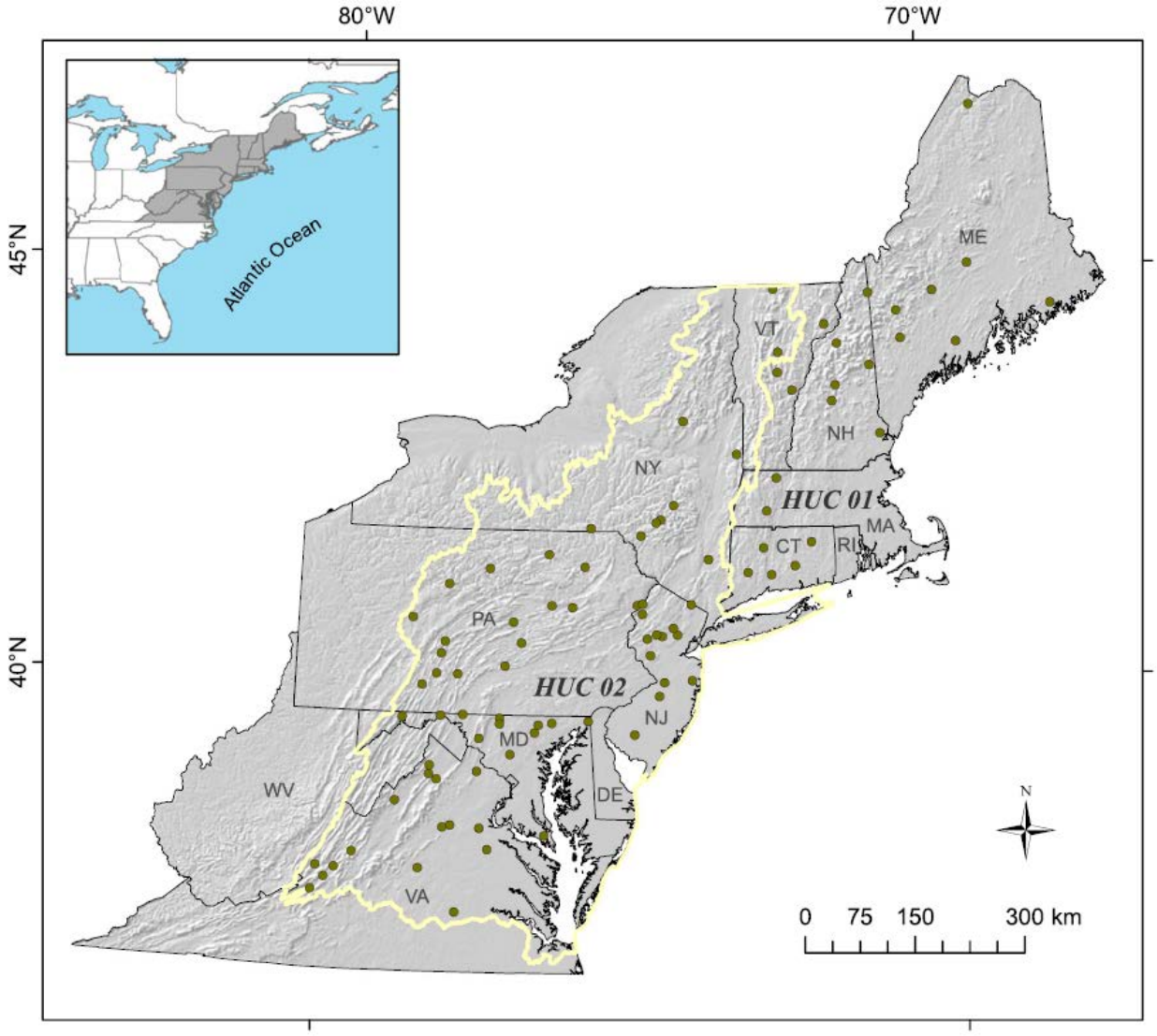

Figure 7.28. Study area used by Collins (2019). The dots show the location of streamflow gauges used in the study.

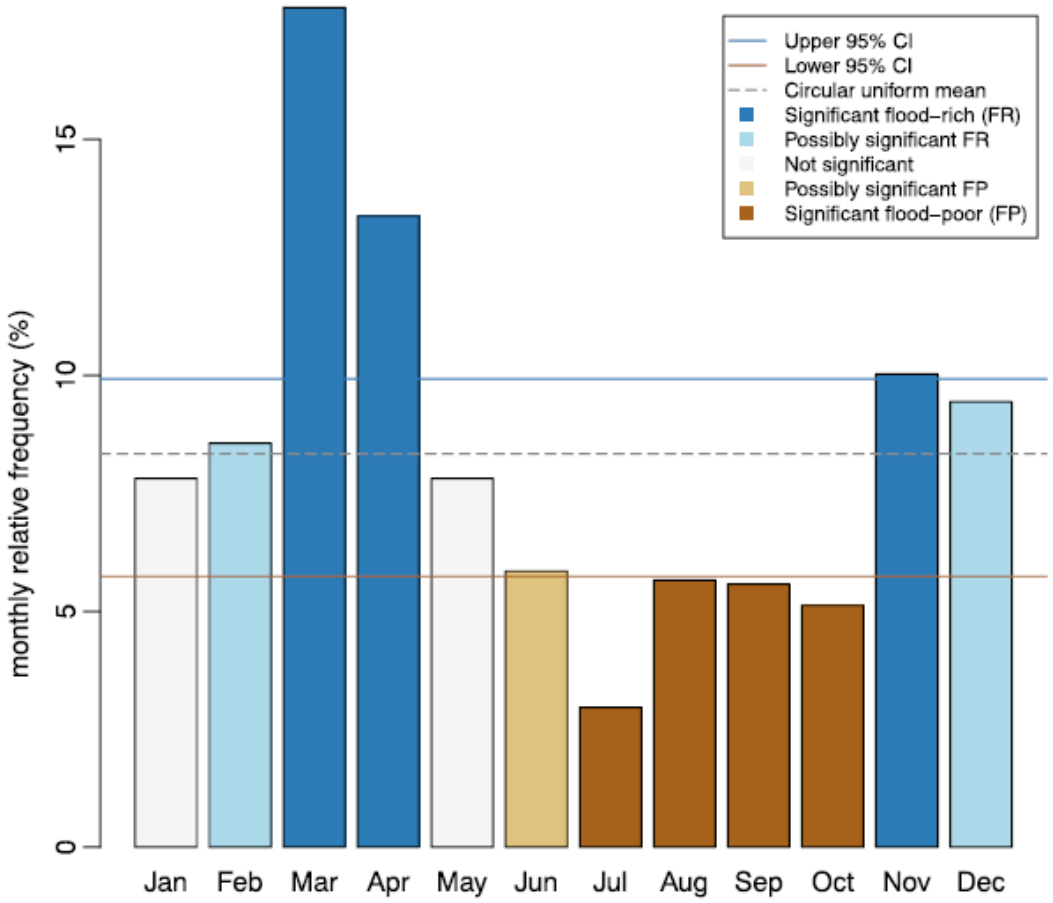

Figure 7.29. Illustrative example of flood seasonality classification. (Source: Collins 2019.)

Collins (2019) manually classified significant flood-rich (see Figure 7.29) months at streamflow gauges within or spanning seasons defined as winter (DJF), spring (MAM), summer (JJA), and fall (SON). Some streamflow gauges showed multiple flood seasons and modality was also included in the classification. The author assessed within-season flood timing trends by converting day-of-year of floods to angular values. The angular values were tested using Mann-Kendall nonparametric test to assess if the values for a season increased (flood occurred later) or decreased (floods occurred earlier). Each flood season at sites with multiple flood seasons was analyzed separately because the different flood seasons could result from different flood-causing mechanisms. Examples of bimodal flood seasonality and unimodal winter-spring seasonality are shown in left and right panels of Figure 7.30, respectively.

The streamflow gauges were classified into 11 seasonal patterns of which four were unimodal, six were bimodal, and one was trimodal (Collins 2019). Over 90 percent of the gauges belonged to three types (Figure 7.31). Of all 90 streamflow gauges, 36 had a unimodal spring (MAM) pattern, 20 had a unimodal winter-spring (DJF-MAM) pattern, and 26 had a bimodal pattern with a spring (MAM) and a fall-winter (SON-DJF) mode. The remaining eight streamflow gauges were not classified into the dominant three types.

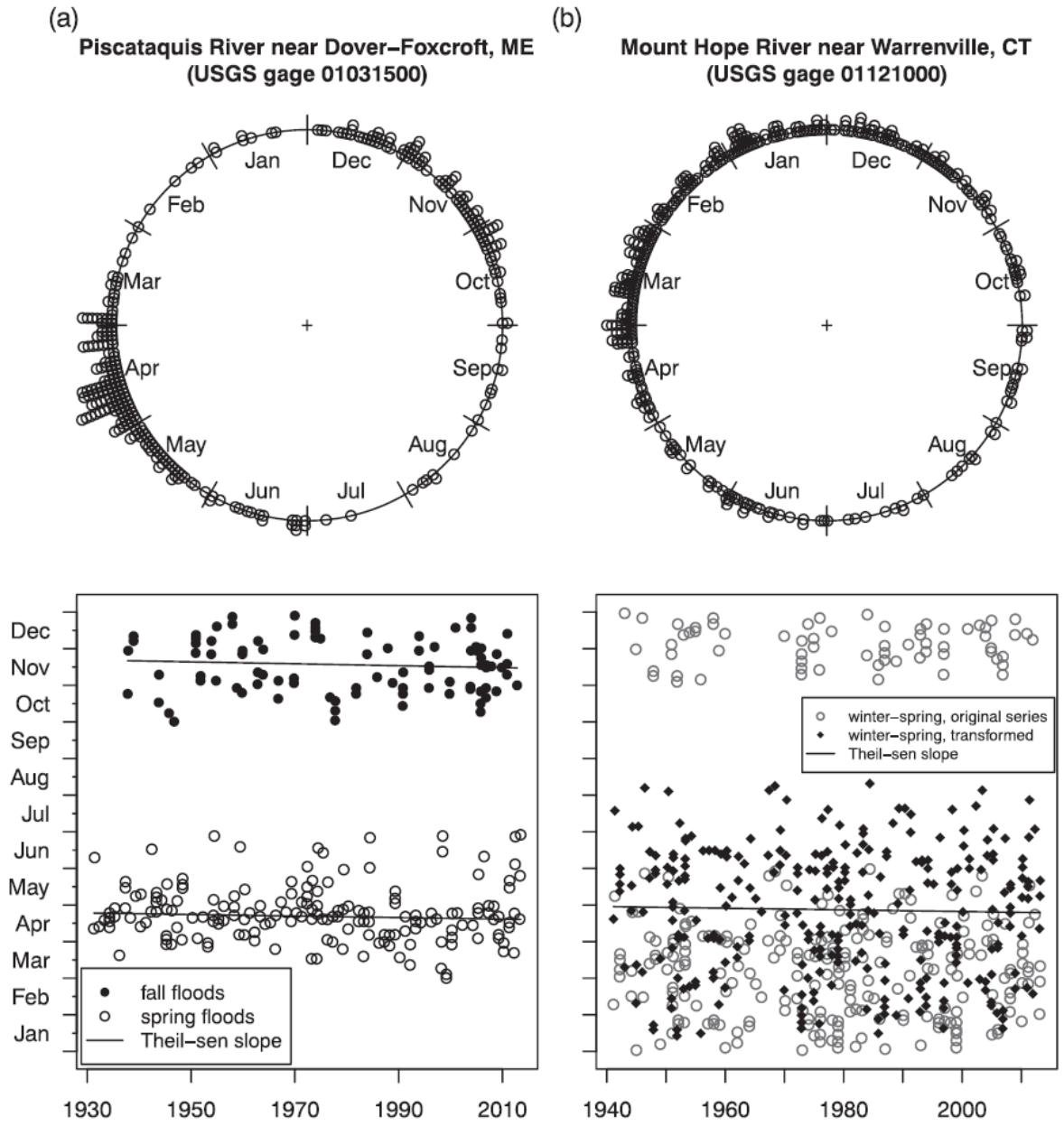

Figure 7.30. Examples of: (a) left panel: bimodal flood seasonality shown in circular coordinates (top) and trend analyses for spring and fall (bottom) and (b) right panel: unimodal winter-spring flood seasonality (top) and trend analysis (bottom). The vertical axes on the trend plots are day-of-year angular values labeled as months of the year. Transformation refers to slightly increasing or decreasing the angular value of flood dates by a constant, if the flood season spanned the end/start of the year, such that floods would plot correctly in a Cartesian space for trend analysis. In these examples, the trends are negative and not statistically significant at $p < 0.05$. (Source: Collins 2019.)

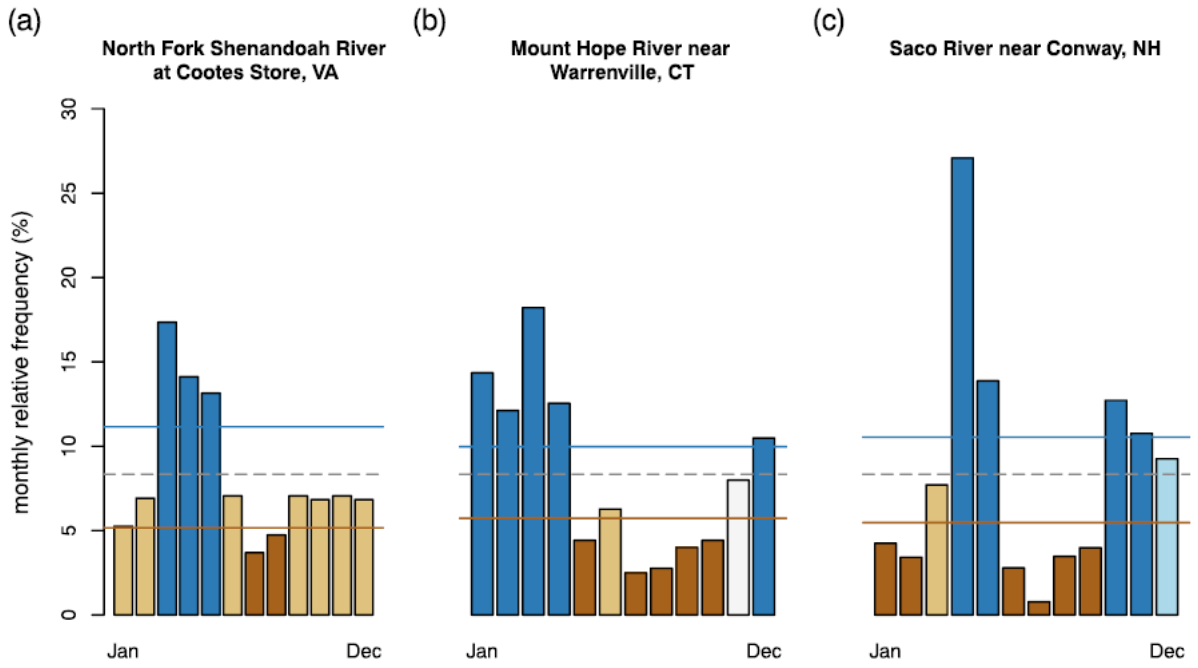

Figure 7.31. The three dominant flood seasonality types: (a) unimodal spring, (b) unimodal winter-spring, and (c) bimodal spring and fall-winter patterns. (Source: Collins 2019.)

Table 7.3. Within-season trends of earlier and later flood timing. (Source: Collins 2019.)

	Season 1			Season 2			Season 3		
	n	Later	Earlier	*n*	Later	Earlier	*n*	Later	Earlier
Spring	63	41 (2)	22 (1)						
Winter–spring	21	14 (0)	7 (1)						
Winter	5	0 (0)	5 (2)	12	8 (0)	4 (1)			
Summer	1	0 (0)	1 (0)	4	1 (0)	3 (0)			
Fall				9	5 (0)	4 (0)	2	2 (1)	0 (0)
Fall–winter				6	2 (0)	4 (0)			
Total	90	55 (2)	35 (4)	31	16 (0)	15 (1)	2	2 (1)	0 (0)

Note. Values in parentheses indicate the number of stations with *p* values < 0.05.

Collins (2019) noted that the streamflow gauges show a mix of earlier and later within-season trends with very few that are statistically significant (Table 7.3). The author concluded that the historical flood seasons have been stable in the annual cycle across the region. However, the author also examined if previously documented trends in annual flood counts were driven by changes in frequency of floods during cold or warm seasons. Figure 7.32 shows the trends in time for all-water-year floods, cold season (Nov-May) floods, and warm season (Jun-Oct) floods. The full water year and the warm season trends are

highly significant but the cold season trend is not significant. Collins (2019) concluded that the upward trend in the warm season flood counts is an important driver to the increasing trends in peaks-over-threshold counts per water year documented by other researchers.

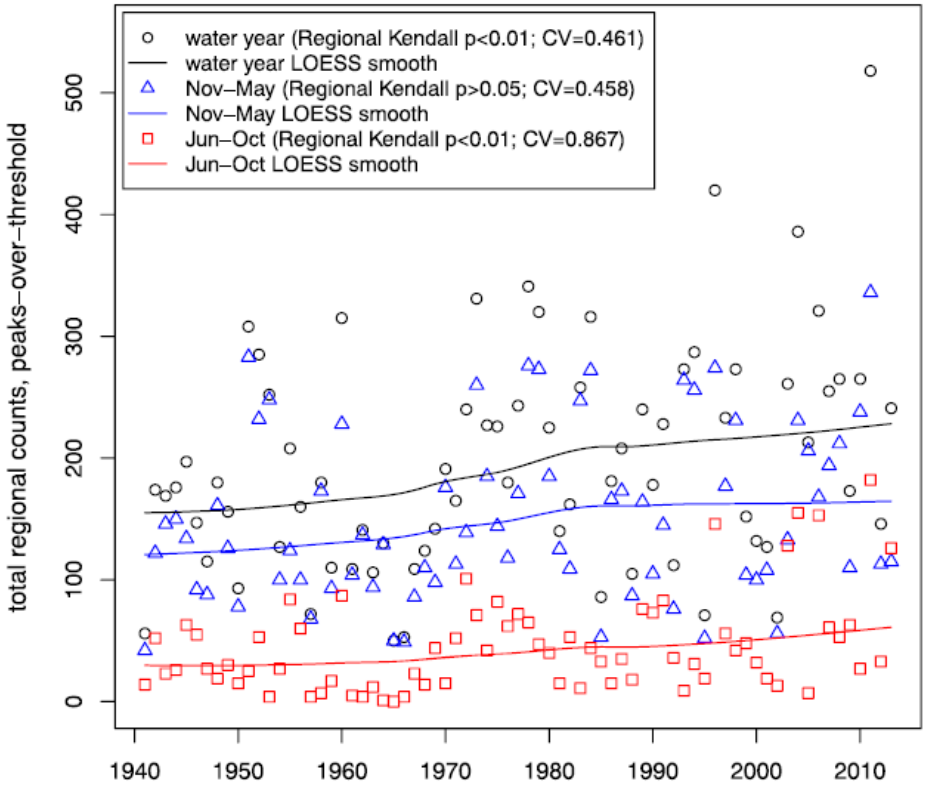

Figure 7.32. Trends in peaks-over-threshold counts for 65 sites across the northeast U.S. with streamflow data from 1941 through 2013. Black: water year, blue: cold season (Nov-May), and red: warm season (Jun-Oct). (Source: Collins 2019.)

Glas et al. (2019) estimated correlations between historical streamflow and climate for 97 streamflow gauges across New York state. The authors state that to understand the effects of climate change on streamflow, hydrologic response to temperature and precipitation needs to be examined at the mesoscale, like the hydrologically diverse setting of New York state. The state is at the intersection of the New England, Mid-Atlantic, Ohio, and Great Lakes hydrologic regions. Moisture is transported into the region from the Atlantic Ocean, the Gulf of Mexico, and the Great Lakes. The authors used daily mean discharge from 97 streamflow gauges, 16 of which were reference drainage basins with minimal disturbance and 83 gauges were distributed across the state with some degree of human influence. Records with 80 percent completeness were used and missing values were filled using monthly means and maintenance of variance extension technique. The filled streamflow record had 87 percent of the gauges with 56 years of continuous record starting in 1961 and the remaining gauges had continuous records starting in years between 1963 and 1975. Drainage areas for these streamflow gages varied over about three orders of magnitude (10 to 9,000 km^2).

Glas et al. (2019) used monthly temperature and precipitation data for the time period 1961-2016 from the PRISM dataset. Monthly gridded PRISM data were resampled over a finer grid and spatially averaged over the drainage area for each streamflow gauge. Streamflow data were standardized and then clustered using the Pearson correlation coefficients as a measure of similarity. Six clusters were used to represent

the diverse topography and climate regions within the New York state. A peaks-over-threshold method was used to identify floods and the identified events were tested for independence.

Glas et al. (2019) reported that the six clusters contain streamflow gauges with closely correlated annual flows (Figure 7.33). The authors noted that the clusters were spatially coherent but not necessarily confined to major drainage basin divides of topographic positions.

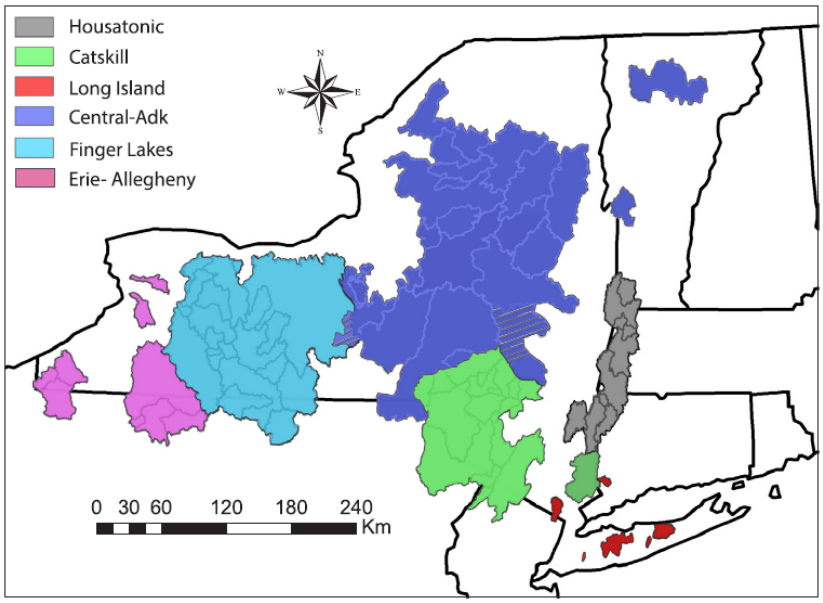

Figure 7.33. Drainage areas used in the study colored by cluster. Hatched areas indicate overlap between clusters. (Source: Glas et al. 2019.)

Change point analysis of peaks-over-threshold data for the clusters revealed shifts toward more frequent peaks in all clusters (Figure 7.34). Shifts toward more frequent peaks primarily occurred between 1968 and 1973 with some additional shifts in 1990 and 1995. Glas et al. (2019) noted that most change points in peaks-over-threshold frequency were accompanied by statistically significant gradual trends.

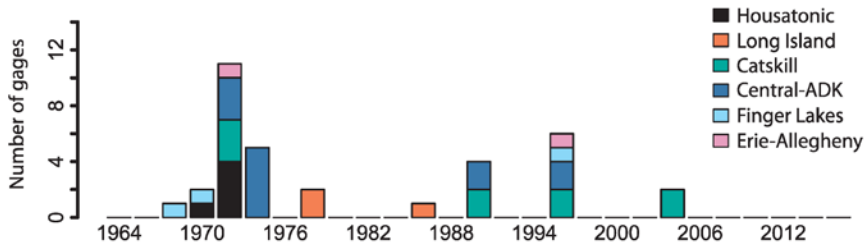

Figure 7.34. Years of occurrence of significant ($p \leq 0.1$) positive change points in peak-over-threshold counts for the six clusters. (Source: Glas et al. 2019.)

7.2.2 Projected Changes in Streamflow

Boyer et al. (2010) examined potential changes in hydrology of tributaries to St. Lawrence River in Québec, Canada. Three GCMs (HadCM3, CSIRO-Mk2, and ECHAM4) and two future scenarios (SRES A2 and B2) were used. Projected daily climate series were generated using 1961-1990 historical data with a perturbation factor derived from monthly differences in temperature and precipitation predicted by the GCMs. The study focused on five tributaries to the St Lawrence River (Figure 7.35).

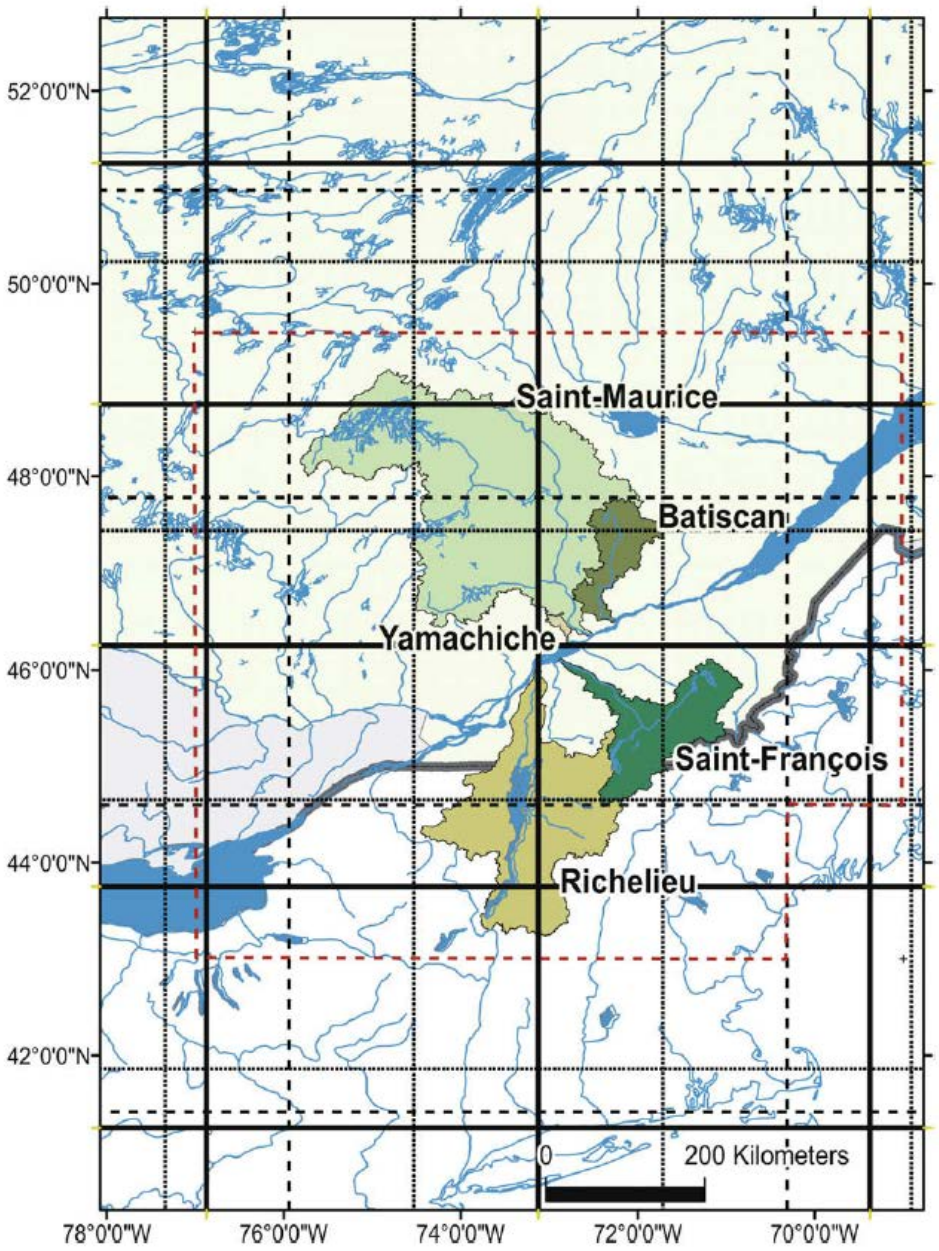

Figure 7.35. Tributaries of the St. Lawrence River. The solid black lines represent the HadCM3 grid, the dashed black lines represent the CSIRO-Mk2 grid, and the black dotted lines represet the ECHAM4 grid. The red dashed lines delineate the polygon for which projected changes were calculated. (Source: Boyer et al. 2010.)

Boyer et al. (2010) used a lumped hydrologic model, Service Hydrométéorologique Apports Modules Intermédiaires (HSAMI), that uses linear reservoirs to represent snowpack and melt, surface runoff and baseflow discharge, and groundwater. Snowpack accumulation and melt is simulated using a degree-day approach. Evapotranspiration is estimated from daily maximum and minimum temperatures. Water exchanges horizontally and vertically are accomplished using empirical formulations and the model parameters are adjusted during calibration using the 1961-1990 period.

Boyer et al. (2010) noted that using the perturbation factor approach results in the implicit assumption that biases in the GCMs are similar during historical and future periods and that the daily to interannual variability of climate variables from the historical period are maintained in simulated series. They also noted that this approach may not be suitable for analysis of extreme statistics (e.g., floods). However, because snow accumulation is relatively insensitive to frequency distribution of precipitation, the perturbation factor may be suitable for estimating snow accumulation-related indices. The authors selected three future time periods—2010-2039, 2040-2069, and 2070-2099. With the three GCMs and two emission scenarios for each future time period, 18 future hydrologic simulations were performed using the calibrated HSAMI model.

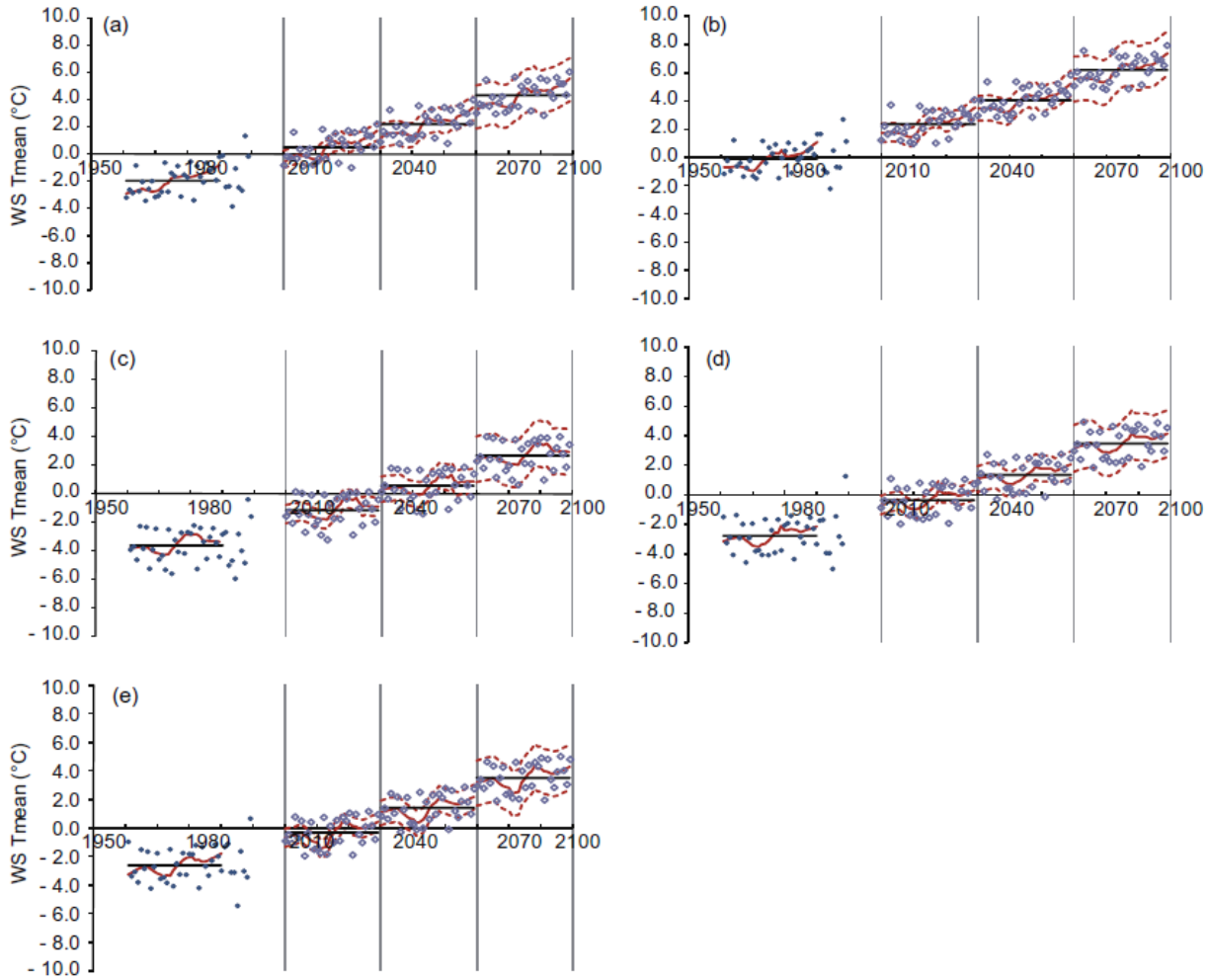

Figure 7.36. Winter-spring mean temperatures for the reference (historical) and future time periods: (a) St-François, (b) Richelieu, (c) Batiscan, (d) Yamachiche, and (e) St-Maurice River Basins. (Source: Boyer et al. 2010.)

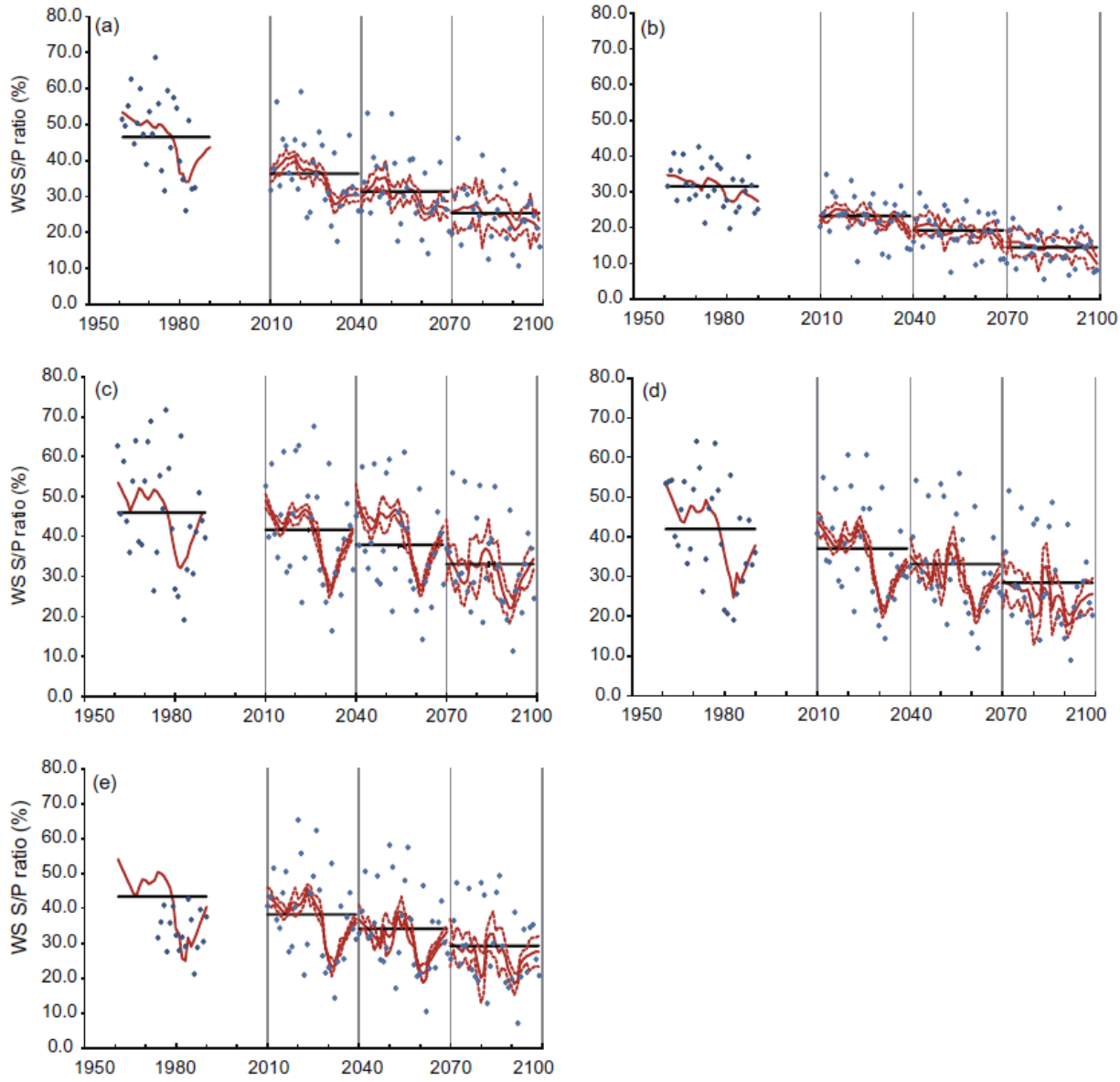

Figure 7.37. Winter-spring snow to precipitation ratio for the reference (historical) and future time periods: (a) St-François, (b) Richelieu, (c) Batiscan, (d) Yamachiche, and (e) St-Maurice River Basins. (Source: Boyer et al. 2010.)

Boyer et al. (2010) calculated the winter-spring mean temperatures (Figure 7.36), winter-spring snow/precipitation ratio (Figure 7.37), and WSCVD (Table 7.4) from the reference (historical) and future time period hydrologic simulations. Figure 7.36 shows that the various tributary river basins crossed the 0°C threshold for winter-spring mean temperature during different decades depending on the latitude of the river basin. All models predicted that the future winter-spring mean temperature would be above 0°C for the southernmost river basin, the Richelieu River Basin. The St-François River Basin will cross the 0°C threshold for winter-spring mean temperature during the 2010-2039 period; the other three river basins will cross the 0°C threshold for winter-spring mean temperature during the 2040-2069 period. Consistent with increase in winter-spring temperatures, the winter-spring snow to precipitation ratio shows declines in all tributary basins (Figure 7.37). The overall mean annual decrease rate for winter-spring snow to precipitation ratio is reported to be 0.15 to 0.2 percent per year. The authors noted that for

all tributary river basins except for the Batiscan River Basin, a trend toward earlier WSCVD was already initiated in the reference period; a shift of 8-12 days was estimated based on observed data from 1932-2004. Future simulations show that WSCVD will be earlier for all tributary river basins (Table 7.4). For Richelieu and Batiscan River Basins, by the end of the 21st century, WSCVD will occur 22 and 34 days earlier, respectively, compared to the reference period.

Table 7.4. WSCVD for the reference (historical) and future time periods and the change in WSCVD for the future time periods compared to the reference period. Date format is DD-MM. (Source: Boyer et al. 2010.)

	All models	Batiscan	Yamachiche	St-Maurice (LaGabelle)	St-François	Richelieu
Horizon 1 2010–2039	Mean	12–04	15–04	20–04	23–03	27–03
	Lower quartile	05–04	07–04	15–04	15–03	21–03
	Upper quartile	21–04	24–04	26–04	31–03	31–03
Horizon 2 2040–2069	Mean	01–04	04–04	10–04	15–03	21–03
	Lower quartile	25–03	29–03	04–04	08–03	16–03
	Upper quartile	10–04	14–04	17–04	23–03	27–03
Horizon 3 2070–2099	Mean	22–03	22–03	31–03	08–03	17–03
	Lower quartile	14–03	14–03	24–03	28–02	12–03
	Upper quartile	01–04	03–04	10–04	16–03	23–03
Reference period	Mean	25–04	27–04	01–05	08–04	08–04
	Lower quartile	24–04	19–04	05–04	31–03	06–04
	Upper quartile	01–05	28–04	16–04	18–04	19–04
Difference between horizon 1 and reference period (days)		−13	−12	−11	−16	−12
Difference between horizon 2 and 1 (days)		−11	−11	−9	−8	−5
Difference between horizon 3 and 2 (days)		−10	−12	−11	−7	−4
Difference between horizon 3 and reference period (days)		−34	−36	−31	−31	−22
Slope of the temporal trend 2010–2100		−0.328	−0.368	−0.324	−0.262	−0.161

Thibeault and Seth (2014) examined changes in selected climate indices in northeast U.S., defined as the area between 38 and 48°N latitude and 67 and 80°W longitude. These climate indices are the 27 core climate indices defined by the Expert Team on Climate Change Detection and Indices (ETCCDI) and are estimated based on daily temperature and precipitation. The authors evaluated observed values of climate indices using the station-based, land-only HadEX2 dataset (1901-2010) and the European Center for Medium-Range Weather Forecasts ERA-Interim reanalysis (1979-2010). Climate indices computed for the future from 23 CMIP5 models were analyzed for historical predictions and the future RCP 8.5 scenario.The base period for model simulations was 1961-1990. The temporal evolution of climate indices simulated by CMIP5 models were evaluated for 1950-2099 period that were a combination of 1950-2005 historical simulations and 2006-2099 RCP 8.5 future scenario.

Thibeault and Seth (2014) noted that temperature-related indices (e.g., cold spell duration, cool nights, warm nights, highest annual minimum temperature, tropical nights, and warm spell duration) show significant trends in the historical records, which is consistent with recent warming. The temporal evolution of selected temperature-related climate indices is shown in Figure 7.38. Figure 7.39 shows the changes in the distributions of selected multimodel average historical and RCP 8.5 climate indices.

Thibeault and Seth (2014) found that trends in precipitation-related climate indices were positive and significant. January and July 1-day and 5-day maximum precipitation time evolution and spatial patterns of late 21st century changes from the late 20th century are shown in Figure 7.40. By late 21st century, January 1-day maximum precipitation is projected to increase 23 percent and July 1-day maximum precipitation is projected to increase 6 percent; the corresponding increases for 5-day maximum precipitation are 22 and 6 percent, respectively. While differences in January maximum 1- and 5-day precipitation are significant at 95 percent confidence level across the northeast U.S., the July significant metrics are limited to northern New England and adjacent areas in Canada. Significant changes in July 5-day maximum precipitation are also seen over the Appalachians and coastal regions.

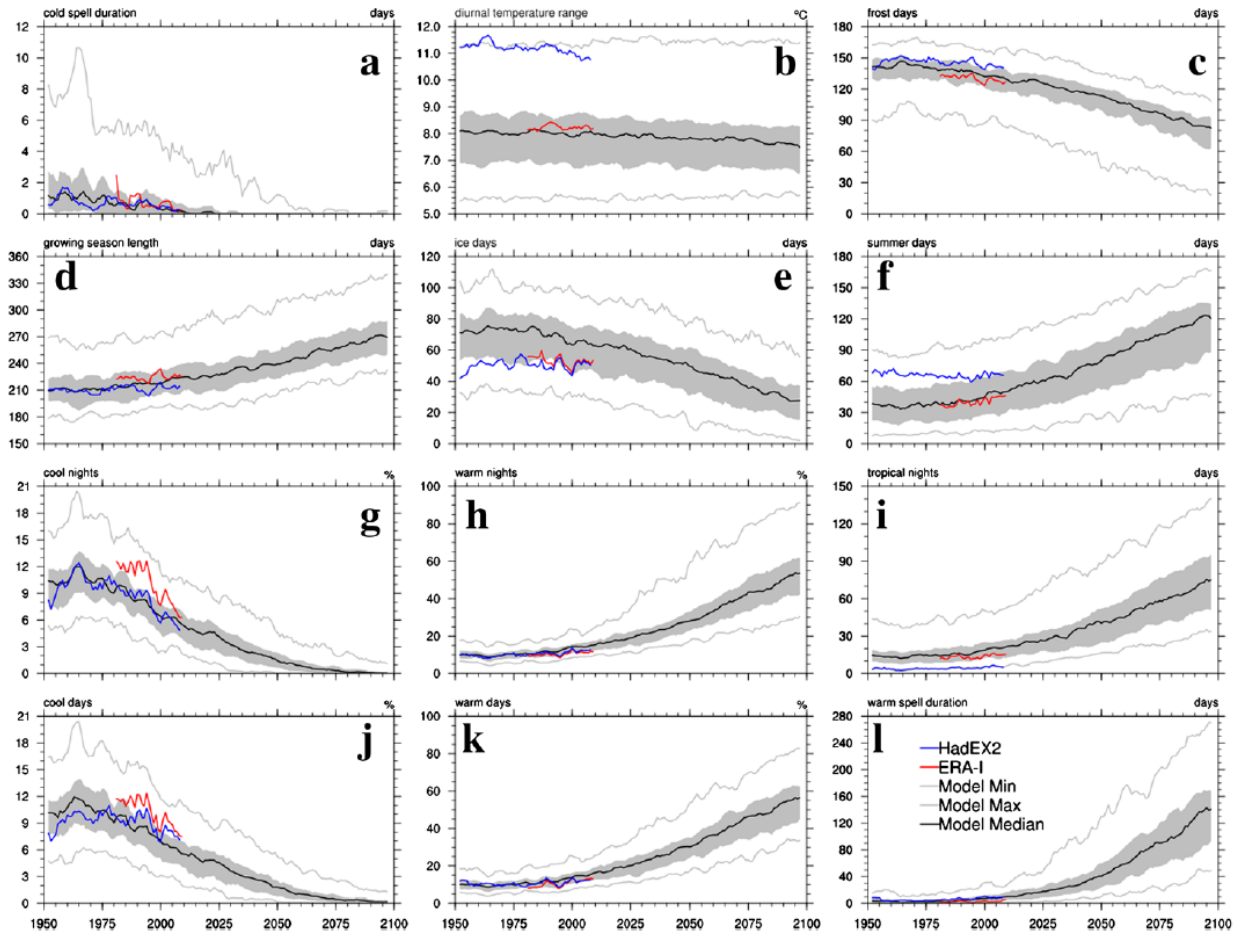

Figure 7.38. Temporal evolution of selected temperature-related climate indices: (a) cold spell duration (days), (b) diurnal temperature range (°C), (c) frost days (days), (d) growing season length (days), (e) ice days (days), (f) summer days (days), (g) cool nights (percent), (h) warm nights (percent), (i) tropical nights (days), (j) cool days (percent), (k) warm days (percent), and (l) warm spell duration (days). Multimodel medians are denoted by solid black lines, minimum and maximum are denoted by gray lines, shading represents interquartile range, and blue and red lines show HadEX2 and ERA-I observation-based values of climate indices. (Source: Thibeault and Seth 2014.)

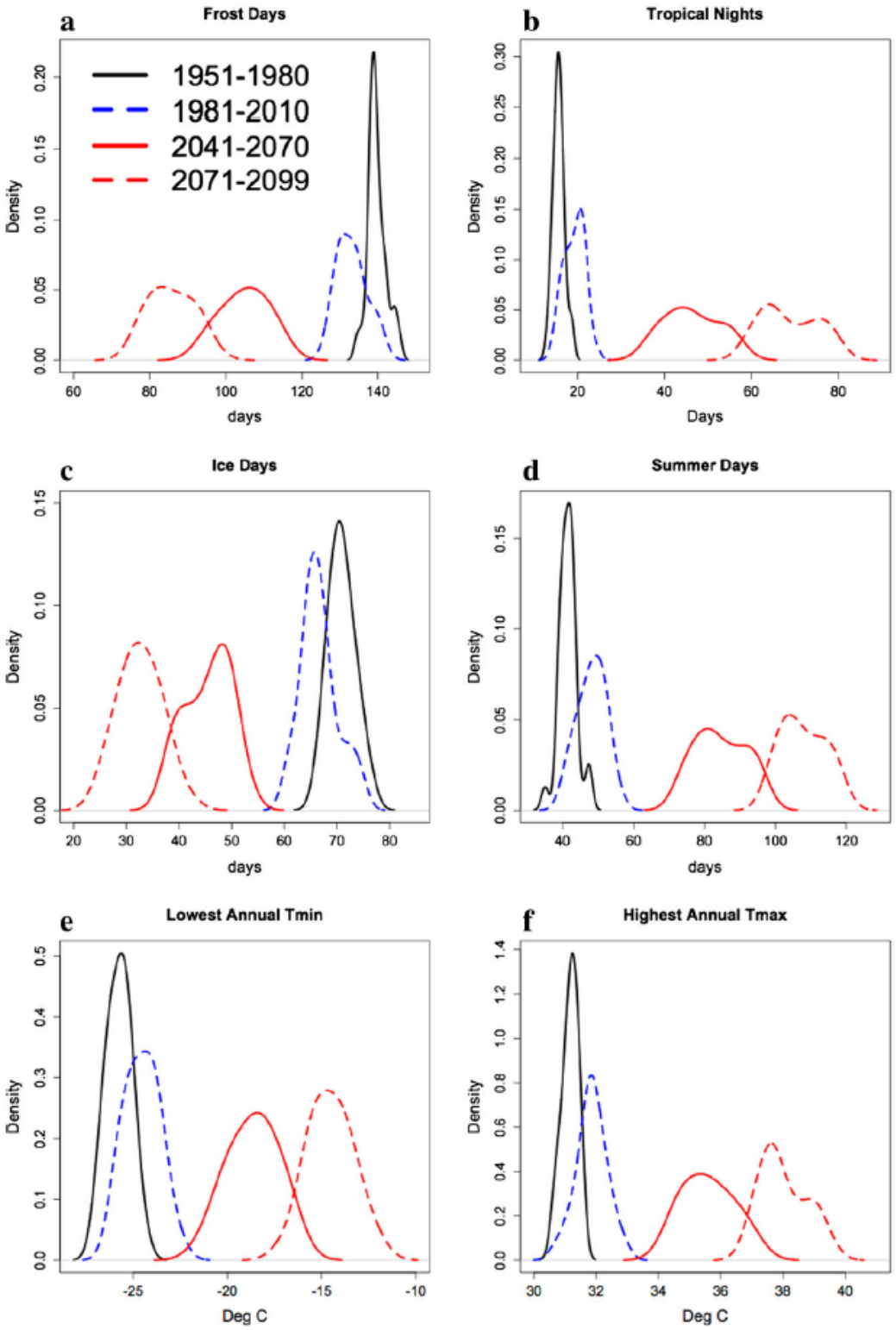

Figure 7.39. Changes in the distributions of selected multimodel average historical and RCP 8.5 climate indices. Black curves represent the 1951-1980 distributions, dashed blue curves represent the 1981-2010 distributions, solid red curves represent the 2041-2070 distributions, and dashed red curves represent the 2071-2099 distributions. (Source: Thibeault and Seth 2014.)

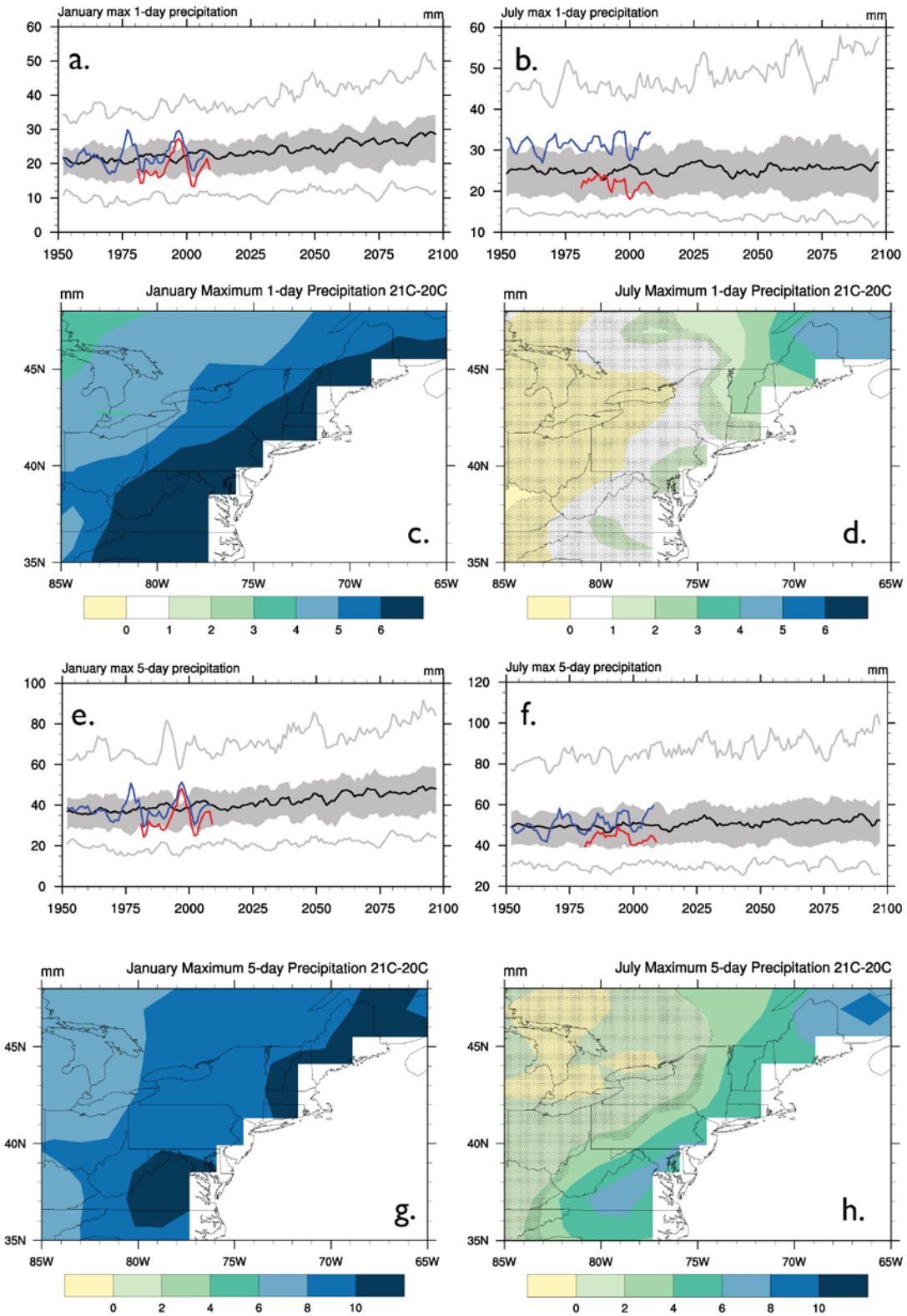

Figure 7.40. (a, b, e, f) Temporal evolution of January (left column) and July (right column) 1- and 5-day maximum precipitation (mm). (c, d, g, h) Spatial pattern of changes in 1- and 5-day maximum precipitation for 2070-2099 compared to 1971-2000. (Source: Thibeault and Seth 2014.)

Johnson et al. (2015) performed hydrologic modeling in 20 large U.S. river basins to estimate streamflow and water-quality sensitivity to climate change and urbanization scenarios. The river basins located in the northeast U.S. were the Susquehanna and the Merrimack River Basins (Figure 7.41). Hydrologic modeling was performed using the Soil and Water Assessment Tool (SWAT) that uses a SCS curve number approach to estimate surface runoff. Water balance computations also include simulation of subsurface flows, evapotranspiration, soil storage, and deep seepage losses. SWAT uses 2001 National Land Cover Database for land use data. Water management and operational features (e.g., irrigation) were included in the model if they were expected to modify streamflow at downstream locations by 10 percent or more. Potential evapotranspiration was estimated using the Penman-Monteith method that included a plant growth model. Historical meteorological time series were obtained for multiple stations within each river basin from the 2006 BASINS 4 meteorological database. The individual river basin models were calibrated using a representative HUC-8 subbasin within the river basins.

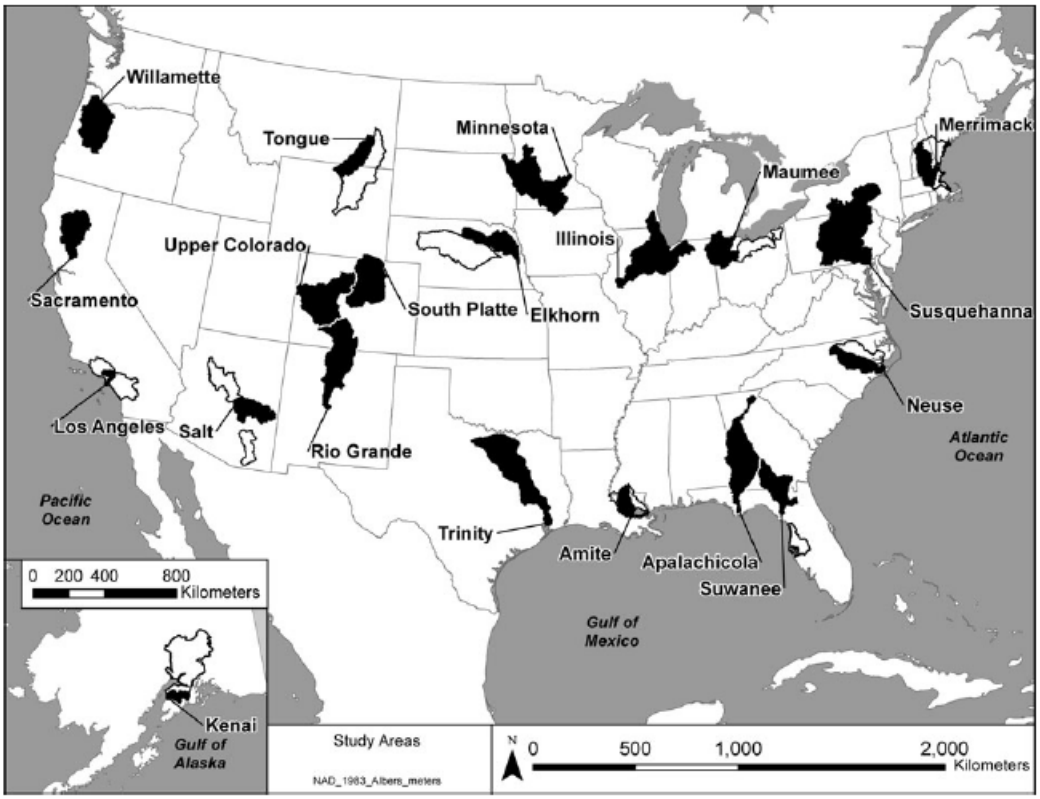

Figure 7.41. The 20 river basins studied by Johnson et al. (2015).

Climate change scenarios were taken from the NARCCAP that uses different regional climate models driven by outputs from four CMIP3 GCMs (Johnson et al. 2015). A total of six GCM/RCM combinations (six NARCCAP scenarios) were used to develop future scenarios. NARCCAP climate outputs were interpolated to each weather station used in the study and a change factor approach was used to create climate scenarios for input to SWAT. Change factors were calculated as the change in mid-21st century predictions relative to the 1971-2000 time period (the baseline period). Urbanization scenarios were based on projected mid-21st century changes in housing density from U.S. Environmental Protection Agency (EPA) Integrated Climate and Land Use Scenarios dataset.

Medians of the six NARCCAP scenarios' average annual temperatures in the Susquehanna and Merrimack River Basins during mid-21st century were a little over 2.5°C warmer compared to the baseline period (Johnson et al. 2015). Medians of the six NARCCAP scenarios' average annual

precipitation in the Susquehanna and Merrimack River Basins during mid-21st century were about 5 and 7 percent greater than that during the baseline period. Basin impervious covers for the Susquehanna and Merrimack River Basins were 1.6 and 5 percent, respectively, in 2001 and increased by 0.1 and 1.2 percent, respectively by mid-21st century.

Johnson et al. (2015) evaluated four streamflow change indices: total streamflow, average annual 7-day minimum streamflow, average annual 1-day maximum streamflow, and the date of annual streamflow centroid. Table 7.5 summarizes these indices for the Susquehanna and the Merrimack River Basins. The change in Susquehanna River average annual 1-day maximum streamflow was statistically significant, an approximately a 21 percent increase from baseline. The change in Merrimack River average annual 7-day minimum streamflow was statistically significant, an increase of 23 percent from baseline. The change in Merrimack River date of annual streamflow volume was also statistically significant, occurring 15 days earlier compared to baseline. These changes do not appear to be a result of urbanization but do show a dependence on warming temperatures, particularly the advancement of streamflow centroid date.

Table 7.5. Changes in streamflow indices for mid-21st century compared to the late-20th century in the Susquehanna and Merrimack River Basins based on mid-century hydrologic simulations by Johnson et al. (2015).

Streamflow Index	Susquehanna River Basin		Merrimack River Basin	
	Change from Baseline	Statistically Significant?	Change from Baseline	Statistically Significant?
Total Streamflow	7 percent	No	10 percent	No
Average Annual 7-day Minimum Streamflow	-1 percent	No	23 percent	Yes
Average Annual 1-day Maximum Streamflow	21 percent	Yes	1 percent	No
Date of Annual Streamflow Centriod	-6 days	No	-15 days	Yes

Demaria et al. (2016) evaluated trends and changes in streamflow characteristics including 3-day peak flows, 7-day low flows, and mean baseflows in the northeast U.S. (Figure 7.42). The VIC model, complemented by a channel routing method, was run at 158 selected drainage basins in the midwest and northeast U.S. Bias-corrected and statistically downscaled CMIP5 climate scenarios were used to provide future climate projections to the VIC model as inputs. Based on the model results, the authors concluded that over the northeast U.S., both precipitation and temperature are projected to increase for the future period (2028-2082) compared to the historical period (1951-2005; Table 7.6). Precipitation will increase, particularly in winter. Temperatures will also increase with winter increases being the largest. Evapotranspiration is projected to increase all through the year except winter; the authors attributed reduced winter evapotranspiration to decreased sublimation from reduced snowpacks. Snow-water equivalents show striking reductions in the future, from springtime decrease of 13 percent in places to wintertime decrease of over 41 percent in places for the RCP 8.5 scenario.

Figure 7.43 shows the trends in the three streamflow indices based on the hydrologic simulations. Within most of the northeast U.S., 3-day peak flows are projected to increase for both RCP scenarios except for the extreme northeast part of the region. Under RCP 4.5, low flows show a mix of upward and downward trends with a few upward trends being significant. Under RCP 8.5, a majority of the northeast U.S. shows statistically significant downward trends. Very few baseflows show significant trends for either RCP scenario. Demaria et al. (2016) also estimated the magnitude of 3-day peak flows and 7-day low flows for an AEP of 0.01 from a fitted GEV distribution both for the historical and the future period. Figure 7.44 shows the changes in the estimated magnitudes of 3-day peak flows and 7-day low flows corresponding

to an AEP of 0.01. For the 3-day peak flows, there is a increasing trend, in places exceeding 30 percent, in the southern part of the northeast U.S. and a decreasing trend, in places exceeding 25 percent, in the northern part of the northeast U.S. For the 7-day low flows, most of the northeast U.S. showed declines, in places exceeding 80 percent.

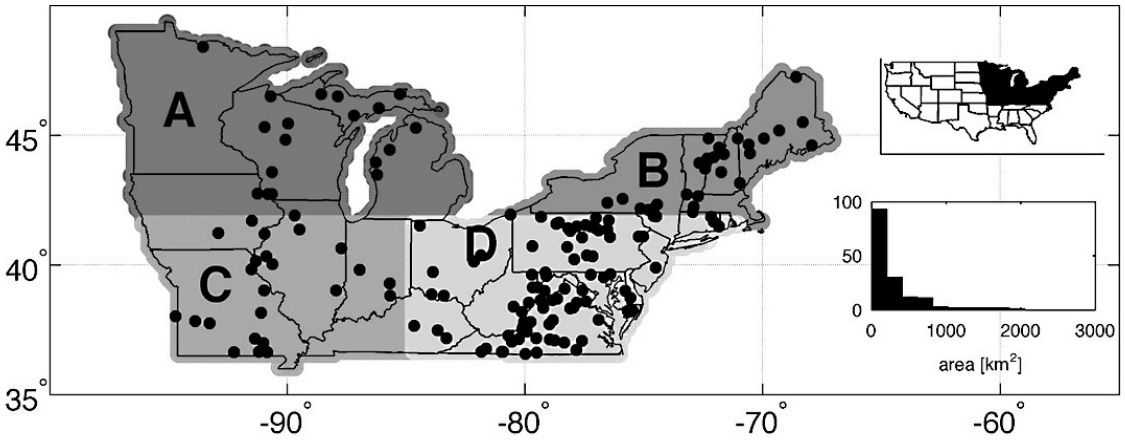

Figure 7.42. The midwest and northeast U.S. region studied by Demaria et al. (2016). The dots represent the locations of drainage basins. Subregions B and D encompass the northeast U.S. region as defined by NCA3 and NCA4. The inset shows the histogram of drainage basin areas. (Source: Demaria et al. 2016).

Table 7.6. Changes in future (2028-2082) seasonal temperature and precipitation inputs and modeled seasonal hydrologic fluxes compared to the historical period (1951-2005) over the northeast U.S. Values in bold are statistically significant at $\alpha = 0.05$.

Input or Modeled Flux (Units)	Season	RCP 4.5	RCP 8.5
Precipitation (percent)	Winter (DJF)	**10.4 – 12.5**	**11.3 – 12.6**
	Spring (MAM)	**7.1 – 9.1**	**12.0 – 12.7**
	Summer (JJA)	**7.3 – 9.0**	**7.6 – 8.5**
	Fall (SON)	**8.6 – 8.8**	**6.5 – 7.1**
Temperature (°C)	Winter (DJF)	**2.7 – 2.9**	**3.6 – 4.0**
	Spring (MAM)	**2.6**	**3.2 – 3.3**
	Summer (JJA)	**2.5**	**3.3 – 3.4**
	Fall (SON)	**2.5 – 2.6**	**3.3**
Evapotranspiration (mm/day/seas)	Winter (DJF)	-0.2 – **1.8**	**-0.6 – 2.3**
	Spring (MAM)	**11.7 – 14.0**	**15.3 – 18.1**
	Summer (JJA)	**18.7 – 19.2**	**22.0 – 25.2**
	Fall (SON)	**12.3 – 13.6**	**14.5 – 15.3**
Soil Moisture (mm/day/seas)	Winter (DJF)	**2.4 – 4.3**	**2.3 – 5.3**
	Spring (MAM)	-0.2 – **0.2**	-0.1 – 0.0
	Summer (JJA)	**-1.1** – 0.2	**-1.8 – -1.4**
	Fall (SON)	**-0.6 – 0.0**	**-2.3 – -1.2**
Snow-Water Equivalent (mm/day/seas)	Winter (DJF)	**-31.8 – -17.0**	**-41.8 – -21.4**
	Spring (MAM)	**-33.7 – -13.4**	**-40.6 – -15.9**
	Summer (JJA)	**-0.1 – 0.0**	**-0.1 – 0.0**
	Fall (SON)	**-0.5 – -0.2**	**-0.6 – -0.3**

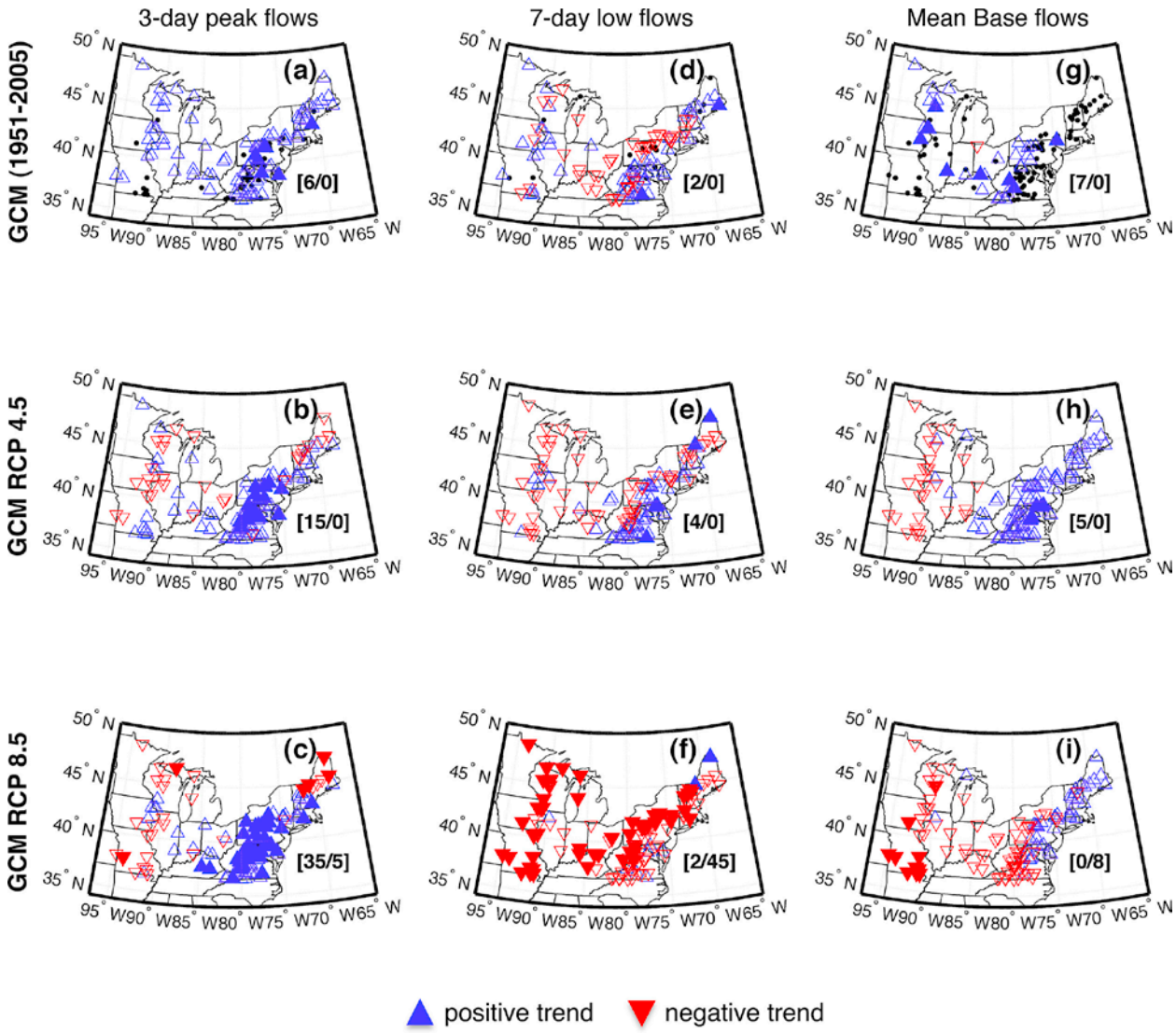

Figure 7.43. Trends in 3-day peak flow (left column), 7-day low flows (middle column), and annual mean baseflows (right column) for historical period (1951-2005, top row) and future RCP 4.5 (middle row) and RCP 8.5 (bottom row) scenarios (2028-2082). Black dots in the top row indicate locations of drainage basins where statistically significant point changes were detected. The numbers in the lower-right corners indicate the number of statistically significant increasing/decreasing trends. (Source: Demaria et al. 2016.)

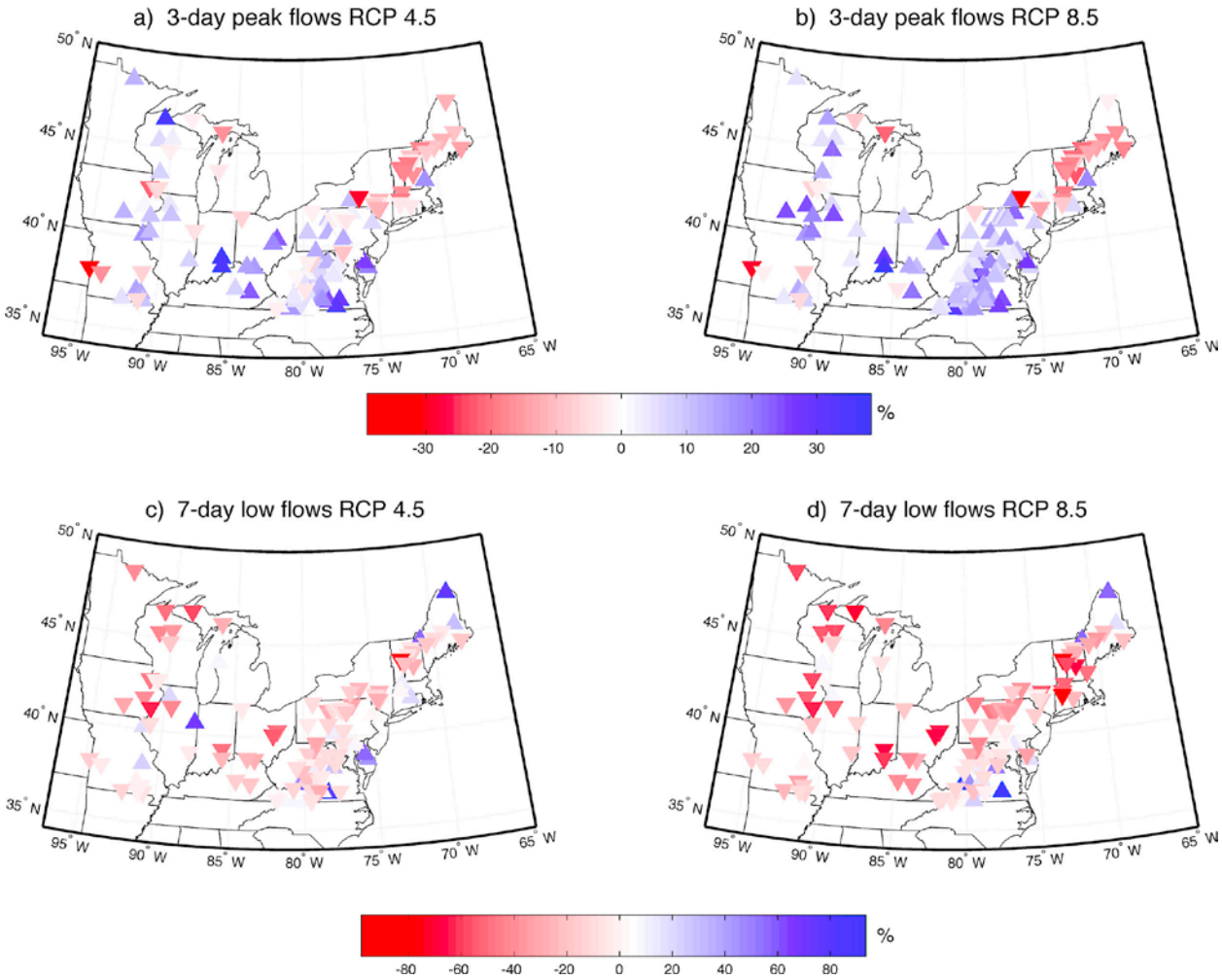

Figure 7.44. Percent changes in 3-day peak flow (top row) and 7-day low flows (bottom row) at an AEP of 0.01 for RCP 4.5 (left column) and RCP 8.5 (right column). (Source: Demaria et al. 2016.)

Demaria et al. (2016) also conducted an over/under-the-threshold analysis of simulated daily streamflow. The thresholds were set as the 10th and 90th percentile of daily streamflow from historical VIC simulations. A frequency analysis using counts over/under-the-threshold was performed and compared to corresponding frequencies estimated from the historical simulations. The authors concluded that compared to the historical period, future daily peak flow frequencies would increase 12 to 19 percent under the RCP 4.5 scenario and increase about 19 percent under the RCP 8.5 scenarios. Under both RCP scenarios, daily low-flow frequencies are projected to increase in the southern part of the northeast U.S. and decrease in the northern part of the northeast U.S.

7.3 Hydrologic Impacts in the Northeast – the NRC Context

- The northeast U.S. experienced a dry period in the 1960 and wet periods in the 1970s and 2000s. The mean annuals cycle of streamflow for three river basins in the northeast U.S. seem to be caused by annual cycles of evapotranspiration and snowmelt, not precipitation. Some, although weak, correlations between NAO, AO, and AMO and the three river basins' hydrology exist, both in undisturbed, small and larger, more regulated drainage areas.
- The streamflow peak during spring shows a clear shift to earlier in the season, by as much as 10 days in 2014 compared to mid-20th century. There seems to be periods in the historical record when frequency of floods increased-these periods occurred around 1970, 1990, and 1995.
- The winter-spring mean temperature in drainage areas of selected tributaries to the St. Lawrence River, depending on their latitude, will cross the freezing threshold during various decades of the 21st century resulting in projected reduced snow to total precipitation ratio and large shifts of winter-spring center-volume date to earlier in spring.
- Peak streamflow magnitude is projected to increase and low flow magnitudes is projected to decrease in the northeast region as the 21st century progresses, particularly for RCP 8.5 scenario.

7.3.1 Flooding

Many hydrometeorological parameters that influence floods are not directly addressed in the NCAs. Some of the studies summarized above have attempted to investigate the impacts of climate change on runoff characteristics in the northeast region. Some of these studies used mean streamflow indicators (i.e., mean annual, seasonal, or monthly flows). Others have investigated the impacts of climate change on flood frequency and seasonality. However, these studies generally have not addressed floods of interest to the NRC, particularly for safety analysis and review, which include those that occur at significantly shorter timescales (hours to days) and almost always are in the tails of the distribution, away from the mean. Therefore, direct conclusions regarding shorter-duration, lower-frequency floods of interest to the NRC are difficult to draw. In addition, uncertainties arising from GCM differences, uncertainties in hydrologic models, uncertainties in socioeconomic responses, and uncertainties in water management can further complicate assessment of future floods.

Nevertheless, certain conclusions can be made that will give the NRC greater insights into flood analyses and their reviews. First, a site-specific analysis should be performed to assess the impacts of climate change on the behavior of floods. A change in the mean behavior of floods can also reflect a change in the behavior in the tails. It is clear that the practical resolution of GCMs is going to remain incompatible with the need for a local-to-regional-scale flood assessment. Therefore, further investigations, which may include exploring dynamical downscaling and nesting of hydrological models, are needed to couple the outputs of GCMs to hydrologic models.

Second, significant uncertainty in the predictions of hydrologic models (both aleatory and epistemic) will exist for the foreseeable future and can directly affect estimates of flood magnitudes under altered climate scenarios. A clear framework for enumerating and attributing the sources of these uncertainties, explicitly accounting for these uncertainties in flood estimation approaches, and propagating the uncertainties throughout flood analyses should be used. This framework will assist the NRC in investing resources to improve the parts of a flood assessment where uncertainties can be reduced given newer data sets and additional information. Given that climate change research, hydrologic understanding including newer

data sets, and water-management practices are expected to continually evolve, a periodic refinement of site-specific flood assessments should be made.

Third, a site-specific assessment of flood-protection and mitigation will be very useful from a safety perspective. It is noted that NRC current practice for permit and license application reviews relies on site-specific hydrologic engineering assessments that include both floods caused by multiple mechanisms relevant for the site and low-water issues. The site-specific flood assessment, including quantification of associated uncertainties, can facilitate clear articulation of risk faced by a plant and provide useful information for risk-informed licensing decisions.

7.3.2 Low Flows

Many hydrometeorological parameters that influence low flows are not directly addressed in the NCAs. Some of the studies summarized above have attempted to investigate the impacts of climate change on runoff characteristics in the northeast region. These studies used mean streamflow and low-flow indicators (i.e., mean annual and 7Q10). These metrics are useful to the NRC in the review of water use and environmental impacts of plants. Additional low-flow metrics useful to the NRC include the persistence and frequency of low flows, both seasonally and in the context of multi-year low-flow events, that are not directly addressed in current studies.

Site-specific assessments may be needed to assess the characteristics of low-flow metrics under climate change scenarios. Some large-scale atmospheric patterns (e.g., PNA, NAO, and PDO) are related to low-flow events in the northeast region. Regional and local characteristics, including streamflow generation, urbanization and population growth, and water-management practices, would influence low flows at spatiotemporal scales of interest to NRC licensing. Dynamically downscaled GCM outputs, nested climate and hydrologic modeling, and inclusion of water-management practices in low-flow assessments would be needed, with particular focus on seasonal to interannual persistence of low flows, to support NRC licensing.

As stated before, uncertainties in all aspects of climate hydrology assessments are expected to exist at significant levels for the foreseeable future. Given these uncertainties, decision-making would benefit from a framework for enumerating and attributing the sources of these uncertainties, explicitly accounting for these uncertainties in hydrologic estimation approaches and propagating the uncertainties throughout hydrologic analyses. This framework will assist the NRC in investing resources to improve the parts of low-flow assessment where uncertainties can be reduced given newer data sets and additional information. A periodic refinement of site-specific low-flow assessments can assist plants in mitigating the effects of sustained low-flow events on energy production and the environment.

7.4 Summary and Discussion

Studies of changes in observed floods over the last several decades in the northeast region show that the peak streamflow timing is more related to annual cycles of evapotranspiration and snowmelt, rather than that of precipitation. Therefore, rising temperatures can shift winter-spring streamflow peaks to earlier in the season, driven by earlier snowmelt timing. This shift in snowmelt can lead to increased likelihood of wet antecedent conditions conducive to larger floods from extratropical storms and remnants of summer hurricanes. The changes in winter-spring streamflow timing is a result of rising temperatures with the additional effect that length of winter may shorten. Large springtime precipitation events, more likely to occur as rainfall, may lead to increased flood magnitudes, aided by more rapid snowmelt.

The NCA has provided useful information about projected changes in precipitation, runoff, and soil moisture from climate models. To bridge between climate projections that are typically made at a grid resolution between 50 and 200 km and the hydrologic information needed to assess climate change impacts on water resources, some hydrologic modeling studies provide projections of hydrologic parameters such as streamflow, snowpack, and soil moisture in small to large river basins. Overall, warming in the future can lead to changes in precipitation, runoff, and soil moisture in the northeast region. More specifically, increases in extreme precipitation have implications for floods and changes in temperature can affect snow-water equivalent accumulation with subsequent effects on late-winter to early spring streamflow timing. In general, previous studies examined mean changes and floods of relatively frequent occurrence rather than hydrologic extremes of particular interest to NRC, and were not performed at the site level; thus, future studies are needed to assess hydrologic changes in the northeast region at spatial and temporal scales more relevant to NRC needs. With CMIP5 simulations that contain larger number of climate model ensembles, future studies may provide increased confidence in flood discharge changes over the next century.

In general, the climate research community has not focused on evaluating trends and impacts of meteorological (and by extension, hydrologic) events of exceedance probabilities that are of interest to the NRC for permitting and licensing. The assessment of trends and impact at annual exceedance probabilities of interest to NRC also is limited by the fact that current climate models have significantly larger uncertainties for these events, therefore limiting the usefulness of predictions that may have large uncertainties. Moreover, uncertainties in climate model predictions are carried through and combined with uncertainties in hydrologic and hydraulic modeling approaches employed in hydrologic engineering assessments including PFHAs. Therefore, a consistent framework for enumerating, attributing, and incorporating these uncertainties, both in climate models and in hydrologic engineering assessments, should be used in site-specific PFHAs for permitting and licensing to clearly articulate the confidence associated with predictions at low annual exceedance probabilities.

8.0 Federal Climate Assessment and Modeling Activities

This section provides an overview of recent climate assessment and modeling activities, as well as guidance developed by federal agencies and interagency initiatives. This overview focuses on information with potential relevance to NRC's mission.

8.1 U.S. Global Change Research Program

Four U.S. climate modeling centers participate in the World Climate Research Programme (WCRP) sponsored Coupled Model Intercomparison Project Phase 6 (CMIP6), which contributes to the Intergovernmental Panel on Climate Change (IPCC) Sixth Assessment (AR6) Report. The four modeling centers are Department of Energy's Energy Exascale Earth System Model (E3SM), NOAA's Geophysical Fluid Dynamics Laboratory (GFDL), NASA's Goddard Institute of Space Studies (GISS), and National Science Foundation's National Center for Atmospheric Research (NCAR). A CMIP6 Model Analysis Workshop was held on 25-28, March, 2019, in Barcelona, Spain, to provide a forum to update and exchange about the developments and progress of simulations and analysis within Phase 6 of the Coupled Model Intercomparison Project (CMIP6). The workshop was hosted by the Barcelona Supercomputing Center (BSC), and was jointly organized by the World Climate Research Program (WCRP) Working Group on Coupled Modeling (WGCM) CMIP Panel and the European Commission Horizon 2020 projects PRIMAVERA (PRocess-based climate sIMulation: AdVances in high-resolution modeling and European climate Risk Assessment), and EUCP (European Climate Prediction system). The workshop gathered 249 participants from 26 different countries around the world. Representatives from at least 20 CMIP6-Endorsed Model Intercomparison Projects (MIPs) and 25 modeling groups were present. Scientifically, the workshop was structured around three major cross-cutting questions: (1) How does the Earth system respond to forcing? (2) What are the origins and consequences of systematic model biases? (3) How can we assess future climate change given climate variability, predictability and uncertainty in scenarios?

The last session of the workshop included a final discussion of the emerging properties of the CMIP6 ensemble and the way forward toward CMIP7 (https://cmip6workshop19.sciencesconf.org/data/CMIP6AnalysisWorkshop_FinalDiscussion_190328_FINAL.pdf). Based on preliminary results presented at the workshop, emergent properties of the CMIP6 ensemble can be summarized as follows:

- Improvements have been made to models from CMIP5 to CMIP6, including new physical insights in the atmosphere, ocean, sea ice, and land surface utilizing new observations. In many cases, changes in the detailed representation of prognostic cloud and aerosol processes have been implemented.
- Consequences of model developments are now being carefully assessed.
- Initial results show that some of the new CMIP6 models have a higher equilibrium climate sensitivity (ECS) than their CMIP5 counterparts (from about 6 years ago); the climate science community is actively investigating this important topic and peer-reviewed papers are already in the works.
- WGCM will work with the community to compile emerging ECS properties in a peer-reviewed perspective paper as input to the assessment of ECS in the IPCC AR6.

It was noted that the timeline for CMIP6 is delayed. Factors contributing to the delays include: (1) essential inputs rely on single people and most of this work is unfunded (e.g., forcing data); (2) although MIPs were entirely voluntary for modeling groups, most aspired to run many of the MIPs, with the

consequence of a heavy human and computational load. To ensure timely delivery and enhanced quality control for the forcing data, it was noted that program-level support is needed. Furthermore, the provision and archiving of CMIP products and model development require substantial efforts that must be better funded. There are enough experiments and research questions in CMIP6 to fuel research over the next phase for CMIP7.

The U.S. Climate Modeling Summit convened the fifth annual meeting of the six U.S. climate modeling centers on April 3–4, 2019. The purpose of the Summit was to improve the coordination and communication of national climate modeling goals and objectives. The Summit brought together representatives from the U.S. "CMIP-class" climate model development centers and from operational climate-prediction programs. Specifically, two representatives—one lead and one additional delegate—from each of the following groups were invited to participate in the Summit: GFDL Climate Model/Earth System Model), Climate Forecast System, GISS (Model E), Goddard Earth Observing System (GEOS-5), Community Earth System Model, and Energy Exascale Earth System Model (E3SM). The Summit was coordinated by the UGSCRP Interagency Group on Integrative Modeling (IGIM). At the fifth annual meeting, a workshop on "Modes of Variability" was held on the first day. The purpose of the workshop was to bring together experts on modes of variability (e.g., Quasi-Biennial Oscillation [QBO], Madden-Julian Oscillation [MJO], El Niño-Southern Oscillation [ENSO]) and scientists at the U.S. modeling centers to review recent advances in understanding the different modes of variability and evaluate how well they are simulated in the current generation of climate models and coordinate development of metrics and diagnostics for model evaluation. The workshop provided a forum for discussions to prioritize research and development for the modeling centers.

8.2 Federal Climate Change and Water Working Group

The federal Climate Change and Water Working Group (CCAWWG) provides engineering and scientific collaborations in support of water management under a changing climate. Participating agencies include: U.S. Army Corps of Engineers (USACE), U.S. Bureau of Reclamation, NOAA, U.S. Geological Survey (USGS), EPA, Federal Emergency Management Agency, National Aeronautics and Space Administration (NASA), and U.S. Department of Agriculture. The working group's collaboration informs and coordinates with higher-level interagency activities such as the U.S. Global Change Research Program's Adaptation Science Interagency Working Group, Council of Environmental Quality's Climate Preparedness and Water Resources Work Group, the Office of Science and Technology Policy Committee on Environment and Natural Resources' Subcommittee on Water Availability and Quality, and the Advisory Committee on Water Information's Water Resources Adaptation to Climate Change Workgroup.

The USACE Civil Works Program published the Engineering and Construction Bulletin (ECB) No. 2016-25, "Guidance for Incorporating Climate Change Impacts to Inland Hydrology in Civil Works Studies, Designs, and Projects" (USACE 2016). The ECB recognizes that in some geographical locations and for some impacts that are relevant to the USACE, climate change may be shifting, not only the climatological baseline, but also the natural variability about that baseline (USACE 2016). ECB 2016-25 noted that projections of climate change and impacts at local scales can be highly uncertain and proposed a qualitative assessment that may assist in future project modifications and consideration of alternatives ((examples of the qualitative assessment were included). It also required the qualitative analysis to be performed for all hydrologic studies at inland watersheds at the time of its issuance. Figure 8.1 is the flow chart included in ECB No. 2016-25; it lays out the elements of the qualitative analysis.

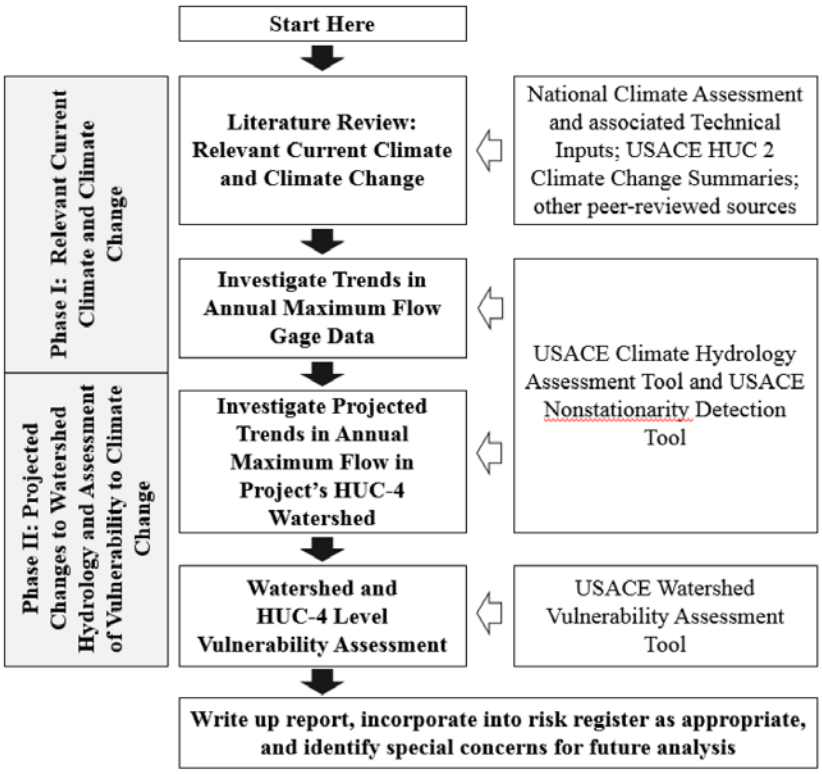

Figure 8.1. Flow chart for qualitative assessment of the impacts of climate change in hydrologic analyses (source: USACE 2016).

The USACE has also developed a web-based qualitative Climate Hydrology Assessment Tool available publicly at http://corpsclimate.us/ptcih.cfm. However, the USACE cautions that the climate hydrology output may be limited in precision, may not adequately represent watershed complexities including snowmelt and regulation, and may only be suitable for watershed-scale decisions. At the time of the publication of ECB No. 2016-25, USACE does not require qualitative assessment of climate change impacts on probable maximum flood because the existing body of research in this area is insufficient.

8.2.1 USACE Responses to Climate Change Program

The USACE also has a Responses to Climate Change Program to understand the potential impacts of climate change on natural and human-made systems (USACE 2017). As part of this program, the USACE is preparing 21 regional climate syntheses. These regions are at the scale of a two-digit Hydrologic Unit Code across the continental United States, Alaska, Hawaii, and Puerto Rico (Figure 8.2). USACE noted that outputs from climate models are coherent and useful at the scale of 2-digit HUCs and that confidence in climate model outputs declines for areas smaller than 4-digit HUCs. The regional syntheses summarize observed and projected climate and hydrological patterns as reported in national and regional reports and peer-reviewed literature. The syntheses for Regions 5, 10, and 11 were published in January 2015; that of Region 4 in April 2015; that of Region 9 in May 2015; and that of Region 7 in June 2015. The syntheses assess the vulnerability of each region to USACE business lines, including navigation, flood risk management, water supply, ecosystem restoration, hydropower, recreation, emergency management, regulatory mission, and military programs against several climate variables, including increased ambient temperatures, increased maximum temperatures, increased storm intensity and frequency, and sea-level rise.

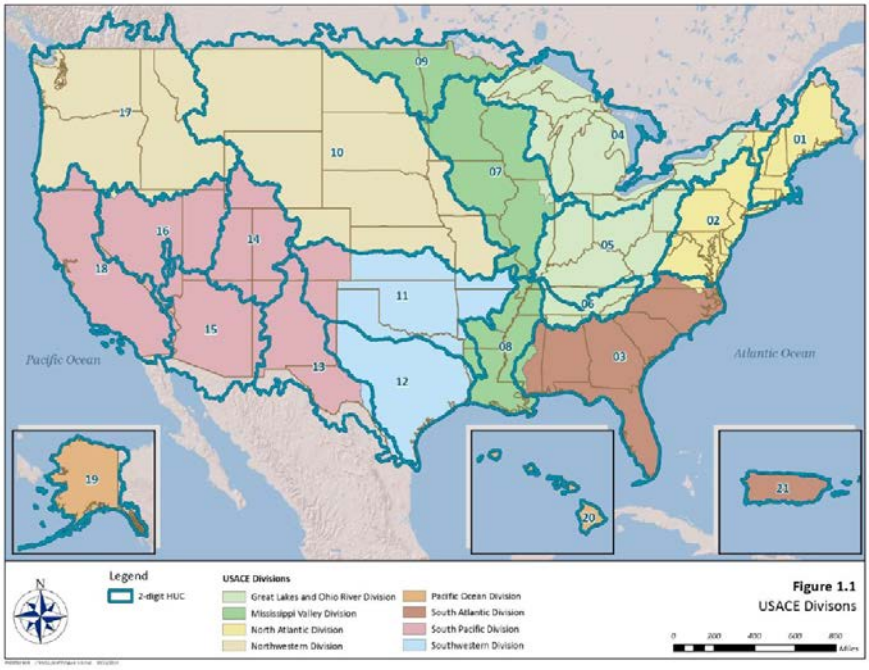

Figure 8.2. Regions used in the USACE Responses to Climate Change Program. The northeast region consists of all or parts of Water Resources Regions 01, 02, 04, and 05 (source: USACE 2015a).

USACE reviewed studies that evaluated both trends in observed hydroclimatic records and trends that are projected to occur as the 21st century progresses. The findings are summarized using a matrix for each Water Resources Region (2-digit HUC). Figures Figure 8.3-Figure 8.6 show these matrices for Regions 01, 02, 04, and 05.

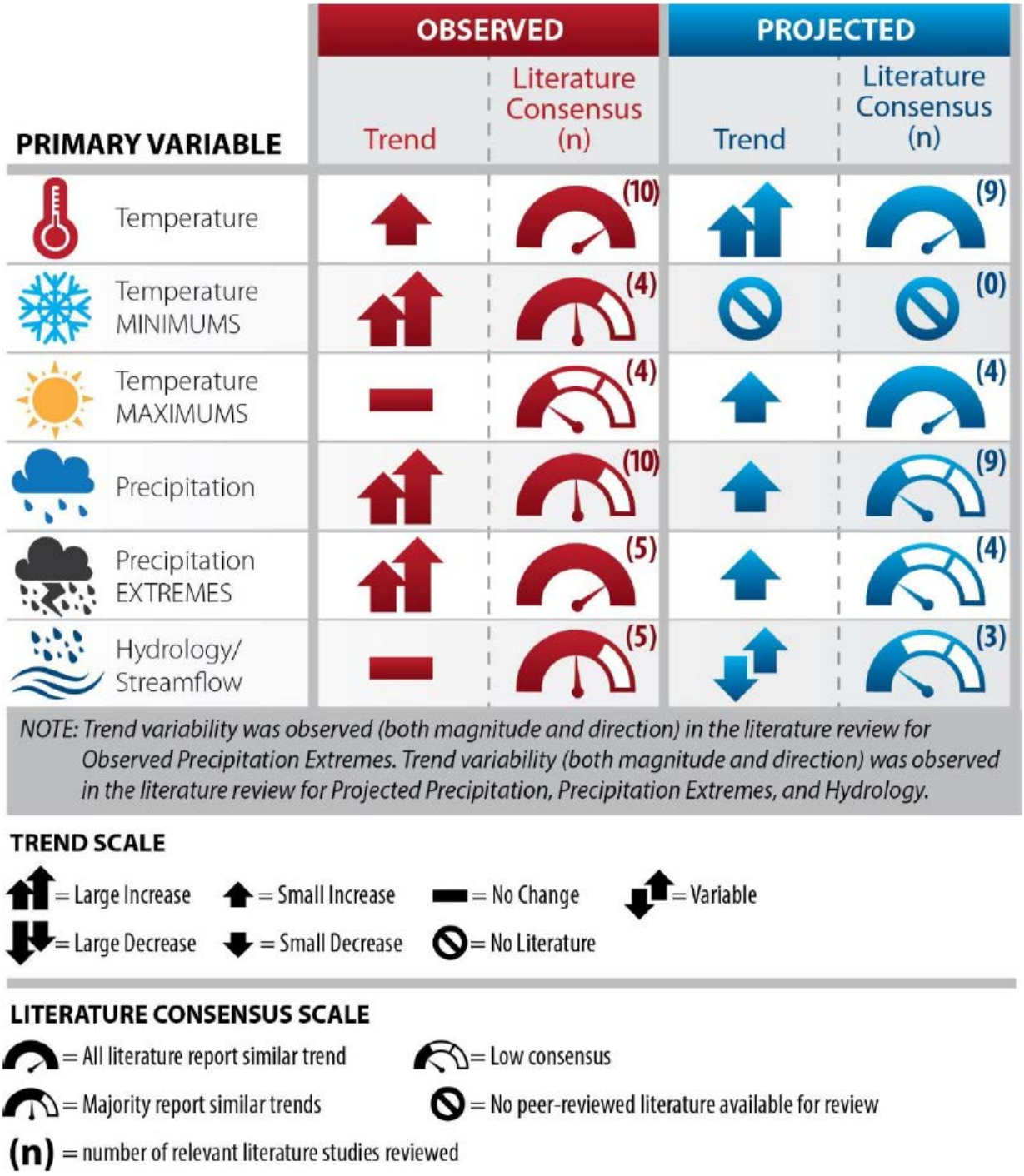

Figure 8.3. Summary of observed and projected climate trends compiled by USACE Responses to Climate Change Program – Water Resources Region 01. (Source: USACE 2015a.)

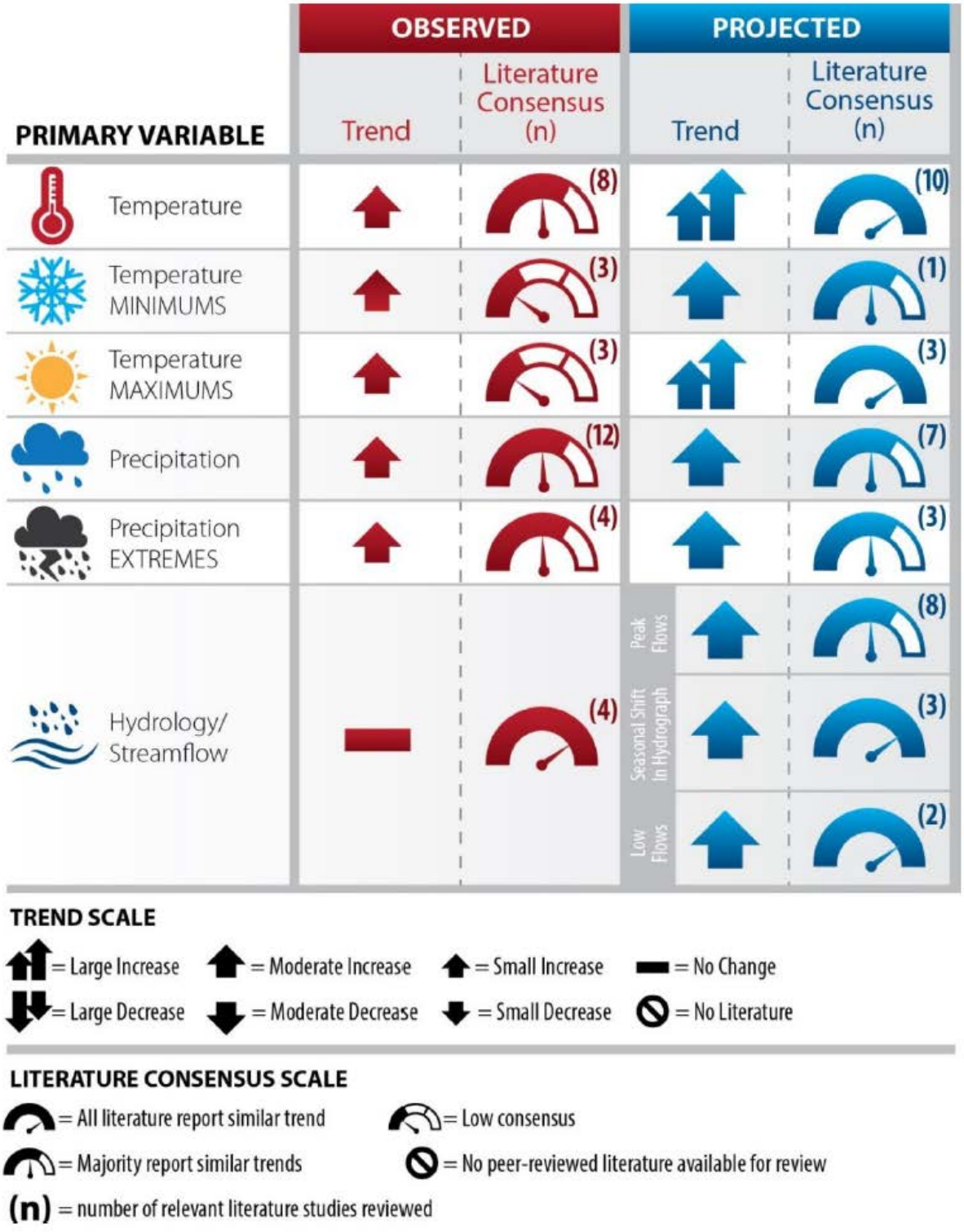

Figure 8.4. Summary of observed and projected climate trends compiled by USACE Responses to Climate Change Program – Water Resources Region 02. (Source: USACE 2015b.)

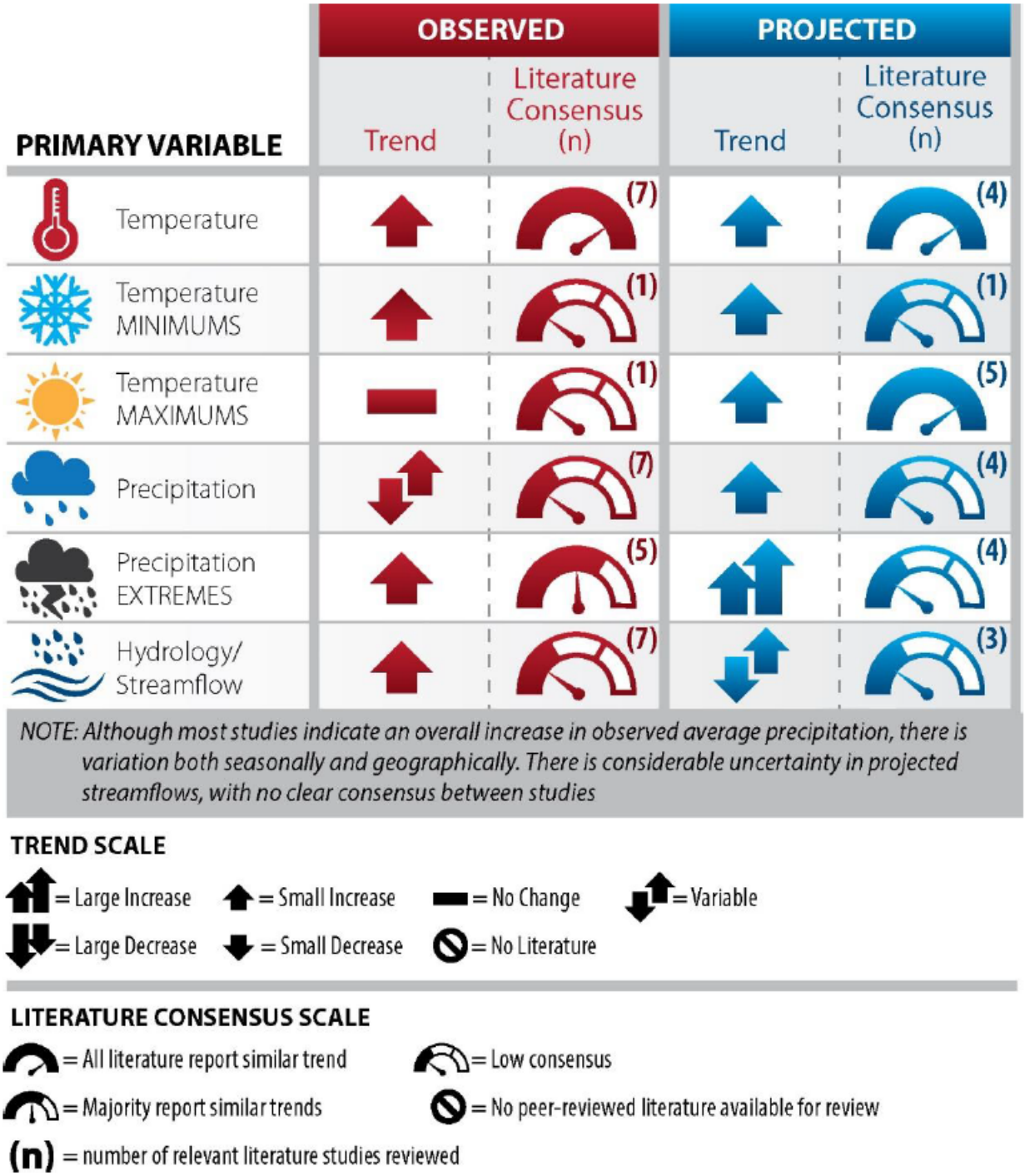

Figure 8.5. Summary of observed and projected climate trends compiled by USACE Responses to Climate Change Program – Water Resources Region 04. (Source: USACE 2015c.)

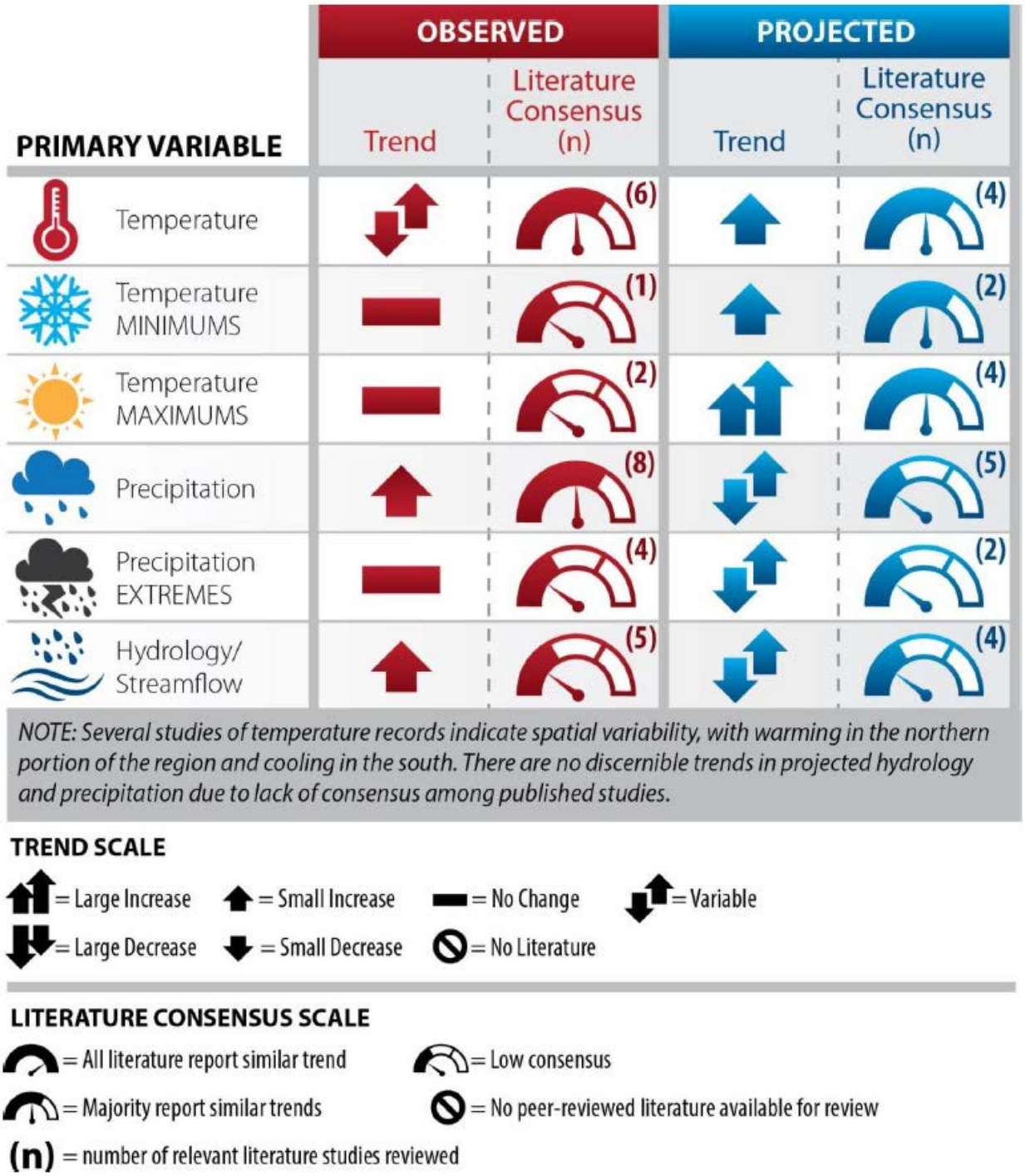

Figure 8.6. Summary of observed and projected climate trends compiled by USACE Responses to Climate Change Program – Water Resources Region 05. (Source: USACE 2015d.)

8.2.2 NOAA State Climate Summaries

The NOAA NCEI has released a set of state climate summaries containing information on historical climate variations and trends, future climate model projections of climate conditions, and past and future

sea-level and coastal-flooding conditions. These state climate summaries build on information provided in the 2014 National Climate Assessment (NCA3) and contain three types of information: key messages, narrative summaries, and downloads. The downloads include state summaries, high-resolution figures suitable for report or presentations, and supplemental web graphics.

The description of historical climate conditions for each state are based on an analysis of core climate data (the data sources are described in the supplementary online material). However, to help understand, prioritize, and describe the importance and significance of different climate conditions, additional input was derived from climate experts in each state, some of whom are authors on these state climate summaries. In particular, input was sought from the NOAA Regional Climate Centers and from the State Climatologists. The historical climate conditions are meant to provide a perspective on what has been happening in each state and what types of extreme events have historically been noteworthy, to provide a context for assessment of future impacts.

The future climate scenarios are intended to provide an internally consistent set of climate conditions that can inform analyses of potential impacts of climate change. The scenarios are not intended as projections as there are no probabilities for their future realization attached. They simply represent an internally consistent climate picture under certain assumptions about the future pathway of greenhouse gas emissions. The future climate scenarios are based on well-established sources of information. No new climate model simulations or downscaled data sets were produced for use in these state climate summaries. State climate summaries (including those in the northeast region) can be found at https://statesummaries.ncics.org.

8.2.3 EPA Report on Climate Change Indicators in the United States

The EPA has released an externally peer-reviewed report describing a variety of climate change indicators in the United States as of 2016. The information provided gives a good national overview, with some regions highlighted for particular variables. The resources page lists other good sources of information. This report is available at https://www.epa.gov/sites/production/files/2016-08/documents/climate_indicators_2016.pdf.

8.3 (U.S.-Canada) International Joint Commission

Canada and the United States signed the Boundary Waters Treaty in 1909 that authorizes the International Joint Commission (IJC) to regulate shared water issues, investigate transboundary issues, and recommend solutions related to the Great Lakes. The IJC establishes boards, task forces, and work groups to assist in carrying out its activities. For example, the Great Lakes Science Advisory Board provides scientific advice to the IJC and the Great Lakes Water Quality Board assists the IJC in identifying emerging issues and recommending solutions to complex water-quality challenges in the Great Lakes. As described in Chapter 5, the IJC directed the IUGLSB to improve understanding of how the Great Lakes function, how water levels in the lakes are changing, and what potential management options may be available relative to changing water levels in the future. In addition, NOAA's Great Lakes Environmental Research Laboratory conducts research on the dynamic environment and ecosystems of the Great Lakes and its coastal regions.

9.0 References

Barnes EA and L Polvani. 2013. Response of the midlatitude jets, and of their variability, to increased greenhouse gases in the CMIP5 models. *Journal of Climate*, 26, 7117-7135, doi:10.1175/JCLI-D-12-00536.1.

Barnes EA, LM Polvani, and AH Sobel. 2013. Model projections of atmospheric steering of Sandy-like superstorms. *Proceeding of the National Academy of Science*, 110(38), 15211-15215.

Berton R, CT Driscoll, and JF Adamowski. 2017. The near-term prediction of drought and flooding conditions in the northeastern United States based on extreme phases of AMO and NAO. *Journal of Hydrology*, 553, 130-141.

Blackmon, ML. 1976. A climatological spectral study of the 500mb geopotential height of the Northern Hemisphere. *J. Atmos. Sci*., 33, 1607–1623.

Blake ES, TB Kimberlain, RJ Berg, JP Cangialosi, and JL Beven II. 2013. *Hurricane Sandy*. Tropical Cyclone Report, National Hurricane Center, National Weather Service. Available at https://www.nhc.noaa.gov/data/tcr/AL182012_Sandy.pdf.

Bourgouin, P. 2000. A method to determine precipitation types. *Weather and Forecasting*, 15(5), 583–592. https://doi.org/10.1175/ 1520-0434(2000)015<0583:AMTDPT>2.0.CO;2

Boyer C, D Chaumont, I Chartier, and AG Roy. 2010. Impact of climate change on the hydrology of St. Lawrence tributaries. *Journal of Hydrology* 384, 65-83.

Carter E and S Steinschneider. 2018. Hydroclimatological drivers of extreme floods on Lake Ontario. *Water Resources Research*, 54, 4461–4478. https://doi.org/10.1029/2018WR022908.

Chang EKM. 2013. CMIP5 projection of significant reduction in extratropical cyclone activity over North America. *Journal of Climate* 26, 9903–9922, doi.org/10.1175/JCLI-D-13-00209.1.

Chavas, DR, and KA Emanuel. 2010. A QuikSCAT climatology of tropical cyclone size. *Geophys. Res. Lett*., 37, L18816, doi:10.1029/2010GL044558.

Coffel, ED, Horton, RM, and de Sherbinin A. (2018). Temperature and humidity based projections of a rapid rise in global heat stress exposure during the 21st century. *Environmental Research Letters*, 13, 014001.

Colle, BA, Z Zhang, KA Lombardo, E Chang, P Liu, and M. Zhang. 2013. Historical evaluation and future prediction of eastern North American and western Atlantic extratropical cyclones in the CMIP5 models during the cool season. Journal of Climate, 26, 6882-6903, doi:10.1175/JCLI-D-12-00498.1.

Collins MJ. River flood seasonality in the Northeast United States: Characterization and trends. *Hydrological Processes* 33, 687–698.

Compo, GP, JS Whitaker, and PD Sardeshmukh. 2006. Feasibility of a 100-year reanalysis using only surface pressure data. *Bull. Amer. Meteor. Soc*., 87, 175–190.

Coumou D, Petoukhov V, Rahmstorf S, Petri S and Schellnhuber HJ. 2014. Quasi-resonant circulation regimes and hemispheric synchronization of extreme weather in boreal summer. *Proc. Natl Acad. Sci*. 111 12331–6.

DeConto RM, and D Pollard D. 2016. Contribution of Antarctica to past and future sea-level rise. *Nature*, 531, 591–597.

Delworth, TL, AJ Broccoli, A Rosati, RJ Stouffer, V Balaji, JA Beesley, WF Cooke, KW Dixon, J Dunne, KA Dunne, JW Durachta, KL Findell, P Ginoux, A Gnanadesikan, CT Gordon, SM Griffies, R Gudgel, MJ Harrison, IM Held, RS Hemler, LW Horowitz, SA Klein, TR Knutson, PJ Kushner, AR Langenhorst, H Lee, S Lin, J Lu, SL Malyshev, PC Milly, V Ramaswamy, J Russell, MD Schwarzkopf, E Shevliakova, JJ Sirutis, MJ Spelman, WF Stern, M Winton, AT Wittenberg, B Wyman, F Zeng, and R Zhang. 2006. GFDL's CM2 global coupled climate models. Part I: formulation and simulation characteristics. *Journal of Climate*, 19, 643–74.

Delworth, TL, A Rosati, W Anderson, AJ Adcroft, V Balaji, R Benson, K Dixon, SM Griffies, H Lee, RC Pacanowski, GA Vecchi, AT Wittenberg, F Zeng, and R Zhang. 2012. Simulated climate and climate change in the GFDL CM2.5 high-resolution coupled climate model. *Journal of Climate*, 25, 2755–81.

Demaria EMC, RN Palmer, and JK Roundy. 2016. Regional climate change projections of streamflowcharacteristics in the Northeast and Midwest U.S. *Journal of Hydrology: Regional Studies* 5, 309-323.

Diffenbaugh NS and M Ashfaq. 2010. Intensification of hot extremes in the United States. *Geophysical Research Letters* 37(15), doi: 10.1029/2010GL043888.

Dudley RW, GA Hodgkins, MR McHale, MJ Kolian, and B Renard. 2017. Trends in snowmelt-related streamflow timing in the conterminous United States. *Journal of Hydrology*, 547, 208-221.

Easterling DR, KE Kunkel, JR Arnold, T Knutson, AN LeGrande, LR Leung, RS Vose, DE Waliser, and MF Wehner. 2017. Precipitation change in the United States. In: *Climate Science Special Report: Fourth National Climate Assessment, Volume I*, Wuebbles DJ, DW Fahey, KA Hibbard, DJ Dokken, BC Stewart, and TK Maycock (eds.). U.S. Global Change Research Program, Washington, D.C., USA, pp. 207-230, doi: 10.7930/J0H993CC.

Emanuel, K. 1994. *Atmospheric Convection*. 580 pp., Oxford Univ. Press, New York.

Evans C, KM Wood, SD Aberson, HM Archambault, SM Milrad, LF Bosart, KL Corbosiero, CA Davis, JR Dias Pinto, J Doyle, C Fogarty, TJ Galarneau, CM Grams, KS Griffin, J Gyakum, RE Hart, N Kitabatake, HS Lentink, R McTaggart-Cowan, W Perrie, JF Quinting, CA Reynolds, M Riemer, EA Ritchie, Y Sun, and F Zhang. 2017. The extratropical transition of tropical cyclones. Part I: Cyclone evolution and direct impacts. *Monthly Weather Review*, 145, 4317-4344, doi:10.1175/MWR-D-17-0027.1.

Falcone JA. 2011. GAGES–II—Geospatial attributes of gages for evaluating streamflow: U.S. Geological Survey metadata. Available at http://water.usgs.gov/GIS/metadata/usgswrd/XML/gagesII_Sept2011.xml.

Feng Z, LR Leung, S Hagos, RA Houze, Jr, CD Burleyson, and K Balaguru. 2016. More frequent intense and long-lived storms dominate the trend in central U.S. rainfall. *Nature Communications* 7, 13429, doi: 10.1038/ncomms13429.

Feng, Z, RA Houze, Jr., LR Leung, F Song, J Hardin, J Wang, W Gustafson, Jr., and C Homeyer. 2019. Spatiotemporal characteristics and large-scale environment of mesoscale convective systems east of the Rocky Mountains. *J. Clim*., doi:10.1175/JCLI-D-19-0137.1.

Feng, Z, LR Leung, RA Houze, Jr., S Hagos, J Hardin, Q Yang. B Han, and J Fan. 2018. Structure and evolution of mesoscale convective systems: Sensitivity to cloud microphysics in convection-permitting simulations over the U.S. *J. Adv. Model. Earth Syst.*, 10, doi: 10.1029/2018MS001305.

Gaborit E, V Fortin, B Tolson, L Fry, T Hunter, AD Gronewold. 2017a. Great Lakes runoff inter-comparison Project, phase 2: Lake Ontario (GRIP-O). *Journal of Great Lakes Research* 43, 217-227, https://doi.org/10.1016/j.jglr.2016.10.004.

Gaborit E, V Fortin, X Xu, F Seglenieks, B Tolson, LM Fry, T Hunter, F Anctil, and AD Gronewold. 2017b. A hydrological prediction system base don the SVS land-surface scheme: efficient calibration of GEM-Hydro for streamflow simulation over the Lake Ontario basin. *Hydrol. Earth Syst. Sci.* 21, 4825-4839.

Garner AJ, ME Mann, KA Emanuel, RE Kopp, N Lin, RB Alley, BP Horton, RM DeConto, JP Donnelly, and D. Pollard. 2017. Impact of climate change on New York City's coastal flood hazard: Increasing flood heights from the preindustrial to 2300 CE. *Proceedings of the National Academy of Sciences of the United States of America*, 114(45), 11861-11866.

Gertler CG and PA O'Gorman. 2019. Changing available energy for extratropical cyclones and associated convection in Northern Hemisphere summer. *Proceedings of the National Academy of Sciences of the United States of America*, 116(10), 4105-4110. https://dx.doi.org/10.1073/pnas.1812312116

Glas R, D Burns, and L Lautz. 2019. Historical changes in New York State streamflow: Attribution of temporal shifts and spatial patterns from 1961 to 2016. *Journal of Hydrology* 574, 308-323.

GLERL (Great Lakes Environmental Research Laboratory). 2019. About our Great Lakes: Lake by Lake Profiles. Accessed August 2, 2019 at https://www.glerl.noaa.gov/education/ourlakes/lakes.html.

Griffin, KS, and LF Bosart. 2014. The extratropical transition of Tropical Cyclone Edisoana (1990). *Mon. Wea. Rev*., 142, 2772–2793, doi:10.1175/MWR-D-13-00282.1.

Haarsma, RJ, W Hazeleger, C Severijns, H de Vries, A Sterl, R Bintanja, GJ van Oldenborgh, and HW van den Brink. 2013. More hurricanes to hit western Europe due to global warming. *Geophysical Research Letters*, 40, 1783–88.

Hart RE and JL Evans. 2001. A climatology of the extratropical transition of Atlantic tropical cyclones. *Journal of Climate*, 14(4), 546–564.

Held, IM, and E O'Brien. 1992. Quasigeostrophic turbulence in a three-layer model: Effects of vertical structure in the mean shear. *J. Atmos. Sci*., 49, 1861–1870.

Hirsch RM. 1982. A comparison of four streamflow record extension techniques. Water Resources Research, v. 18, no. 4, p. 1081–1088.

Hodges, KI. 1999. Adaptive constraints for feature tracking. *Mon. Wea. Rev*., 127, 1362–1373.

Horton R, G Yohe, W Easterling, R Kates, M Ruth, E Sussman, A Whelchel, D Wolfe, and F Lipschultz. 2014. Ch. 16: Northeast. *Climate Change Impacts in the United States: The Third National Climate Assessment*, JM Melillo, Terese (TC) Richmond, and GW Yohe, (eds.). U.S. Global Change Research Program, 371-395. doi:10.7930/J0J1012N.

Hu A and SC Bates. 2018. Internal climate variability and projected future regional steric and dynamic sea level rise. *Nature Communications*, 9, 1068.

Huang P, II Lin, C Chou, and RH Huang. 2015. Change in ocean subsurface environment to suppress tropical cyclone intensification under global warming. *Nature Communication*, 6, 7188.

Jarvinen, BR, CJ Neumann, and MAS Davis. 1984. *A tropical cyclone data tape for the North Atlantic Basin, 1886-1983: Contents, limitations, and uses*. NOAA Tech. Memo. NWS NHC 22, 21 pp.

Jelesnianski CP, J Chen, and WA Shaffer. 1992. *SLOSH: Sea, Lake, and Overland Surges from Hurricanes*. NOAA Tech. Report NWS 48, 1992.

Johnson T, J Butcher, D Deb, M Faizullabhoy, P Hummel, J Kittle, S McGinnis, LO Mearns, D Nover, A Parker, S Sarkar, R Srinivasan, P Tuppad, M Warren, C Weaver, and J Witt. 2015. Modeling streamflow and water quality sensitivity to climate change and urban development in 20 U.S. watersheds. *Journal of the American Water Resources Association* 51(5), 1321-1341.

Joyce, TM, Y-O Kwon, and L Yu. 2009. On the relationship between synoptic wintertime atmospheric variability and path shifts in the Gulf Stream and the Kuroshio Extension. *J. Climate*, 22, 3177–3192.

Kay, JE, C Deser, A Phillips, A Mai, C Hannay, G Strand, et al. 2014. The Community Earth System Model (CESM) large ensemble project: A community resource for studying climate change in the presence of internal climate variability. *Bulletin of the American Meteorological Society*, 96, 1333–1349. https://doi.org/10.1175/BAMS-D-13-00255.1.

Knutson, TR, JJ Sirutis, M Zhao, RE Tyleya, M Bender, GA Vecchi, G Villarini, and D Chavas. 2015. Global projections of intense tropical cyclone activity for the late twenty-first century from dynamical downscaling of CMIP5/RCP4.5 scenarios. Journal of Climate, 28, 7203-7224, doi:10.1175/JCLI-D-15-0129.1.

Komurcu M, KA Emanuel, M Huber, and RP Acosta. 2018. High-resolution climate projections for the northeastern United States using dynamical downscaling at convection-permitting scales. *Earth and Space Science*, 5, 801–826. https://doi.org/10.1029/2018EA000426.

Kopp RE, RM Horton, CM Little, JX Mitrovica, M Oppenheimer, DJ Rasmussen, BH Strauss, and C Tebaldi. 2014. Probabilistic 21st and 22nd century sea-level projections at a global network of tide-gauge sites. *Earth's Future*, 2, 383–406, doi:10.1002/2014EF000239.

Kopp RE, CC Hay, CM Little, and JX Mitrovica. 2015. Geographic variability of sea-level change. *Current Climate Change Reports*, 1, 192-204. http://dx.doi.org/10.7282/T37W6F4P.

Kopp RE, A Broccoli, B Horton, D Kreeger, R Leichenko, JA Miller, JK Miller, P Orton, A Parris, D Robinson, CP Weaver, M Campo, M Kaplan, M Buchanan, J Herb, L Auermuller and C Andrews. 2016. *Assessing New Jersey's Exposure to Sea-Level Rise and Coastal Storms: Report of the New Jersey Climate Adaptation Alliance Science and Technical Advisory Panel.* Prepared for the New Jersey Climate Adaptation Alliance. New Brunswick, New Jersey: Rutgers University.

Kossin JP. 2018. A global slowdown of tropical-cyclone translation speed. *Nature*, 558, 104, https://doi.org/10.1038/s41586-018-0158-3.

Kossin JP, KA Emanuel, and GA Vecchi. 2014. The poleward migration of the location of tropical cyclone maximum intensity. *Nature* 509, 350-352, doi: 10.1038/nature13278.

Kunkel KE, MA Palecki, L Ensor, D Easterling, KG Hubbard, D Robinson, and K Redmond. 2009. Trends in twentieth-century U.S. extreme snowfall seasons. *Journal of Climate* 22, 6204-6216.

Kunkel KE, DA Robinson, S Champion, X Yin, T Estilow, and RM Frankson. 2016. Trends and extremes in Northern Hemisphere snow characteristics. *Current Climate Change Reports*, 2, 65-73. http://dx.doi.org/10.1007/s40641-016-0036-8.

Kunkel KE, LE Stevens, SE Stevens, L Sun, E Janssen, D Wuebbles, J Rennells, A DeGaetano, and JG Dobson. 2013. Regional Climate Trends and Scenarios for the U.S. National Climate Assessment: Part 1. Climate of the Northeast U.S. *NOAA Technical Report NESDIS 142-1*. 87 pp. National Oceanic and Atmospheric Administration, National Environmental Satellite, Data, and Information Service, Washington, D.C. Available at http://www.nesdis.noaa.gov/technical_reports/NOAA_NESDIS_Tech_Repor t_142-1-Climate_of_the_Northeast_U.S.pdf.

Kunkel KE, DR Easterling, DAR Kristovich, B Gleason, L Stoecker, and R Smith. 2012. Meteorological causes of the secular variations in observed extreme precipitation events for the conterminous United States. *J. Hydrometeor.,* 13, 1131–1141, https://doi.org/10.1175/JHM-D-11-0108.1.

Lackmann, GM. 2015. Hurricane Sandy before 1900 and after 2100. *Bull. Am. Meteorol. Soc*., 96, 547–560.

Landsea, CW, and JL Franklin. 2013. Atlantic hurricane database uncertainty and presentation of a new database format. *Mon.Wea. Rev.*, 141, 3576–3592, doi:10.1175/MWR-D-12-00254.1.

Lin Y, W Dong, M Zhang, Y Xie, W Xue, J Huang, and Y Luo. 2017. Causes of model dry and warm bias over central U.S. and impact on climate projections. *Nature Communications* 8, 881, doi: 10.1038/s41467-017-01040-2.

Lin N, RE Kopp, BP Horton, and JP Donnelly. 2016. Hurricane Sandy's flood frequency increasing from year 1800 to 2100. *Proceeding of the National Academy of Sciences*, 113(43), 12071-12075.

Lin N, K Emanuel, M Oppenheimer, and E Vanmarcke. 2012. Physically based assessment of hurricane surge threat under climate change. *Nature Climate Change*, 2(6), 462–467.

Lins HF. 2012. USGS Hydro-Climatic Data Network 2009 (HCDN-2009). U.S.Geological Survey Fact Sheet 2012–3047. Available at https://pubs.usgs.gov/fs/2012/3047/.

Lopez H, R West, S Dong, G Goni, B Kirtman, S-K Lee, and R Atlas. 2018. Early emergence of anthropogenically forced heat waves in the western United States and Great Lakes. *Nature Climate Change* doi:10.1038/s41558-018-0116-y.

Lucas C, B Timbal, and H Nguyen. 2014. The expanding tropics: a critical assessment of the observational and modeling studies. *WIREs. Clim. Change* 5, 89–112.

Luettich RA, JJ Westerink, and NW Scheffner. 1992. *ADCIRC: An Advanced Three-dimensional Circulation Model for Shelves, Coasts and Estuaries, Report 1: Theory and Methodology of ADCIRC-2DDI and ADCIRC-3DL DRP Technical Report DRP-92-6*. (Department of the Army, US Army Corps of Engineers, Waterways Experiment Station, 1992).

Lunkeit, F, K Fraedrich, and SE Bauer. 1998. Storm tracks in a warmer climate: Sensitivity studies with a simplified global circulation model. *Climate Dyn*., 14, 813–826.

Lynch C, A Seth, and J Thibeault. 2016. Recent and projected annual cycles of temperature and precipitation in the northeast United States from CMIP5. *Journal of Climate*, 29, 347-365.

Massey N, R Jones, FEL Otto, T Aina, S Wilson, JM Murphy, D Hassell, YH Yamazakif and MR Allen. 2015. Weather@home development and validation of a very large ensemble modeling system for probabilistic event attribution. *Quarterly Journal of the Royal Meteorological Society*, 141, 1528–45.

Melillo JM, TC Richmond, and GW Yohe (eds.). 2014. *Climate Change Impacts in the United States: The Third National Climate Assessment*. U.S. Global Change Research Program, 841 pp. doi:10.7930/J0Z31WJ2.

Miller K, RE Kopp, BP Horton, JV Browning, and AC Kemp. 2013. A geological perspective on sea-level rise and its impacts along the U.S. mid-Atlantic coast. *Earth's Future*, 1, 3–18, doi:10.1002/2013EF000135.

Miralles DG, Teuling AJ, van Heerwaarden CC and Vil`a-Guerau de Arellano J. 2014. Mega-heatwave temperatures due to combined soil desiccation and atmospheric heat accumulation. *Nat. Geosci*. 7 345–9.

NCEI (National Centers for Environmental Information). 2016a. *U.S. Climate Atlas*. Available at http://www.ncdc.noaa.gov/climateatlas/.

NCEI (National Centers for Environmental Information). 2018. *Comparative Climatic Data For the United States Through 2018*. NOAA NCEI, Ashville, North Carolina. Available at https://www.ncdc.noaa.gov/sites/default/files/attachments/CCD-2018.pdf.

NCEP (National Centers for Environmental Protection). 2019. *Hurricane Agnes – June 14-25, 1972*. Accessed August 19, 2019 at https://www.wpc.ncep.noaa.gov/tropical/rain/agnes1972.html.

Neumann, CJ, BR Jarvinen, CJ McAdie, and GR Hammer. 1999. *Tropical cyclones of the North Atlantic Ocean, 1871–1999*. NOAA/NWS/NESDIS Historical Climatology Series 6-2, 206 pp.

NRC (U.S. Nuclear Regulatory Commission). 2016. Guidance for Activities Related to Near-Term Task Force Recommendation 2.1, Flooding Hazard Reevaluation; Focused Evaluation and Integrated Assessment. Interim Staff Guidance JLD-ISG-2016-01. Available at https://www.nrc.gov/docs/ML1609/ML16090A140.pdf.

NRC (U.S. Nuclear Regulatory Commission). 2018. *Information Digest, 2018-2019*. NUREG-1350, Volume 30. Accession No. ML18226A114. Accessed October 22, 2018 at https://www.nrc.gov/reading-rm/doc-collections/nuregs/staff/sr1350/.

NRCC (Northeast Regional Climate Center). 2019. *Climate Normal Maps*. Available at http://www.nrcc.cornell.edu/regional/climatenorms/climatenorms.html.

NWS (National Weather Service). 2012. Hurrican Irene, August 21-30, 2011. Service Assessment. National Oceanic and Atmosphric Administration National Weather Service, September 2012. Accessed August 12, 2019 at https://www.weather.gov/media/publications/assessments/Irene2012.pdf.

O'Gorman PA. 2010. Understanding the varied response of the extratropical storm tracks to climate change. *Proceedings of the National Academy of Sciences*, 107(45), 19176–19180, doi:10.1073/pnas.1011547107.

Patricola CM and MF Wehner. 2018. Anthropogenic influences on major tropical cyclone events. Nature, 563, 339. https://doi.org/10.1038/s41586-018-0673-2.

Pierce DW, DR Cayan, and BL Thrasher. 2014. Statistical downscaling using Localized Constructed Analogs (LOCA). *Journal of Hydrometeorology* 15, 2558–2585, doi: 10.1175/JHM-D-14-0082.1.

Prein AF, C Liu, K Ikeda, R Bullock, RM Rasmussen, GJ Holland, and M Clark. 2017a. Simulating North American mesoscale convective systems with a convection-permitting climate model. *Climate Dynamics*, https://doi.org/10.1007/s00382-017-3947-8.

Prein AF, RM Rasmussen, K Ikeda, C Liu, MP Clark, and GJ Holland. 2017b. The future intensification of hourly precipitation extremes. *Nature Climate Change*, 7, 48–52, doi: 10.1038/nclimate3168.

Reed AJ, ME Mann, KA Emanuel, N Lin, BP Horton, AC Kemp, and JP Donnelly. 2015. Increased threat of tropical cyclones and coastal flooding to New York City during the anthropogenic era. *Proceeding of the National Academy of Sciences*, 112, 12610–12615.

Risser MD and MF Wehner. 2017. Attributable human-induced changes in the likelihood and

magnitude of the observed extreme precipitation during Hurricane Harvey. *Geophysical Research Letters*, 44(24), 12,457-412,464. https://dx.doi.org/10.1002/2017gl075888.

Sallenger Jr AH, KS Doran, and PA Howd. 2012. Hotspot of accelerated sea-level rise on the Atlantic coast of North America. *Nature Climate Change*, 2, 884-888.

Schulte JA, RG Najjar, and M Li. 2016. The influence of climate modes on streamflow in the mid-Atlantic region of the United States. *Journal of Hydrology: Regional Studies* 5, 80-99.

Sherwood SC. 2018. How important is humidity in heat stress? *Journal of Geophysical Research: Atmospheres* 123, 11,808–11,810. https://doi.org/10.1029/2018JD028969.

Staten, PW, L Jian, KM Grise, SM Davis, and T Birner. 2018. Re-examining tropical expansion. *Nature Climate Change*, 8, 768-775. https://doi.org/10.1038/s41558-018-0246-2.

Taylor KE, RJ Stouffer, and GA Meehl. 2012. An overview of CMIP5 and the experiment design. Bulletin of the American Meteorological Society 93, 485–498.

Thibeault JM and A Seth. 2014. Changing climate extremes in the Northeast United States: observations and projections from CMIP5. *Climate Change* 127, 273-287.

Tolson BA and CA Shoemaker. 2007. Dynamically dimensioned search algorithm for computationally efficient watershed model calibration. *Water Resour. Res.*, 43, W01413, https://doi.org/10.1029/2005WR004723.

USACE (U.S. Army Corps of Engineers). 2015a. *Recent US Climate Change and Hydrology Literature Applicable to US Army Corps of Engineers Missions – New England Region 01*. Civil Works Technical Report, CWTS 2015-20, USACE, Washington, D.C.

USACE (U.S. Army Corps of Engineers). 2015b. *Recent US Climate Change and Hydrology Literature Applicable to US Army Corps of Engineers Missions – Mid-Atlantic*. Civil Works Technical Report, CWTS 2015-09, USACE, Washington, D.C.

USACE (U.S. Army Corps of Engineers). 2015c. *Recent US Climate Change and Hydrology Literature Applicable to US Army Corps of Engineers Missions – Great Lakes Region 04*. Civil Works Technical Report, CWTS 2015-07, USACE, Washington, D.C.

USACE (U.S. Army Corps of Engineers). 2015d. *Recent US Climate Change and Hydrology Literature Applicable to US Army Corps of Engineers Missions – Ohio Region 05*. Civil Works Technical Report, CWTS 2015-05, USACE, Washington, D.C.

USACE (U.S. Army Corps of Engineers). 2016. *Guidance for Incorporating Climate Change Impacts to Inland Hydrology in Civil Works Studies, Designs, and Projects*. Engineering and Construction Bulletin, No. 2016-25, Corps of Engineers Civil Works, Washington, D.C.

USACE (U.S. Army Corps of Engineers). 2017. *Responses to Climate Change*. Available at http://corpsclimate.us/index.cfm.

USGCRP (U.S. Global Change Research Program). 2017. *Climate Science Special Report: Fourth National Climate Assessment, Volume I*, Wuebbles DJ, DW Fahey, KA Hibbard, DJ Dokken, BC Stewart, and TK Maycock (eds.), Washington, D.C., USA, 470 pp., doi: 10.7930/J0J964J6.

USGCRP (U.S. Global Change Research Program). 2018. *Impacts, Risks, and Adaptation in the United States: Fourth National Climate Assessment, Volume II*, Reidmiller DR, CW Avery, DR Easterling, KE Kunkel, KLM Lewis, TK Maycock, and BC Stewart (eds.), Washington, D.C., USA, 1515 pp. doi: 10.7930/NCA4.2018.

USGS (U.S. Geological Survey). 1975. *Hurricane Agnes rainfall and floods, June-July 1972*. U.S. Geological Survey Professional Paper 924, 403 p. Available at https://pubs.usgs.gov/pp/0924/report.pdf.

USGS (U.S. Geological Survey). 2006. *Flood of April 2–3, 2005, Neversink River Basin, New York*. U.S. Geological Survey Open-File Report 2006–1319, 98 p.

USGS (U.S. Geological Survey). 2009. *Characteristics of the April 2007 flood at 10 streamflow-gaging stations in Massachusetts*. U.S. Geological Survey Scientific Investigations Report 2009–5068, 75 p. Available at http://pubs.usgs.gov/sir/2009/5068.

USGS (U.S. Geological Survey). 2012. *Magnitude of flood flows for selected annual exceedance probabilities in Rhode Island through 2010 (ver. 1.2, revised March 2013)*. U.S. Geological Survey Scientific Investigations Report 2012–5109, 81 p. Available at http://pubs.usgs.gov/sir/2012/5109.

USGS (U.S. Geological Survey). 2013. *Monitoring storm tide and flooding from Hurricane Sandy along the Atlantic coast of the United States, October 2012*. U.S. Geological Survey Open-File Report 2013–1043, 42 p. Available at http://pubs.usgs.gov/of/2013/1043/.

USGS (U.S. Geological Survey). 2015a. *Flooding in the Northeastern United States, 2011*. U.S. Geological Survey Professional Paper 1821, 32 p. Available at http://dx.doi.org/10.3133/pp1821.

USGS (U.S. Geological Survey). 2015b. *Analysis of storm tide impacts from Hurricane Sandy in New York*. U.S. Geological Survey Scientific Investigations Report 2015–5036, 75 p. Available at http://dx.doi.org/10.3133/sir20155036.

van Oldenborgh GJ, K van der Wiel, A Sebastian, R Singh, J Arrighi, F Otto, K Haustein, S Li, G Vecchi, and H Cullen. 2017. Attribution of extreme rainfall from Hurricane Harvey, August 2017. *Environmental Research Letters*, 12(12). https://dx.doi.org/10.1088/1748-9326/aa9ef2

van Weverberg, K, AM Vogelmann, W Lin, EP Luke, A Cialella, P Minnis, et al. 2013. The role of cloud microphysics parameterization in the simulation of mesoscale convective system clouds and precipitation in the tropical Western Pacific. *Journal of the Atmospheric Sciences*, 70(4), 1104–1128. https://doi.org/10.1175/jas-d-12-0104.1.

Vecchi, GA et al. 2006. Weakening of tropical Pacific atmospheric circulation due to anthropogenic forcing. *Nature*, 441, 73–76.

Wang SYS, L Zhao, JH Yoon, P Klotzbach, and RR Gillies. 2018. Quantitative attribution of climate effects on Hurricane Harvey's extreme rainfall in Texas. *Environmental Research Letters*, 13(5). https://dx.doi.org/10.1088/1748-9326/aabb85.

Vose RS, DR Easterling, KE Kunkel, AN LeGrande, and MF Wehner. 2017. Temperature changes in the United States. In: *Climate Science Special Report: Fourth National Climate Assessment, Volume I*, Wuebbles DJ, DW Fahey, KA Hibbard, DJ Dokken, BC Stewart, and TK Maycock (eds.). U.S. Global Change Research Program, Washington, D.C., USA, pp. 185-206, doi: 10.7930/J0N29V45.

Yang, Q, R. Houze, Jr., LR Leung, and Z Feng. 2017. Environments of long-lived mesoscale convective systems over the central United States in convection permitting climate simulations. *J. Geophys. Res.*, 122, doi: 10.1002/2017JD027033.

Yin, JH. 2005. A consistent poleward shift of the storm tracks in simulations of the 21st century climate. *Geophys. Res. Lett*., 32, L18701, doi:10.1029/2005GL023684.

Zarzycki, CM. 2018. Projecting changes in societally impactful northeastern U.S. snowstorms. *Geophysical Research Letters*, 45, 12,067–12,075. https://doi.org/10.1029/2018GL079820.

Pacific Northwest
NATIONAL LABORATORY

www.pnnl.gov

902 Battelle Boulevard
P.O. Box 999
Richland, WA 99352
1-888-375-PNNL (7665)

U.S. DEPARTMENT OF
ENERGY